Technische Universität München

Fakultät für Informatik
Computer Aided Medical Procedures (I-16)

Tomographic Reconstruction beyond Classical X-ray CT

Jakob Vogel

Vollständiger Abdruck der von der Fakultät für Informatik der Technischen Universität München zur Erlangung des akademischen Grades eines

Doktors der Naturwissenschaften (Dr. rer. nat.)

genehmigten Dissertation.

Vorsitzender:		Univ.-Prof. Dr. Nils Thürey
Prüfer der Dissertation:	1.	Univ.-Prof. Dr. Nassir Navab
	2.	Univ.-Prof. Dr. Franz Pfeiffer
	3.	Univ.-Prof. Dr. Joachim Hornegger Friedrich-Alexander-Universität Erlangen-Nürnberg

Die Dissertation wurde am 07. Juli 2015 bei der Technischen Universität München eingereicht und durch die Fakultät für Informatik am 14. September 2015 angenommen.

Tötschling, Sontheim, München, Waldshut
July 2016

Abstract

Visual illustrations are an important tool in natural sciences and engineering, considering that such information is quite natural for the human mind. For centuries, researchers were required to possess considerable artistic skills to accurately reproduce their own impressions, both in terms of shape and colour. In fact, arts and science have often occurred in conjunction, considering the inventions and studies of Leonardo da Vinci, for example. This situation changed considerably with the invention of photography around 1830, turning the illustration process into a largely technical one, thus making images feasible in more cases.

Another leap was Wilhelm Conrad Röntgen's discovery of X-rays in 1895. Their properties are of high interest for physicists, but the fact that they can penetrate matter and expose photographic paper afterwards has made their discovery epochal. For the first time, internal structures could be imaged in a seemingly safe, non-invasive way. For this reason, X-ray transillumination has become a key technology particularly in medicine, providing patient-specific and accurate anatomical images in a short time, thus paving the way towards evidence-based medicine. Obversely, it also took time to realise the perils of ionising radiation.

The next major advancement in medical imaging was the development of X-ray computed tomography (CT) during the 1960s. Instead of a projection, a three-dimensional structure is computed from several X-ray images of a static scene. Like that, the perspective and appearance of the illustration is not predetermined, but can be chosen retrospectively. Together with other imaging modalities such as magnetic resonance imaging, ultrasonography, or nuclear functional imaging, X-ray CT has become an integral part of medical diagnosis, intervention planing and monitoring.

Computers form a key component of CT systems, and since the design of the first devices, computer technology has improved dramatically. For years, computing a CT reconstruction imposed a considerable burden onto the machinery, and simplifications and rough approximations have been used. Only in recents years, processors, particularly graphics processors, have become sufficiently fast to abandon the classical way of computing tomographic reconstructions, thus allowing to consider new problems.

This thesis discusses three such problems 'beyond' current practice, after reviewing the history and established methods of tomographic reconstruction.

As first problem, the possibility of reconstructing a scene even from incoherent projections is investigated. Standard CT requires the projection images to show the same static object from different perspectives, but in reality, data acquisition may be too slow for this to be true,

for example when imaging a beating heart. In order to still reconstruct a useful shape with an acceptable level of motion-related artefacts, special measures must be taken to compensate. This thesis presents a level-set-based method combining shape and motion field reconstruction.

Second, raw measurements for tomographic reconstruction are usually acquired in gantry-based devices where the sensors take a pre-determined, standard trajectory known to work in general cases. Still, there are cases where irregular, patient-specific acquisition of the input perspectives would be beneficial. This is of particular interest when radioactive tracers are involved where measurements drop off exponentially with distance, and the detector should be as close as possible to the patient. The thesis demonstrates an acquisition scheme designed to yield optimal sensor paths for such cases.

Finally, the thesis describes a novel constrained tomographic reconstruction method for X-ray scattering tensors, using data obtained in a grating-based X-ray interferometry setup and the respective forward model proposed by Malecki *et al.* [Mal14]. While standard CT limits itself to attenuation information, phase-shift and scattering data can also be acquired in an appropriately equipped setup, and tomographic reconstruction of the latter signal component is of particular interest. Unlike attenuation CT where scalar values are reconstructed, tensor-valued data will need to be recovered, thus presenting new challenges in terms of computing and constraining iterates and visualising results.

Zusammenfassung

Bildliche Darstellungen sind ein wichtiges Mittel in den Natur- und Ingenieurswissenschaften, da Bilder für den Menschen sehr selbstverständlich sind. Über Jahrhunderte hinweg mussten Forschende beträchtliche künstlerische Fähigkeiten besitzen um ihre eigenen Eindrücke im Hinblick auf Form und Farbe exakt wiederzugeben. Tatsächlich waren Kunst und Wissenschaften oft eng verknüpft, so beispielsweise in den Erfindungen und Studien von Leonardo da Vinci. Dies änderte sich erheblich mit der Erfindung der Photographie um 1830, wodurch sich der Bildgebungsprozess zu einem eher technischen Verfahren wandelte, und so auch die häufigere Erstellung von Bildern ermöglichte.

Ein weiterer Schritt war die Entdeckung der Röntgen-Strahlen durch Wilhelm Conrad Röntgen im Jahr 1895. Die genauen Eigenschaften dieser Strahlung sind für Physiker von großem Interesse, aber die Tatsache, dass sie Materie durchqueren und anschließend Photopapier belichten können, machen sie zu einer bahnbrechenden Entdeckung. Zum ersten Mal konnten so verdeckte Strukturen in einem scheinbar sicheren Verfahren sichtbar gemacht werden. Aus diesem Grund wurde die Röntgen-Durchleuchtung zu einer Schlüsseltechnologie, vor allem in der Medizin, wo dank ihrer patienten-spezifische, exakte anatomische Bilder in kurzer Zeit erstellt werden können. So wurde dieses Bildgebungsverfahren zu einem wichtigen Teil moderner Evidenz-basierter Medizin. Auf der anderen Seite dauerte es auch einige Zeit bis die Gefahren ionisierender Strahlung verstanden wurden.

Die nächste große Entwicklung im Bereich der medizinischen Bildgebung war die der Röntgen-Computertomographie (CT) während der 1960er Jahre. Statt einer einfachen Projektion wird aus mehren Röntgen-Bildern die dreidimensionale Struktur einer statischen Szene berechnet. Dadurch sind Blickwinkel und Erscheinung der Darstellung nicht mehr ab dem Aufnahmezeitpunkt vordefiniert, sondern können im Nachhinein frei gewählt werden. Zusammen mit anderen bildgebenden Verfahren wie Magnetresonanz-Tomographie, Ultraschall-Sonographie oder nuklearmedizinischer Bildgebung wurde Röntgen-CT zu einem integralen Bestandteil medizinischer Diagnostik und wird ebenso verwandt für die Planung von Eingriffen und bei der Überwachung von Heilungsverläufen.

Rechner sind eine Schlüsselkomponente von CT-Systemen, und die Computertechnik hat sich seit den ersten derartigen Geräten geradezu dramatisch entwickelt. Über lange Jahre hinweg stellte die Berechnung einer CT-Rekonstruktion für die Prozessoren eine komplexe, langwierige Aufgabe dar, weswegen vereinfachende Annahmen nötig wurden. Erst seit relativ kurzer Zeit sind die Rechenkerne, vor allem Graphik-Prozessoren, schnell genug um sich von

den klassischen Berechnungsverfahren zu lösen und neue Fragen anzugehen.

Diese Arbeit beschäftigt sich mit drei derartigen Problemstellungen „jenseits“ aktuell praktisch eingesetzter Technik. Zuvor werden die Geschichte und die bewährten Methoden zur tomographischen Rekonstruktion beleuchtet.

Als erstes Problem wird die Frage untersucht, ob eine Szene auch rekonstruiert werden kann, wenn die Projektionen durch Bewegung nicht „stimmig“ sind. Eigentlich erfordert CT ja, dass die Eingabedaten ein statisches Objekt aus verschiedenen Perspektiven zeigen. In Wirklichkeit jedoch kann die Datenaufzeichnung zu langsam sein, beispielsweise wenn ein schlagendes Herz aufgenommen werden soll. Um trotzdem eine sinnvolle Rekonstruktion zu erhalten, die durch bewegungsbedingte Bildfehler allenfalls begrenzt verfälscht ist, müssen spezielle Maßnahmen getroffen werden. Diese Arbeit stellt hierzu einen Methode vor, bei der, basierend auf einer Niveaumenge, die gleichzeitige Rekonstruktion von Form und Bewegung versucht wird.

Weiter werden die Ausgangsmessungen für tomographische Verfahren normalerweise in speziellen Scannern aufgenommen, bei denen sich die Mess-Sensoren in einer vorbestimmten Weise um die Zielregion bewegen bzw. fest angeordnet sind. Es gibt jedoch Fälle, in denen eigens errechnete Patienten-spezifische Perpektiven von Vorteil wären. Derartiges ist von besonderem Interesse wenn radioaktive Kontrastmittel verwendet werden, bei denen die Strahlung mit wachsender Entfernung exponentiell abnimmt, und die Gammakamera als Strahlungssensor dementsprechend möglichst nahe am Patienten messen sollte. Die Arbeit stellt ein Steuerschema vor, das für derartige Szenarien einen optimalen Pfad ergibt.

Zuletzt beschäftigt sich diese Arbeit mit einer neuen Rekonstruktionsmethode für anisotropische, tensor-wertige Röntgenstreuung, die insbesondere die getroffenen Annahmen als Nebenbedingung berücksichtigt. Dieser Teil der Arbeit nutzt Daten aus einem Gitter-basierten Aufbau zur Röntgen-Interferometrie und verwendet die von Malecki *et al.* [Mal14] vorgeschlagene mathematische Modellierung. Während sich nämlich klassisches CT auf die Abschwächung der Röntgenstrahlung beschränkt, können in entsprechend ausgerüsteten Messaufbauten auch die Phasenverschiebung und die Streuung gemessen werden. Die tomographische Rekonstruktion der letztgenannten Komponente ist von speziellem Interesse, wobei jedoch keine skalaren Werte, sondern Tensoren berechnet werden müssen. Dadurch ergeben sich neue Herausforderungen im Hinblick auf das Rekonstruktionsverfahren, aber auch auf die Darstellung der Ergebnisse.

Contents

Part I.

Basics

1. About Images

Thousands of years ago, in the Palaeolithic Age, when humanity was still organised into small nomadic groups of foragers, some of them have taken the time to create astonishing cave art. Among the most notable examples are the cave paintings of Altamira [San80; Car03] and Lascaux [Bre52]. The fact that illustrations of the ancients survived for (potentially far) more than 10'000 years appears to be fantastic, and their discovery in the late 19$^{\text{th}}$ century initially incited considerable scepticism [Car02]. Since, however, archeologists and art historians have accepted them as genuine and produced several theories about the motivation of what they refer to as Parietal Art.

Independent of this question – may it be shamanism, hunting magic, or plainly art – there is another intriguing aspect concerning these paintings: Despite the fact that many years and dramatic social, philosophical, technological and scientific advances separate 'us' from 'them', seeing their designs of horses, deers and aurochs, we can empathise with these ancient tribes. Every human being, independent of education or experience, can simply develop vivid ideas of what mattered for a society of hunter-gatherers.

Unlike such illustrations, people struggle much more with ancient writing. Understanding age-old characters can quickly become a highly complicated endeavour, often requiring skills in cryptanalysis. An example is the deciphering of the Egyptian hieroglyphs by Jean-François Champollion [Cha22], based on the famous *Rosetta Stone*, and Kahn [Kah96a] lists many more such examples. But even when language and glyphs are perfectly known, like Latin or sometimes even contemporary texts, translating and interpreting a document can be a task for an expert.

Consequently, independent of who is communicating information to whom, there appears to be a fundamental difference in how text (or even data) and graphical illustrations are perceived by the human mind. Among the first scholars to develop a modern theory about visual perception was Hermann von Helmholtz [Hel67]. In short, he explains vision as a two-stage process where optical stimuli, the sensation, are transformed into a perception. The first stage is truly unconscious and described to be of a rather 'technical' nature, encompassing colour and stereo-vision, for instance. In particular, it can not be influenced by knowledge or experience, a conclusion Helmholtz bases on recurring optical illusions that can not be avoided. On the other hand, the second stage appears to organise the sensation into semantic entities of a higher order and deducts features based on experience, such as shape from shading or words and glyphs from lines. Particularly this second phase is of a logical, but still subconscious

nature. The entire process is hence referred to as *unconscious inference* – a construct which was met with scepticism[1] at the time. As justification, Helmholtz explicates that an individual will typically not be able to tell exactly why he or she arrived at a certain impression, which stimuli have lead to it, which have been (unwillingly) discarded, and which parts of the perception are experience-based. In particular, the eye reports impressions necessarily as true, and does not subject them to rational scrutiny. Finally, Helmholtz also distinguishes between passively perceiving things and actively observing them, where senses are tuned to collect particular impressions that the conscious mind is interested in. Later, Karl Popper [Pop72] would stress this distinction and define observation as key scientific activity, as necessary tool to challenge hypotheses.

Despite their age, Helmholtz' conclusions are highly respected to this day, and perception and gestalt psychology (Wolfgang Metzger [Met53], for instance) have extended our understanding of the visual sense over the years. In a nutshell, vision appears to be an intricate pre-rational system to quickly perceive large amounts of information by subconsciously interpreting stimuli in the light of one's experience. In real life, this mechanism – together with other senses – allows us to quickly orient ourselves, perceive a complex environment with situation-dependent focus and abstraction, and to attach meaning to objects.

Aware of his powerful visual sense, in spite of it falling prey to illusions at times and its inherent subjective nature,[2] (re-)creating visual impressions via images, models and sculptures seems to be a natural activity for humans,[3] and archeologists have found such evidence from many cultures and ages. The reasons for crafting such a depiction can be different: Remembering activities, idolising or taming supernatural powers, coping with traumata, to name a few. In all such cases, studying the images, the impressions subconsciously spark the observer's imagination and serve as starting point for associative chains. Written text and spoken language, on the other hand, are usually processed by the conscious mind and require knowledge of context and conventions.

1. Apparently, at earlier times, logical conclusions have been considered to be exclusive to a conscious, intelligent mind. Particularly since the invention of computers, we seem to be more comfortable with Helmholtz' concept of unconcious inference.
2. Popper [Pop72] interprets Heisenberg's uncertainty principle [Hei27], originally a finding related to quantum physics, abstractly as general acknowledgement of subjectiveness. Consequently, there is no way to perceive an arbitrarily objective impression.
3. We even expect extraterrestrials to rely on their eyes: Two *Pioneer* spacecraft launched in 1972 and 1973 carry plaques showing sketches, and the *Arecibo message* transmitted in 1974 is effectively a two-dimensional image showing sketches and data. See Kahn [Kah96b] for an early account of research towards logic- and image-based interstellar communication as pursued by Drake and Sagan, for instance.

Figure 1.1.: The famous *Face on Mars* as photographed by NASA's Viking 1 Orbiter spacecraft in July 1976. A combination of shadows, bluriness and noise deceives the human mind into seeing a human face, a shape well-known from experience. *(NASA/JPL)*

1.1. Arts and Sciences

Taking into account the wide range of creative activities leading to images, the focus needs to be restricted. In a first refinement step, consider natural sciences in general: As collaborative activity, they inherently rely on communication of experiments, observations, and conclusions. In a classical setting, a researcher will try to deduce an *explicandum* – an effect or condition to be explained – by proposing a logically sound *explicans* – a hypothesis. These expressions have been borrowed from Popper's theory about the progress of scientific knowledge [Pop72]. Further following his concept, public communication of the two would lead to colleagues challenging the *explicans*, in an attempt to falsify it.

Exploiting the specialised visual sense, images can be used very advantageously in publishing and discussing scientific work. For instance, an unknown *explicandum*, a novel visual *observation*, is – trivially – best presented as faithful reproduction. By examining such an image, a peer with a different background is downright challenged to question interpretations. A written text describing the same observation would necessarily be biased and devoid of many alternatives. Instead, it would be a description of the particular *impression* a conscious mind had, and thus filtered and abstracted by its experience. Furthermore, a novel, complex concept or model (an *explicans*) can often be conveniently presented as illustration with high information density. On the other hand, factual information such as hypotheses, interpretations, experimental data or conclusions can be more precisely stated as written text or with tables of numbers.

Consequently, images play a vital role in natural sciences since centuries. Originally, researchers were required to possess considerable artistic skills to accurately reproduce their own impressions – both in terms of shape and colour – and arts and sciences have long occurred in conjunction. Famous examples are known from anatomy, archeology, architecture, astronomy, biology, botany, geography, and microscopy, among many others. In most such cases, by means of traveling or creating novel optical devices, individuals acquired and shared

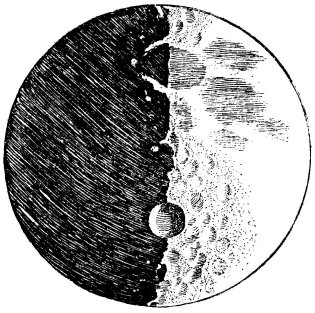

(a) Galilei's moon, 1610 *(Wikimedia Commons)*

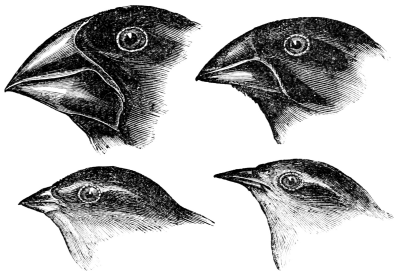

(b) Darwin's finches, 1845 *(Wikimedia Commons)*

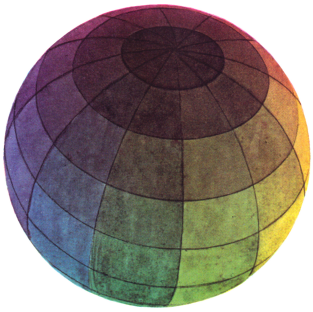

(c) Runge's colour sphere, 1810

Figure 1.2.: Early scientific drawings. Taken from the original publications by Galilei [Gal10], Darwin [Dar45], and Runge [Run10]. *(Public Domain)*

previously unknown impressions of exotic plants and animals, of microbes only observable through a microscope, or of planets only visible as small bright dots in the night sky without a telescope. Consider, for instance, the various studies by Leonardo da Vinci, the sketches of the moon by Galileo Galilei [Gal10], the drawings in the books by Charles Darwin [Dar45] or the colour theories of Johann Wolfgang von Goethe and Philipp Otto Runge [Run10]. In many fields, these abilities have been canonicalised, and to this day, engineering and architecture students spend considerable time practicing technical drawing.

1.2. Photography

However, this situation changed fundamentally with the development of modern photography by Joseph Nicéphore Niépce in 1822 (cf. Barthes [Bar80]). While components have been known before, namely the pinhole camera (*camera obscura*) since the ancient world, and photo-sensitive chemicals like silver chloride since the middle ages, the major novelty was to fix the exposed light-sensitive material afterwards, thus making the picture permanent and copiable. Already in the 1840s, the new technology has been sufficiently improved, for instance by Louis Daguerre, to allow its wider-spread use. The impact of this invention onto the illustration process is two-fold: First, light directly and immediately exposes a photographic medium and thus creates an image capturing an exact moment, without an artist-scientist carefully trying to reproduce an (potentially biased) impression faithfully. Second, imaging has become a largely technical and mechanised process, thus making images feasible in more cases. Of course, photography still requires technical and ideally aesthetic skills. (See the essays of Susan Sontag [Son77] or Roland Barthes [Bar80] for a more universal, philosophical introduction into photography and its implications.)

In the roughly two centuries since the invention of photography, technology has changed dramatically. Colours, not just brightness, could be acquired, the photo-sensitive material has

evolved and was eventually replaced by electronic sensors, and exposure time was reduced to first enable shooting of movies and later even high-speed sequences. In our age, photography is a key technology in many scientific fields, not only when conveying information. Particularly whenever remote sensing, robotics, or unusual spatial or temporal resolution are involved, like in space exploration, oceanography, physics, or surveying, it has become a scientific tool of its own.

1.3. Computers and Networks

Like in many other fields, computers and networks have had tremendous impact on imaging. Storing pictures in digital memory leads to technical implications, but also aesthetic and philosophical ones. (See the vanguard work of Abraham A. Moles [Mol71] for a comprehensive discussion.) In particular, computers have enabled to acquire novel kinds of images, fuse input from several sources, and provide finding aids to work with many images.

In this context, it must also be noted that computers can easily generate synthetic, photo-realistic images, with correct perspectives and shadows, or alter original images. In terms of trustworthiness, this is a step backward, and photographies have largely lost the connotation of undoubtedly reproducing reality. Instead, information about the source of an image is much more important in present days.

Furthermore, in recent years, due to cheap storage and overwhelming speed of processors and data links, images and videos have become ubiquitous, also in science. In the battle for research money and public perception, research institutes have started to generate spectacular images for public relation purposes. In astronomy for instance, a domain particularly dependent on the taxpayer's goodwill, the well-known colourful pictures are heavily post-processed following cultural memes [Kes12; Web15] and have not much to do with actual research imagery, but still carry the aura of scientific incorruptibility.

Considering the different motivations for creating images, their purposes and the wide spectrum between accurate reproduction and artistic interpretation, even in science, this thesis will restrict itself to a particular subset of mechanised imaging. The intent is to produce best-possible, unbiased images of actual settings, intended for scientific and engineering use, with a particular focus on medical imaging.

2. X-rays, Among Others

Visible light only makes up a relatively small range of the entire electromagnetic spectrum. First fundamental ideas about the nature of light were developed in the 17$^{\text{th}}$ century. At that time, Christiaan Huygens [Huy90] came up with wave optics, and Isaac Newton [New04] refracted a beam of white light into the colour spectrum using a prism. In 1800, astronomer Friedrich Wilhelm (William) Herschel [Her00] decomposed sunlight into a spectrum, and noticed that a thermometer showed increased temperature 'below' visible red light. A year later, physicist Johann Wilhelm Ritter [Rit06] performed the same experiment and found that silver chloride, a light-sensitive salt, is darkened 'above' visible violet light. Like that, the two researchers added the infra-red and ultra-violet ranges to the known spectrum. (See fig. 2.1.)

Therefore, at the time of its invention, photography was apparently limited to producing views of scenes that either emit such light themselves, or are illuminated by a light source. Only in rare cases, when an object is sufficiently transparent or thin, like in microscopy, light passing through matter could be captured. Consequently, in order to "perceive whatever holds / the world together in its inmost folds" as *Doctor Faustus* proclaims[1] in Goethe's tragedy [Goe08], samples still needed to be cut open for investigation and photographic reproduction.

2.1. X-radiation

This changed in November 1895, when Wilhelm Conrad Röntgen discovered X-rays [Rön95; Rön96], thus extending the known spectrum[2] beyond ultra-violet light. Operating an electrical discharge tube as described by William Crookes [Cro79] that was covered with black cardboard, Röntgen noticed that a fluorescent screen was still showing a typical glow. He concluded that a previously unknown kind of radiation was responsible, conducted all kinds of optical experiments and termed the phrase *X-rays*. Note that the tube itself was known since 1878, and other scientists including Philip Lenard [Swi96; Lan97], Nikola Tesla[3] and Ivan Pavlovich Puluj [Pul96] noted effects on photographic plates before, but it was Röntgen's achievement to thoroughly investigate and precisely characterise X-radiation based on rigor-

1. English translation by George Madison Priest.

2. For completeness, it must be added that the extension of the electromagnetic spectrum towards the lower frequencies has been predicted theoretically by James Clerk Maxwell [Max65] in 1865. Heinrich Hertz [Her87] proved Maxwell's equations experimentally in 1886.

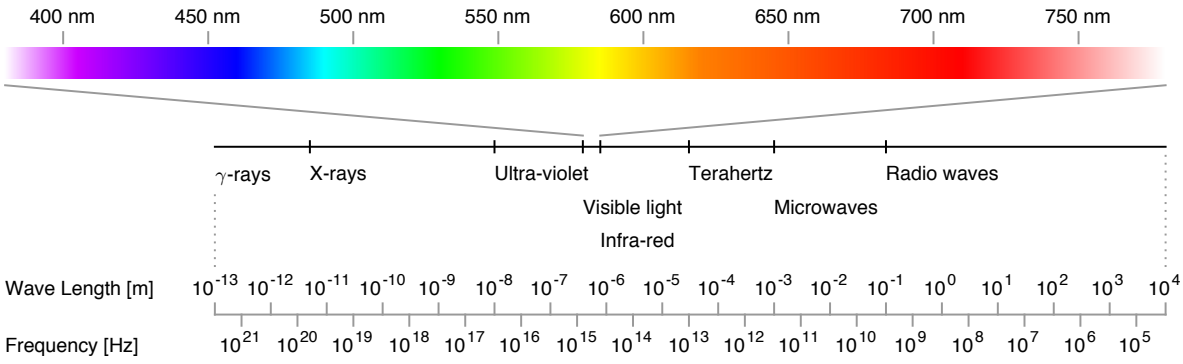

Figure 2.1.: Electromagnetic spectrum. The human eye can only perceive a relatively small band between wavelengths of about 380 nm (violet) and 780 nm (red). X-rays and γ-radiation have considerably smaller wavelengths.

ous experimentation. Within only a couple of weeks, Röntgen performed all studies feasible at the time, thus providing a complete description that represented the state of knowledge for about an entire decade [Lan97].

X-radiation is an important finding of physics and related domains, but a particular property gives them greater importance: X-rays penetrate matter, are attenuated on the way and expose a photographic plate afterwards. (See fig. 2.2.) Unlike photography, the developed image will not only show the surfaces of the respective closest objects, but a superposition of structure-specific absorptions within a certain cone-shaped field of view: The inside of an object, projected onto a two-dimensional image. From the very beginning on, an iconic (and still somewhat blurry) X-ray image of Berta Röntgen's hand (see fig. 2.13(a)) was published along with the physical description, and early reviews [Swi96] explicitly mention and reproduce it. The interest is easily explained: Röntgen has discovered humankind's first way to inspect "inmost folds" in a (seemingly) non-invasive way. Exactly this made the news of the discovery spread like a wildfire, with *Nature* publishing an English translation [Rön96] of the original paper [Rön95] only within a month. Röntgen received the Nobel prize in physics for his work in 1901. (See Landwehr [Lan97], Patton [Pat96] and Eisenberg [Eis96] for early X-ray history.)

2.1.1. Generation of X-rays

Before continuing the discussion of the use of X-rays for imaging, take a purely physical and technical perspective: X-rays occur in nature, and can be generated artificially. Astronomy is heavily interested in the first category [Trü97], but active imaging requires the latter.

3. Sometimes, Nikola Tesla is identified as true discoverer of X-light, allegedly kept from earlier publication by a fire in his laboratory in March 1895. (See, for instance, Hrabak *et al.* [Hra08] or Mahaffey [Mah14].) A brilliant man, Tesla surely possessed both, ability and equipment, to generate X-rays and to note their presence, but his first (known) article on the topic only dates to March 1896, giving full credit to Röntgen [Tes96].

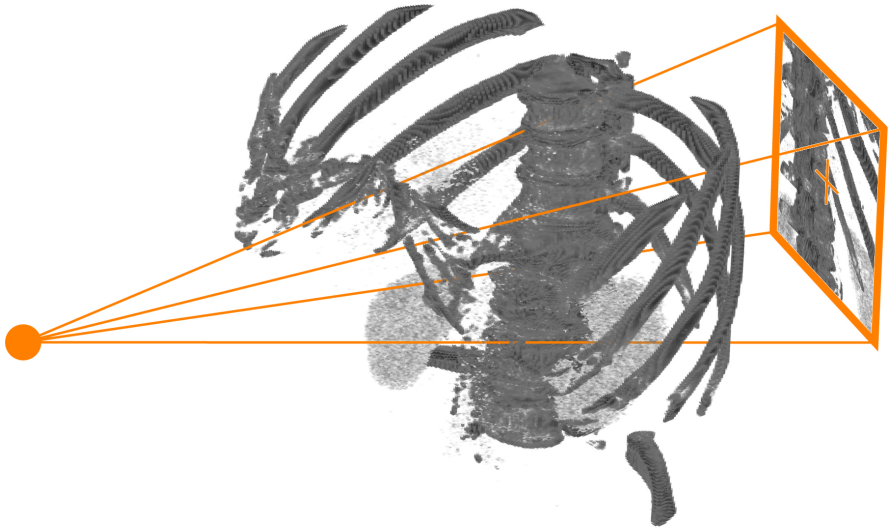

Figure 2.2.: X-ray geometry: The radiation is generated at a point-like source (orange dot, left), traverses an object of interest (such as a human thorax, indicated by the gray skeleton), and is recorded afterwards (orange screen, right). The image contains a superposition of structures from the entire cone- or pyramid-shaped field of view. Ideally, as long as the image is taken directly without an intensifier and when using a line-focus tube, the setup is perfectly described by the pinhole model (an application of the intercept theorem), and distortion-free.

X-ray tubes

A common method to produce X-rays is to use vacuum tubes. The basic idea is to generate a stream of electrons in an evacuated environment, and to accelerate these electrons away from a cathode (negative electrical charge) towards a suitable target anode (positive electrical charge). The individual electrons of this beam will abruptly lose their kinetic energy upon impact. Following the law of energy conservation, this will lead to an effect such as heat or light, and the dissipation of X-ray photons if the acceleration voltage and target materials (tungsten, or a tungsten alloy) are chosen correctly.

As mentioned above, Röntgen originally used a *Crookes tube* [Cro79] to generate X-rays. Such a tube is not entirely evacuated and contains some residual gas molecules which are ionised in the strong electrical field between cathode and anode. That is, electrons on the highest electron shells of the individual atoms are torn away, thus turning the (electrically neutral) atoms to (positively charged) ions. In such a setup, the number of remaining molecules limits the strength of the electron beam, and thus of the X-radiation. The amount of residual gas is hard to control, making the X-ray production hardly predictable and potentially dangerous.

In 1913, William D. Coolidge invented the *Coolidge tube* [Coo16] which has effectively become the standard since about 1920 [Hak14]. (See fig. 2.3(a) for a schematic drawing.) In this setup, the electron beam is generated by thermionic emission [Gut73; Pre85], that is a filament is heated up, and electrons are dissipated. This filament also serves as cathode of the

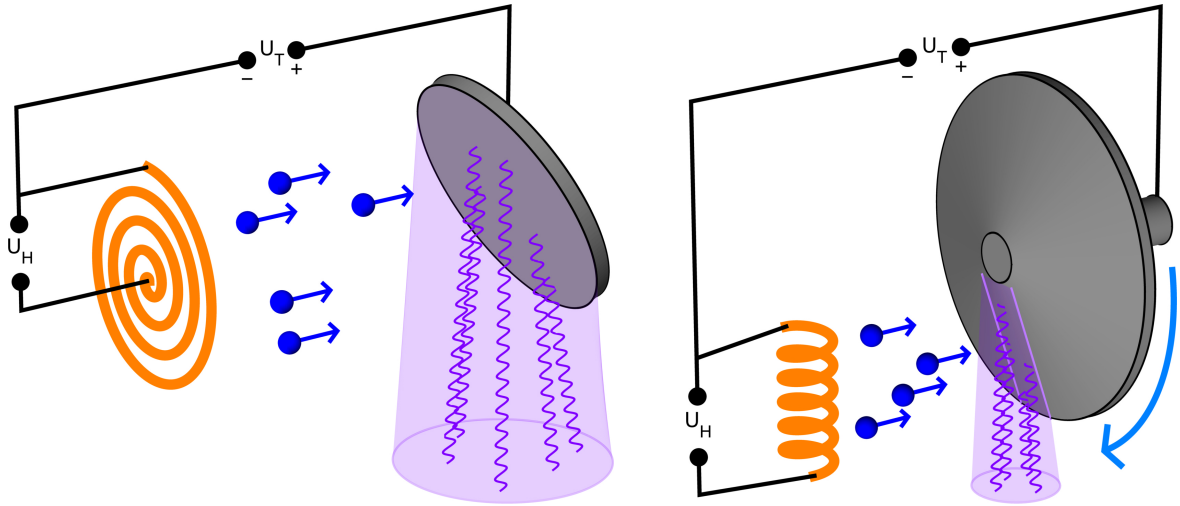

(a) Original design with spiral-shaped cathode and static anode.

(b) Modern 'line focus' design with helical cathode and rotating anode.

Figure 2.3.: Schematic design of Coolidge-type 'hot cathode' X-ray tubes. Electrons (blue) are emitted from a glowing cathode (orange) in an evacuated environment and accelerated towards a target anode (gray) manufactured from a durable metal alloy. Upon impact, X-rays (violet) are emitted. Modern tubes use rotating anodes to reduce wear.

electron acceleration component, while the anode is kept as before. For this reason, Coolidge tubes are also referred to as *hot cathode*, and Crookes tubes as *cold cathode* tubes.

Apart from X-rays, the tubes generate considerable heat and require cooling particularly of the anode. Still, the process damages the target over time. In order to reduce wear, modern tubes use a rotating anode. Like that, the beam is not concentrated to a single area. Interestingly enough, William Herbert Rollins mentioned the rotating anode already in 1899 [Rol03, Note 50], but it was formally patented only in 1916, also by Coolidge [Coo17]. The modern setup where anode and tube form an electric motor was patented in 1927 [Bou33]. Furthermore, in order to produce sharp images, line focus cathodes are used, making the radiation appear to originate from a single small spot,[4] thus reducing blurring artefacts. This cathode design was invented by Otto Goetze [Goe26] in 1918. (See fig. 2.3(b).)

Electrons and X-rays

With either of the setups in place, consider now the interaction between the electron beam and the atoms of the target anode. As already stated, the impact of the electrons eventually leads to X-rays. Among several effects causing them, the two most relevant ones are *bremsstrahlung* (deceleration radiation) and *characteristic radiation*, a variant of *X-ray fluorescence*.

4. Later, the X-ray cone-beam setup will be modeled as pinhole camera.

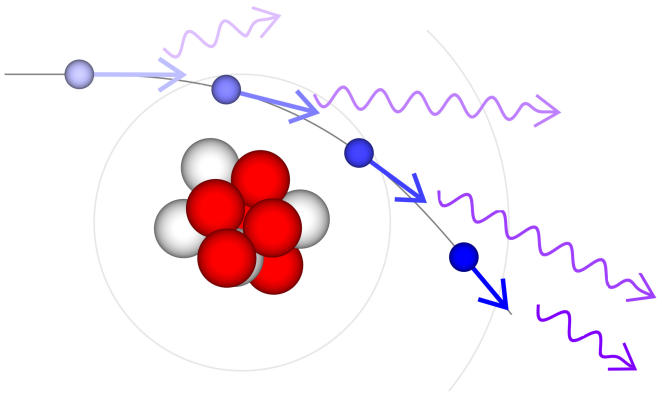

Figure 2.4.: When passing through the electric field between a nucleus and the electron shell, a free electron is deflected and slowed down. Consequently, a continuous spectrum of X-rays is emitted, an effect called *bremsstrahlung* (deceleration radiation). A similar concept is synchrotron radiation where the deflection is caused by magnetic fields.

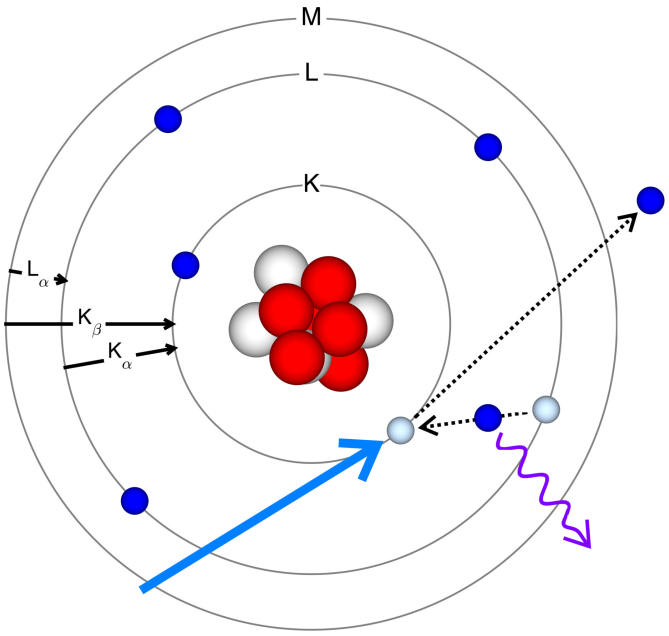

Figure 2.5.: Characteristic X-radiation is due to an external stimulus (blue arrow) kicking out an electron from a low shell. In case of an X-ray tube, this stimulus will usually be caused by a colliding free electron. The 'hole' is immediately filled by an electron from a higher shell. Due to the law of energy conservation, an X-ray photon (violet) is emitted while falling down. The electron shells have discrete energy levels depending on the chemical element, and a transition between certain shells will require or yield a characteristic energy. This effect is also causing X-ray fluorescence.

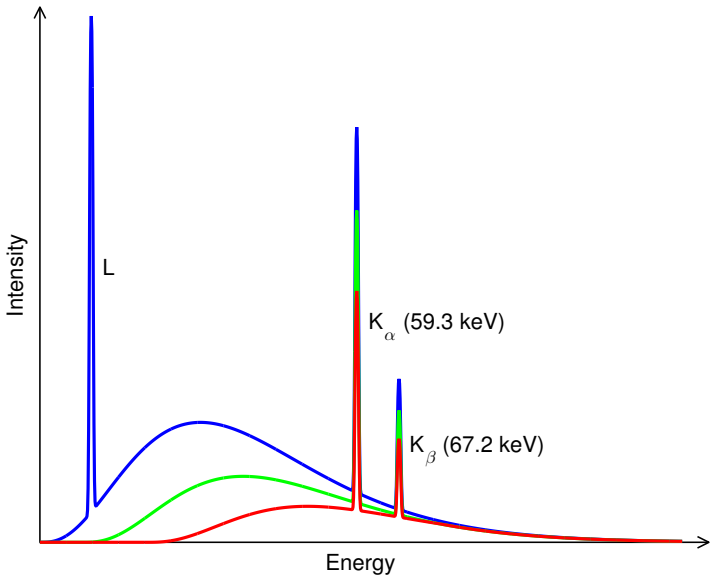

Figure 2.6.: Schematic X-ray spectrum for a tungsten anode. It consists of several characteristic spikes, and a continuous spectrum caused by bremsstrahlung. Note that this sketch is simplified; in reality, each spike consist of a group of spikes, depending on the subshells involved. The lower energies are undesired and removed by adding respective filters into the X-ray beam, causing the original spectrum (blue) to be 'shifted' up towards higher energies (green and red). This also happens while measuring, an effect referred to as *beam hardening*.

Bremsstrahlung is caused when an electron passes an atomic nucleus in close vicinity, traveling through the electric field between the core and its shell electrons. Carrying a negative charge, the electron will be deflected towards the nucleus, thus losing speed. The difference in kinetic energy is compensated for by the emission of X-ray photons. (See fig. 2.4.) The energy of the latter depends on the initial speed of the electron and distance to the core. For this reason, the X-ray bremsstrahlung energy spectrum caused by a beam of many electrons will be continuous [Buz08].

In addition to bremsstrahlung, characteristic radiation will appear. This effect was discovered by Charles Glover Barkla [Bar17], a work which was awarded with the 1917 Nobel prize in physics [Bar20]. In this case, the electron beam causes shell electrons to be kicked from an anode atom, thus ionising it. If such a 'hole' appears on a lower electron shell (particularly 'K'), an electron from a higher shell ('L' or 'M') will drop down to fill it, thus minimising the energy. Falling down, the energy imbalance is compensated by emitting an X-ray photon. Electron shells have discrete energy levels depending on the chemical element. The transition of an electron between two such (sub-)shells will, therefore, yield (or require) a characteristic energy [Des05]. (See fig. 2.5.) Consequently, all X-ray photons caused by this effect will appear as characteristic spikes in the energy spectrum. Particularly prominent are the K_α transitions from L to K, and the K_β transitions from M to K, both at a relatively high energy.

Consequently, the X-ray spectrum generated by a tube will be a combination of the two effects: A continuous spectrum caused by bremsstrahlung, and some very characteristic spikes. The positions of the latter depend on the materials used for manufacturing the anode. As will be seen later, this raw spectrum needs to be filtered in order to avoid unsuitable radiation energies. (See fig. 2.6 for a sketch.)

Synchrotron

Another means to produce X-rays is based on *synchrotrons*. In this case, the electron beam is generated using a ring-shaped accelerator and sent through *wigglers* and *undulators*, effectively sequences of electro-magnetic fields. As described above for bremsstrahlung, the beam is deflected to follow a wave-shaped trajectory and consequently slowed down, again leading to the production of X-ray photons. This kind of radiation is referred to as *synchrotron radiation*, and can be controlled very well to yield a desired energy spectrum by setting suitable parameters [Win97]. In contrast to X-ray tubes, however, a synchrotron requires a large facility, and its use is typically restricted to research institutions [Dow99; Mar12b].

2.1.2. Interaction of X-rays and Matter

Once a X-ray beam is available, it can be sent through matter. Traveling along, this beam is attenuated, effectively causing the 'look inside' as described above when used to finally expose a photographic plate. Like in the target anode of the X-ray tube, this is due to an interaction of X-rays and matter on an atomic scale. Among several effects, the two most important ones are *photoelectric absorption* and *Compton scattering*.

Atomic Scale

Photoelectric absorption of photons is the micro-scale process leading to the photoelectric effect. Observed and investigated by several researchers for several years, a satisfactory explanation was developed by Albert Einstein [Ein05] in 1905, and was awarded with the Nobel prize in physics in 1921. An X-ray photon of sufficient energy will displace a shell electron, typically on a low shell, and its entire energy will be converted into kinetic energy. If there are higher shells, an electron will drop down to minimise the atom's energy. Like in the case of characteristic X-radiation as generated in X-ray tubes, an electron transitioning to the lower shell will emit an X-ray photon, following the law of energy conservation. (See fig. 2.7.) The latter effect leads to X-ray fluorescence.

The second relevant effect is Compton scattering [Com23]. Besides the photoelectric effect, it conclusively shows the wave-particle duality of light, and Arthur H. Compton received the 1927 Nobel prize in physics [Com27] for its discovery. In this case, the photon interacts with a quasi-free electron on an outer shell. The electron is kicked out from its shell, and some of the photon's energy is converted into the electron's kinetic energy. Unlike the first case, however,

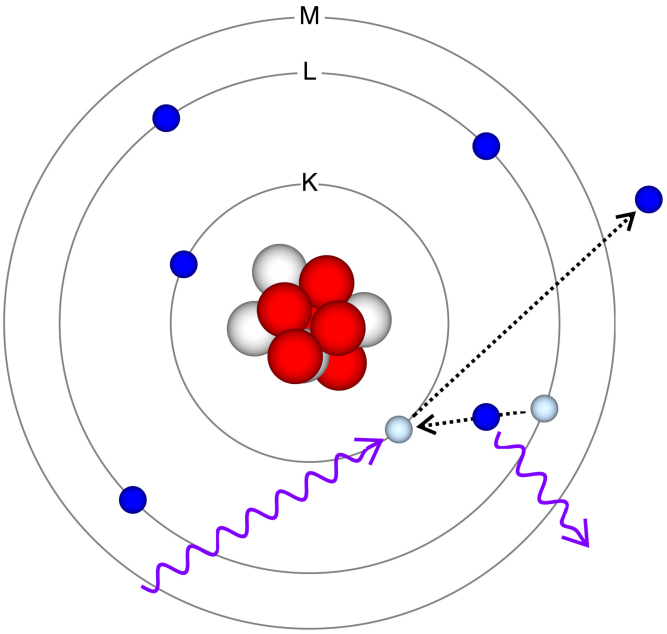

Figure 2.7.: Photon absorption and X-ray fluorescence: An X-ray photon kicks out an electron from a electron shell, is completely absorbed, and another electron from a higher shell will fill the gap. Again, a new X-ray photon of a characteristic energy is emitted to compensate for the energy difference, causing X-ray fluorescence. Losing a negative charge, the atom is 'ionised'.

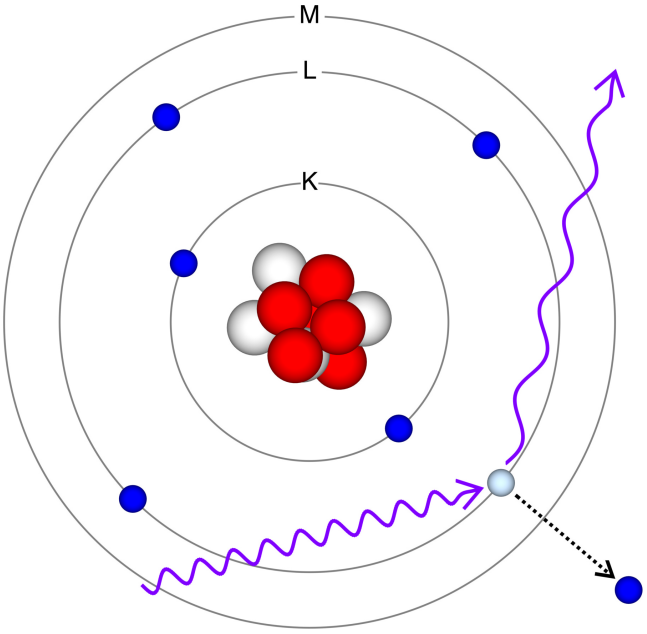

Figure 2.8.: Compton scattering: An X-ray photon again kicks out an electron, typically from an outer shell, but is not entirely absorbed. The photon 'survives' but loses some of its energy. Also in this case, the atom is 'ionised'.

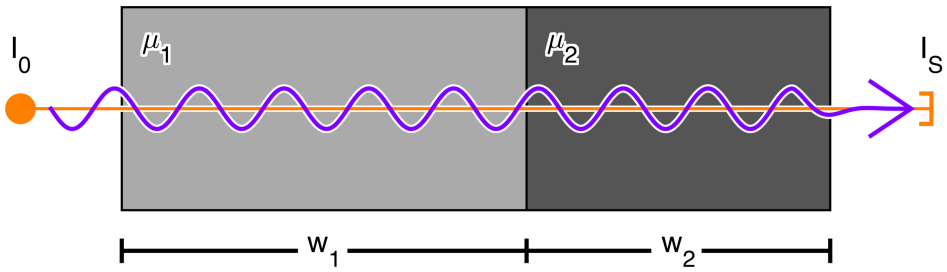

Figure 2.9.: Modeling X-ray attenuation: An X-ray source (orange dot, left) emits monochromatic X-radiation with initial intensity I_0. The detector (orange 'bucket', right) reads a radiation intensity of $I_S = I_0 \cdot \exp\left(-\int_L \mu(\mathbf{x})\ \mathrm{d}\mathbf{x}\right)$, following the Beer-Lambert law. In this case, assuming two discrete blocks with lengths w_1, w_2 and homogeneous attenuation coefficients μ_1, μ_2 in vacuum, the expected sensor reading is $I_S = I_0 \cdot \exp\left(-\mu_1 \cdot w_1 - \mu_2 \cdot w_2\right)$.

the photon is not entirely absorbed and only loses some of its energy. It continues onwards with a larger wave length. (See fig. 2.8.)

Note that in both cases, the atoms temporarily lose an electron and thus a negative charge, turning it into an ion. For this reason, X-radiation is referred to as 'ionising' radiation. Furthermore, there are more effects eventually causing the attenuation of the X-ray beam. (See Buzug [Buz08, chap. 2.3.2] for an extensive description.)

Macroscopic Scale

Seen from a macroscopic perspective, the absorption of X-radiation intensity is given by the *Beer-Lambert law* [Bou29; Lam60; Bee52]. Assume a X-ray source emitting a beam of initial intensity I_0, and an X-ray sensor on the far side of a sample object, measuring an attenuated, residual intensity of I_S. Furthermore, let L denote the line of sight between source and detector, and $\mu : \mathbb{R}^3 \to \mathbb{R}$ a function mapping a location $\mathbf{x}$ to a respective local attenuation coefficient $\mu(\mathbf{x})$. (See fig. 2.9 for a sketch.) Then, according to this law, the two intensities will be considered to be related as follows:

$$I_S = I_0 \cdot \exp\left(-\int_L \mu(\mathbf{x})\ \mathrm{d}\mathbf{x}\right) \tag{2.1}$$

Note that this equation is only an approximation assuming monochromatic X-radiation, that is, a single spike in the energy spectrum. In reality, though, the X-light will be polychromatic, and there will be X-ray photons of a range of energies. Interacting with matter, lower energies are attenuated to a higher degree. Consequently, comparing the energy spectrums before and after crossing the sample object, the second spectrum will not just be scaled down, but lower energies will be affected over-proportionally. This 'shifting' effect towards higher energies is called *beam hardening* [Her09]. Taking the energy dependence into account, a more accurate mathematical description of the attenuation is, following Kak *et al.* [Kak87, chap. 4.1.2] or

Buzug [Buz08, chap. 2.4]:

$$I_S = \int_0^{E_{\max}} I_0(E) \cdot \exp\left(-\int_L \mu(E, \mathbf{x})\ \mathrm{d}\mathbf{x}\right) \mathrm{d}E \tag{2.2}$$

In general, the exact attenuation measured at the far side depends on several properties, such as the thickness of the specimen, its density, its material, and, again, the energy of the radiation [Buz08, chap. 2.4].

In practical settings, particularly medicine, exposure of the sample to X-ray photons of low energy is largely undesirable. As will be seen below, exposure to ionising radiation should generally be avoided as far as possible, and over-proportionally attenuated ranges of the energy spectrum will not yield additional information. For this reason, low energies will be blocked by adding a filter of a suitable material, like aluminum, into the X-ray beam directly at the tube, thus 'pre-hardening' it. (See fig. 2.6.)

2.2. γ-radiation

Shortly after the discovery of X-rays, in 1896, Antoine Henri Becquerel began a series of experiments originally intended to show fluorescence of matter when excited under various lighting conditions, including X-light, and he describes his progress in a series of articles [Bec96a; Bec96b; Bec96c; Bec96d; Bec96e; Bec96f]. He was able to demonstrate that uranium salts could in fact expose photographic paper wrapped into a black envelope, but he realised that this effect can even be observed without excitation, i.e. in the absence of external light. Ruling out other effects such as chemical reactions, he concluded that uranium salts emit radiation of some sort themselves.

Following up Becquerel's experiments, Pierre Curie and Marie Skłodowska Curie discovered more powerful, previously unknown chemical elements showing the same behaviour, and coined the term *radioactivity* [Cur98; Cur03]. For their pioneering work, all three of them received the 1903 Nobel prize in physics [Bec03; Cur05].

In 1898, Ernest Rutherford began to investigate the radiation emitted by radioactive substances, and was able to distinguish two different kinds of radiation that he called α- and β-radiation [Rut99]. Later, both would be identified as particle radiation, helium nuclei ($^4_2\mathrm{He}^{2+}$) in case of α-radiation, and electrons (e^-) in case of β-radiation. Rutherford received the 1908 Nobel prize in chemistry [Rut08a] for his achievements.

In 1900, Paul Villard observed a third kind of particularly strong radiation [Bec01] which, unlike the other two known kinds of radiation, could not be deflected by magnetic fields. Furthermore, it required much more material to entirely absorb it. Following his scheme, Rutherford introduced the name *γ-radation* in 1903 [Rut03], but it took until 1914 that he was able to show, together with Edward Andrade, that γ-radiation is an electro-magnetic radiation [Rut14], as X-radiation and visible light are. Like that, the electromagnetic spectrum was extended beyond the energy range of X-rays, towards even higher energies. (See fig. 2.1.)

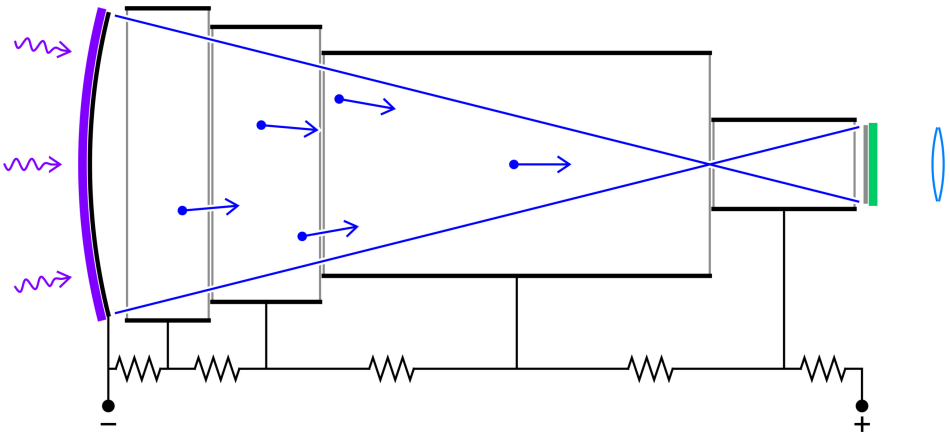

Figure 2.10.: Image intensifier: X-rays (violet, left) cause the emission of electrons (blue) from a photocathode (violet/black). The electron beam is focused by means of electrostatic lenses (black/gray), and causes an image on the secondary fluorescent screen (green, right) that can be enlarged by 'usual' optical means. Using an intensifier, the brightness of the image is improved several 100 times. Note that the image is slightly distorted due to the radial geometry.

Due to the close relation between γ-radiation and X-rays, the interaction with matter is very similar, and the same attenuation effect can be expected. The major difference is the generation of radiation in practical setups: X-rays are typically generated using electrical devices such as tubes, but γ-radiation is generated 'naturally' by suitable radioactive isotopes.

2.3. Making Radiation Visible

After a radiation beam has been attenuated by an object of interest, the remaining problem is to record an image. As has been mentioned before, X-rays and also γ-rays expose photo-sensitive material, particularly photographic plates and film. This discovery has already been made before Röntgen, and he formally describes it in the initial publication [Rön95; Rön96]. A particularly beneficial aspect of this approach is that a relatively low dose is enough to create an image of good quality [Kas01; Kas03], but the exposed medium needs to be developed after exposure. (See Haus *et al.* [Hau96] for a comprehensive history of X-ray film and its development.)

Recall that Röntgen's interest in 'the new kind of rays' was not triggered by exposed film, but by the reaction of a photo-fluorescent screen that happened to be around. In contrast to film, such a screen immediately produces a visible image, as the material – excited by invisible rays – emits light of a wavelength that the human eye can see. As the news of the discovery spread around the world, Thomas Alva Edison was quickly intrigued, started to look into optimal fluorescent materials, and identified calcium tungstate. Already in 1896, he

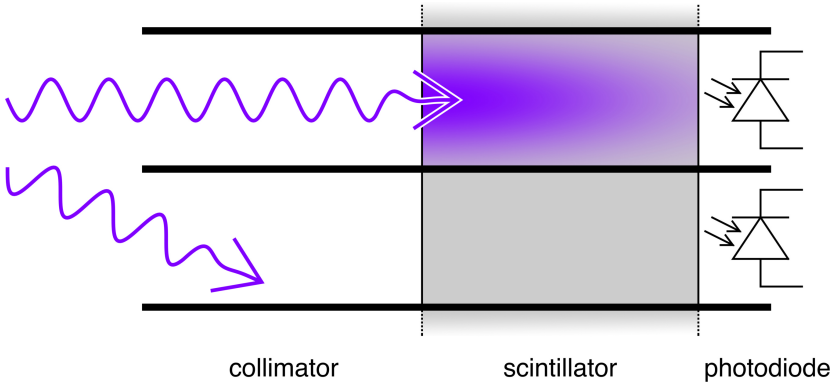

Figure 2.11.: Schematic design of a scintillator-based digital X-ray detector. The basic idea is to let a X-ray photon excite a scintillator crystal, thus converting high-energy X-light or γ-radiation to a flash of low-energy light that can be detected by photo-diodes. In order to reduce measurement noise, a collimator (also referred to as 'anti-scatter grid' [Buz08]) is added, annihilating all erratic photons not coming from a certain direction of interest. Several such sensors arranged in a grid make up a camera.

patented a bright fluorescent lamp [Edi07] creating light by exciting this material with X-rays. As will be seen later, Edison quickly withdrew from experimenting with X-rays, but the idea of fluoroscopy was established. A fluoroscopic image is usually rather dim, thus constantly requiring strong radiation to produce an image. Even more, the viewer is quite likely to also expose himself to ionising radiation.

In the early years, viewers were required to examine fluoroscopic images in the dark, and their vision needed to be adapted beforehand, for instance by wearing goggles with red glasses [Hak14]. This changed with the invention of image intensifiers. The original idea goes back to the late 1920s, when Gilles Holst and Jan Hendrik de Boer [Hol30; Hol34] of *Philips* invented a special vacuum tube where an image produced on a primary (input) fluorescent screen causes a photocathode to emit a beam of electrons towards a secondary (output) fluorescent screen. On the way, this beam is accelerated and focused by means of electrostatic lenses, causing an amplified image to appear on the secondary screen. (See fig. 2.10.) This technique was initially used for night-vision equipment, that is, to make dim visible light and infrared light visible. In the late 1940s, the technology was adapted to X-ray imaging by Lloyd P. Hunter and Richard L. Longini [Hun51; Col48] of *Westinghouse*, and the first X-ray intensifier, the *Fluorex*, became commercially available in the 1950s [Hak14], thus enabling work under daylight conditions. The intensified image was originally viewed via mirrors or periscopes, but soon the image was recorded by a television camera and shown on a respective screen.

In recent years, particularly the last two decades, it has become relevant to digitise the images. Image intensifiers are still used, and their amplified images as recorded by a camera

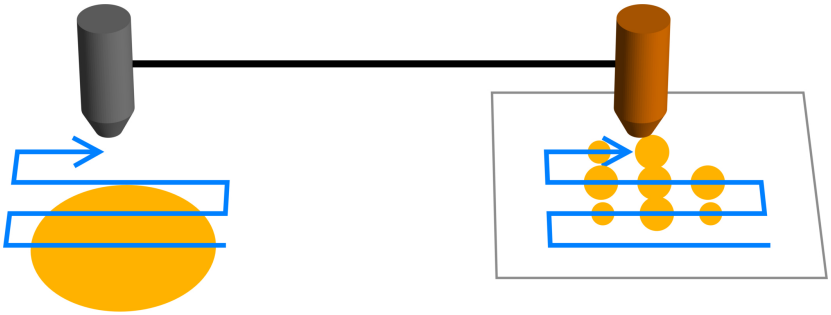

Figure 2.12.: Rectilinear scanner: A single radiation sensor (gray) moves over a specimen, following a regular grid (blue arrow), and a mechanically coupled printhead (orange) moves along. At discrete positions, the measurement obtained from the sensor leads to an appropriate mark on the paper, creating a two-dimensional 'projective' image.

can be digitised like any other picture. Still, in order to simplify the devices and to enable advanced image processing, there has been a move towards radiation sensors providing digital information right away. Interestingly enough, this move has begun already in the 1950s in the field of nuclear medicine. A particularly prominent and wide-spread design is based on 'observing' a scintillation crystal. Incoming radiation photons of high energy will trigger a visible light pulse of lower photon energy within the crystal that can be detected by means of photodiodes, and electronically forwarded as counting impulse. The detector is usually extended by a collimator, a metal grid restricting the field of view to a narrow cone and thus limiting the influence of erratic photons. (See fig. 2.11.) This principle – at the time still based on a photomultiplier tube instead of semiconductors – was originally developed by Samuel C. Curran [Cur48; Cur49] during the Manhattan Project in the 1940s, as alternative to other radiation and radioactivity detector designs such as particularly the Geiger-Müller counter [Rut08b; Gei28].

While electric detectors were originally only able to measure a single scalar activity, first two-dimensional images could be produced with the rectilinear scanner. Invented and improved by Benedict Cassen during the early 1950s [Cas49; Cas50; All51; Bla96], such a device systematically scans along a grid and stores the accumulated counts by exposing a film using an auxiliary light controlled by the electrical impulses sent by a radiation sensor and moving in conjunction with it. (See fig. 2.12.) Soon afterwards, in 1958, Hal O. Anger patented the *Anger camera* [Ang61], the first imaging device to use a scintillation crystal and a grid of sensors (photomultiplier tubes) to create the image. Today, digital systems typically use flat-panel detectors essentially following the same design principle, only using semiconductors instead of tubes. (See Cherry *et al.* [Che12c, chap. 7ff.] or Buzug [Buz08, chap. 2.5] for a detailed description and discussion of contemporary radiation detector design principles and their characteristics.)

2.4. Ionising Radiation and Medicine

So far, the physical process of generating radiation and creating an image has been described. Returning to the earlier discussion of imaging from a more abstract viewpoint, it must be be noted that X-ray images do not only recreate a sensation as photographs usually do, but they constitute 'transillumination' pictures of an unique and, at the time, novel kind. As such, they provide insight into the anatomy and potentially even the metabolism of a specific patient, and Röntgen's contemporaries quickly embraced X-ray imaging as invaluable tool. In particular, the discovery is probably the first step on a path towards what we call 'evidence-based medicine' today, as it seriously limited the uncertainty where, due to a lack of data, even well-trained physicians are forced to resort to elaborate, experience-based guessing.

However, the author even would argue that X-ray imaging introduced scientific approaches into clinical practice. In the previous chapter, it has been reasoned that images play a key role in science, particularly when communicating new findings. In contrast to own perception, an image enables physicians to unbiasedly discuss a case with colleagues, or to compare features with cases reported in literature, thus closing the gap between scientific work and day-to-day patient care. The patient-specific acquisition of images of different kinds, along with other data, is routine nowadays, and it started with X-ray imaging.

2.4.1. Radiology

The use of X-light for transillumination in medicine is referred to as *radiology*. This field has been born immediately with the first publications and public demonstrations, for instance during a session on 23rd January 1896 where Röntgen X-rayed the hand of anatomist Rudolf Albert von Kölliker [Lan97]. (See fig. 2.13(a).) In the typical setup, an external source yields X-radiation which passes through the patient's body, is attenuated, and finally leads to an image being acquired on the far side. (See fig. 2.2.)

In first medical applications, X-rays have been used directly to image structures with high X-light contrast such as bones and teeth, or also foreign bodies such as bullets, lost needles, among others [Hay96]. Particularly the latter category quickly made X-rays prominent with army field surgeons, starting in the Spanish-American War [Bro95b], and especially during the First World War [Cur21]. Already during the first year after their discovery, clinicians also came up with the idea to inject or swallow agents to improve the contrast where usually only little to none would be visible. Among the earliest examples are the works of Haschek *et al.* [Has96] and Braus [Bra96] who both contrasted the vessels of hands using rather adventurous chemicals such as mercury. (See fig. 2.13(b), and refer to DiSantis [DiS96] for early medical practitioners.)

Quickly, radiology has been established in many medical fields, such as chest [Hei96], abdomen [Goo96], urological [Pol96a], heart and vascular imaging [Abr96; Fer96; Wak11], or in neurology [Huc96], to name a few. To this day, radiology is primarily used to yield anatomical

(a) Bertha Röntgen's hand [Rön95], December 1895 *(Wellcome Library, London)*

(b) Mercury-contrasted vessels [Bra96], 1896 *(Universitätsbibliothek Heidelberg)*

Figure 2.13.: Early medical X-ray imaging. *(Public Domain)*

information, or, in natural words, to image the body as it is, potentially supported by contrast agents. In general, there are two large fields of application: The first is diagnostic imaging, that is the pre-operative collection of information, often by means of exposing film, even in our digital era. The other is interventional imaging, where X-rays are used intra-operatively, mainly for navigation and monitoring purposes, for instance during resections or biopsies. In the latter case, fluoroscopic images are usually preferred, in order to have real-time imaging.

2.4.2. Nuclear Imaging

Concerning the more energetic γ-rays, it would theoretically be possible to use them for exactly the same purposes as described above for X-light. In fact, however, X-radiation is perfectly enough to transilluminate a human body, and nuclear imaging is usually used for a different purpose: Functional imaging, that is the collection of information about dynamic processes in the human body, particularly concerning the metabolism, by tracing a radioactive substance, a so-called radiopharmaceutical or tracer, administered to the patient's body. Consequently, in the typical setup, an internal radioactive distribution (eventually) emitting γ-rays is observed from the outside using passive sensors, and anatomical features are usually not directly shown.

Figure 2.14.: Nuclear imaging: A radiopharmaceutical is administered to the patient, and taken up by specific organs depending on the exact type of tracer used. The γ-rays will radiate in all directions, but a detector with a collimator attached will only see the photons coming from about the direction it is facing to. The image does not show the anatomy such as the bones in this sketch, but only the radioactively marked organ, the kidneys in this example. Note that, unlike X-ray transillumination, there is no external radiation source. (Cf. fig. 2.2.)

(See fig. 2.14.)

The original idea of tracing radioactive markers from the outside in order to understand the previously unknown mechanics within an organic system is due to George Charles de Hevesy [Chr24a; Chr24b; Chi35; Hev36] who was awarded with the 1943 Nobel prize in chemistry [Hev44] for his invention. (See Levi [Lev67; Lev76] for a detailed account of Hevesy's work.) Following the advent of nuclear medicine during the late 1940s, this idea was adapted from general research work to patient-specific diagnostic imaging.

As described in section 2.3, it took some time to develop appropriate two-dimensional radiation detectors yielding complete images. The starting point of medical functional imaging is marked by the development of the rectilinear scanner [Cas49; Cas50; All51], and the Anger camera [Ang61] is effectively still the standard means of acquisition. (See Pollycove [Pol96b], Blahd [Bla96] and Lottes *et al.* [Lot00] for a more detailed history of nuclear imaging.)

Today, the acquisition of nuclear images is referred to as *scintigraphy*, and it is usually used in cancer diagnosis and tumour localisation. In this case, the idea is simply that tumour tissue exhibits over-proportional energy consumption. Consequently, a suitable tracer emitting γ-radiation, often a radiopharmaceutical based on metastable technetium-99 (^{99m}Tc) is injected into the patient's bloodstream, and concentrates in cancer tissue. Observing this process with a gamma camera from outside, a radioactive hotspot will emerge in the image, hinting at cancerous tissue. (See Cherry *et al.* [Che12c, chap. 5] for more details about radiopharmaceuticals.)

2.4.3. Hazards and Perils

There is, however, also another medical perspective onto ionising radiation: Depending on the dose, it can inflict both, deterministic as well as stochastic health effects.

The first reports surfaced very soon after the discovery of X-rays: For instance, an anonymous letter to the editors of *Nature* [R96] describes the case of a man who used to demonstrate the novel technology during the summer of 1896, thus frequently exposing his hand to X-light. Consequently, he suffered from *radiation dermatitis*, a *deterministic* effect initially similar to sunburn, began to treat it in a, from our modern perspective, shockingly naïve way, and continued to expose his hand on a regular basis.

The same behavioural pattern can be observed in many instances during the first decade, also among highly trained scientists, physicians and engineers. Initial warning signs such as dermatitis or general discomfort have often been ignored, people continued to irradiate their extremities with high doses, and quickly showed signs of severe skin damage such as *ulcera*, and finally *cancer*. The latter condition is usually a *stochastic* effect, caused by damaged genetic information that the body fails to repair, but in the case of these early victims and their enormous doses, the consequences became overwhelmingly certain. At this stage, the typical medical response was a series of amputations, initially individual fingers, then the hand, and finally the entire arm, without a chance to stop the spread of metastases. The patients died cruelly within a relatively short time.

A particularly prominent early case is the death of Clarence M. Dally [Bro95a], a glassblower and technician working on X-ray tubes for Thomas Edison. His death in 1904 was widely communicated in the newspapers [NYW03; NYT04], and – also because his own eye was damaged by X-light – led Edison to abandon his pioneering research in this direction, for fear of the "hidden perils" [NYW03]. Another prominent victim is Mihran Kassabian [Bro95c], a pioneer of X-ray research who succumbed to the cancer in 1910, despite the fact that he himself described X-light as "irritant" [Kas00] a decade earlier. There are also famous women among this group, for instance Elizabeth Fleischman Ascheim [Bro95b] who died in 1905, or Marie Skłodowska Curie in 1934. Curie definitely suffered from radiation-induced cancer, but people argue whether her physical experiments (and thus radioactive materials) [Cur38] are to blame, or her X-ray exposure during the First World War [Cur21] where she played a key role in equipping the French army with X-ray devices.

Also in medical and clinical practice, X-rays have initially been handled rather carelessly, and over-exposure of patients has been common, particularly due to the fact that the human can not feel the rays themselves directly, only their effects – at which time it may be too late. Allegedly, the first US medical malpractice lawsuit is exactly due to such an accident [Ber01]. Similarly, the medical operators – radiologists, technicians and nurses – have not been properly protected in the very beginning, and it took time to introduce lead aprons, lead glass, and other protective gear. As most extreme example, a head-worn fluoroscopic screen [Hak14] was

Figure 2.15.: Radiology monument on the premises of St. Georg Hospital in Hamburg, Germany. Listing 359 names, it is dedicated to "the röntgenologists and radiologists of all nations, physicians, physicists, chemists, technicians, laboratory assistants and nurses who sacrificed their lives struggling against the diseases of their fellow human beings. They were heroic pioneers enabling successful and safe application of X- and Radium-rays in medicine."

quite common in the early years, and surgeons operated while constantly transilluminating the patient and also themselves. Consequently, the death toll among the early practitioners was considerable: The *Radiology Monument* situated on the premises of St. Georg Hospital in Hamburg, Germany, is dedicated to the commemoration of 359 victims from around the world [Vog06]. (See fig. 2.15.)

Even after the adverse effects of X-rays have become clear, it took time to understand that they are inflicted by the rays themselves, and that they are not just byproducts of the electrical currents, or random chemicals such as air turning into ozone under X-illumination. Also, the distinction between deterministic and stochastic conditions was initially not discussed, and a proper nomenclature needed to be found. In this context, two particular scientists deserve mentioning: Among the earliest to understand the dangers of ionising radiation was William Herbert Rollins who described respective animal experiments and proposed protective equipment [Rol03, Notes 123ff., 136, 139, 145, 170]. The first to properly investigate the influence of ionising radiation onto genetic information was geneticist Hermann Joseph Muller [Mul27], who managed to artificially create mutations by means of X-irradiation when experimenting with fruit flies. This lead him to explain radiation-induced cancer as being caused by DNA damaged beyond feasible repair during photon-matter-interaction as described above.

As the perils of X- and γ-radiation have become clear, physicians need to carefully trade

off the expected insight with the potential harm before acquiring an image. This is especially important when treating young patients [Gri96], or when using X-radiation for screening purposes, that is, for monitoring the health of the population in a wide-spread manner, in order to detect particular diseases as early as possible. An important historical example is tuberculosis screening[5] based on chest fluoroscopy [Hei96], but the use of X-rays for screening purposes has largely been abandoned in general. The only remaining exception is breast cancer screening using *mammography* [Dod96; BfS15a], due to the large number of new cases per year, and the high mortality rate.[6] Still, in recent years, the average radiation dose caused by medical imaging increased,[7] and even accidental over-exposures have still been reported quite recently [Koe01a; Koe01b]. Such cases usually occur in interventional settings like angiography, and sometimes, even skin grafts have been necessary to treat the wounds.

Note, however, that the effects of ionising rays on tissue can also be exploited for therapeutical purposes in a field referred to as *radiotherapy* [Due97], extending the field of *nuclear medicine* beyond imaging. In particular, they can be used to kill cancer cells, and this application is thus, besides tumour resection and chemotherapy, among the primary tools of *oncology*. The technique shares many properties with the imaging techniques discussed in this thesis, but will need to be omitted from further discussion.

Before closing the section on the dangers of ionising radiation, a particularly pointless example of fluoroscopy outside of the medical domain must be mentioned: In 1919, a decade after the enthusiastic early years, the shoe-fitting 'pedoscope' [Low27] was invented. Installed in stores selling footwear, this device allowed customers to X-ray their feet in order to control the fit of shoes, promising a more 'scientific' way to do so. This assumption is plainly wrong, but the devices still survived until the 1970s [Duf00]. Years before their final withdrawal, clinical cases have been discussed where shop assistants have been critically irradiated by accident due to poor maintenance [Kop57], but apparently, the pedoscopes were just too important, attracting children and, along with them, their free-spending parents. (See Schoenen [Sch07] for an extensive general collection of remarkable cases connected to radiation-induced accidents, also including radioactive sources.)

5. In Germany, tuberculosis screening of the general public was terminated during the 1980s [Wik15], and Bavaria was the last German country to formally abandon the respective law in March 2000 [VwReformG]. For refugees, however, tuberculosis screening appears to be still mandatory. In 2015, due to a capacity bottleneck, the city of Berlin has even acquired a new mobile X-ray unit contained in a truck trailer, thus reviving an idea from the 1950s [Ges15; RBB15].
6. Note that mammography screening is disputed, not so much because of radiation effects, but due to a high number of false positives – women wrongly diagnosed with cancer. Its positive effects appear to be limited to certain age groups [Lau15; Zin15].
7. For Germany, see the statistics provided by the *Bundesamt für Strahlenschutz* [BfS15b]. The increase appears to be due to normal radiographs being replaced by tomographic images, thus incurring a higher radiation dose per exposure.

2.5. Material Science and Security

Besides medicine, the two other fields heavily relying on X-rays are *non-destructive testing* and *security monitoring* as done routinely at air- and seaports. Concentrating on the former domain, a typical example is the inspection of welding seams by transillumination. This is particularly important when constructing modules that will be subject to high pressure such as oil or gas pipelines, large forces or weights such as bridges, or that will be used within sensitive installations such as nuclear power-plants or chemical manufacturing facilities. The technical development largely went in parallel with the medical counterparts.

The most remarkable difference to medical imaging is that, depending on the thickness and absorption of the material, transillumination will be performed using radioactive sources containing a suitable isotope, rather than an X-ray tube. The imaging process is then referred to as *gammagraphy*. Despite many industrial standards (for instance [ISO 4993] and [ISO 5579], among many others), several serious accidents involving abandoned, unmarked isotope sources have been reported, also by the International Atomic Energy Agency (IAEA) [Whe00; Tur02; Bug09].

3. Volumetric Imaging and Computed Tomography

X-RAY IMAGES have justifiably revolutionised medicine, but their projective nature makes them hard to interpret: Due to their character as transillumination pictures, they will show a superposition of all attenuating structures between radiation source and image sensor, and they will exhibit perspective foreshortening. The latter effect will be more prominent the closer the (ideally point-like) source and the (potentially large) detector are to each other.

Consequently, X-ray images are easier to interpret for flat structures, like human hands, or when looking for obvious targets with strong contrast, such as bullets. In case of more complex structures, such as the head or the thorax, a cross-sectional image is preferable, and a stack of such 'slices' would convey a volumetric impression of the region of interest. (See fig. 3.1.) This is exactly the idea of *tomography*, a word made up from the ancient greek words τομή (tomé, section) and γράφειν (gráphein, to write).

It is important to note that today, digital tomographic images are no longer considered to be a stack of slices, but a single volumetric image. It is quite common that radiologists browse through (artificial) two-dimensional slices extracted from such a three-dimensional image, but considerably more advanced, sometimes highly specialised visualisation methods have been developed, particularly three-dimensional, coloured renderings [Eng06; Eng04]. The key conclusion to draw is that, unlike two-dimensional modalities such as classical radiography, volumetric imaging provides the means to retrospectively choose a perspective. In this work, the respective techniques are used to visualise concepts and results, but a proper discussion of them is, unfortunately, outside of the scope.

Furthermore, volumetric images are no longer exclusively used to look at things, but they serve as foundation for computerised data processing. In the last decades, the vast field of computer-aided medicine has emerged, and people use volumetric images to automatically label organs, diagnose conditions, plan interventions, among many others, and apply advanced techniques such as artificial intelligence or machine learning to them.

3.1. Conventional Tomography

Today, tomography is often associated with Computed (or Computerised) Tomography, but the original idea – in an analogue version – dates back to the time of the Great War, and it was invented independently for multiple times. The idea is to jointly move X-ray source and film during acquisition in an opposite sense, thus only projecting a single slice-shaped region

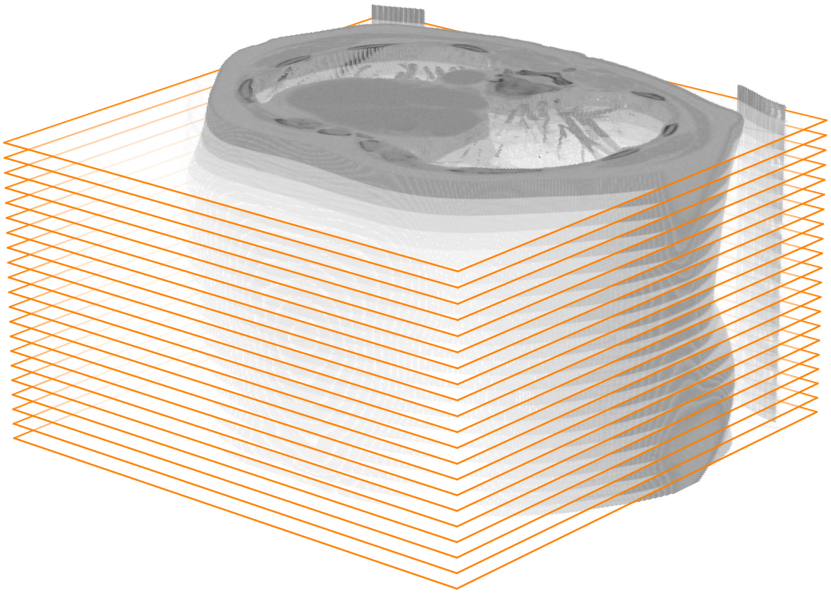

Figure 3.1.: The paradigm of tomographic imaging is to acquire one or more cross-sectional slices, rather than projective transilluminations. A stack of such slices produces a volumetric impression of the region of interest, such as a human thorax as in this sketch. Today, volumetric imaging is quite common in medicine, and the datasets are used as input for advanced data processing.

statically. Consequently, mainly this region of interest will be visible on the developed picture, and structures above and below will be blurred away, as their projections changed during the imaging process. (See fig. 3.2 and fig. 3.3 for sketches; cf. Herman [Her09, chap. 2.2].)

The first one to describe the acquisition of sectional images was André Bocage who patented several tomographic imaging setups in 1921 [Boc22; Mer98], based on his wartime experience. A little earlier, in 1916, Carlo Baese already patented an apparatus to fluoroscopically locate bullets using similar motion schemes [Bae17], but did not try to record a permanent tomographic image. Some time after Bocage and independent of his patent, the first images were produced by Alessandro Vallebona around 1930 [Val30; Val31; Bis05]. Other important contributors were Bernard Georg Ziedses des Plantes [Zie31; Zie32], Jean Kieffer [Kie34] and Gustav Grossmann [Gro38; Cha38]. Not only are there several independent inventors, there are also other names besides 'tomography', and such methods have also been referred to as *planigraphy* or *stratigraphy*, depending on the exact implementation [Buz08, chap. 3.2], and also on the inventor. (For an extensive history of the field, see Littleton *et al.* [Lit96].)

Before the introduction of Computed Tomography as described below, conventional tomography was a common clinical modality. In fact, it has still survived to this day [Dob03], appropriately extended by computer technology [Str79] to remove the blurring effects, but the name was changed to *tomosynthesis*, to avoid confusion. With ongoing development, it is even possible to remark a certain convergence of the related technologies.

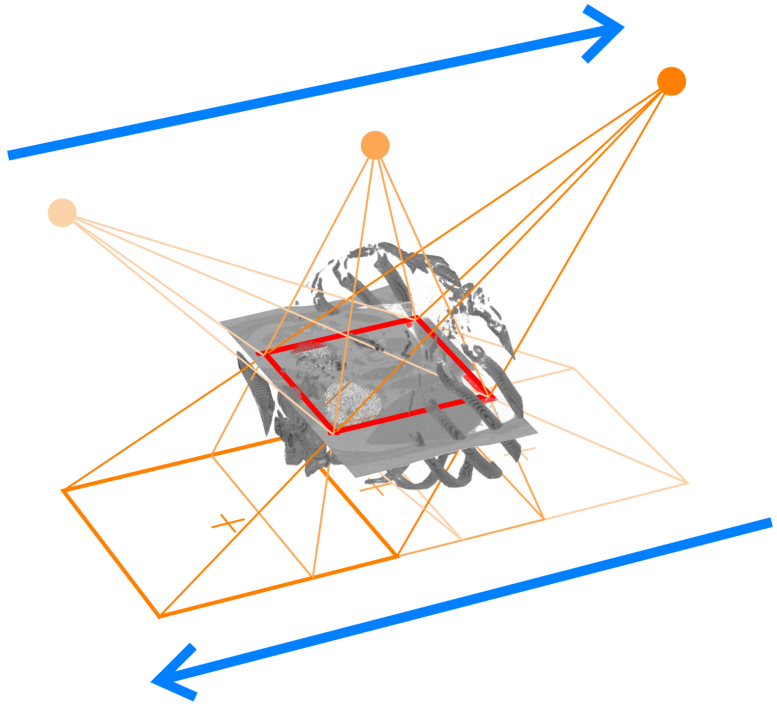

Figure 3.2.: Conventional tomography: The X-ray source (orange dots, top) and the film (orange squares, bottom) are moving simultaneously, only keeping a single region (red square) in constant focus. Like that, the film will be exposed several times, but structures above and below the static focus region are blurred away, creating a (potentially hazy) sectional image.

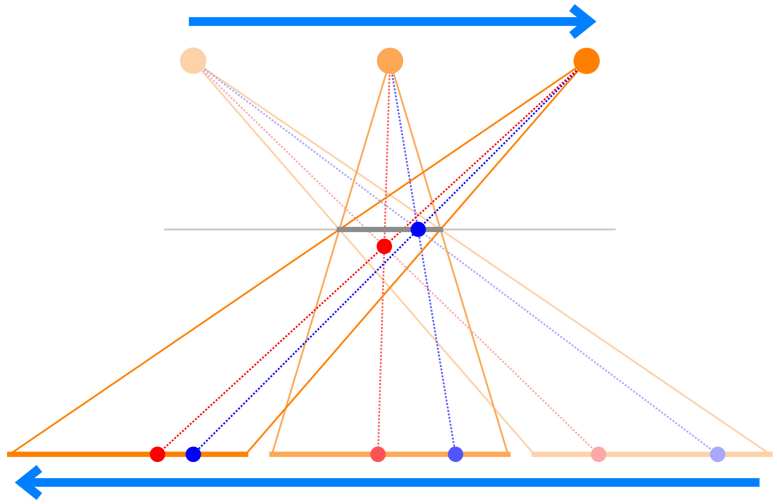

Figure 3.3.: In conventional tomography, points in the focus plane (center blue dot) are projected to a single, static position on the image, despite the synchronous motion of X-ray source and film (bottom blue dots). Points off the focus plane (center red dot) are projected to different spots (bottom red dots), and are thus blurred 'away'.

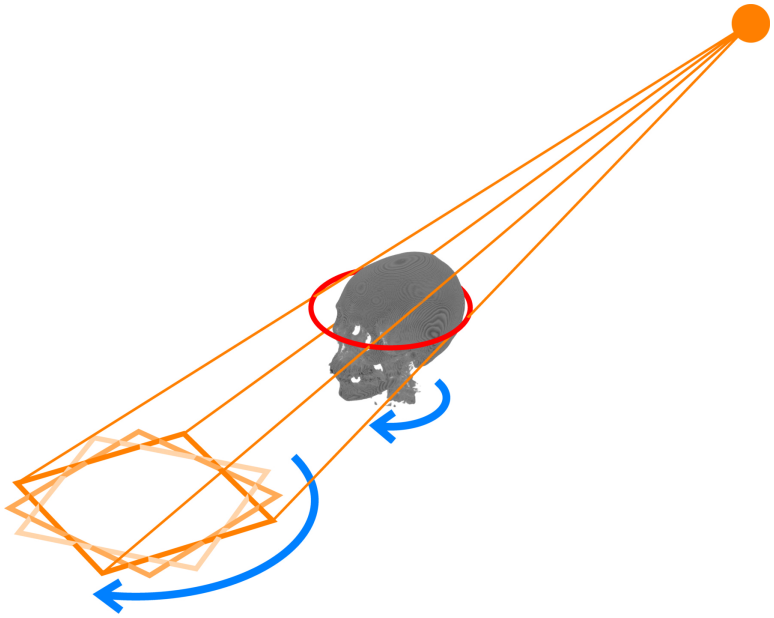

Figure 3.4.: Transaxial conventional tomography: The X-ray tube is static, but the patient and the film are rotated synchronously, leading to a conventional tomogram of the focus slice (red circle). Due to the cone-shaped geometry and limited film size, this setup does not appear to be suitable for larger objects of interest. Apparently, it was mainly intended for brain imaging.

3.2. X-rays and Transmission Computed Tomography (CT/TCT)

Among the different motion schemes used in conventional tomography, a particularly interesting one is transaxial tomography. The invention is usually attributed to William Watson [Wat40], but others, particularly Bocage, seem to have thought of it before. In this case, the tube is static, but patient and film are rotated synchronously, leading to the known effect of keeping a single slice in focus, and blurring structures above and below. The tube is still above the section of interest, and the acquired image is two-dimensional. (See fig. 3.4.)

At the same time of Watson's patent application, in 1939, the first real forerunner to Computed Tomography was invented by Gabriel Frank [Fra42]: *Back-projection*. His approach was entirely relying on analogue, optical mechanisms, but it shares the basic principle with modern scanners, and the entire device is inherently aimed towards transaxial tomographic, slice-wise imaging: A specimen is transilluminated by a fan of X-rays, and a single line-shaped, one-dimensional projection is acquired on film wrapped around a drum. Afterwards, specimen and film drum are slightly rotated in a synchronous fashion, and another such projection is acquired, until the full 360° have been sampled. Consequently, the film will contain a *sinogram*, an image where one axis relates to the viewing angle, and the other to a translational offset. (See figs. 3.6 and 3.7.) In a separate step after development, this sinogram is back-projected onto a secondary, flat film which again rotates synchronously. Each line of the sinogram is

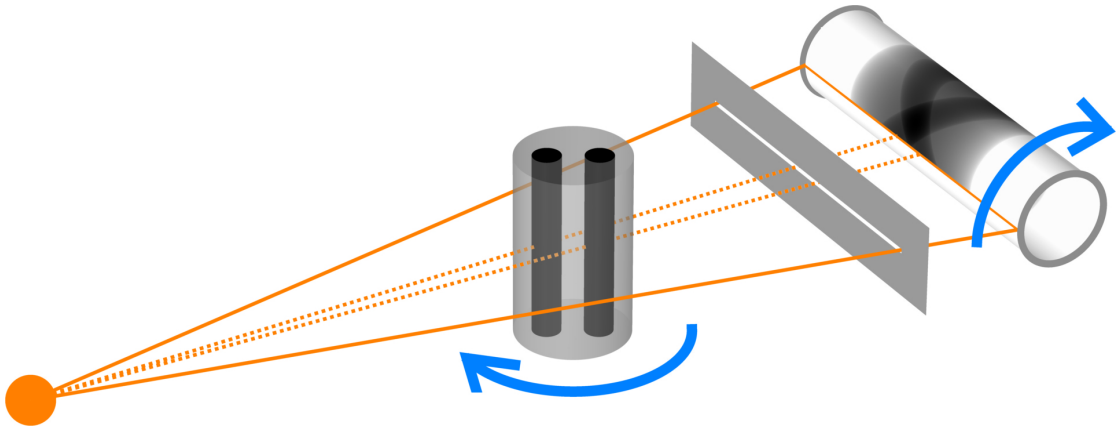

(a) Forward projection. X-rays are emitted from a source (orange circle), transilluminate the specimen (for better visibility a simple target with two rods), pass a diaphragm, and expose a film on a roll, leading to a sinogram. Specimen and film roll rotate synchronously.

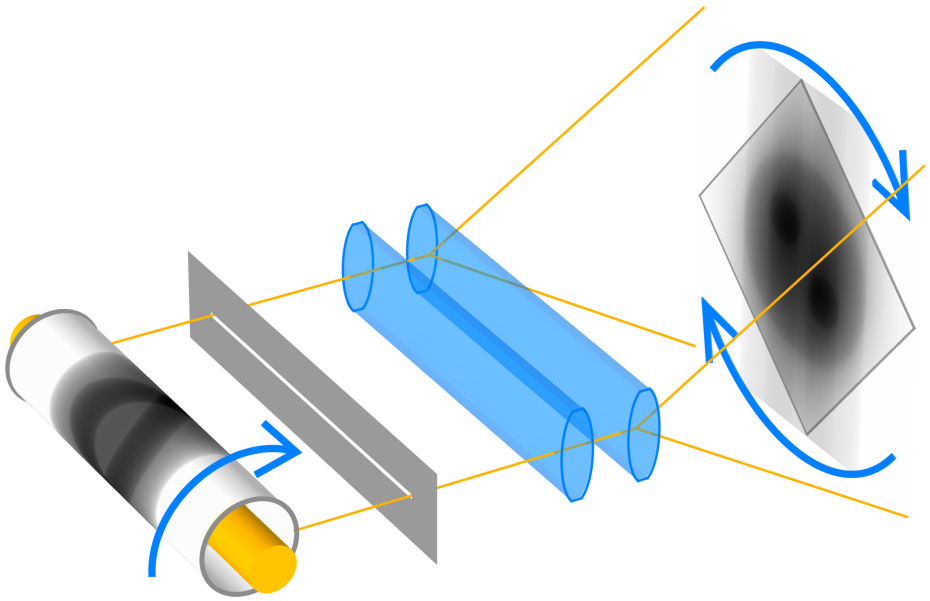

(b) Backward projection. The developed film roll with the sinogram is illuminated from within (yellow), the light is focused by means of another diaphragm and fanned out using lenses, to eventually expose a flat film. The latter and the film roll rotate synchronously again, leading to a cross-sectional image.

Figure 3.5.: Optical X-ray tomography as initially proposed by Frank [Fra42] and later improved by Edholm [Edh77]. This general principle still applies today, but particularly the back-projection has been computerised, and data is processed more accurately, thus reducing blur.

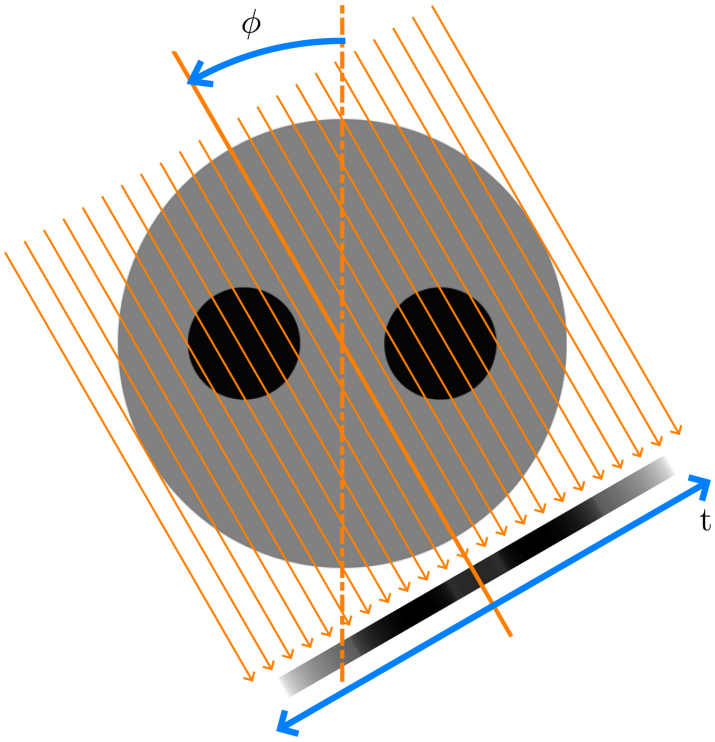

Figure 3.6.: Considering the setup shown in fig. 3.5, a single projection is acquired at an angle ϕ, leading to a one-dimensional projection with running index t. Parallel incoming X-rays are depicted in this sketch, for simplicity.

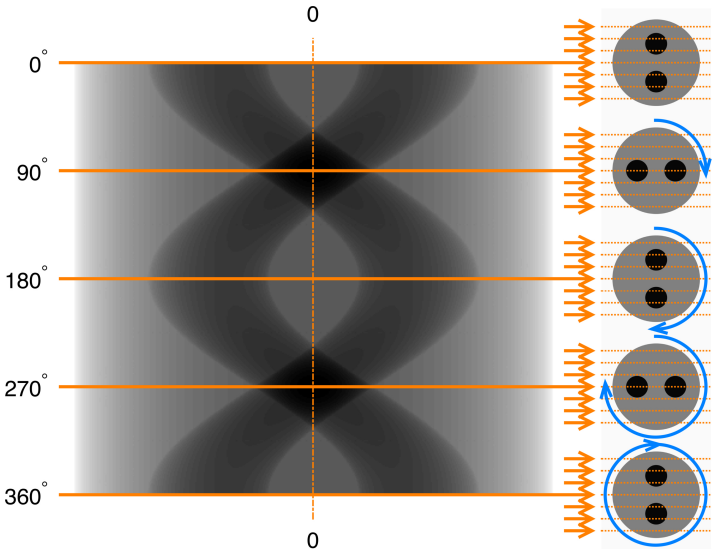

Figure 3.7.: Several projection operations as shown in fig. 3.6 lead to a two-dimensional image, a so-called *sinogram*. One axis corresponds to the angle, the other to the offset. In this sketch, each row of the sinogram contains the projection acquired at a single specific angle ϕ.

fanned up and projected over the entire image, and as result of these multiple, overlaid exposures, a blurry cross-sectional image will become visible on the secondary film. (See fig. 3.5.) This process can be thought of as 'intersecting' different well-known lateral views to come up with a cross-sectional image optimally explaining the measured observations. Note that exact knowledge of the perspective is essential, a constraint guaranteed in this case by mechanical coupling. In 1977, even after digital systems have been presented, the purely optical approach of back-projection was improved by Paul Edholm [Edh77] by adding a de-blurring component.

Apparently, the optical and mechanical approach was not particularly successful in clinical practice, probably due to the troublesome two-stage process, or for being too blurry. Some twenty years later, in 1963, however, the problem of reconstructing a cross-sectional image from a sinogram was revisited by Allan MacLeod Cormack. At that time, Cormack published two articles [Cor63; Cor64] where he treated it from a mathematical perspective: The sinogram, after some post-processing, can be considered to contain line integrals, based on the Beer-Lambert law as stated in eq. (2.1), and Cormack devised a mathematical framework and closed-form solution equations for computing a reconstruction of the original image. This, together with sufficiently mature computer technology, lead to the computerisation of the back-projection process, and thus lay the foundations for Computed (or Computerised) Tomography (CT). Working on non-medical settings, another researcher publishing on the topic was William H. Oldendorf [Old61; Old63].

The most important step towards wide-spread clinical use was the development of licensed, easily usable scanning systems. This work was first done at *EMI* laboratories by Godfrey Newbold Hounsfield during the late 1960s and early 1970s, and very early medical research on brain tumours was done by James Ambrose. The novel system was widely published in 1973, in a series of publications [Hou73a; Amb73; Per73], and the technology was quickly adopted. More traditional suppliers of medical imaging technology soon followed with own CT scanning systems. The novel imaging modality has had a tremendous clinical impact, combining novel imaging with relatively simple acquisition, and Cormack and Hounsfield jointly received the 1979 Nobel prize in medicine [Cor79; Hou79] for their work. (See Webb [Web90], Evens [Eve96] and Buzug [Buz08] for a detailed history of Conventional and Computed Tomography.)

From a technical perspective, the development of Computed Tomography scanners over the years to present time happened in a series of steps. The first question was the choice of an appropriate radiation source, and X-ray tubes have not necessarily been the most prominent choice, but people also planned to use radioactive isotopes for transmission imaging. This idea was prominent in related fields [Kuh66], too. The second question was the actual scanning pattern, i.e. the mechanics within the scanner, to acquire the input sinogram. The first four canonical scanner generations are all focussing on slice-based data acquisition, starting with a single rotating and translating source/detector pair, and leading to more complex geometries involving different fan-shaped combinations of a single source and multiple detectors [Her09; Buz08]. (See fig. 3.8.) Like that, a series of cross-sections could be scanned, and radiologists

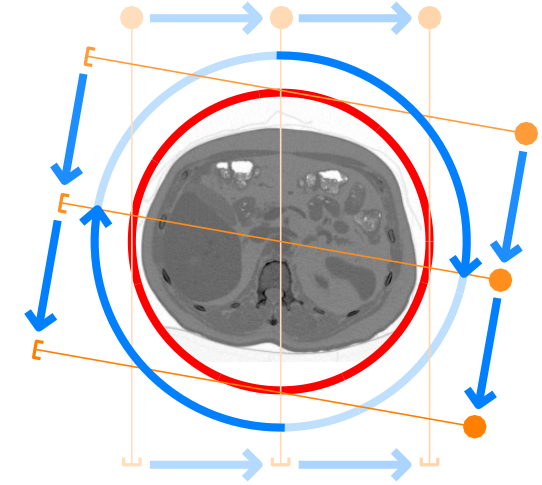

(a) Pencil beam, rotating and translating pair of X-ray source and single detector. (1^{st} gen.)

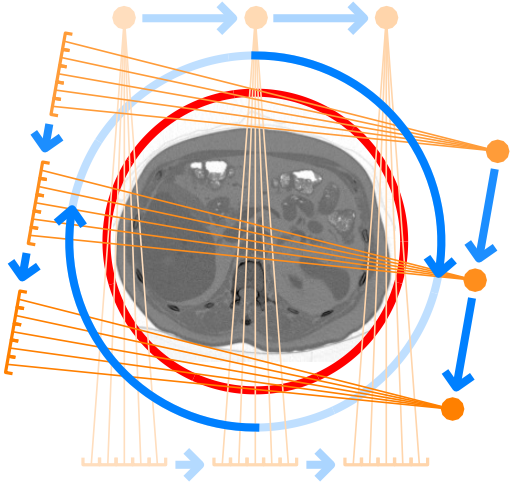

(b) Fan beam, rotating and translating arrangement of source and multiple detectors. (2^{nd} gen.)

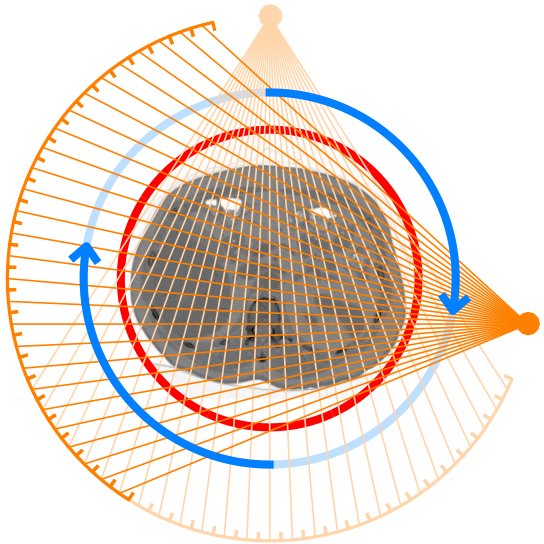

(c) Fan beam, rotating arrangement of source and multiple detectors. (3^{rd} gen.)

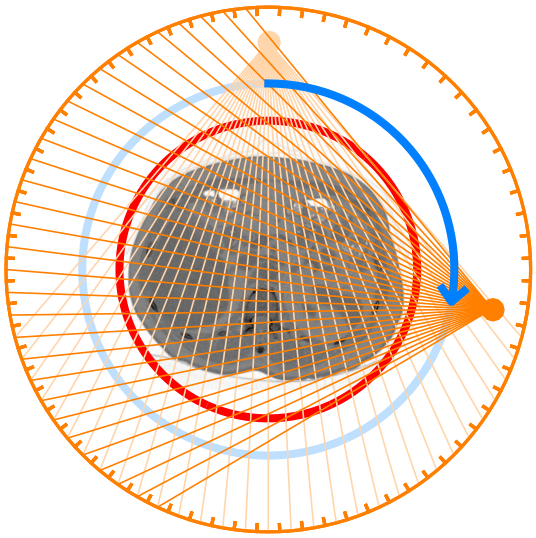

(d) Fan beam, rotating source and static detector ring. (4^{th} gen.)

Figure 3.8.: Classical slice-based CT scanning patterns, commonly referred to as generations one through four. Orange dots indicate the location of the X-ray source, single X-ray sensors are drawn as 'buckets'. Blue arrows denote motion patterns of the source/sensors arrangement. In reality, 4^{th} generation data is read out slightly differently as 'inverse fans'.

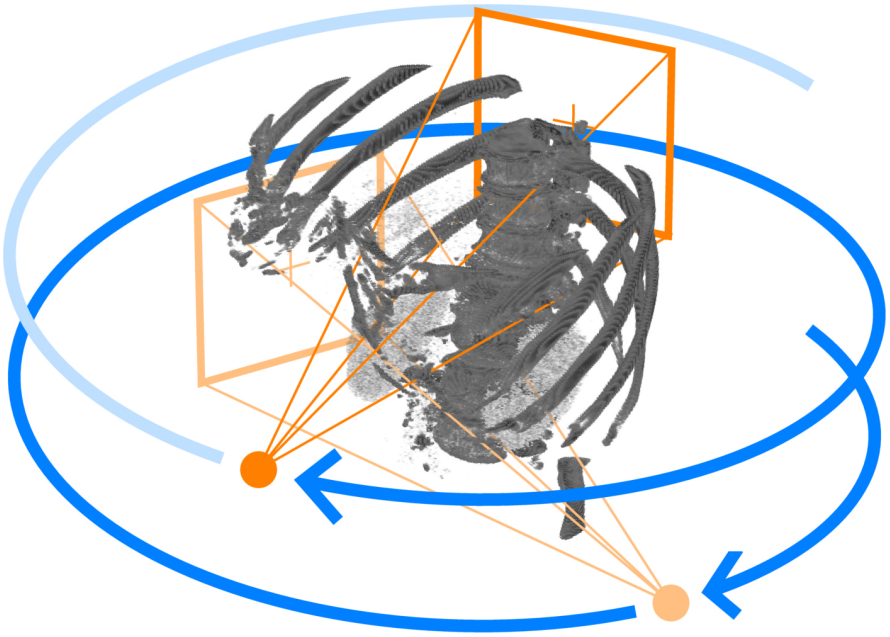

Figure 3.9.: Modern CT scanners use several improvements to quickly acquire data, such as helical trajectories and cone-shaped fields of view.

were able to browse through a stack of transaxial tomographic slices. (See fig. 3.1.)

Unfortunately, slice-based scanning is not sufficiently quick for moving organs such as the heart or the lung, and images may show motion artefacts. Compared to the original generations, modern CT scanners employ a series of improvements to make heart and lung imaging feasible, and they are vaguely referred to as 5^{th}, 6^{th} and 7^{th} generation scanners. First and foremost, modern devices are multi-line scanners, that is, they acquire multiple slices at the time, eventually leading back to the paradigm of cone-shaped acquisition geometries [Buz08, chap. 3.9]. Next, scanners may rotate more than one radiation source around the patient, and dual-source setups appear to be a particularly popular design. A very influential invention are the helical (also 'spiral') trajectories as proposed by Willi A. Kalender [Kal90]. There, the patient is moved through the scanning apparatus while the X-ray component is rotating, rather than doing individual slice-wise rotations and only moving the patient in-between. (See fig. 3.9.) Finally, a special CT-variant has been developed for cardiac imaging, Electron Beam CT [Buz08, chap. 3.8]. Vice versa, classically two-dimensional imaging modalities such as angiography or mammography systems have been equipped to also produce volumetric images.

Despite their technical differences, all these different scanner setups all share the same basic principles, and the tomographic images can be reconstructed using the same mathematical methods. Details about the numerical reconstruction process are discussed in chapter 4.

Note that, from a strict perspective, CT images are interpreted differently than classical X-ray images: The latter (unless post-processed) usually show *transmission* information, that

is, the radiation that still passes through a specimen. For CT, it makes more sense to consider *attenuation* or *absorption* information, as will be seen in chapter 4. Both 'flavours' are highly related, as can be concluded from the Beer-Lambert law in eq. (2.1). Recall that, according to this law, the original measured intensity is given by the relation

$$I_S = I_0 \cdot \exp\left(-\int_L \mu(\mathbf{x})\ \mathrm{d}\mathbf{x}\right) \tag{3.1}$$

where the transmitted intensity I_S on the far side is given based on a line integral over location-specific attenuation values $\mu(\mathbf{x})$, along a ray L. For CT, the forward model is rewritten to a 'pure' line-integral:

$$-\ln\left(\frac{I_S}{I_0}\right) = \int_L \mu(\mathbf{x})\ \mathrm{d}\mathbf{x} \tag{3.2}$$

This makes it easier to tackle the reconstruction problem mathematically, and abstracts away context-specific information, the initial intensity I_0 and the actually measured value I_S.

Also note that while the general term 'Computed Tomography' is often used in conjunction with X-ray imaging, the idea of computerised cross-sectional imaging is much more universal. Consequently, the term 'Transmission Computed Tomography' (TCT) has been proposed for X-ray CT.

3.3. Nuclear Imaging and Emission Computed Tomography (ECT)

The need for distinguishing X-ray CT from other tomographic modalities becomes clear when considering that scintigraphy, the probably most prominent two-dimensional nuclear imaging modality, has also been extended to yield volumetric images. In this case, the general term 'Emission Computed Tomography' (ECT) may be used. Again, the idea is to administer a radiopharmaceutical tracing metabolic processes, to detect the rays coming from within the patient's body, and to reconstruct a volumetric approximation of the distribution of radioactivity. An unexpected radiation hotspot may hint at cancer tissue, for instance. The imaging modality is thus not anatomical, that is intended to show body structures, but functional, that is intended to visualise processes going on in the body of the patient. (See section 2.4.2, and refer to Pollycove [Pol96b] for a detailed history of nuclear imaging.)

3.3.1. Single Photon Emission Computed Tomography (SPECT)

The straight-forward extension of planar scintigraphy to volumetric imaging is Single Photon Emission CT (SPECT). Instead of a single static gamma-camera, the detector is rotated around the patient, and – like in TCT – images are correlated with the perspective, i.e. the position of the sensor while detecting the γ-photon counts must be well-known. 'Intersecting' such views from well-distributed perspectives leads to a volumetric view of the radioactivity distribution. (See fig. 3.10.) Again, details about the reconstruction are postponed to chapter 4.

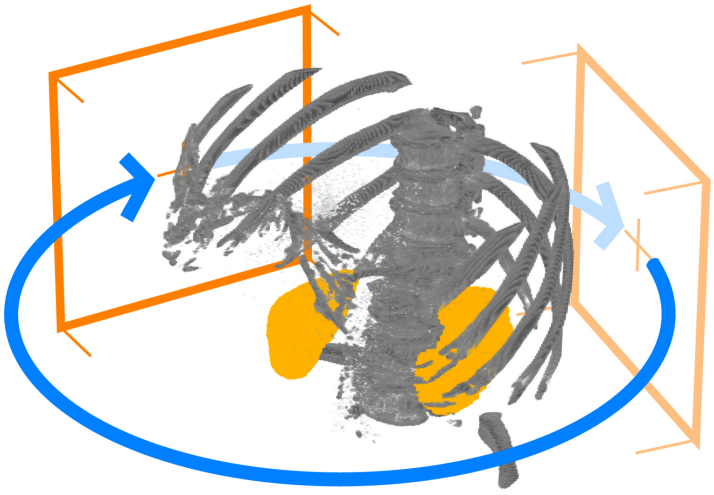

Figure 3.10.: In a SPECT setup, at least one gamma-camera rotates around the patient and observes γ-rays, in this sketch emitted from radioactively marked kidneys. By correlating radiation counts and camera perspectives, the three-dimensional distribution can be recovered.

As described for X-ray CT, there have been conventional, non-computerised forerunners to SPECT. The first was published in 1963 by David Kuhl and Roy Edwards [Kuh63], where stereoscopic rectilinear scanning is employed to obtain several exposed films, and then the work suggests to super-impose them. The same paper mentions transmission scanning and sketches the TCT process, the authors can thus also be considered to be among the pioneers of X-ray CT. In 1965, Harper *et al.* [Har65] suggested the use of Anger cameras instead and drafted another conventional 'reconstruction' method. The real forerunner to SPECT, however, was published by Anger *et al.* [Ang67] in 1967. Still conventionally producing images, a patient was now rotated in front of a (heavy and thus static) camera.

Also in this case, the conventional imaging systems do not appear to have been very successful outside of research institutions. Again, the computerisation of the image building process became key on the way towards wide-spread clinical use, and Budinger *et al.* [Bud74] appear to be among the first contributors. (See Webb [Web90] for a more complete history of SPECT imaging.)

From a physical point of view, the forward model for SPECT is more complicated than the one for X-rays as given in eq. (3.2). Recall that there is an (unknown) radioactivity distribution within the region of interest. If, as result of nuclear decay events, γ-photons are emitted, these photons will encounter the same attenuation effects discussed above for transmitted X- or γ-photons. Consequently, on top of the radioactivity distribution which one seeks to reconstruct, attenuation values also need to be considered. Following Kak *et al.* [Kak87, chap. 4.1.2] and Lasser [Las11a, chap. 1.3.2], a suitable equation is:

$$I_S = \int_L f(\mathbf{x}) \cdot \exp\left(-\int_{L(\mathbf{x})} \mu(\mathbf{y})\, \mathrm{d}\mathbf{y}\right)\, \mathrm{d}\mathbf{x} \tag{3.3}$$

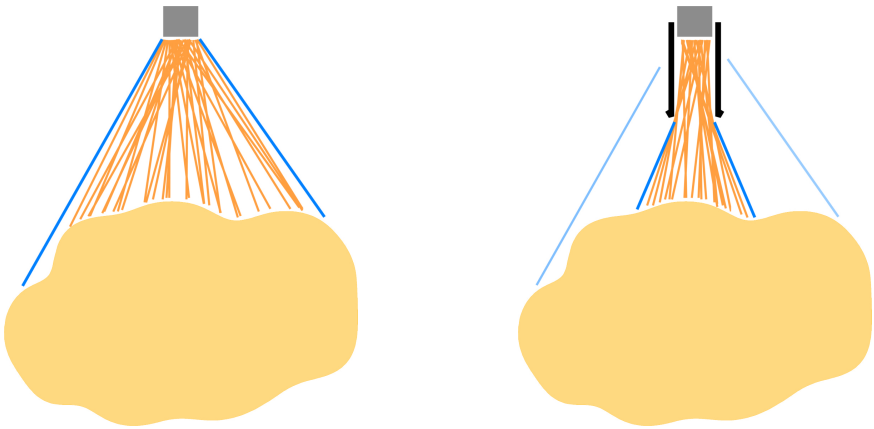

Figure 3.11.: A sensor observing a radiation distribution will typically count photons emitted from a larger region. The field of view can be restricted by means of *collimation*: A metal shielding (black) around the sensor (gray) will narrow down the field of view (blue), thus leading to better images, but the photons suppressed by collimation will be lost.

Considering a line-shaped field of view L for a single sensor, the measured intensity I_S is the line integral over the unknown radioactive intensity distribution $f(\mathbf{x})$, weighted by the accumulated attenuation along the partial ray $L(\mathbf{x})$ between position $\mathbf{x}$ and the sensor.

When practically reconstructing an activity distribution, the attenuation usually needs to be considered. Ideally, a registered CT-image allows to use realistic, patient-specific values for attenuation correction. Depending on the setting, simplified values are often used instead.

3.3.2. Positron Emission Tomography (PET)

Considering SPECT (and scintigraphy), an important feature is the use of strong collimation, thus narrowing down the sensor-wise fields of view to narrow cones. Without, it would be hard to relate individual measurements with spatial locations, particularly for a human observer, thus leading towards increased blurriness. The drawback, however, is that many potential measurements are physically suppressed by the collimation material. This situation is not desirable as the patient's radiation exposure is defined by the amount of injected activity, and a scanning device should pick up as many measurements as possible, in order to maximise image quality at a certain exposure level. (See fig. 3.11.)

An alternative to radiopharmaceuticals emitting γ-photons directly (based on ^{99m}Tc, for instance) is the use of *positron* emitters. Theoretically predicted in 1928 by Paul A. M. Dirac's quantum theory of electrons [Dir28], and experimentally demonstrated in 1933 by Carl D. Anderson [And33], the positron (e^+) is the electron's (e^-) anti-particle. That is, it carries a positive instead of a negative charge, but shares (almost) all other properties. Unless in a complete vacuum, a positron will collide with a free electron, and the two particles will be annihilated, leading to two γ-photons of a well-defined energy of 511 keV to be emitted in

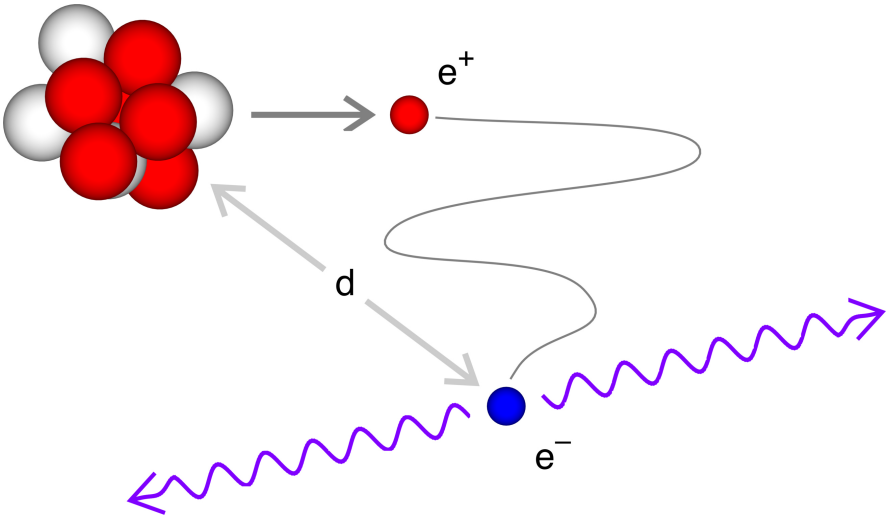

Figure 3.12.: Following a primary decay event, a positron (e^+) is emitted. This particle will rapidly lose kinetic energy and annihilate with an electron (e^-) within a certain distance d from the primary event. According to Cherry *et al.* [Che06], d will typically be between 0.01 cm and 0.1 cm. The energy balance is leveled after annihilation by the emission of two γ-photons of 511 keV energy that are sent off in opposite directions.

opposite direction [Che06]. Again, the findings of the two researchers have been awarded with Nobel prizes in physics in 1933 and 1936, respectively [Dir33; And36].

Originally, the positron has been demonstrated in the context of cosmic radiation. In 1934, Iréne and Frédéric Joliot-Curie found a first decay reaction where a radioactive substance emits positrons [Cur34]. In such a case, the positron will have a very short lifetime and annihilate within a short distance of the nucleus, typically between 0.01 cm and 0.1 cm away [Che06], leading to the γ-photon-burst in opposite directions as described above. (See fig. 3.12.)

This particular behaviour can be exploited advantageously for imaging purposes. First of all, due to the well-defined energy level, it is rather simple to differentiate between relevant photons and background radiation. Second, instead of collimation, one can detect coincident gamma photons, and deduce that an annihilation event happened along the respective 'line of response' (LOR). For that reason, positron imaging systems typically employ sensor rings observing a region of interest and collect such LORs. Based on them, tomographic reconstruction techniques can be used to compute the volumetric radioactivity distribution, leading to Positron Emission (Computed) Tomography (PET). (See fig. 3.13.)

Looking back into history, the use of positron emitters for imaging purposes goes back to Frank R. Wrenn [Wre51] and Gordon L. Brownell [Bro53; Bro99], originally with static opposite detectors. The first ring-shaped detector (nick-named 'head-shrinker') was built by Robertson *et al.* [Rob73] during the early 1960s. Again, a decisive event was the move towards computerised tomographic reconstruction. This probably happened for the first time within

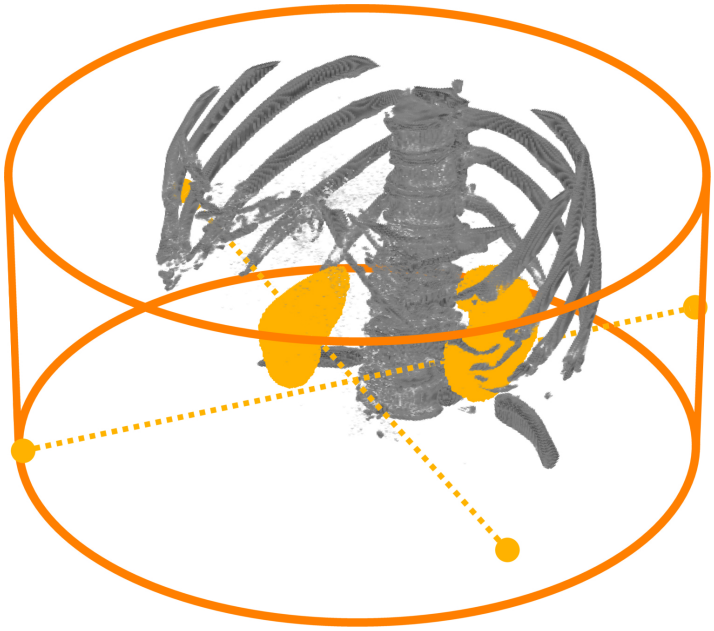

Figure 3.13.: In a PET system, coincident γ-photons are detected by means of a detector ring (orange) without collimation. Connecting the detection spots (yellow dots) leads to a *line of response* (yellow dotted lines) which are known to pass through radioactive area. Based on many such LORs, the radioactivity distribution can be recovered.

the Brownell group, and pioneering work has been published by David A. Chesler [Che71; Che73a; Che73b] in the early 1970s. After these initial steps, the first PET systems were developed by Michael E. Phelps and Michel Ter-Pogossian [Ter75; Phe75], particularly the first human-sized scanners [Phe76; Hof76; Ter79]. (See Cherry *et al.* [Che06] for technical details, and Webb [Web90] and Nutt [Nut02] for more information on the history of PET.)

The physical forward model of PET is similar to the one of SPECT as defined in eq. (3.3). Again following Lasser [Las11a, chap. 1.3.3], a suitable equation is:

$$g = \int_L f(\mathbf{x}) \cdot \exp\left(-\int_{L^+(\mathbf{x})} \mu(\mathbf{y})\ \mathrm{d}\mathbf{y} - \int_{L^-(\mathbf{x})} \mu(\mathbf{y})\ \mathrm{d}\mathbf{y}\right)\ \mathrm{d}\mathbf{x} \tag{3.4}$$

Here, L does no longer denote the field of view of a particular sensor (as used to be the case for X-ray CT and SPECT), but a line of response (LOR) defined by the two sensors actually discovering the coincident γ-photon burst. Similarly, g can be considered a 'LOR-intensity'. $L^+(\mathbf{x})$ and $L^-(\mathbf{x})$ are partial lines between position $\mathbf{x}$ and the two sensors. They are used, as for SPECT, to accumulate the radiation attenuation caused by the anatomy. Considering that these two partial lines together form the full line of response, the attenuation information becomes independent of the position $\mathbf{x}$, and eq. (3.4) can be simplified [Las11a, chap. 1.3.3]:

$$g = \exp\left(-\int_L \mu(\mathbf{y})\ \mathrm{d}\mathbf{y}\right) \int_L f(\mathbf{x})\ \mathrm{d}\mathbf{x} \tag{3.5}$$

This product cleanly separates attenuation information from the radioactivity distribution. The first factor deals with attenuation $\mu(\mathbf{x})$ and resembles the Beer-Lambert law as given in eqs. (2.1) and (3.1), respectively. The second factor concerns the radioactivity distribution $f(\mathbf{x})$ and is a simple line-integral resembling eq. (3.2). This decomposition is the foundation for elegant attenuation correction schemes for PET.

3.3.3. Multi-modality Scanners (SPECT-CT and PET-CT)

There are two reasons – a perception-related one, and a technical one – why emission CT should be operated in conjunction with a transmission CT system, eventually leading to SPECT-CT and PET-CT. First, the functional ECT images do not show the full anatomy by design and have less resolution than TCT images. During diagnosis, it is highly desirable to have both image components available, and to relate functional with anatomical information. This could be done by retrospective registration of the images, but a coherent acquisition of all signals during the same session is clearly superior.

Second, as has been described for both, SPECT and PET, knowledge of the radiation attenuation is necessary for reconstructing good activity distributions. This fact has become obvious quite soon, and early scanners already took an additional external radiation source for transmission measurements along [Kuh66].

Consequently, 'multi-modal' scanners, SPECT-CT and PET-CT [Bey00; Boc00], have become the *de-facto* clinical standard. (Also see Ziegler *et al.* [Zie00].) Such scanners are effectively a combination of two scanning systems in a single gantry, and acquire input data from the same (quasi-)static scene. During reconstruction, the transmission information is used to compute the emission image.

Quite recently, however, Defrise *et al.* [Def12] have published a special algorithmic improvement for time-of-flight PET (TOF-PET). The latter is an extension of PET which attracts the community's interest already for several years: TOF-PET does not only measure coincident γ-photons, but also the (extremely small) temporal delay between the two detections of a single line of response (LOR). Based on it, it is possible to roughly locate the positron annihilation along the LOR. Using a probabilistic approach [Def14], the authors are apparently able to recover an attenuation map from TOF-PET-data. That is, they claim to arrive at a result comparable to PET-CT, but without a distinct transmission measurement.

3.4. Other Biomedical Imaging Modalities

So far, this chapter has outlined transmission and emission CT as fundamental (medical) imaging techniques, and the thesis will restrict itself to discussing related aspects. However, there are further (even tomographic) imaging modalities that deserve brief mentioning.

3.4.1. Ultrasonography

A very well-known and – due to its non-invasiveness and the relatively cheap scanning devices – widely used medical imaging modality is *ultrasonography*. Originally developed for naval warfare (sound navigation and ranging – sonar) and non-destructive testing, the technology was adapted for medical imaging from the 1940s on [Gol96].

The best-known variant of it is *echography*: An ultrasound pulse is sent from a so-called transducer into the patient's tissue. Depending on the anatomy, this sound pulse travels some distance until it has been fully reflected, and returns to the transducer which is now set into receiving mode. Based on such echoes, cross-sectional (and thus tomographic) or even volumetric images can be computed. Even more, by exploiting the Doppler effect, echography is also able to yield functional images, showing information about blood flow, for instance. (For historical and technical details, see Goldberg *et al.* [Gol96] and Budinger [Bud97]; the latter also contains a comparison to other imaging modalities.)

In addition to echoes, it is also possible to consider true ultrasound transmission, both in the sense of amplitudes as well as propagation times. Like in X-ray CT, a pulse is generated on one side, attenuated while on the way through the patient's body, and measured on the other side by a receiver. Based on a more complex forward model, tomographic reconstruction methods can be used to compute an ultrasound transmission map from many such individual measurements. There has been extensive research on the topic, but currently, there appears to be only limited practical interest. (See Kak *et al.* [Kak87, chap. 4.3] or Deans [Dea07, chap. 1.4] for details and references.)

3.4.2. Magnetic Resonance Imaging (MRI/NMR)

Another important medical imaging modality is *(Nuclear) Magnetic Resonance Imaging*[1] *(MRI, formerly NMR)*. First proposed by Paul C. Lauterbur [Lau73] in the early 1970s, MRI employs the nuclear spin for imaging purposes. Together with Peter Mansfield, the other MRI pioneer, Lauterbaur received the 2003 Nobel prize in medicine [Lau03; Man03].

Very briefly and superficially, an atomic nucleus with an odd number of subatomic particles exhibits a magnetic moment, the spin. This applies particularly to the hydrogen nucleus (a single proton) which is practically omnipresent in organic tissue. In the presence of a strong magnetic field, the moments of the nuclei align to the field lines. Using an additional, orthogonal magnetic field, the spinning nuclei can be excited (to 'wobble'). Afterwards, they will return to their equilibrium state and send out a radio-magnetic wave while doing so. The latter signal can be received using an antenna, and it depends on the chemical element and the strength of magnetic field. By using overlaying magnetic 'gradient fields', the resonance signal can be read out systematically over a volume of interest and processed into a volumetric image.

1. Note that the modality is related to atomic nuclei, but not to radioactivity. To make this clear for the general public, the term 'nuclear' has largely been dropped from the name.

(See Dawson [Daw13], Meaney [Mea96] and Budinger [Bud97] for historical and technical details; again, note the comparison of different imaging modalities in the latter article.) While there exist special MR image reconstruction algorithms, the usual reconstruction techniques are relatively similar and have originally been used directly. (See Kak *et al.* [Kak87, chap. 4.4] or Deans [Dea07, chap. 1.7] for details and references.)

MRI is usually used for anatomical imaging. X-ray CT and MR images are largely complimentary, and there are certain diagnostic settings where either of the modalities yields better results in terms of resolution and contrast. An obvious advantage of MRI is the fact that the patient is not exposed to ionising radiation, but the effects of the magnetic fields are sometimes disputed. MRI can also be used for *functional* imaging of the brain (fMRI) based on blood oxygenation [Oga90], and will thus show brain activity. Another well-known anatomical subdomain is *diffusion tensor imaging (DTI or MR-DTI)* [Le 86; Fil09]: Instead of measuring the anatomy directly, water perfusion is tracked to obtain anatomical information. Again, DTI is particularly interesting for brain imaging. A third subdomain is *phase contrast MRI* [Mar12a; Mor82; Dij84; Bry84] (4D flow MRI), a functional modality primarily intended for measuring blood flow: As usual, the nuclei of the blood will respond to the magnetic fields while moving through the vessels, but the motion causes the response signal, an electro-magnetic wave, to be phase-shifted. Exploiting this, flow MRI is able provide two co-registered volumetric images, an anatomical picture, and a vector-valued velocity distribution. This is particularly interesting for cardiac imaging, and current research aims towards combining flow MRI with *computational fluid dynamics (CFD)* [Kol15b; Kol15a].

Finally, inspired by SPECT-CT and PET-CT, it has been suggested to combine MRI with emission CT [Sha97]. In this case, the computation of attenuation information from MRI is more challenging, but such a device offers the chance to visually relate emission (tumour) information with anatomy that is more advantageously depicted in MR images.

3.4.3. Other Modalities

The modalities described so far have all very high clinical relevance and are used on a regular basis. There are some further imaging techniques which are intended for research work or that are still in development.

Optical Tomography The term *optical tomography* [Ntz05; Las11a] does not appear to be entirely well-defined, and it relates to a group of optical methods designed to yield volumetric data. They differ with respect to illumination, optics, presence of fluorescent tracers, and physical effect used for tomography. In its most basic variant, the approach is similar to X-ray CT, but due to increased scattering, the modality appears to be confined to small-animal-imaging for now.

Electron Microscopy Tomographic methods are also used in the context of *electron microscopy* [Fra06; Dea07, chap. 1.6]. A recent example is Cryo-Electron Tomography (CET) [Luč05]. In this case, a very tiny sample of molecular scale is observed in an electron microscope, and images are acquired from different perspectives. Afterwards, a volumetric image is recovered from the individual views. Unlike other methods, the CET community appears to rely on heavier post-processing and model-fitting [Che12a] once the tomographic image has been reconstructed, due to a reportedly low signal-to-noise ratio.

4. Reconstructing Images

Several imaging setups have been described so far, along with respective mathematical *forward models*. These equations effectively specify how a physical process interacting with a certain sample leads to measurements. These sensor readings are derived from specific properties of the specimen which are linked to the imaging process, like the ability to attenuate radiation in case of X-rays.

Based on such data, the *reconstruction* process aims to recover the sample's (unknown) properties from the measurement. In case of X-ray CT, the objective is to compute an attenuation map of the specimen from the X-ray images. In mathematics, such problems are generally referred to as *inverse problems*. According to Jacques Hadamard's [Had02] definition, a problem is *well-posed* if a solution exists after all, if this solution is unique, and if this solution depends continuously on the initial conditions. Unfortunately, this is typically not the case for tomographic reconstruction problems, due to discretisation, incomplete measurements and noise. An important aspect is, therefore, awareness and proper handling of this *ill-posedness*.

4.1. Analytical Reconstruction

There are many methods to compute tomographic reconstructions which can be categorised into two large classes by general architecture. The first such class contains the *analytical* methods: The inversion problem has been tackled theoretically, and closed-form solution equations have been developed 'on paper'. Based on these equations, a fast computer programme can be implemented that turns measurements into tomographic images. Analytical methods are often quite strict in terms of assumptions concerning acquisition geometries, noise characteristics, among others, making them rather static and less flexible. Consequently, analytically reconstructed images are prone to show noise and artefacts. To a certain degree, such difficulties can be controlled quite well, and due to their speed, analytical methods are used in most clinical X-ray CT systems to this day.

This chapter is intended to convey an overview about common mathematical approaches to tomographic reconstruction. Less common methods, exact definitions, proofs, and related general concepts such as linear systems will be omitted, and the reader is referred to the respective literature. Books providing in-depth discussions have been published by Natterer [Nat86; Nat01b], Natterer *et al.* [Nat01c], Herman [Her09], Deans [Dea07], Kak *et al.* [Kak87], Helgason [Hel99], among others. For a very practical discussion, see Buzug [Buz08].

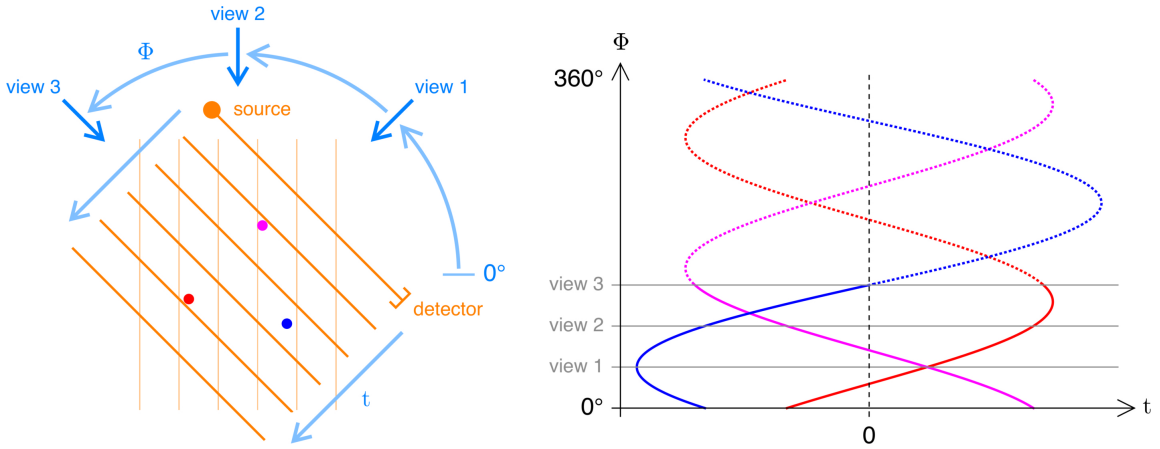

Figure 4.1.: The two-dimensional Radon transform considers all line integrals over a certain signal f (left). Polar coordinates are typically used to denote individual lines, and are used to store the integral values into a so-called sinogram (right). The name is due to the sine-shaped traces left by the original signal. (Cf. figs. 3.6 and 3.7.)

4.1.1. The Radon Transform and Its Inversion

The analytical methods discussed in this section mainly relate to slice-based X-ray data, that is, a single two-dimensional cross-section. As has already been discussed for the analogue case in the context of Frank's back-projection patent [Fra42] (section 3.2), the problem is the reconstruction of a two-dimensional attenuation map based on a set of one-dimensional projections contained in a sinogram. (See figs. 3.6, 3.7, and 4.1.)

In order to tackle the reconstruction problem, the attenuation map is considered as function

$$f : \Omega \to \mathbb{R} \tag{4.1}$$

where $\Omega \subset \mathbb{R}^2$ denotes the *volume of interest*. The map assigns an attenuation value $f(\mathbf{x})$ to every location $\mathbf{x} = (x, y)^T \in \Omega$. Aim of the reconstruction process is the recovery of f based on many line integrals

$$\mathcal{R}f(L) = \int_L f(\mathbf{x})\ \mathrm{d}\mathbf{x} \tag{4.2}$$

that have been systematically acquired. Interestingly enough, this problem has first been described from a purely theoretical perspective by Johann Radon [Rad17; Rad86; Rad07] in 1917, and the link between Radon's work and computed tomography was only discovered and confirmed in the 1970s. (See section 4.9.)

Definition 4.1 (Radon Transform)**.** *Let $f : \mathbb{R}^n \to \mathbb{R}$ be sufficiently nice. Let $\mathcal{R}f : \mathbb{R}^{n-1} \to \mathbb{R}$ denote f's integral over a given $(n-1)$-dimensional linear manifold of $\mathbb{R}^n$. Then, the transform*

$$f \mapsto \mathcal{R}f \tag{4.3}$$

from the original signal to ***all*** *its respective integrals is called the* ***Radon Transform*** *of f.*

The original two-dimensional Radon Transform ($n = 2$) is, therefore, the process of mapping a two-dimensional signal to *all* its line integrals,[1] yielding a sinogram. In order to encode these lines, *polar coordinates* (t, ϕ) are commonly used:

$$\mathcal{R}f(t, \phi) := \int f(t\cos\phi - s\sin\phi, t\sin\phi + s\cos\phi)\ \mathrm{d}s \tag{4.4}$$

This scheme was already employed while describing Frank's analogue setup. (See fig. 4.1.) Alternatively, lines can also be encoded using a normal vector $\mathbf{n} = (\cos\phi, \sin\phi)^T$ and a center-offset t. Defining the normal's orthogonal vector $\mathbf{n}^\perp = (-\sin\phi, \cos\phi)^T$, eq. (4.4) can be re-written:

$$\mathcal{R}f(t, \mathbf{n}) := \int f(t\mathbf{n} + s\mathbf{n}^\perp)\ \mathrm{d}s \tag{4.5}$$

Having described the 'forward' setting, two interesting problems arise: Can the Radon transform be inverted, i.e. is it possible to recover f based on its line integrals? If so, is there a closed-form equation? Radon has answered the first question positively, and demonstrated a very theoretical solution which relies massively on the availability of all (infinitely many) line integrals. Unfortunately, the latter assumption is not realistic in practical settings, rendering Radon's equation unsuitable to serve as basis for implementing an image reconstruction programme [Smi77]. (See the original theorem [Rad17, thm. III], and Deans [Dea07, chap. 5f.] or Natterer [Nat86, chap. 2.2] for a full discussion of Radon's approach and its properties.)

Before focusing on computationally feasible reconstruction methods, note that the two-dimensional Radon transform is the mathematical counterpart of the acquisition paradigm used in a first-generation 'pencil-beam' X-ray CT scanning setup (see fig. 3.8(a)) where the data is provided by a translating and rotating source/detector-pair. For more modern architectures featuring fan-beam-geometries, the data needs to be sorted and interpolated to parallel-beam projections [Kak87, chap. 3.4.3] if analytical methods for inverting the Radon transform are to be used for image reconstruction. This process is called *rebinning*. Also note that the measured raw intensities follow the Beer-Lambert law, and must be preprocessed to pure line-integrals following eq. (3.2). (This entire section is based on Deans [Dea07, chap. 2, 5f.]; also see Buzug [Buz08, chap. 5.2f.], Natterer [Nat86, chap. 2], or Kak *et al.* [Kak87, chap. 3.1] for further details.)

4.1.2. Fourier-Based Reconstruction

In 1956, unaware of Radon's work and unrelated to tomographic imaging, astronomer Ronald N. Bracewell published an important result [Bra56; Bra67] relating the Radon transform with the Fourier transform [Fou22]. (See Herman [Her09, chap. 6.5] or Natterer *et al.* [Nat01c, chap. 1.3.1] for details on the Fourier transform; see section 4.9 for the historical background.)

1. Note that the extension of Radon's work to three dimensions leads to integrals over planes. On the other hand, the so-called *ray transform* always considers one-dimensional manifolds (line integrals) independent of the dimension. Clearly, the two transforms are equivalent for two dimensions.

Theorem 4.2 (Fourier Slice Theorem, Central Slice Theorem, Projection-Slice Theorem)**.** *Let $f : \mathbb{R}^2 \to \mathbb{R}$ be sufficiently nice. Let $\mathcal{F}_n$ denote the n-dimensional Fourier transform. Then:*

$$(\mathcal{F}_2 f)(t, \phi) = (\mathcal{F}_1(\mathcal{R}f(\cdot, \phi)))(t) \tag{4.6}$$

According to this theorem, the Fourier coefficients of a single projection equal the Fourier coefficients of the (unknown) signal f within a line-shaped region. (See fig. 4.2.) In natural language, the Fourier coefficients of the signal f can be assembled by properly copying the Fourier coefficients of the individual projections, and an inverse Fourier transform will yield f. However, on the way, polar coordinates need to be converted into Cartesian coordinates. (See fig. 4.3.) The quality of the reconstruction depends massively on the use of proper interpolation techniques during this so-called *regridding* stage as small, well-localised interpolation errors in Fourier space have global effects in the Cartesian domain. For this reason and despite its speed, Fourier-based reconstruction is rather uncommon for medical applications. However, it seems to be popular for tomographic reconstruction from synchrotron acquisitions, due to the massive amount of data and comparatively low noise levels [Dow99; Mar12b]. A suitable implementation is *gridrec* [OSu85] where interpolation is based on prolate spheroidal wave functions.[2]

Note that Cormack's original papers [Cor63; Cor64] also exploit the tight connection to the Fourier transform in order to reconstruct images, but they do so in a slightly different sense. Besides the Fourier transform, the relation to other transforms has also been investigated [Dea07, chap. 4]. (This entire section is based on Deans [Dea07, chap. 6]; also see Natterer [Nat86, chap. 5.2], Kak *et al.* [Kak87, chap. 3.2], Herman [Her09, chap. 9.2], or Buzug [Buz08, chap. 5.3] for further details.)

4.1.3. Back-Projection Methods

A different, slightly slower image reconstruction method avoiding the regridding problem is *back-projection*. As has been done mechanically in Frank's apparatus [Fra42], the idea is to 'smear' back the individual measurements along the respective rays and to add up all these images. (See fig. 4.4.)

Definition 4.3 (Back-Projection)**.** *Let $f : \mathbb{R}^2 \to \mathbb{R}$ be sufficiently nice. Let $g := \mathcal{R}f$ denote the Radon transform of f. Then,*

$$(\mathcal{R}^* g)(x, y) := \int_0^\pi g(x \cos\phi + y \sin\phi, \phi)\ \mathrm{d}\phi \tag{4.7}$$

is the (simple, unfiltered) ***back-projection*** *of g.*

2. Prolate spheroidal wave functions are known to be well-localised in both, Cartesian and Fourier space, thus limiting the impact of interpolation errors. (For details, see Slepian, Landau and Pollak [Sle61; Lan61; Lan62; Sle64].)

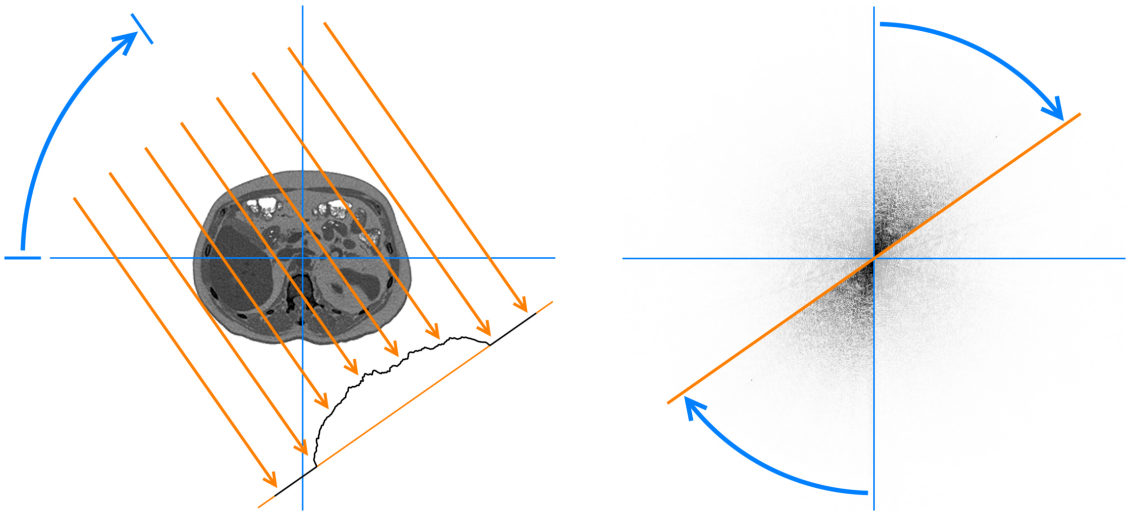

(a) Line integral in Cartesian space.

(b) Fourier coefficients in frequency space.

Figure 4.2.: Following the projection slice theorem, the Fourier coefficients $\mathcal{F}_2 f$ of the unknown image signal f can be recovered from the known projections $\mathcal{R}f$. In more detail, the one-dimensional Fourier decomposition of a single projection, $\mathcal{F}_1(\mathcal{R}f(\cdot, \phi))$, yields the Fourier coefficients along a line orthogonal to the viewing direction in frequency space (orange line). Having collected sufficiently many projections, application of the inverse Fourier transform will yield the reconstructed image. Note that interpolation issues may arise. (See fig. 4.3.)

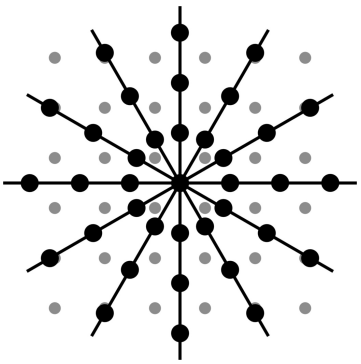

Figure 4.3.: While copying coefficients during Fourier reconstruction, data discretised using polar coordinates (black dots) needs to be 'regridded' to Cartesian coordinates (grey dots). Consequently, there are many noisy samples at the center, and few remote samples at larger distances. The quality of the interpolation process massively affects the reconstructed image.

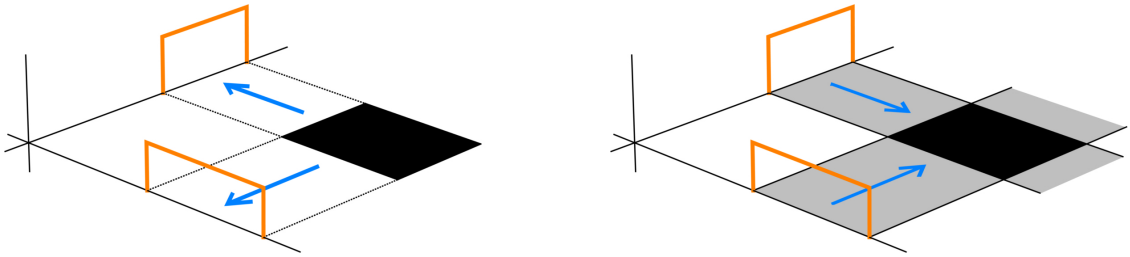

(a) Projection. (b) Back-projection.

Figure 4.4.: The idea of back-projection is to 'smear back' the projections along their respective rays over the volume of interest and to accumulate all these images, leading to a blurry 'reconstruction' of the original image.

Back-projecting the measured values will lead to a somewhat blurry reconstruction of the original signal. This is obviously due to 'shadows' of the original shape smeared over the entire reconstruction. A possible solution would be to post-process the back-projection in order to de-blur it. (See Buzug [Buz08, chap. 5.6ff.] or Herman [Her09, chap. 9.4] for further details.)

Another way to produce sharp images is to filter the measured values before back-projection. This approach is probably the most commonly used analytical reconstruction method, particularly in clinical devices, and is usually referred to as *filtered back-projection (FBP)*. Already mentioned by Bracewell in 1967 [Bra67], the decisive study was published by G. N. Ramachandran and A. V. Lakshminarayanan ('Ram-Lak') in 1971 [Ram71].

Theorem 4.4 (Filtered Back-Projection)**.** *Let $f : \mathbb{R}^2 \to \mathbb{R}$ be sufficiently nice. Let $g := \mathcal{R}f$ denote the Radon transform of f, and $\mathcal{R}^*$ the back-projection operator. For a given ϕ, define the* ***filtered projection***

$$g^\delta(t, \phi) := (\delta * g(\cdot, \phi))(t) \tag{4.8}$$

where $\delta(x) \approx |x|$ is a ***filter*** *and $*$ the one-dimensional convolution. Then, $\mathcal{R}^* g^\delta$ is the* ***filtered back-projection****, and $f \approx \mathcal{R}^* g^\delta$ if the filter is chosen appropriately.*

The reconstruction by back-projecting filtered projections leads to a visually sharp image. However, this will also lead to increased noise and image artefacts. (See fig. 4.5.) For this reason, different filter functions have been proposed for the discrete reconstruction from actual data, depending on the practical settings. The 'classical' choice $\delta(x) = |x|$ is commonly referred to as *Ram-Lak* or *Ramp* filter. Note that the convolution is usually computed as product in Fourier space, and also that pre-filtering can improve Fourier-based reconstruction as well. (This entire section is based on Deans [Dea07, chap. 6]; also see Natterer [Nat86, chap. 5.1], Herman [Her09, chap. 7f.], Kak *et al.* [Kak87, chap. 3.3], or Buzug [Buz08, chap. 5.6ff.] for further details.)

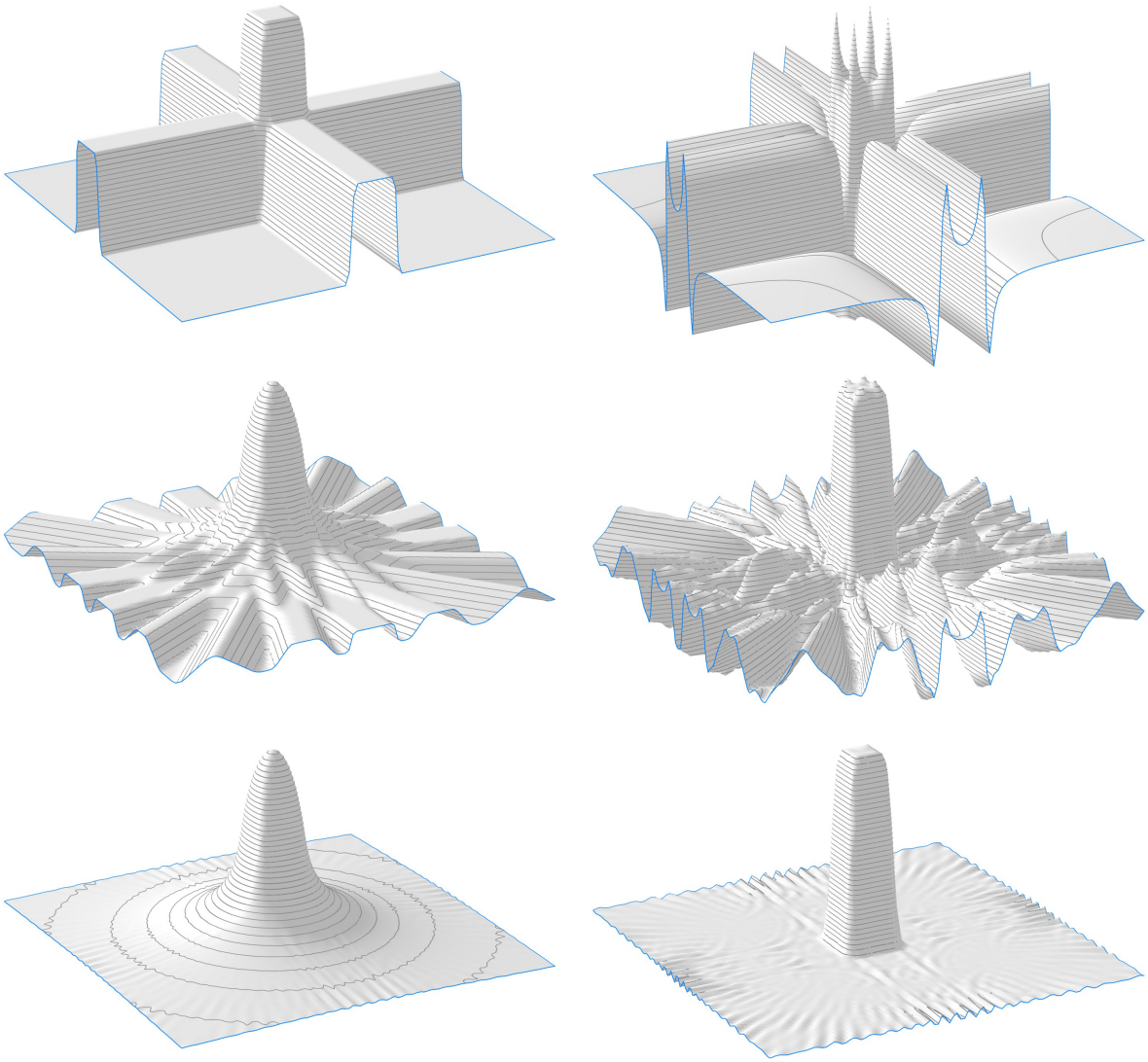

Figure 4.5.: Comparison of unfiltered (left column) and *Hann*-filtered back-projection (right) for a growing number of input projections of a simple square-shaped phantom. (First row: 2 projections at 0° and 90°; second: 9 projections every 20°; third: 45 projections every 4°.) The unfiltered version exhibits considerable smoothing while the filtered version recovers a better, sharper square-shape. However, noisy artefacts appear as well in the latter case.

4.1.4. Other Analytical Reconstruction Settings

This section has introduced the concepts of the most common and fundamental analytical reconstruction techniques. Over the years, several additional reconstruction approaches have been suggested for inverting the Radon transform, that is, the parallel-beam line-integrals reconstruction setting. (For instance, see Natterer [Nat86, chap. 5.6] or Deans [Dea07, chap. 7].)

In addition, specialised closed-form methods for related problems have been published. Particularly important is the so-called *Feldkamp (FDK)* algorithm [Fel84] which supports cone-beam shaped geometries for line-integral-data. Similar closed-form equations for fan-beam ('divergent') geometries have been proposed. (See Herman [Her09, chap. 10] or Kak *et al.* [Kak87, chap. 3.4] for further details.) For emission CT, several analytical solutions to inverting the attenuated ray transform have been suggested [Mar84; Nat01a]. (For a review, see Finch [Fin03].)

4.2. Algebraic Reconstruction as Least Squares Problem

While analytical methods are fast and well-understood, they are also rather static. It is possible to extend such methods, particularly by pre- and post-processing data, but in order to support iterative processes enforcing constraints, a more general, algebraic approach can be taken. As the name implies, *algebraic* or *series expansion* methods discretise the volume of interest, leading to linear systems.

4.2.1. Building the Linear System

In contrast to the analytical setting, the number of dimensions no longer needs to be predetermined. Therefore, the objective is to reconstruct an (unknown) scalar-valued signal

$$f : \Omega \to \mathbb{R} \tag{4.9}$$

where $\Omega \subset \mathbb{R}^n$ denotes a n-dimensional *volume of interest*. In order to recover f, a set of J scalar measurements is available. The physical *model* linking the signal to the specific scalar measurement m_j, $j \in \{1, ..., J\}$, is defined generically:

$$\mathcal{M}_j : (\Omega \to \mathbb{R}) \to \mathbb{R} \tag{4.10}$$

This mapping is required to be linear, and the jth scalar measurement is given by

$$m_j = \mathcal{M}_j(f). \tag{4.11}$$

These definitions are deliberately chosen to be very generic, in order to support as many settings as possible. In case of X-ray CT, $\mathcal{M}_j$ will continue to be defined as line integral along a certain corresponding line L_j:

$$\mathcal{M}_j(f) = \int_{L_j} f(\mathbf{x}) \, \mathrm{d}\mathbf{x} \tag{4.12}$$

Of course, full projections will continue to be recorded, but the model treats these pictures as sets of individual pixel measurements. In other words, j will extend over all pixels of all projective images, and the index will also be used to refer to geometric information (as has been done implicitly by introducing line L_j).

Reconstructing the signal requires a way to deal with f. Consequently, the function needs to be discretised with respect to a set of I suitably chosen spatial *basis functions* $b_i : \Omega \to \mathbb{R}$:

$$f(\cdot) \approx \hat{f}(\cdot) := \sum_{i=1}^{I} c_i \; b_i(\cdot) \tag{4.13}$$

The coefficients c_i are initially unknown, and recovering them is synonymous with solving the inverse problem. Once the coefficients are computed, a discrete approximation of the original signal can be computed via the synthesis operator given in eq. (4.13). Note that the actual set of basis functions can be chosen arbitrarily, but certain choices are particularly common, among them pixels (two-dimensional) and voxels (three-dimensional), or 'blobs' [Her09, chap. 6.5] as smooth variant of the former. Other basis functions such as wavelets or the Fourier basis are also possible [Jaf01].

The discrete signal $\hat{f}$ is required to approximate the (unknown) continuous signal f. Consequently, applying the measurement models $\mathcal{M}_j$ to $\hat{f}$ is required to yield values similar to the original measured values, and eq. (4.11) becomes:

$$m_j \approx \mathcal{M}_j(\hat{f}) = \mathcal{M}_j \left(\sum_{i=1}^{I} c_i \, b_i \right) \tag{4.14}$$

Exploiting the fact that the $\mathcal{M}_j$ are required to be linear, eq. (4.14) can be re-arranged:

$$m_j \approx \sum_{i=1}^{I} c_i \; \mathcal{M}_j(b_i) \tag{4.15}$$

Note that in this expression, only the coefficients c_i are unknown. In particular, factors $a_{ji} := \mathcal{M}_j(b_i)$ can be precomputed, and they describe the contribution of basis function b_i to measurement m_j. Defining the *coefficient vector* $\mathbf{c} = (c_i) \in \mathbb{R}^I$ and vector $\mathbf{a}_j = (a_{ji}) \in \mathbb{R}^I$, eq. (4.15) can be written as scalar product:

$$m_j \approx \langle \mathbf{a}_j, \mathbf{c} \rangle = \mathbf{a}_j^T \mathbf{c} \tag{4.16}$$

Considering all J measurements, a *measurement vector* $\mathbf{m} = (m_j) \in \mathbb{R}^J$ can be defined, and all the scalar products defined in eq. (4.16) can be collected into a linear system:

$$\mathbf{m} \approx \begin{pmatrix} — \; \mathbf{a}_1^T \; — \\ — \; \mathbf{a}_2^T \; — \\ \vdots \\ — \; \mathbf{a}_J^T \; — \end{pmatrix} \mathbf{c} =: A\mathbf{c} \tag{4.17}$$

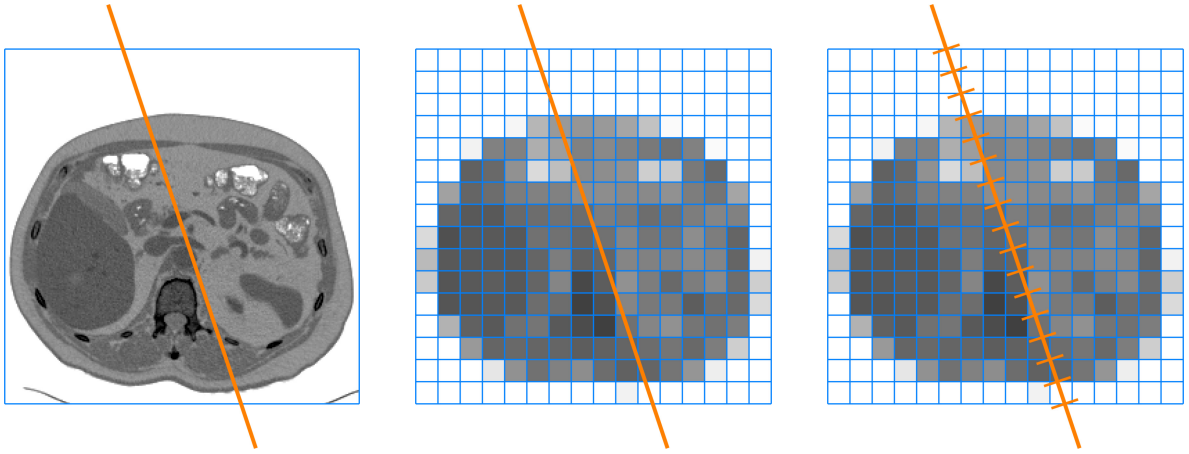

(a) Continuous signal, continuous integral: $\mathcal{M}_j(f)$

(b) Discrete signal, continuous integral: $\mathcal{M}_j(\sum_{i=1}^{I} c_i\, b_i)$

(c) Discrete signal, discrete integral: $\sum_{i=1}^{I} c_i\ \mathcal{M}_j(b_i)$

Figure 4.6.: In case of X-ray CT, the original measurement is a line integral over a continous function, but the objective is the reconstruction of a pixelised approximation which is supposed to yield very similar integrated values, by design of the problem. The line integral over the pixelised mesh is replaced with a discrete sum of pixel-wise line integrals.

Note that this system cleanly partitions the problem into the *system matrix* $A \in \mathbb{R}^{J\times I}$ containing a geometric description of the scanning setup, the *measurement vector* $\mathbf{m}$ containing the values measured in a particular experiment, and the unknown *coefficient vector* eventually leading to the signal. To clarify the reasoning used in eqs. (4.14) and (4.15), consider the case of X-ray CT and a pixel-based discretisation: The original measurement is physically explained as line integral over the signal. During reconstruction, pixel-wise attenuation values need to be computed, and the corresponding (artificial) line integral over the pixel mesh ideally leads to a value very close to the originally measured one. Due to the linearity of the integration, the integral over the mesh is replaced with a discrete sum of pixel-wise line integrals which can be pre-computed and stored in the system matrix. (See fig. 4.6)

The linear system set up in eq. (4.17) is not exact, due to the ill-posedness of the reconstruction process caused by measurement errors and the discretisation. Furthermore, the matrix is usually not square. For both reasons, an exact solution cannot be expected, and the corresponding *least-squares problem* may be solved instead:

$$\arg\min_{\mathbf{c}} \left\{ \frac{1}{2} \|A\mathbf{c} - \mathbf{m}\|_2^2 \right\} \tag{4.18}$$

Recall that the solution to eq. (4.18) is given by the *normal equation*:

$$A^T A\mathbf{c} = A^T \mathbf{m} \tag{4.19}$$

In order to solve eq. (4.19) for a coefficient vector, the usual standard methods could be used in theory: One could compute a Gaussian elimination, or employ matrix decompositions

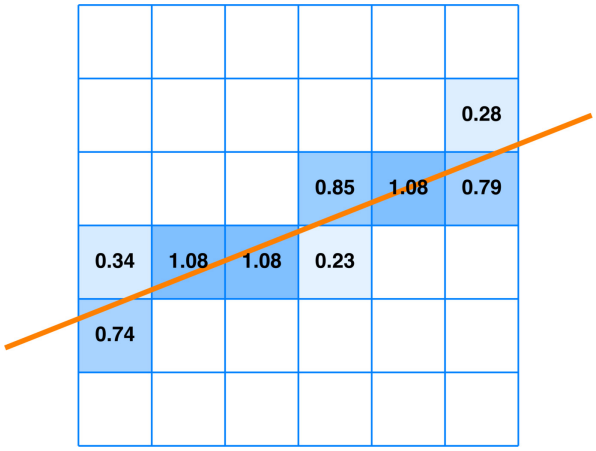

Figure 4.7.: Each row of the CT system matrix describes a ray. In case of a pixel basis, projector software computes the entries $a_{ji} = \mathcal{M}_j(b_i)$ in real-time as ray-pixel intersections.

such as LU, QR, SVD (possibly with truncation [Han87]), among others [Str09]. Apart from toy examples and very small setups, however, these approaches will not work due to the prohibitively large size[3] of the system matrix.

Consequently, iterative methods [Saa03; Bar94; Bri00] will be used that do not require knowledge of the full matrix, but only intermediate results such as its application to a vector, $A\mathbf{c}$, or the one of its transpose, $A^T\mathbf{m}$. In order to compute such results, the respective system matrix entries obviously cannot be queried from memory, but are computed in real-time by *projector software* simulating the measurement process. This is particularly necessary in case of X-ray CT due to large voxel counts, and projectors are used since many years [Sid85]. Luckily, X-ray setups follow the mathematical camera models used in computer graphics and computer vision, enabling the fallback to techniques established in these fields for describing systems, and for quickly and accurately simulating rays intersecting voxels. (See fig. 4.7, and Hartley *et al.* [Har04] for details on camera models in computer vision.)

Also note that $A\mathbf{c}$ is the *forward projection* of the discretised signal $\hat{f}$, based on its coefficient vector $\mathbf{c}$. Vice versa, $A^T\mathbf{m}$ is the *backward projection* of the measurement vector $\mathbf{m}$. In case of parallel-beam X-ray CT, $A\mathbf{c}$ is thus a discretised approximation of the Radon transform as defined in eqs. (4.2) and (4.3), and similarly, $A^T\mathbf{m}$ is a discretised approximation of the back-projection operation given in eq. (4.7).

The next sections will discuss several approaches to iterative inversion that are commonly used in tomographic reconstruction, and the selection is non-exhaustive. (See Saad [Saa03],

3. For instance, the problem of reconstructing a 512×512 pixel image ($I = 262{,}144$) from 180 parallel projections of 600 pixels each ($J = 108{,}000$), a realistic, small two-dimensional setting, leads to a system matrix containing 28,311,552,000 entries. Assuming single-precision floating point numbers (4 bytes), this matrix would have over 113 gigabytes (over 105 gibibytes), and thus by far too much for the working memory of most computers.

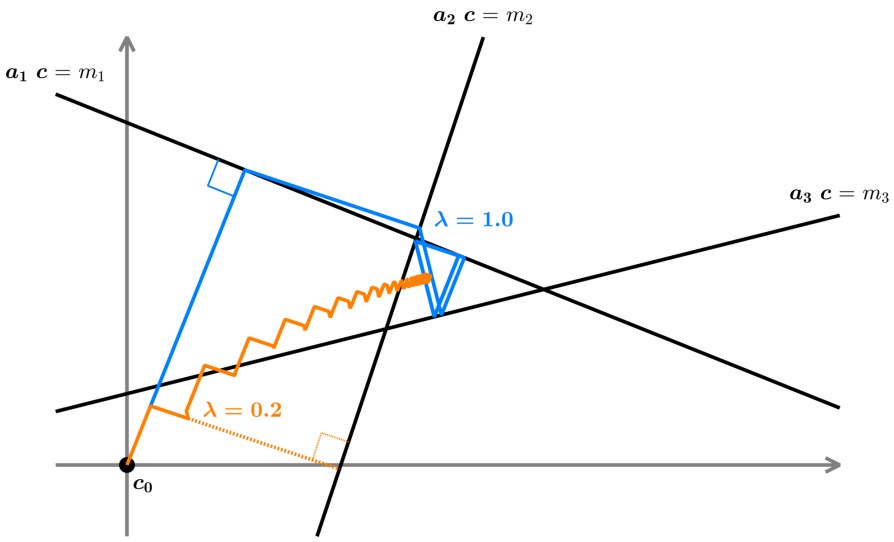

Figure 4.8.: The Algebraic Reconstruction Technique (ART) considers each row of the linear system as hyperplane, and iteratively projects a solution estimate orthogonally onto these hyperplanes until convergence (blue trajectory). However, there may not be a unique solution despite a large number of iterations. Using relaxation, the steps are not taken fully, and convergence may be improved by avoiding far positions (orange trajectory, $\lambda = 0.2$). In this plot, every line represents a row of a two-dimensional, over-determined, noisy linear system.

Barrett *et al.* [Bar94], or Briggs *et al.* [Bri00] for a discussion of general iterative inversion techniques; for further details on algebraic methods in the context of tomographic imaging, see Buzug [Buz08, chap. 6.1f.], or Kak *et al.* [Kak87, chap. 7].)

4.2.2. Algebraic Reconstruction Technique (ART)

The first iterative method widely used for tomographic reconstruction was the *Algebraic Reconstruction Technique (ART)*, published by Gordon *et al.* [Gor70] in 1970. This method has been identified to be a variant of Kaczmarz's method [Kac37], proposed in 1937.

Considering the original linear problem $A\mathbf{c} = \mathbf{m}$, every row $\mathbf{a}_j^T \in \mathbb{R}^I$ of $A \in \mathbb{R}^{J \times I}$ describes an $(I-1)$-dimensional hyperplane, together with the respective measurement m_j: The normal vector of the jth hyperplane is given by $\mathbf{a}_j$, the distance to the origin by m_j. In case of a square matrix ($I = J$) of full rank, all J such hyperplanes intersect in a single point, the solution vector $\mathbf{c}$ to the system $A\mathbf{c} = \mathbf{m}$. If A is overdetermined ($J > I$) and noisy, there will not be a single intersection point anymore, but a 'hotspot' can be expected where all hyperplanes pass in close proximity.

Exploiting this concept, the idea of Kaczmarz is now to iteratively project solution estimates $\mathbf{c}^{(q)}$ orthogonally onto these hyperplanes, yielding new estimates $\mathbf{c}^{(q+1)}$. (See fig. 4.8.) The process starts at an arbitrary location, often $\mathbf{c}^{(0)} = \mathbf{0}$, and terminates once the solution estimates have converged. Note that the same hyperplane will be visited multiple times, and

the number of iterations will typically exceed the number of hyperplanes. Mathematically, the single such projection performed in iteration q is given as follows:

$$\mathbf{c}^{(q)} = \mathbf{c}^{(q-1)} + \lambda(q) \cdot \frac{m_{j(q)} - \mathbf{a}_{j(q)}^T \mathbf{c}^{(q-1)}}{\mathbf{a}_{j(q)}^T \mathbf{a}_{j(q)}} \mathbf{a}_{j(q)} \tag{4.20}$$

Here, $j(q)$ is simply a mapping from the current iteration index q to a row $j(q)$ of the linear system, and the simplest choice is $j(q) = (q \mod J) + 1$. Convergence can be improved by *randomising* the selection of rows by defining $j(q)$ appropriately [Her93], effectively breaking 'evil' cycles. The relaxation factor $\lambda(q) \in (0, 1]$ can be used to reduce the step size per iteration which may help to improve convergence in noisy settings [Her78]. In Kaczmarz's original version, the updates were not relaxed, and $\lambda(q) = 1$. It has been shown that ART converges towards the solution of the least-squares problem given in eq. (4.18) if this regularisation factor approaches 0 with increasing number of iterations [Cen83].

In general, ART yields stable results that usually exceed the quality of normal analytical methods, and its mathematical properties are well-understood. In particular, ART does not impose special requirements onto A, and is able to tackle eq. (4.17) directly. Considering only a single row of the linear system at the time, however, ART is a so-called *row-action* method [Saa03, chap. 8.2], and is not particularly fast to converge. Furthermore, this design inhibits optimised interfacing with the projector software. (See Natterer [Nat86, chap. 5.3], Herman [Her09, chap. 11], Kak *et al.* [Kak87, chap. 7.1f.], Buzug [Buz08, chap. 6.3] or particularly Sørensen *et al.* [Sør14] for further details on ART.)

4.2.3. Simultaneous Iterative Reconstruction Technique (SIRT)

From an engineering point of view, a reconstruction algorithm is ideally defined in terms of forward ($A\mathbf{c}$) and backward projections ($A^T\mathbf{m}$). This enables easy interfacing with projector software whose core functionality exactly consists of these methods. The first and easiest example of such a method is the *Simultaneous Iterative Reconstruction Technique (SIRT)* published by Gilbert [Gil72] in 1972. Again, this algorithm has been identified as rediscovery of the *Landweber* method [Lan51] known since 1951.

The core concept behind SIRT is the residual of the linear system defined in eq. (4.17):

$$r(\mathbf{c}) := \mathbf{m} - A\mathbf{c} \tag{4.21}$$

Given a signal estimate $\mathbf{c}$, the residual is actually the error between the true measurement $\mathbf{m}$ and a simulated measurement obtained by forward-projecting the estimate via $A\mathbf{c}$. Starting at some initial solution estimate, SIRT iteratively determines this residual, projects it back along the rays and updates the estimate with it. In natural language, SIRT iteratively 'smears' back the error over the solution estimate until the latter perfectly explains the measurements, yielding the following update equation:

$$\mathbf{c}^{(q)} = \mathbf{c}^{(q-1)} + \lambda(q) \cdot A^T(\mathbf{m} - A\mathbf{c}^{(q-1)}) \tag{4.22}$$

Again, q denotes the iteration index, and $\lambda(q)$ a relaxation factor. (See alg. 4.1.) In order for eq. (4.22) to converge, the relaxation must be chosen sufficiently small.[4]

$\mathbf{c} = \mathbf{c}_0$	{initialise estimate, $\mathbf{c}_0 = \mathbf{0}$ without prior knowledge}
for iteration q **do**	
$\widetilde{\mathbf{m}} = A\,\mathbf{c}$	{project current estimate to obtain pseudo-measurement}
$\mathbf{r} = \mathbf{m} - \widetilde{\mathbf{m}}$	{compute error with respect to actual measurement}
$\widetilde{\mathbf{c}} = A^T\mathbf{r}$	{back-project error to obtain update}
$\mathbf{c} = \mathbf{c} + \lambda(q) \cdot \widetilde{\mathbf{c}}$	{apply relaxed update to estimate}
end for	

Algorithm 4.1: Simultaneous Iterative Reconstruction Technique (SIRT)

Note that from a mathematical point of view, the Landweber method is a gradient descent method on the least-squares problem. It is a simple example of a larger class of related approaches, and the generic form is referred to as *CQ* method [Byr02]. In general, the Landweber method is rather slow to converge [Slu90], but related methods with improved behaviour have been suggested [Cen01b; Cen01a]. (See Herman [Her09, chap. 12.2], Kak *et al.* [Kak87, chap. 7.3], or Sørensen *et al.* [Sør14] for further mathematical details.)

It has been mentioned above that many clinical scanners use analytical methods for image reconstruction. Interestingly, the very first prototype scanners used a SIRT-like row-wise iterative scheme back-projecting the residual, as stated in Hounsfield's early patent [Hou73b].

4.2.4. Simultaneous Algebraic Reconstruction Technique (SART)

Comparing ART and SIRT, a hybrid of the two would be beneficial: A method combining the better convergence behaviour of ART with the favourable forward/backward projection interface of SIRT. The respective algorithm is known as the *Simultaneous Algebraic Reconstruction Technique (SART)* and has been published by Andersen *et al.* [And84] in 1984.

Unlike above, the update equation of SART is typically given with respect to the single coefficient c_i:

$$c_i^{(q)} = c_i^{(q-1)} + \lambda(q) \cdot \frac{1}{\sum_j a_{ji}} \sum_j a_{ji} \frac{m_j - \mathbf{a}_j^T \mathbf{c}^{(q-1)}}{\sum_{i'} a_{ji'}} \tag{4.23}$$

Once more, q denotes the iteration index, and $\lambda(q)$ a relaxation factor. Despite this seemingly complex notation, after substituting variables, SART can also be considered as Landweber-style method [Byr02]. (See alg. 4.2; for mathematical details, see Kak *et al.* [Kak87, chap. 7.4].)

4. A theoretical bound can be computed based on the largest eigenvalue of $A^T A$ [Byr02]. For a practical setup, an empirical approach is usually necessary.

$\mathbf{c} = \mathbf{c}_0$	{initialise estimate, $\mathbf{c}_0 = \mathbf{0}$ without prior knowledge}
$\mathbf{s} = A\ \mathbf{1}$	{compute row-sums of A by projecting ones}
$\mathbf{t} = A^T\mathbf{1}$	{compute column-sums of A by back-projecting ones}
for iteration q **do**	
$\widetilde{\mathbf{m}} = A\ \mathbf{c}$	{project current estimate to obtain pseudo-measurement}
$\mathbf{r} = \mathbf{m} - \widetilde{\mathbf{m}}$	{compute error with respect to actual measurement}
$\widetilde{\mathbf{r}} = \mathbf{r} \oslash \mathbf{s}$	{normalise error by component-wise division by row-sums}
$\widehat{\mathbf{c}} = A^T\ \widetilde{\mathbf{r}}$	{back-project normalised error to obtain update}
$\widetilde{\mathbf{c}} = \widehat{\mathbf{c}} \oslash \mathbf{t}$	{normalise update by component-wise division by column-sums}
$\mathbf{c} = \mathbf{c} + \lambda(q) \cdot \widetilde{\mathbf{c}}$	{apply relaxed update to estimate}
end for	

Algorithm 4.2: Simultaneous Algebraic Reconstruction Technique (SART)

4.2.5. Conjugated Gradients on the Normal Equation (CGNE)

Apart from algorithms (re-)discovered within the tomographic reconstruction community such as the ones described so far, there are additional methods for iteratively solving linear systems in mathematics. Particularly well-known for its rapid convergence [Slu86] is the method of *Conjugate Gradients (CG)* [She94] proposed by Hestenes and Stiefel [Hes52; Sti52] in 1952.

Considering the least-squares problem stated in eq. (4.18), recall that a solution can be found via the normal equation $A^TA\mathbf{c} = A^T\mathbf{m}$ given in eq. (4.19). Define auxiliary variables

$$B := A^TA \tag{4.24}$$

$$\mathbf{k} := A^T\mathbf{m} \tag{4.25}$$

for brevity, and note that $B \in \mathbb{R}^{I\times I}$ is *square*, *symmetric* and *positive-definite*. Based on them, define furthermore the *quadratic form*

$$g(\mathbf{c}) = \frac{1}{2}\mathbf{c}^TB\mathbf{c} - \mathbf{k}^T\mathbf{c}. \tag{4.26}$$

Due to the properties of B, function g will exhibit a favourable bowl-like shape around a minimal point where the gradient becomes zero, $\nabla g(\mathbf{c}) = \mathbf{0}$. (See fig. 4.9.) This gradient computes as

$$\nabla g(\mathbf{c}) = B\mathbf{c} - \mathbf{k}, \tag{4.27}$$

leading to the essential idea behind the *relaxation technique*: A vector $\mathbf{c}$ solving the linear system $B\mathbf{c} = \mathbf{k}$ ($\Rightarrow B\mathbf{c} - \mathbf{k} = \mathbf{0} = \nabla g(\mathbf{c})$) also minimises the quadratic form $g(\mathbf{c})$. The gradient is exactly the residual of the linear system, the normal equation in this case. Turning this relation around, instead of solving the normal equation $A^TA\mathbf{c} = B\mathbf{c} = \mathbf{k} = A^T\mathbf{m}$, one can also search for a minimum of the corresponding quadratic form $g(\mathbf{c})$ when computing a least-squares image reconstruction.

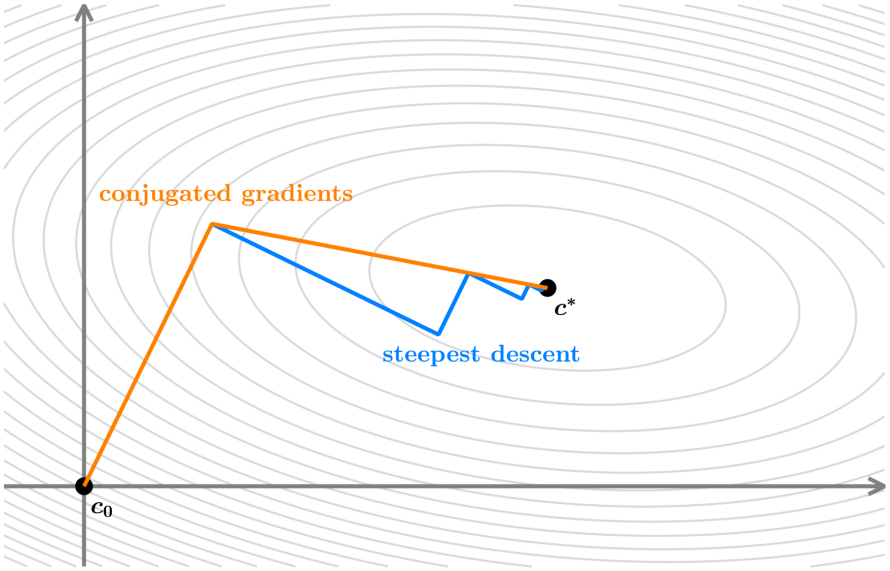

Figure 4.9.: A typical quadratic form corresponding to a normal equation (symmetric, positive-definite) will have a (possibly elongated) bowl-like shape. Searching for the minimum $\mathbf{c}^*$ using steepest descent from an initial position $\mathbf{c}_0$ may lead to zig-zagging (blue trajectory). The method of conjugated gradients uses an optimal scheme to reach the minimum quickly (orange trajectory) with a minimal number of iterations.

This minimisation problem is non-linear, and a possible approach to solving it would be *steepest descent (gradient descent)*: The gradient is known to point towards the direction of steepest ascent, and 'walking back' along the negative gradients will lead towards the minimum. More specifically, the iterative process evaluates the gradient $\nabla g(\mathbf{c})$ at the current location $\mathbf{c}$, follows its negative direction towards a relative minimum, and computes a new gradient there. This process continues until the minimum has been reached. Unfortunately, this method leads to 'zig-zagging', the method takes many more steps than necessary. In particular, the trajectory may search along the same direction several times. (See fig. 4.9.) Note that the Landweber method (SIRT) is exactly gradient descent on the least-squares problem, just usually without maximal step lengths.

The idea of CG is to restrict oneself to a minimal set of search directions, and to take the optimal step size such that a second search along the same direction is superfluous. In order to achieve this without knowing the solution beforehand, the concept of B-orthogonality[5] (*conjugacy* with respect to matrix B) is employed. In short, CG starts at an arbitrary initial location, and evaluates the gradient to obtain a search direction. Then, a new estimate is computed by moving along this search line to the point as 'close' as possible to the solution with respect to B-orthogonality. Once there, a new search direction is computed that is required to be B-orthogonal to all previous search directions. Exploiting the interrelations,

5. Two vectors $\mathbf{x}$, $\mathbf{y}$ are orthogonal if $\mathbf{x}^T\mathbf{y} = 0$. They are B-orthogonal with respect to matrix B if $\mathbf{x}^T B\mathbf{y} = 0$.

this can be achieved by taking the gradient at the new location, and making it B-orthogonal to the previous search direction by a variant of the Gram-Schmidt method. The search directions are thus B-conjugated gradients, giving the name to the method. (See alg. 4.3 and fig. 4.9.)

An important feature of CG is the fact that there is an upper bound on the number of iterations: CG is guaranteed to find the optimal solution to the least-squares problem in as many steps as there are dimensions, grace to the mutually B-orthogonal search directions combined with optimal step lengths. This result is of a rather theoretical nature in case of the normal equation as given in eq. (4.19), as there are still I unknowns,[6] much more than feasible iterations. Convergence studies [Slu86; Slu90] show, however, that CG practically converges very quickly towards the solution in average cases.

It turns out that CG, like other methods, converges fastest if matrix B features clustered eigenvalues. In two dimensions, the surface produced by the corresponding quadratic form will resemble a round bowl in such a case where CG can simply head for the minimum, rather than a narrow valley. This leads to the idea of *preconditioning* [Bar94, chap. 3]: Assume a matrix $M \approx B$ which is easy to invert. Then, the linear system

$$M^{-1}B\mathbf{c} = M^{-1}\mathbf{k} \tag{4.28}$$

has the same solution as the original system, but it will be more suitable for inversion. The selection of an optimal preconditioner M^{-1} is generally a complicated endeavour for large systems such as the one arising in tomographic reconstruction. General preconditioners such as diagonal (scaling) matrices have limited impact, and better schemes require in-depth analysis of the actual case at hand. For example, special preconditioners have been proposed for PET [Mum94; Fes99] and SPECT [For89; Lal95].

Summing up, CG is an optimisation method showing rapid convergence behaviour, particularly when supported by preconditioning. As will be seen below, it can be extended to optimise non-linear functions, and can serve as basis for more advanced reconstruction problems. (This entire section is based on the excellent tutorial by Shewchuk [She94] which contains many additional details including a proper derivation; also see Sluis *et al.* [Slu90] for a comparison with SIRT.)

4.3. Algebraic Reconstruction via Likelihood Maximisation

The reconstruction methods presented so far essentially assume well-posed settings with relatively good measurements. Particularly the least-squares methods are robust to noisy input to a certain degree, but none of them model the statistical properties of the measurement process. As the trend goes towards minimising radiation exposure, and thus towards lower photon counts, this question becomes increasingly important. Particularly in nuclear imaging where

6. I was the number of basis functions, that is, the number of pixels in the reconstructed image, for instance.

$\mathbf{c} = \mathbf{c}_0$ {initialise estimate, $\mathbf{c}_0 = \mathbf{0}$ without prior knowledge}

{compute initial search direction via residual/gradient of the quadratic form}
$\widetilde{\mathbf{m}} = A\ \mathbf{c}$ {project initial estimate}
$\mathbf{r} = A^T(\mathbf{m} - \widetilde{\mathbf{m}})$ {compute residual of the normal equation}
$\mathbf{d} = M^{-1}\ \mathbf{r}$ {compute initial search direction with pre-conditioning}
$\delta_{\text{new}} = \mathbf{r}^T\mathbf{d}$ {compute energy norm}

for iteration q **do**
{perform optimal update along search direction $\mathbf{d}$}
$\mathbf{p} = A\ \mathbf{d}$
$\alpha = \delta_{\text{new}}/(\mathbf{p}^T\mathbf{p})$ {compute optimal step size}
$\mathbf{c} = \mathbf{c} + \alpha\ \mathbf{d}$ {apply update to estimate}

{compute next search direction via residual/gradient of the quadratic form}
if necessary **then**
$\widetilde{\mathbf{m}} = A\ \mathbf{c}$ {compute exact residual every now and then}
$\mathbf{r} = A^T(\mathbf{m} - \widetilde{\mathbf{m}})$
else
$\mathbf{r} = \mathbf{r} - \alpha\ A^T\mathbf{p}$ {estimate residual with reduced effort if possible}
end if
$\mathbf{s} = M^{-1}\ \mathbf{r}$ {apply pre-conditioning}
$\delta_{\text{old}} = \delta_{\text{new}}$
$\delta_{\text{new}} = \mathbf{r}^T\mathbf{s}$ {compute energy norm}

{make next search direction A^TA-orthogonal (conjugate) to previous direction}
$\beta = \delta_{\text{new}}/\delta_{\text{old}}$ {compute A^TA-orthogonal projection of $\mathbf{s}$ onto $\mathbf{d}$}
$\mathbf{d} = \mathbf{s} + \beta\ \mathbf{d}$ {remove A^TA-orthogonal component (Gram-Schmidt)}
end for

Algorithm 4.3: Conjugated Gradients on the Normal Equation (CGNE) with pre-conditioning. Use the identity $M^{-1} = \mathbf{I}$ to disable the latter. (Adapted from Shewchuk [She94, chap. B3].)

radiopharmaceuticals are injected, likelihood-based methods are the standard since decades, in order to support lower activity doses.

4.3.1. The Statistical Nature of Measuring

In X-ray transmission CT, the common assumption is that the measurement obtained at the sensor is exactly the expected value considering the setting, potentially subject to some noise. In emission tomography, however, the photon count read by a gamma camera needs to be understood as sampled from a probability distribution.

Again, the radioactivity distribution will be considered as signal f, discretised into coefficient vector $\mathbf{c}$ as defined above in eq. (4.13). Then, in the fashion known from eq. (4.16), the *expected* photon count $\overline{m}_j$ for observation j can be computed as follows for **emission** CT:

$$\overline{m}_j = \sum_i a_{ji} c_i = \mathbf{a}_j^T \mathbf{c} \tag{4.29}$$

This equation can be considered as *forward model*, and $a_{ji} = \mathcal{M}_j(b_i)$ again denotes a *system matrix* entry. This time, however, the model needs to be interpreted in a probabilistic way:

$$a_{ji} := \mathrm{P}[\text{ photon contributes to measurement } j \mid \text{decay event in domain of basis function } i\ ] \tag{4.30}$$

If the *expected* photon counts $\overline{m}_j$ could be measured in reality, the least-squares methods as presented in section 4.2 could be used directly. For the *physical* measurements m_j, however, it can be derived theoretically [Bar81; Bar97] that the values are *Poisson*-distributed with respect to the expectation:

$$m_j \sim Poi\{\overline{m}_j\} \tag{4.31}$$

This result has also been confirmed experimentally [Can78]. Consequently, the probability to measure a count of exactly m_j is:

$$\mathrm{P}[m_j|\mathbf{c}] = \mathrm{e}^{-\overline{m}_j} \frac{(\overline{m}_j)^{m_j}}{m_j!} \tag{4.32}$$

The probability for the entire measurement vector $\mathbf{m} = (m_j)$ is, therefore,

$$\mathrm{P}[\mathbf{m}|\mathbf{c}] = \prod_j \mathrm{P}[m_j|\mathbf{c}], \tag{4.33}$$

leading to the *reconstruction likelihood* $\mathrm{L}(\mathbf{c}|\mathbf{m}) = \mathrm{P}[\mathbf{m}|\mathbf{c}]$, and – dropping constant summands – the corresponding *reconstruction log-likelihood*

$$l(\mathbf{c}|\mathbf{m}) := \log(\mathrm{L}(\mathbf{c}|\mathbf{m})) = \log(\mathrm{P}[\mathbf{m}|\mathbf{c}]) = \sum_j m_j \log(\overline{m}_j) - \overline{m}_j. \tag{4.34}$$

The tomographic reconstruction problem, that is, the recovery of coefficients $\mathbf{c}$ optimally explaining known measurements $\mathbf{m}$ can then be stated as maximisation problem:

$$\arg\max_{\mathbf{c}} \{\mathrm{L}(\mathbf{c}|\mathbf{m})\} \quad \text{or} \quad \arg\max_{\mathbf{c}} \{l(\mathbf{c}|\mathbf{m})\} \tag{4.35}$$

Note that the likelihood and the log-likelihood have the same maximum. Both these problems are non-linear, and require respective optimisation methods, as will be discussed below. Usually, the log-likelihood $l(\mathbf{c}|\mathbf{m})$ is preferred to work with as its derivatives are easier to compute. (See section 4.3.4.)

Before focusing on optimisation, note that similar equations can be derived for X-ray transmission CT as well. The number of photons detected in such a setup also follows a Poisson distribution, and this number is proportional to the intensity I_S as given by the Beer-Lambert law in eqs. (2.1) and (3.1), respectively. Consequently, the expected photon count for **transmission** CT is essentially a discrete variant of these equations:

$$\overline{m}_j = m_0 \cdot \exp\left(-\sum_i a_{ji} c_i\right) \tag{4.36}$$

Here, m_0 denotes the number of X-ray photons generated by the tube, a value proportional to the initial intensity I_0. From this point on, techniques derived for emission CT can also be used for transmission CT settings if the different definition of the measurement expectation is taken into account. In this work, likelihood-based methods will be considered for *emission settings only*, and the respective transmission variants will be omitted from further discussion.

(This section is based on the derivation presented by Shepp *et al.* [She82], and on Buzug [Buz08, chap. 6.5]; also see Fessler [Fes00] for an extensive discussion.)

4.3.2. Maximum-Likelihood Expectation-Maximisation (ML-EM)

Probably the most-used optimisation algorithm for solving the likelihood maximisation problem as defined in eq. (4.35) is *Maximum-Likelihood Expectation-Maximisation (ML-EM)*. It was first published by Shepp and Vardi [She82] in 1982 and uses the *expectation maximisation* method [Dem77; Wu83] to recover the unknown coefficients $\mathbf{c}$. This leads to the following multiplicative update equation:

$$c_i^{(q)} = c_i^{(q-1)} \frac{1}{\sum_j a_{ji}} \sum_j a_{ji} \frac{m_j}{\mathbf{a}_j^T \mathbf{c}^{(q-1)}} \tag{4.37}$$

The variable q once again denotes the iteration index. (See alg. 4.4.)

With improving detector technology, it has become possible to distinguish individual photons. In such a setup, images need to be reconstructed based on lists of detection events instead of accumulated counts. A variant of ML-EM has been suggested for such *list-mode* data [Bar97; Par98; Byr01], leading to a similar update equation, but a different algorithm.

4.3.3. Separable Paraboloid Surrogates (SPS)

An alternative class of methods employs the *optimisation transfer principle* [De 93; De 95; Lan95] and uses *paraboloid surrogates* to maximise the likelihood: Rather than maximising

$\mathbf{c} = \mathbf{c}_0$	{initialise estimate, $\mathbf{c}_0 = \mathbf{1}$ without prior knowledge}
$\mathbf{t} = A^T\mathbf{1}$	{compute column-sums of A by back-projecting ones}
for iteration q **do**	
$\widehat{\mathbf{m}} = A\ \mathbf{c}$	{project current estimate to obtain pseudo-measurement}
$\widetilde{\mathbf{m}} = \mathbf{m} \oslash \widehat{\mathbf{m}}$	{compute ratios by component-wise division}
$\widehat{\mathbf{c}} = A^T\ \widetilde{\mathbf{m}}$	{back-project ratios to obtain update}
$\widetilde{\mathbf{c}} = \widehat{\mathbf{c}} \oslash \mathbf{t}$	{normalise update by component-wise division by column-sums}
$\mathbf{c} = \mathbf{c} \odot \widetilde{\mathbf{c}}$	{apply update to estimate by component-wise multiplication}
end for	

Algorithm 4.4: Maximum-Likelihood Expectation-Maximisation (ML-EM)

the likelihood function itself, the idea is to locally fit a simple paraboloid at the location of the current estimate. That paraboloid serves as surrogate target function to maximise, and due to its simple shape, its maximum is known. Consequently, the estimate is moved to this maximum, where a new surrogate paraboloid is fit. Again, this project continues until convergence. (See fig. 4.10, and Fessler [Fes00] for more details.)

Among the methods using surrogates, a more common one is the *Separable Paraboloid Surrogates (SPS)* [Erd99b; Erd99a] approach. In this case, the paraboloid curvature is pre-computed, and a relaxation scheme is usually used. The method has been adapted for emission tomography by Ahn *et al.* [Ahn03], and it relies on the measurement-wise log-likelihood and its derivatives:

$$h_j(\widehat{m}) = m_j \log(\widehat{m}) - \widehat{m} \tag{4.38}$$

$$\dot{h}_j(\widehat{m}) = \frac{m_j}{\widehat{m}} - 1 \tag{4.39}$$

$$\ddot{h}_j(\widehat{m}) = -\frac{m_j}{\widehat{m}^2} \tag{4.40}$$

In these equations, $\widehat{m}$ denotes an estimate for the *expected* jth measurement, and m_j the *actual* measurement, as usual. Based on these equations, SPS pre-computes the paraboloid curvature as $-\ddot{h}_j(m_j)$, and during iteration, the gradient $\dot{h}_j(\widehat{m})$ is evaluated to obtain the next iterate. (See alg. 4.5.) Furthermore, it is possible to compute an upper bound for the solution, enabling range checks and clipping during iteration [Ahn03].

4.3.4. Likelihood Maximisation as Non-Linear Problem

Apart from specialised approaches, usual gradient-based non-linear optimisation methods can also be used to maximise the likelihood or log-likelihood as defined in eq. (4.35). Note that both equations are differentiable, but the log-likelihood is easier to handle. Using eq. (4.39),

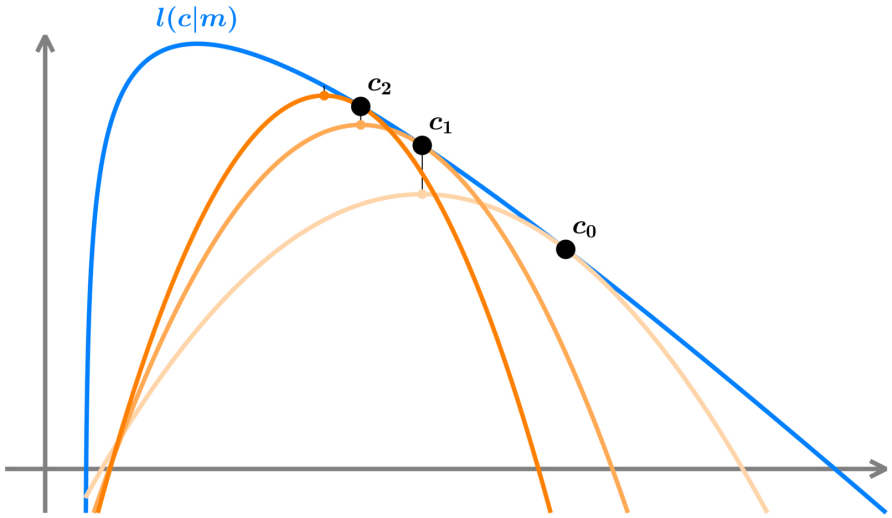

Figure 4.10.: Optimisation transfer: Rather than maximising the original target function (blue, likelihood for a single measurement) directly, one can locally fit a surrogate curve (orange parabola) at the current estimate $\mathbf{c}_q$ and 'jump' to the surrogate's known maximum $\mathbf{c}_{q+1}$. This procedure can be repeated until convergence, leading to an iterative optimisation scheme. Note the warning of Fessler [Fes00] that such a sketch 'does not do full justice to the problem, since 1D functions are usually fairly easy to maximise,' unlike the multi-dimensional likelihood maximisation problem.

$\mathbf{c} = \mathbf{c}_0$	{initialise estimate, $\mathbf{c}_0 = \mathbf{0}$ without prior knowledge}
$\mathbf{s} = A\ \mathbf{1}$	{compute row-sums of A by projecting ones}
$\mathbf{g}^{\mathrm{PC}} = \mathbf{1} \oslash \mathbf{m}$	{pre-compute curvature as $-\ddot{h}_j(m_j)$ by component-wise inversion}
$\mathbf{d}^{\mathrm{PC}} = A^T(\mathbf{s} \odot \mathbf{g}^{\mathrm{PC}})$	{back-projection of component-wise products}
for iteration q **do**	
$\widehat{\mathbf{m}} = A\ \mathbf{c}$	{project current iterate to obtain mean-measurement estimate}
$\dot{\mathbf{h}} = (\mathbf{m} \oslash \widehat{\mathbf{m}}) - 1$	{compute gradient of log-likelihood $\nabla l(\mathbf{c}\|\mathbf{m}) = (\dot{h}_j(\widehat{m}_j))$}
$\widetilde{\mathbf{c}} = (A^T\ \dot{\mathbf{h}}) \oslash \mathbf{d}^{\mathrm{PC}}$	{compute optimum of surrogate}
$\mathbf{c} = \mathbf{c} + \lambda(q) \cdot \widetilde{\mathbf{c}}$	{apply relaxed update to estimate}
end for	

Algorithm 4.5: Separable Paraboloid Surrogates (SPS)

the components of the latter's gradient compute as follows [Kau93]:

$$\frac{\partial}{\partial c_i} l(\mathbf{c}|\mathbf{m}) = \sum_j \dot{h}_j(\mathbf{a}_j^T \mathbf{c})\ a_{ji} = -1 + \sum_j \frac{m_j}{\mathbf{a}_j^T \mathbf{c}}\ a_{ji} \tag{4.41}$$

While likelihood-based reconstruction is stated as maximisation problem, optimisation algorithms and regularisation schemes (to be discussed in section 4.6) are often designed for minimisation problems. For this reason, the problem is usually recast as minimisation problem, and becomes:

$$\arg\min_{\mathbf{c}} \{-l(\mathbf{c}|\mathbf{m})\} \tag{4.42}$$

For brevity, define the auxiliary energy function $T(\mathbf{c}) = -l(\mathbf{c}|\mathbf{m})$, $\nabla T(\mathbf{c}) = -\nabla l(\mathbf{c}|\mathbf{m})$.

In order to minimise T, a simple option would be gradient descent again. (See section 4.2.5.) In short, starting at an initial estimate, one would evaluate the negative gradient to obtain a search direction of maximal down-hill slope, and perform a line search along this direction to find the minimal value of T. There, a new negative gradient would be evaluated, and the process continues until a minimum has been reached. While leading to results, this method would again exhibit slow convergence behaviour.

Luckily, better minimisation schemes have been devised. In particular, the method of conjugated gradients (see section 4.2.5) has been adapted to this more general setting by Fletcher *et al.* [Fle64]. In contrast to the linear case, however, there are several limitations: First, like other gradient-based approaches, only local optima will usually be found. Second, no assumptions concerning the shape of the function can be made any longer, and the optimal step length needs to be searched iteratively. Finally, the method may get stuck, requiring the process to be reset, thus forgetting about the previous conjugate search directions. Consequently, convergence will be slower. (See Shewchuk [She94, chap. 14] for a concise description including algorithms.) In case of the likelihood-based reconstruction problem for emission CT, special preconditioning and estimation schemes have been proposed [Kau87; Kau93].

Of course, further optimisation schemes exist and could be used to compute the minimum.

4.4. Initialisation, Termination and Constraint Enforcement

Iterative methods share the common framework of evolving an initial estimate over a series of discrete steps, pushing the estimate towards a solution along the way. Several questions arise in this context.

Choice of the Initial Estimate The very first problem is to find an initial estimate. If enough measurements are available, most methods are robust enough to support initialisation with a default value. For additive methods, the default is $\mathbf{0}$, and for multiplicative methods, it is $\mathbf{1}$. Of the methods presented above, only ML-EM belongs into the second category.

Convergence can be improved if a good initial guess is available through *prior knowledge*. A typical choice is to quickly compute a filtered back-projection (FBP, see section 4.1.3), and to use it as initial estimate. Note, however, that FBP can only validly be used for transmission CT settings.

Termination of Iteration The second problem is the termination of the loop. In normal optimisation setting, one would typically monitor the progress of the evolution and stop if there is no further progress. A common measure is the norm of the update: For additive methods, it must be sufficiently different from the null-vector $\mathbf{0}$, and for multiplicative methods from the one-vector $\mathbf{1}$. Similarly, the value of the cost function to minimise could be tracked. The proper choice of a termination condition is usually not simple, and it depends very much on the actual optimisation setting.

For tomographic reconstruction problems, a single iteration of the loop is usually rather costly, due to the large amount of work. For this reason, it can rarely be afforded to iterate until such a termination condition holds. Instead, one typically chooses a fixed number of iterations, and the evolution is strictly terminated afterwards. It has been shown that early termination by iteration number can be considered as regularisation [Def88; Eng00, chap. 6], depending on the optimisation scheme in use. Quite often, lower frequencies are reconstructed first, and consequently, pictures with less iterations are likely smoother and contain less noise. However, note that care must be taken to select the appropriate number of iterations, particularly as the different parts of an image may evolve at different speeds. (See Dutta *et al.* [Dut13] for a discussion in the context of likelihood maximisation.)

Constraint Enforcement Finally, the iteration algorithms obviously do only consider the mathematical setting. It may make sense to interfere with the optimisation process, in order to enforce additional constraints. Note, however, that this may also break convergence.

For instance, both, radiation attenuation in transmission and radioactivity distribution in emission tomography are non-negative entities according to the physical model. Still, during optimisation, negative values may appear. In order to keep the reconstruction realistic, positivity can be enforced by clamping at the end of every iteration. Similarly, it may be possible to compute an upper bound, and it could be enforced similarly. (For SPS, see Ahn *et al.* [Ahn03].)

A similar example is image smoothness, a property particularly desirable in nuclear imaging. A simple approach to favour smoother images is to blur the current estimate in every iteration after the update has been applied.

4.5. Ordered and Unordered Subsets

Particularly for modern diagnostic scanners, forward and backward projection operations will consume considerable time due to the large amount of data involved. With the exception of row-action methods such as ART, these operations define the lower temporal bound for a single iteration of the update loop. In particular, all measurements together are used to compute a single update.

In order to improve convergence speed, the use of subsets has been proposed, leading to so-called *block-action* methods [Egg81; Hud94]. These subsets are created by partitioning the input measurements into K distinct groups. Every iteration of the original method is then extended to process these subsets one after the other, updating the estimate in-between. (See alg. 4.6.)

```
c = c_0                                          {initialise estimate}
S_k = ...                {partition measurement indices {1, ..., J} into K subsets}
for iteration q do
  for subset k do
    c = update(A_{S_k}, c, m_{S_k})        {apply update to estimate based on subset S_k}
  end for
end for
```

Algorithm 4.6: General iterative reconstruction using subsets. The method update$(A, \mathbf{c}, \mathbf{m})$ is an auxiliary function abstractly containing the method-specific update rules. A_{S_k} and $\mathbf{m}_{S_k}$ are row-wise sub-blocks of the original linear system relating to the measurements contained in subset S_k.

An important point in this context is the construction of the subsets. A simple choice would be a randomised selection, leading to so-called *unordered subsets*. Another way to construct the subsets is by sub-dividing the problem into regular blocks, thus splitting up the large reconstruction problem into K similar problems of effectively the same geometry but less measured samples. In most gantry-based systems with well-sorted input data, this can be done by assigning every Kth measurement to the same subset. ($S_1 = \{1, K+1, 2K+1, ...\}$, $S_2 = \{2, K+2, 2K+2, ...\}$, ...) The second approach is commonly referred to as *ordered subsets (OS)* method, and it can be shown to be more promising than randomised subsets [Hud94].

4.6. Regularisation with Differentiable Penalties

At the very beginning of this chapter, the reconstruction problem has been described as ill-posed. The practical consequence is that the recovered images may show noise and artefacts when just minimising the least-squares problem (eq. (4.18)) or maximising the likelihood problem (eq. (4.35)). Despite following different approaches, these two problems effectively

only consist of a *data fidelity* term, and a solution is supposed to optimally explain the physical observations following the respective model.

Images can be improved by imposing additional constraints onto the image. For instance, the solution can be required to optimally fit the input data *subject to* a smooth shape. Mathematically, this can be done by means of *Lagrange multipliers* [Lag97]. Consider a data fidelity term $T(\mathbf{c})$ which is minimised (least-squares fit, negative log-likelihood), and a *penalty function* or *regulariser* $V(\mathbf{c})$. The latter is minimised if the additional constraint is met. Then, the regularised reconstruction problem is:

$$\arg\min_{\mathbf{c}} \{T(\mathbf{c}) + \beta V(\mathbf{c})\} \tag{4.43}$$

Here, β denotes the (chosen) *weight* of the penalty term V, and thus its impact in comparison to the data fidelity term T. V is usually a non-linear function, and for now, it is expected to be continuously differentiable, i.e. $\nabla V(\mathbf{c})$ needs to exist, and it must be continuous.

4.6.1. Tikhonov Regularisation

Within these requirements, penalty functions can be defined freely. A frequent choice is Tikhonov regularisation [Tik63; Phi62], named in honour of Andrey Nikolayevich Tikhonov. The sense of this penalty is to restrict the Euclidean norm of the solution vector, or of a vector derived from it. With L denoting the *Tikhonov matrix*, the penalty is given as follows:

$$V_{\text{Tikhonov}}(\mathbf{c}) = \|L\mathbf{c}\|_2^2 \tag{4.44}$$

L can be used in an application-specific sense, and an operator mapping the coefficients into the Fourier domain can be employed to level the frequencies in the image. More often, however, simple scaling matrices are inserted here. (For more details, also on the background and the relation to other schemes, see Hansen [Han98, chap. 5.1].)

4.6.2. Total Variation Regularisation (TV) and Gibbs Penalties

In the context of imaging and noise suppression, a particularly well-known further regularisation method is the *Total Variation (TV)* penalty [Jor81; Rud92] which limits the variation of the original signal f as given by the norm of its gradient, $\|\nabla f\|_2$. Prior to discretisation, TV is simply defined as:

$$\min_f \int \|\nabla f\|_2 \, \mathrm{d}\mathbf{x} \tag{4.45}$$

Note that in an image, two fundamentally different kinds of intensity or colour variation can be expected: Desired changes are caused by the contrast between different visible objects and their textures, and are required in order to tell things apart. Undesired changes on the other hand are caused by noise, and they happen within image regions that are supposed to be uniform. By tendency, desired changes are supposedly larger in magnitude than undesired

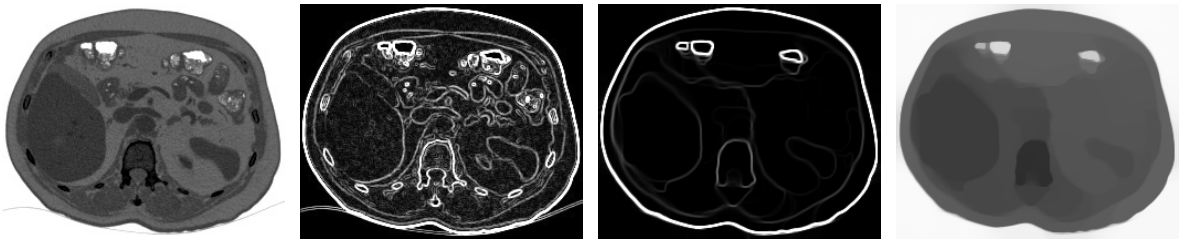

Figure 4.11.: The gradient magnitude picture (center, left) is a measure for the amount of variation encountered in the original image (left). Sparsifying it (center, right) leads to the suppression of small variations, yielding a total-variation-regularised version of the original image (right). In this example, this has deliberatly been done in a very excessive way, leading to typical 'staircasing' artefacts caused by piece-wise constant regions.

changes. A variation-based penalisation scheme needs to consider this difference in order to yield an image with low noise level but sharp features.[7]

To see that TV is exactly doing this, consider its equation after discretisation:

$$V_{\mathrm{TV}}(\mathbf{c}) = \|D\mathbf{c}\|_1 = \sum_i |(D\mathbf{c})_i| \tag{4.46}$$

Here, D denotes an operator mapping the coefficients to gradient norms, for instance by approximation via numerical differentiation. In case of a basis other than pixels or voxels, a basis transform will also be necessary. $D\mathbf{c}$ is effectively a discrete picture showing the variation of the original discretised signal, that is, changes in intensity per location stacked into a vector.

Minimising the ℓ_1-norm of a vector is known to promote its sparsity [Don03; Don06]. A vector is said to be sparse if it has few non-zero entries, but the latter can be of large magnitude.[8] Applying this concept to the discrete 'variation picture' $D\mathbf{c}$, increased sparsity causes many small changes to vanish, but will keep the large ones, thus exactly steering towards a separation between the 'good' and the 'bad' variations. (See fig. 4.11.)

Unfortunately, as sum of absolute magnitudes, the ℓ_1-norm is not continuously differentiable as there are singularities whenever a component reaches the optimal value of 0. Consequently, the usual gradient-based schemes can not be used directly. (See section 4.3.4 for some notes on non-linear optimisation.) For this reason, many specialised optimisation schemes tailored to TV-minimisation have been proposed [Rud92; Blo98; Pan99; Jør11]. (Also see section 4.7 for ℓ_1-optimisation schemes.)

Alternatively, TV can be modified to use a continuously differentiable surrogate of the absolute magnitude $|\cdot|$ which is smooth in the vicinity of 0. This idea leads to *Gibbs* pen-

7. It is disputed, though, whether this model yields good images [Cha97a; Gou01]. Particularly when the wanted and unwanted variations are of similar magnitude, total variation will likely break down.

8. In other words, the ℓ_1-norm penalises smaller components of the vector over-proportionally. Vice versa, the ℓ_2-norm penalises larger components over-proportionally.

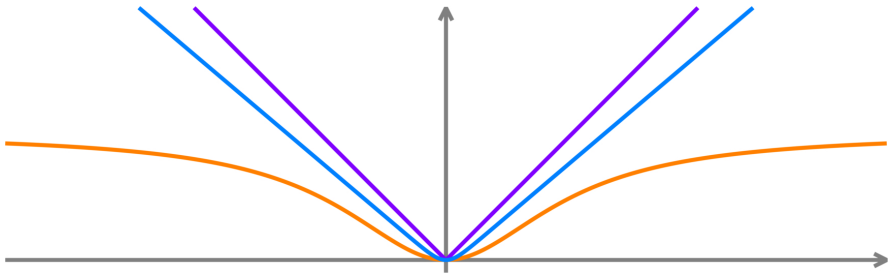

Figure 4.12.: Continuously differentiable surrogates for the absolute magnitude (purple). Shown are the functions proposed by Geman *et al.* [Gem85] (orange) and Green [Gre90a] (blue). Many more alternatives exist.

alties [Gem85; Gre90a]. In case of a two-dimensional pixel basis, it is originally defined as follows:

$$V_{\text{Gibbs}}(\mathbf{c}) = \sum_{r,s} w_{r,s} W(c_r, c_s) \tag{4.47}$$

Here, r and s denote pixel indices,

$$w_{r,s} := \begin{cases} 1 & \text{direct neighbours} \\ \sqrt{1/2} & \text{diagonal neighbours} \\ 0 & \text{else} \end{cases} \tag{4.48}$$

a weighting factor describing whether the pixels are neighbours, and

$$W(x_s, x_r) = \Phi\left(\frac{x_s - x_r}{\delta}\right) = \Phi\left(\frac{|x_s - x_r|}{\delta}\right) = \Phi\left(\frac{x_r - x_s}{\delta}\right) = W(x_r, x_s) \tag{4.49}$$

a symmetric function penalising intensity differences with δ denoting another weighting parameter. The difference can be considered as numerical approximation to the derivative, and the potential $\Phi(\cdot)$ is exactly the continuously differentiable surrogate of $|\cdot|$, and different options have been proposed [Gre90a; Lan90]. (See fig. 4.12.) Equation (4.47) is continuously differentiable if Φ is, and the Gibbs penalty can then be optimised using gradient-based methods, ideally leading to a TV-like image with reduced noise but sharp boundaries.

4.6.3. Regularisation for Least-Squares Approaches

Having described two particularly common continuously differentiable penalty functions, the remaining problem is now to optimise the joint minimisation problem as stated in eq. (4.43). Again, the latter contains both, a data fidelity and a regularisation term.

In case of the least-squares approach, the data term is given by eq. (4.18), and one obtains:

$$T(\mathbf{c}) = \frac{1}{2}\|A\mathbf{c} - \mathbf{m}\|^2 \tag{4.50}$$

$$\arg\min_{\mathbf{c}} \left\{ \frac{1}{2}\|A\mathbf{c} - \mathbf{m}\|^2 + \beta V(\mathbf{c}) \right\} \tag{4.51}$$

When using Tikhonov regularisation, the problem continues to be linear, and the normal equation can be extended appropriately [Han98, chap. 5.1]:

$$(A^T A + \beta L^T L)\, \mathbf{c} = A^T \mathbf{m} \tag{4.52}$$

In general, though, the regularisation term is non-linear, thus rendering the entire penalised reconstruction problem non-linear. In such cases, non-linear optimisation methods such as non-linear CG need to be used. (Again, see section 4.3.4 for some notes on non-linear optimisation.) Note once more that the derivative of the data term is related to the normal equation (4.19)

$$\nabla T(\mathbf{c}) = A^T A\mathbf{c} - A^T \mathbf{m} = A^T(A\mathbf{c} - \mathbf{m}), \tag{4.53}$$

and a simple gradient descent leads to a SIRT/Landweber-style scheme with slow convergence.

4.6.4. Regularisation for Likelihood Maximisation Approaches

For penalised likelihood-based approaches, the problem is obviously always non-linear. Using eq. (4.42), one obtains:

$$T(\mathbf{c}) = -l(\mathbf{c}|\mathbf{m}) \tag{4.54}$$

$$\arg\min_{\mathbf{c}} \{-l(\mathbf{c}|\mathbf{m}) + \beta V(\mathbf{c})\} \tag{4.55}$$

This minimisation problem can be solved using the generic approach already discussed in section 4.3.4 [Kau93]. However, the same equation can also be derived in a Bayesian sense [Lev87]:

$$\mathrm{P}[\mathbf{c}|\mathbf{m}] = \frac{\mathrm{P}[\mathbf{m}|\mathbf{c}] \cdot \mathrm{P}[\mathbf{c}]}{\mathrm{P}[\mathbf{m}]} \tag{4.56}$$

Here, $\mathrm{P}[\mathbf{c}|\mathbf{m}]$ denotes the *posterior* probability to have regularised coefficients $\mathbf{c}$ given the measurements $\mathbf{m}$. An optimal reconstruction needs to maximise this magnitude. $\mathrm{P}[\mathbf{m}|\mathbf{c}]$ is the probabilistic forward model, and exactly the *likelihood* derived above in eq. (4.33). $\mathrm{P}[\mathbf{m}]$ denotes the *prior* probability of the measurement vector. This entity is independent of the unknown coefficients $\mathbf{c}$, and it can be ignored in this context. The other prior, $\mathrm{P}[\mathbf{c}]$, relates to the signal, and it is used to favour signals minimising the penalty V. Following Green [Gre90a], this can be modelled by the following proportion:

$$\mathrm{P}[\mathbf{c}] \propto \exp\left(-\beta V(\mathbf{c})\right) \tag{4.57}$$

Then, dropping $\mathrm{P}[\mathbf{m}]$, eqs. (4.56) and (4.57) can be combined to obtain:

$$\mathrm{P}[\mathbf{c}|\mathbf{m}] = \mathrm{P}[\mathbf{m}|\mathbf{c}] \cdot \mathrm{P}[\mathbf{c}] = L(\mathbf{c}|\mathbf{m}) \cdot \exp\left(-\beta V(\mathbf{c})\right) \tag{4.58}$$

Again, this equation must be maximised to obtain the optimal *a posteriori* estimate respecting the penalisation. Applying the logarithm and turning the problem into a minimisation problem leads to eq. (4.55), as expected.

The maximum *a posteriori* approach may seem somewhat artificial to justify eq. (4.55), but it forms the relevant foundation for making maximum-likelihood algorithms support regularisation. In case of ML-EM (see section 4.3.2), the penalised version is commonly referred to as *One Step Late (OSL)* [Gre90b; Gre90a], and the update equation (4.37) becomes:

$$c_i^{(q)} = c_i^{(q-1)} \frac{1}{\sum_j a_{ji} + \beta \frac{\partial}{\partial c_i} V(\mathbf{c}^{(q-1)})} \sum_j a_{ji} \frac{m_j}{\mathbf{a}_j^T \mathbf{c}^{(q-1)}} \tag{4.59}$$

Consequently, the update in alg. 4.4 is modified accordingly:

$$\widetilde{\mathbf{c}} = \widehat{\mathbf{c}} \oslash (\mathbf{t} + \beta \nabla V(\mathbf{c})) \tag{4.60}$$

Similarly, the method of *Separable Paraboloid Surrogates (SPS)* can be extended to support regularisation [Erd99b; Ahn03]. To do this, the surrogate optimum $\widetilde{\mathbf{c}}$ in alg. 4.5 needs to be changed to consider the gradient of the penalty. For a *single* coefficient c_i, the penalised update becomes:

$$\widetilde{c}_i = \frac{(A^T \dot{\mathbf{h}})_i - \beta \nabla V(\mathbf{c})_i}{d_i^{\mathrm{PC}} + 2\beta \frac{\nabla V(\mathbf{c})_i}{c_i}} \tag{4.61}$$

4.7. Compressive Sensing and Sparse Regularisation

In recent years, following the massive interest caused by the success of *compressive sensing* [Can06], the problem of proper ℓ_1-minimisation and the use of sparsity for optimisation purposes has been extensively re-visited. In the context of tomographic image reconstruction, this concept is primarily relevant in the field of ℓ_1-based *sparse regularisation*. In general, assume a *sparsifying operator* $\mathcal{T}$, and postulate that the solution vector needs to be sparse after application of $\mathcal{T}$. This leads to the following general penalty:

$$V_{\mathrm{Sparse}}(\mathbf{c}) = \|\mathcal{T}\mathbf{c}\|_1 \tag{4.62}$$

A widely used example for such a ℓ_1-penalty has already been described above: Total variation (TV). In this case, $\mathcal{T}$ is the gradient operator, and the idea is to suppress small variations in the signal [Rud92]. (See section 4.6.2.) Whether or not TV leads to better images is disputed [Cha97a; Gou01], and this question depends largely on the properties of the signal one seeks to recover.

Another example for ℓ_1-penalties are *basis-like transforms* which aim to represent a signal sparsely with respect to a finite set of atomic elements. For instance, images are often represented using pixels or voxels as atomic elements. These elements are highly localised in Cartesian space, but not in frequency space. Consequently, a sparse representation would favour black regions in the image. The exact opposite is the Fourier basis [Fou22] where the signal is described by a coefficient vector containing frequency contributions. The basis functions are thus highly localised in frequency space, and it is known that 'sparsifying' the

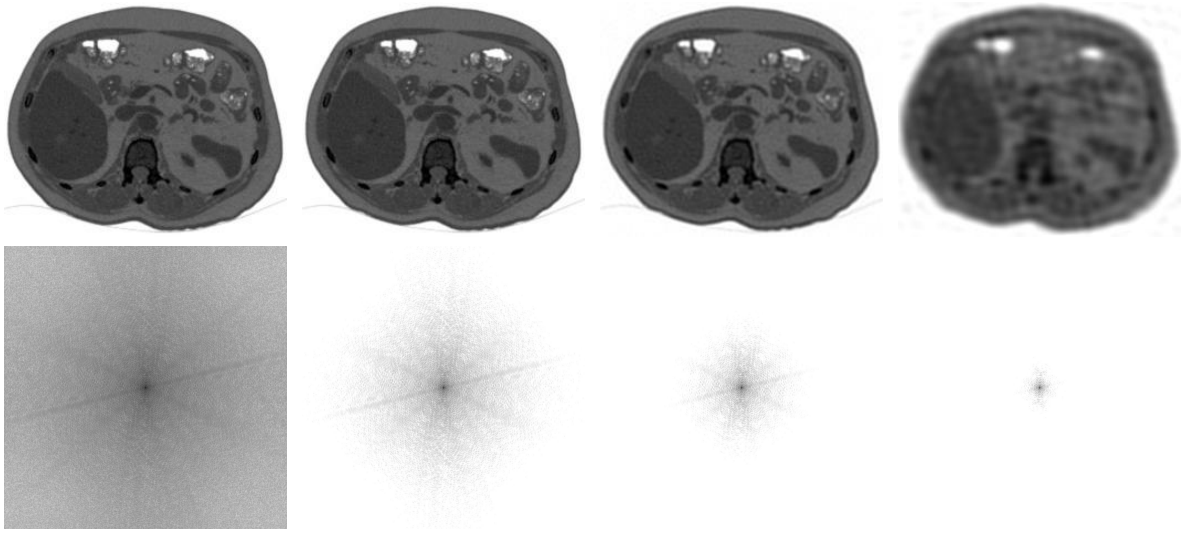

Figure 4.13.: Image reconstruction from sparse Fourier coefficients: Original grey-level picture (left column, top) with respective Fourier coefficient magnitudes (left column, bottom, logarithmic scale with darker colours denoting larger values). A large portion of the Fourier coefficients of smallest magnitude can be discarded by resetting them to 0 (bottom row) before the respective reconstructed images (top row, by inverse Fourier transform) show artefacts.

coefficient vector will first be practically invisible, and eventually lead to smoothing. (See fig. 4.13.)

For most pictures, neither the pixel nor the Fourier basis lead to optimal sparsity. For this reason, other sets of basis functions in-between the two extremes have been developed, leading to *wavelets* [Jaf01] that are somewhat reasonably localised in both, Cartesian and frequency space. The earliest example is the Haar-wavelet [Haa11] proposed in 1911. Effectively, it encodes the signal as superposition of piecewise-constant functions, and 'sparsifying' the respective coefficient vector leads to results similar to total variation minimisation [Ste04]. This entire idea of sparse coefficient vectors with respect to a suitable basis is applied in *lossy compression* schemes such as *JPEG* [Pen93].

Each of these examples constitutes a basis, that is, there is a minimal number of mutually orthogonal basis functions, and the respective coefficient vectors are well-defined. The concept can be extended by dropping the orthogonality constraint, leading to so-called *frames* where the atomic elements are redundant or over-complete. Frames can be more finely tuned towards applications, but they inherently require an additional sparsity constraint to handle the redundancy. More famous examples include ridgelets [Can98], curvelets [Can02; Fri13; Wie15a], and shearlets [Guo07].

In all these cases, operator $\mathcal{T}$ can be defined as *analysis operator*, transforming the pixel coefficients into the coefficients of the respective basis or frame. Its inverse, denoted $\mathcal{T}^*$, is

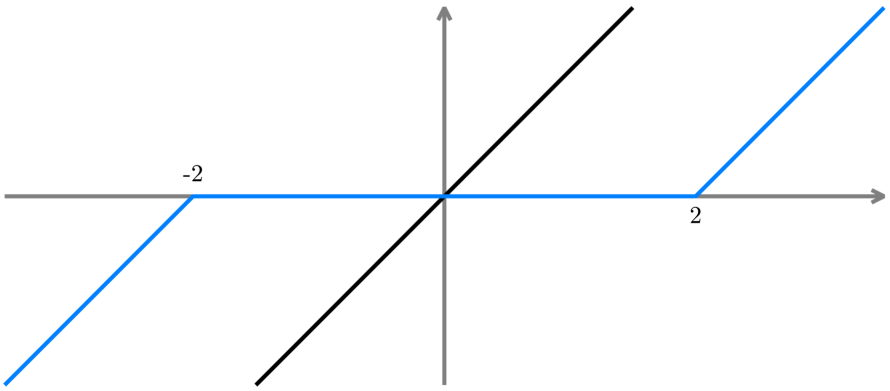

Figure 4.14.: The soft-thresholding operator (blue, S_2) maps values of small magnitude to zero, and increases values of large magnitude, consequently favouring sparse vectors. (Identity in black.)

the *synthesis operator* and yields a pixel representation given coefficients.

Returning to the problem of penalised least-squares-based tomographic reconstruction as defined in eq. (4.51), the objective is then to recover an image which can be encoded sparsely with respect to a certain basis or frame. Consequently, using the two operators, there are two ways to pose the problem, the *analysis approach*

$$\arg\min_{\mathbf{c}} \left\{ \frac{1}{2}\|A\mathbf{c} - \mathbf{m}\|_2^2 + \beta\|\mathcal{T}\mathbf{c}\|_1 \right\}, \tag{4.63}$$

and the *synthesis approach*

$$\mathcal{T}^* \arg\min_{\mathbf{x}} \left\{ \frac{1}{2}\|A\mathcal{T}^*\mathbf{x} - \mathbf{m}\|_2^2 + \beta\|\mathbf{x}\|_1 \right\}. \tag{4.64}$$

In effect, the former optimises with respect to pixels and transforms into coefficients to enforce sparsity, and the latter optimises with respect to coefficients, but transforms to pixels for projection. (For details and a comparison, see Chen *et al.* [Che01] and Elad *et al.* [Ela07].) In either case, a special solver is required which supports the ℓ_1-norm despite its discontinuity.

4.7.1. Iterative Soft-Thresholding Algorithm (ISTA)

Many contemporary optimisation methods rely on *soft-thresholding* [Don95] to minimise ℓ_1-problems. The operator is defined as follows:

$$S_\alpha(x) := \operatorname{sign}(x)\ (|x| - \alpha)_+ = \operatorname{sign}(x)\ \max\{|x| - \alpha, 0\} \tag{4.65}$$

Obviously, smaller values are set to zero, larger values are increased, and S_α is thus referred to as *proximity operator* to the ℓ_1-norm. (See fig. 4.14.)

A rather simple approach exploiting soft-thresholding is the *Iterative Soft-Thresholding Algorithm (ISTA)* [Dau04]. Effectively, it can be described as Landweber method (SIRT) with

additional constraint enforcement via the soft-thresholding operator $S_\alpha(\mathbf{c})$ in every iteration. (See section 4.2.3 for SIRT.) The immediate consequence is that only the unknown iterate itself can be regularised,[9] and penalties on derived values such as $\|\mathcal{T}\mathbf{c}\|_1$ can not be enforced. For this reason, only synthesis problems as given in eq. (4.64) can be solved using ISTA. In particular, it is not applicable to TV-penalised problems as there is no matching synthesis operator in this case.

Furthermore, as a Landweber-method, ISTA is not particularly fast to converge. An improved version is the *Fast Iterative Soft-Thresholding Algorithm (FISTA)* [Bec09d] which improves the speed by a certain relaxation strategy.

4.7.2. Alternating Direction Method of Multipliers (ADMM)

In order to solve problems as stated in eq. (4.63) where the ℓ_1-constraint relates to a derived value, $\|\mathcal{T}\mathbf{c}\|_1$, a more complex approach needs to be taken. A possible option is to apply *splitting*. The idea is to use two distinct variables during optimisation, one minimising the least-squares data fidelity term, and the other one the sparsity constraint. In order for these two split variables to evolve in conjunction, the two are coupled by means of a constraint:

$$\arg\min_{\mathbf{c},\mathbf{z}} \left\{ \frac{1}{2}\|A\mathbf{c}-\mathbf{m}\|_2^2 + \beta\|\mathbf{z}\|_1 \right\} \quad \text{s. t.} \quad \mathcal{T}\mathbf{c} = \mathbf{z} \tag{4.66}$$

The idea of primal-dual splitting is quite flexible, and it allows to interleave different optimisation concepts. Consequently, several such methods have been proposed [Cha11; Cha99], and particularly important are *Split-Bregman* [Gol09] and the *Alternating Direction Method of Multipliers (ADMM)* [Eck92; Boy11].

Focusing on the latter, consider the *augmented Lagrangian* corresponding to eq. (4.66):

$$\mathcal{L}_\rho(\mathbf{c},\mathbf{z},\mathbf{u}) = \frac{1}{2}\|A\mathbf{c}-\mathbf{m}\|_2^2 + \beta\|\mathbf{z}\|_1 + \mathbf{u}^T(\mathcal{T}\mathbf{c}-\mathbf{z}) + \frac{\rho}{2}\|\mathcal{T}\mathbf{c}-\mathbf{z}\|_2^2 \tag{4.67}$$

The chosen parameter ρ couples $\mathcal{T}\mathbf{c}$ and $\mathbf{z}$, and $\mathbf{u}$ denotes a Lagrange multiplier. In general, each iteration q of ADMM consists of three distinct steps evolving estimates of the three unknown vectors $\mathbf{c}$, $\mathbf{z}$, and $\mathbf{u}$:

$$\mathbf{c}^{(q+1)} = \arg\min_{\mathbf{c}} \mathcal{L}_\rho(\mathbf{c},\mathbf{z}^{(q)},\mathbf{u}^{(q)}) \tag{4.68}$$

$$\mathbf{z}^{(q+1)} = \arg\min_{\mathbf{z}} \mathcal{L}_\rho(\mathbf{c}^{(q+1)},\mathbf{z},\mathbf{u}^{(q)}) \tag{4.69}$$

$$\mathbf{u}^{(q+1)} = \mathbf{u}^{(q)} + \mathcal{T}\mathbf{c}^{(q+1)} - \mathbf{z}^{(q+1)} \tag{4.70}$$

Denoting the discretisation of sparsifying operator $\mathcal{T}$ as T, the three sub-problems of ADMM

9. The least-squares problem with ℓ_1-penalty on the solution vector is commonly referred to as *lasso (least absolute shrinkage and selection operator)* problem.

become in the case of eq. (4.67) [Wie15a]:

$$(A^T A + \rho T^T T)\ \mathbf{c}^{(q+1)} = (A^T y + \rho T^T(\mathbf{z}^{(q)} + \mathbf{u}^{(q)})) \tag{4.71}$$

$$\mathbf{z}^{(q+1)} = S_{\beta/\rho}\left(T\ \mathbf{c}^{(q+1)} + \mathbf{u}^{(q)}\right) \tag{4.72}$$

$$\mathbf{u}^{(q+1)} = \mathbf{u}^{(q)} + T\ \mathbf{c}^{(q+1)} - \mathbf{z}^{(q+1)} \tag{4.73}$$

The first sub-problem is a linear problem[10] that can be solved using the methods described above, particularly CG, and its solution constitutes the next estimate for the data fidelity coefficient vector $\mathbf{c}$. The second step minimises the ℓ_1-penalty on the dual variable $\mathbf{z}$, and the last step updates the Lagrange multiplier $\mathbf{u}$. (This section is based on an earlier, non-public draft of [Wie15a]; the published version contains an explicit derivation of the equations.)

In contrast to ISTA, ADMM does not impose requirements onto the optimisation algorithm used within. In its general form, ADMM is very generic, and it can be adapted to many problems and domains. In particular, the method has also been used to implement ℓ_1-penalised maximum-likelihood estimation [Lin10].

4.8. Summary

This section has introduced the most important solution concepts for the tomographic reconstruction problem. Particularly the iterative schemes allow to impose prior knowledge such as smoothness requirements onto the solution, and there are fundamentally two general approaches: Least-squares methods model the imaging setup using a system matrix, assume rather decent measurements and compute a least-squares solution to a noisy, non-square linear system. Likelihood methods on the other hand model data acquisition as stochastic process and compute a maximum-likelihood solution optimally explaining the measurements.

X-ray transmission CT systems usually provide rather nice data, and least-squares approaches can usually be used. In this case, CGNE is probably among the most promising methods. However, likelihood-based methods are frequently and successfully used as well, but they require a proper adaption due to the different expected observations. Emission CT systems on the other hand typically require proper probabilistic modelling, and ML-EM or a comparable method should be used. In both cases, imposing regularising penalties onto the solution may help to compute (at least visually) nicer results. Many more algorithms have been proposed. Still, they usually solve one of the two problems, and differ from the methods presented in this work in smaller or larger details.

The other large group of algorithms besides the iterative methods contains analytical approaches. Being non-iterative, they exhibit tremendous speed, and are still heavily used. Note in particular that they usually assume line integrals, and they can only validly be used for

10. The augmented Lagrangian is similar to Tikhonov regularisation, and the linear system obtained here is similar to the extended normal equation arising for Tikhonov-regularised problems.

transmission CT in this case. There exist special-closed form solutions for other imaging modalities as well. Furthermore, these methods usually do not model noise appropriately, potentially leading to image artefacts. Advanced filtering methods have been proposed to improve closed-form solutions, both in the sense of pre-filtering the input sinogram as well as post-filtering the reconstructed image.

4.9. Short History of the Inversion of Line Integrals

Before closing this chapter, an interesting point should be considered: The problem of reconstructing a function based on known integrals over manifolds – like the inverse Radon transform – appears in several scientific fields, and particularly closed-form solution methods have been independently re-invented multiple times.

The first person reported to have possessed knowledge of an inversion equation is physicist Hendrik A. Lorentz. The result was used in a paper on propagation of light in a crystal by Bockwinkel [Boc06], published in 1906, but Lorentz' own motivation for dealing with the problem is unknown. However, the inversion problem occurs in several sub-fields of optics, for instance interferometry. (See [Dea07, chap. 1.8] for details.) In 1925, physicist George E. Uhlenbeck [Uhl25] published an extension using Fourier coefficients.

Next came mathematician Johann Radon [Rad17; Rad86; Rad07], publishing his independent theoretical work in 1917. In 1934, John [Joh34] re-considered the problem in the context of differential equations. Aware of Radon's work, he established the link to the Fourier transform, thus paving the way towards Fourier-based inversion. Two years later, in 1936, Cramér and Wold [Cra36] dealt with Radon's theory in the context of probability distributions independently of John's work, and also discovered the relation to the Fourier transform. These results were extended by Rényi [Rén52] in 1952.

Also in 1936, and initially unaware of related work, astronomers began to work on inversion problems. At that time, Victor A. Ambartsumian dealt with the problem of reconstructing the speed distribution of the stars in the galaxy from earth-based observations [Amb36; Amb80]. He is usually credited for having computed the first numerical inversion. (See Cormack [Cor82] for details.) With the development of radio-astronomy after the Second World War, the inversion issue surfaced again. Among the earliest examples is the problem of reconstructing images from so-called strip-scans: A target region, the sun at the time, is observed using a long antenna with a trough-shaped reflector. This device measures the accumulated electro-magnetic emissions originating from a strip-shaped region, and thus a line integral over the solar disc. In order to reconstruct a picture, Bracewell proposed the Fourier slice theorem [Bra55; Bra56; Bra67], thus again independently discovering the connection between line integrals and the Fourier transform. (See section 4.1.2). With more complex installations such as antenna arrays, even more problems arised requiring mathematical inversion of integrals. (See [Dea07, chap. 1.5] for details.)

In medical imaging, as has been discussed in section 3.2, the idea of tomographic imaging dates to the first decades of the twentieth century, culminating in Frank's back-projection patent [Fra42]. From a mathematical point of view, the topic was probably first discussed by Jacek Szarski and Tadeusz Ważewski [Sza47] in 1947, however, without providing a solution. The first solution approaches to the computed tomography inversion problem were suggested independently by Cormack [Cor63; Cor64] and Oldendorf [Old61; Old63] in the early 1960s.

It took until the early 1970s to connect the individual threads to form a joint framework of reconstructing signals from known integrals, and particularly to make people aware of Radon's early work[11] [Vai72; Ves74; Cor73]. At the same time, the iterative least-squares methods have been proposed, and Gabor T. Herman [Her09] is among the pioneers. The likelihood-based iterative approach was developed a decade later, and Lawrence A. Shepp is one of the key figures in this respect.

Following the success of medical tomographic imaging and the general interest in the Radon transform triggered by it, many researchers have applied similar techniques in their own field of work. Examples include stress analysis [Wil73], seismography [Ric79] and general geophysics [Din79], among many others. (For many more details on the history and related fields, see Cormack [Cor82], Deans [Dea07] and Helgason [Hel99]; this section is based on these works.)

11. Recall that Hounsfield used an iterative scheme [Hou73b] at the very beginning, due to missing awareness of the analytical inversion schemes.

5. An Outlook over the Original Work Discussed in this Thesis

Having sketched the history and technology behind computed tomography systems, the remainder of this thesis will present a *selection*[1] of original work done by the author. The presented projects all have in common that they constitute tomographic reconstruction problems going beyond the 'classical' settings described until this point.

Part II: Accounting for Motion

In computed tomography systems, the basic assumption is that there are multiple perspectives acquired from a static scene. Knowing the geometry, the perspectives are used to compute a tomographic reconstruction. If the assumption is wrong and inconsistent projection images are used, motion artefacts may occur. For this reason, diagnostic scanners have been optimised to acquire data as quickly as possible. However, with the advent of interventional imaging devices capable of tomographic imaging, the motion problem has recurred. A possible way to deal with motion in software is discussed in part II.

Part III: Optimal Sensor Trajectories

Diagnostic scanning devices are also optimised to cover the volume of interest with as many useful perspectives as possible. In special settings, this set of views will need to be restricted, but even then in a pre-determined way. However, under certain circumstances, it becomes overwhelmingly important to adapt the imaging process to a specific patient. This is particularly true for interventional nuclear functional imaging where the radiation sensors are required to be as close as possible in order to have high statistical value. In this case, the trajectory of the sensor needs to be found in real-time, and part III presents energy measures and a trajectory control scheme for this purpose.

Part IV: X-ray Scattering Tensors

Clinical X-ray CT scanners are limited to measuring the absorption of X-rays. From a physical point of view, additional information – phase contrast and dark-field – could be acquired.

1. A list of further projects is given in appendix A.

These new image signals require new forward models and lead to novel images. Part IV discusses the reconstruction of tensor-valued scattering tensors from dark-field data.

Part II.

Accounting for Motion

6. Dynamic Reconstruction with Level-Sets

Heart-beat and breathing are involuntary motions taking place within the body of every human being, obviously also during the acquisition of X-ray measurements. Tomographic reconstruction methods, however, expect a static scene, and assume that all input images show the same setting from a series of well-known and well-distributed perspectives. If organ movement is not considered, artefacts and blur will become visible in the reconstructed images.

For diagnostic CT scanners, this problem was tackled by 'outracing' the inherent motion during data acquisition as far as possible. The respective clinical scanners are highly specialised data acquisition devices with a very stable gantry, allowing to rotate X-ray source and detector at high speed. Employing further engineering tricks such as the use of multiple sources, cone-beam geometries and helical trajectories, the measurements can be acquired at breath-taking speed. This is even more the case when using special scanners for heart imaging which follow the electron-beam design principle. (See section 3.2, p. 37.) In order to reconstruct a sufficiently nice image, projections from at least 180° are required, and the data could be acquired in 165 ms already in 2006 [Ach06b]. Due to the semicircular trajectory, the respective images are referred to as 'half-scan' reconstructions, and they are computed from contiguously acquired data. Note that heart imaging requires administration of a radio-opaque contrast agent, and the heart rate will be lowered via beta-blockers [Ach06a].

6.1. Interventional Tomographic Cardiac Imaging

Besides diagnostic purposes, X-rays are also used for interventional imaging. A prominent example is *angiography* [Abr96; Fer96; Wak11]. Particularly since the invention and widespread adoption of minimally invasive catheter-based operation techniques such as *stenting*, interventional cardiac imaging has become quite frequent.

The respective images are acquired by means of a so-called *C-arm scanner*. (See fig. 6.1.) The basic design principle is that X-ray source and flat-panel detector are attached to a C-shaped mount, thus allowing rotation around the iso-centre of the assembly. This setup was originally intended to allow easy and flexible re-positioning of the device in interventional settings, but it is now also used to acquire data for tomographic imaging. The latter is sometimes

The project was carried out in cooperation with Andreas Keil in 2008 and 2009 [Kei09a; Kei09b; Kei10b], and it has been discussed extensively in the doctoral thesis of Andreas Keil [Kei10a] and in the diploma thesis of the author [Vog09b]. The discussion here is deliberately short and focuses on the general principle only.

Figure 6.1.: The core component of a C-arm system is the C-shaped mount carrying an X-ray tube (bottom) and a digital flat-panel detector (top). Due to its shape, the assembly can be rotated around an iso-centre. *(Courtesy of José Gardiazabal.)*

treated as separate imaging modality and commonly referred to as *rotational angiography* or *computed tomography angiography (CTA)*. Its primary purpose is not intervention guidance due to the additional radiation exposure incurred by tomographic imaging, but the idea is the combination of diagnosis with intervention at a single location during a single session.

In contrast to a diagnostic scanner, however, the rotating part of a C-arm system is quite large and heavy, and it is not mounted within a stable gantry. For mechanical and security reasons, the devices can thus not rotate as quickly, and they are limited to a 180° degree sweep. Consequently the acquisition cannot be optimised beyond a certain degree, and a sweep will take about 4 to 5 s. During this time, the heart will go through 4 to 7 heart cycles. For this reason, the input projections will show the usual tomographic rotation, and an orthogonal dynamic, non-linear motion caused by the beating heart on top. Consequently, the question arises how the situation of inconsistent projections can be handled in tomographic reconstruction software.

6.2. Non-Applicability of Gating

A classical approach to deal with a supposedly periodic motion is *gating*. In case of heart imaging, *electrocardiography (ECG)* [Coo86; Bar03] can be used to monitor heart activity, and

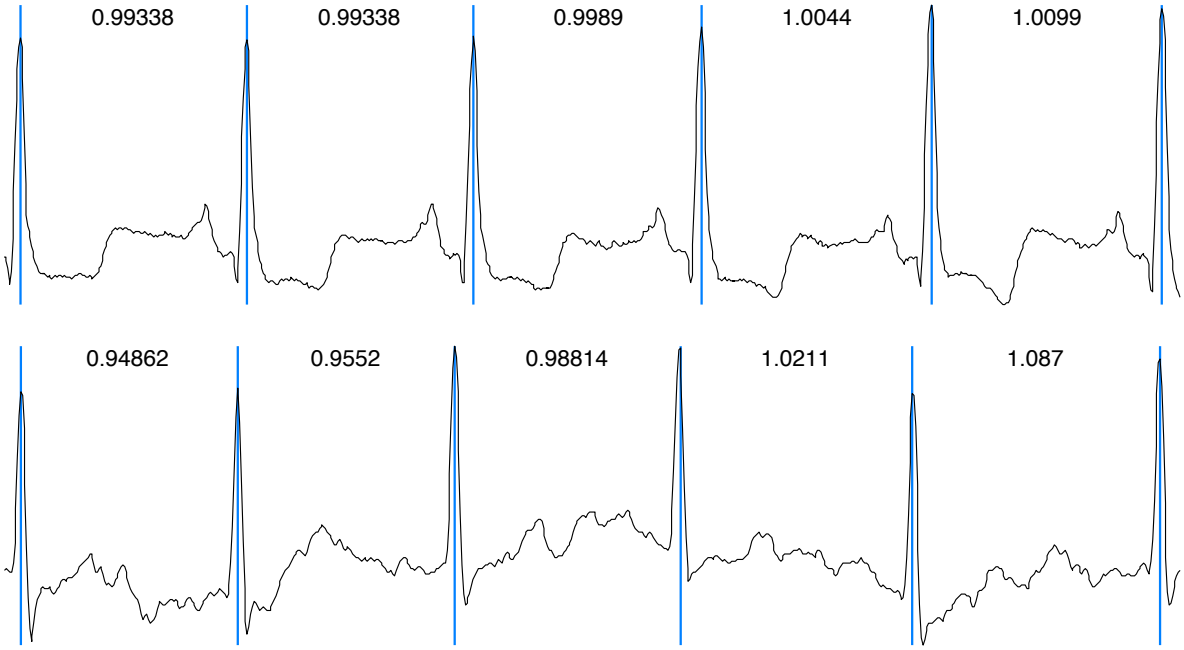

Figure 6.2.: Electrocardiograms of a healty subject (top) and a heart patient (bottom). The former signal shows distinct heart phases of recurring shape and duration. Unfortunately, the patient's ECG is very irregular, making the identification of phases other than the characteristic R-peaks very hard. *(Raw data by courtesy of Günter Lauritsch, Siemens.)*

the assumption is that the heart returns to the same position during every phase of the heart-beat. Following the idea further, projections acquired at the same heart phase are supposed to show a quasi-static setting, even when recorded during different heart cycles. Gating can be used to control data acquisition, and it can also be used to partition a previously recorded dataset retrospectively. Even when no ECG signal is originally available, methods have been proposed to estimate a synthetic ECG signal from the projection images. Consequently, several authors have proposed reconstruction methods essentially relying on the alleged periodicity of the heart-beat [Blo06; Han08; Mov06; Prü06; Sch06]. (For reviews of ECG-gated cardiac CT, see Desjardins *et al.* [Des04] and Achenbach [Ach06a].)

Unfortunately, there are two problems about gating: First, the assumption of periodicity is only very approximate. As demonstrated by Achenbach [Ach06b], the offset between the positions during the same heart phase at different cycles is larger than the diameter of the coronary vessels. However, these vessels are of primary interest, and their reconstruction needs to be reliable. Second, the ECG signal of heart patients is typically very irregular [Ach06b], making the identification of stable phases complicated. This is particularly problematic for patients with pathologies like congenital cardiac defects or a prior bypass-surgery. (See fig. 6.2.)

Consequently, multi-phase reconstructions cannot be expected to yield sufficient results. An alternative approach is to estimate a motion model and a shape from the projections [Kei09a;

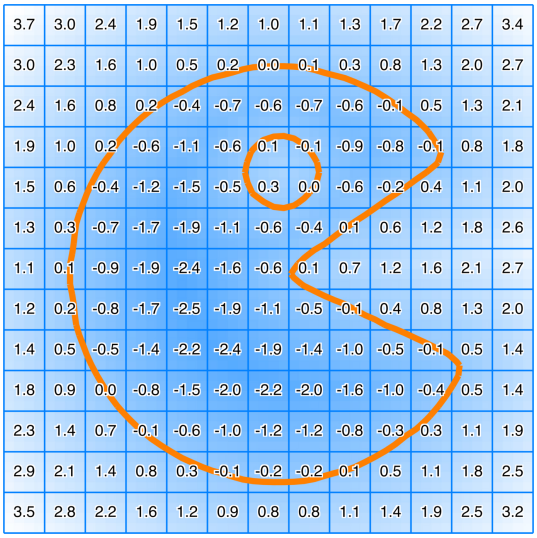

Figure 6.3.: The level-set function encodes a shape (orange) implicitly as zero-level-set. Discretised into voxels (grid), the coefficients can be updated based on constraints, thus moving the zero-interface between the 'inside' as modelled by a negative sign and the 'outside'.

Kei09b; Roh09]. (For a much more detailed review doing justice to the different possible reconstruction methods, see Keil [Kei10a] and Rohkohl [Roh12].)

6.3. Outline of the Proposed Approach

In case of cardiac imaging, the ideal result is a four-dimensional (3D+t) image: A volumetric image of the heart, over time. However, the direct tomographic reconstruction appears to be particularly ill-posed, and this fact suggests to seek a symbolic/binary reconstruction along with a motion model first. In the case at hand, such a symbolic recovery is performed based on the coronary arteries since they are contrasted and cover the motion in the relevant area around the patient's heart. At a later stage, the recovered motion field can be used for a separate tomographic reconstruction.

Therefore, the core idea of the proposed method [Kei09a; Kei09b] is to segment the coronary vessels from the input projections, and to reconstruct a symbolic three-dimensional vessel tree employing a level-set framework [Osh88; Set99]. Originally, the latter can be considered as binary segmentation method. The interface between 'inside' and 'outside' is not modelled explicitly as mesh as is done in *active contour* methods [Kas88], but as the zero-level-set $\Gamma = \{\mathbf{x} | \Phi(\mathbf{x}) = 0\}$ of a so-called level-set function $\Phi : \Omega \subset \mathbb{R}^n \rightarrow \mathbb{R}$, and

$$\Phi(\mathbf{x}) \begin{cases} < 0 & : \mathbf{x} \text{ is inside of the boundary } \Gamma \\ = 0 & : \mathbf{x} \in \Gamma \\ > 0 & : \mathbf{x} \text{ is outside of the boundary } \Gamma. \end{cases} \tag{6.1}$$

Similar to the signal in tomographic reconstruction, this function is discretised into voxels (see fig. 6.3), and evolved in an iterative scheme in order to satisfy constraints which will be based on projections and penalties. The evolution is done by adapting the coefficients, thus moving the interface Γ in the domain of the level-set function Φ by changing its potential. The advantage of the framework is that complex constraints can be included rather easily, thus allowing for extended mathematical modelling.

The rationale for taking this approach is as follows: First, contrasted angiographic X-ray projections usually have a bad image quality, and the varying contrast agent flow may lead to additional inconsistencies. It is hard to track certain key points over the sequence of projections, and a soft coupling in three-dimensional space is highly desirable. Second, as has been outlined above, exact re-positioning and perfectly periodic ECG signals are unrealistically strong assumptions, but the motion is still pseudo-periodic, and an approximate return can be assumed. To this end, a soft coupling in time domain will also prove to be advantageous. Finally, there is no prior knowledge about the topology of the vessel tree, and the level-set paradigm has the further advantage of being able to handle this agnostically.

Although the method uses novel data terms and a new space-time coupling, it shares ideas with some other approaches: Yoon *et al.* [Yoo06] perform a CT-like reconstruction from X-ray data using multiphase level-sets. This work enables the reconstruction of piece-wise constant tissue from very few projections, but it does not deal with motion. Rathi *et al.* [Rat05] and Cremers [Cre06] perform deformable tracking on two-dimensional images using active contours which is related to the proposed time-coupling. Additionally, there is a lot of related work on three-dimensional reconstruction from optical images using level-sets, graph cuts, or voxel occupancy techniques. For instance, Franco *et al.* [Fra05] give a nice derivation and solution to the problem of three-dimensional reconstruction from probabilistic silhouette images in a *synchronised* multi-view environment.

6.4. Methods

In order to implement the proposed symbolic reconstruction approach, several components need to be developed: First, the four-dimensional level-set function $\Phi(\mathbf{x}, t)$ needs to be encoded in a useful way to ensure the coupling requirements outlined above. Then, data fidelity terms need to be developed which use the projected coronary vessels to evolve this function Φ towards a reconstruction of the moving artery tree. Finally, due to the ill-posedness, additional penalty terms are required to make the reconstruction feasible.

Note that the method does not use raw X-ray projections, but pre-processes them to vessel segmentations. This is done by first applying a vessel enhancement filter [Kol95; Fra98] to make the coronary vessels more prominent. Then, a suitable segmentation is computed, effectively turning the projections into 'vessel probability' pictures. (See fig. 6.4.) From an elevated point of view, the method is, therefore, dealing with a dynamic *shape-from-silhouette*

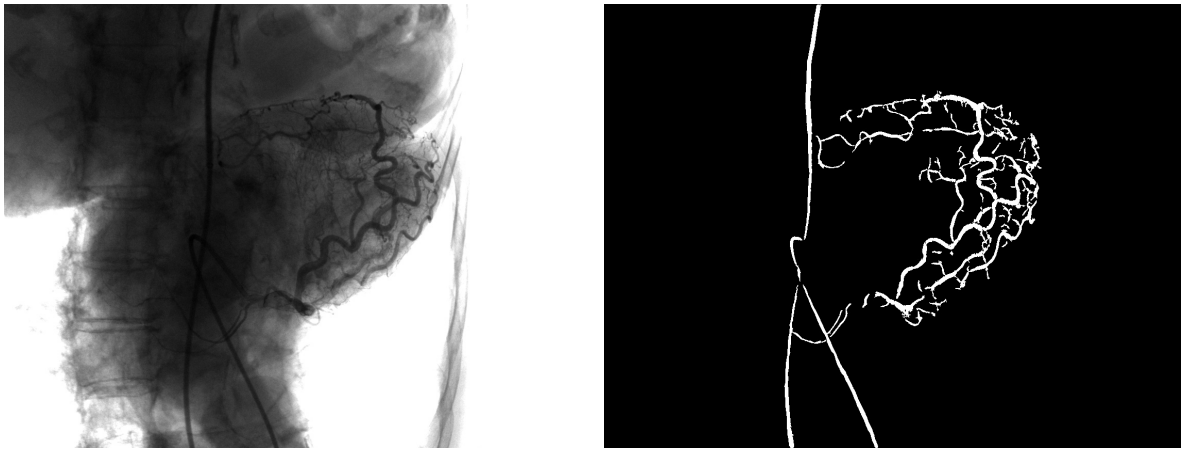

Figure 6.4.: Rather than using raw projections (left), the proposed method considers vessel segmentations (right). Therefore, the method back-projects shadows to obtain a symbolic model. *(Raw data by courtesy of Klinikum Coburg, Germany.)*

problem.

6.4.1. Dynamic Level Sets

Following the level-set approach, define a four-dimensional level-set function $\Phi : \Omega \times \mathrm{T} \to \mathbb{R}$. Here again, $\Omega \subset \mathbb{R}^3$ denotes a spatial volume of interest, and $\mathrm{T} \subset \mathbb{R}$ denotes the temporal range of interest. This function $\Phi(\mathbf{x}, t)$ uses the encoding scheme shown in eq. (6.1): At time t, location $\mathbf{x}$ is 'inside' of a vessel if $\Phi(\mathbf{x}, t) < 0$, and 'outside' if $\Phi(\mathbf{x}, t) > 0$. Over the iterations of the solver algorithm, the coefficients of voxels within the vessel tree will need to assume negative values, and the others positive values. The respective voxel-wise update steps will be controlled via the segmented vessel probability projections.

It would be possible to discretise $\Phi(\mathbf{x}, t)$ directly, leading to a four-dimensional reconstruction problem. Alternatively, one can consider the level-set function $\Phi(\mathbf{x}, t)$ to only be virtual, and decompose it in a way similar to what was proposed by Blume *et al.* [Blu09], as follows:

$$\Phi(\mathbf{x}, t, \boldsymbol{\alpha}) = \Phi_0\big(\boldsymbol{\varphi}(\mathbf{x}, t, \boldsymbol{\alpha})\big) \tag{6.2}$$

Here,

$$\Phi_0 : \left\{ \begin{array}{rcl} \Omega \subset \mathbb{R}^3 & \to & \mathbb{R} \\ \mathbf{x}_0 & \mapsto & \Phi_0(\mathbf{x}_0) \end{array} \right. \tag{6.3}$$

denotes a time-independent reference level-set containing the static prototype shape. The dynamic behaviour is enabled via a separate motion model $\boldsymbol{\varphi}$ mapping point $\mathbf{x}$ at time t to a location $\mathbf{x}_0$ in static reference space using motion parameters $\boldsymbol{\alpha}$. This motion model is only required to be differentiable with respect to the parameters. Considering the decomposed model from eq. (6.2), note that the unknowns to recover are the function Φ_0 encoding the reference shape, and parameter $\boldsymbol{\alpha}$ encoding the motion.

A typical choice for the motion model could be a combination of different contributions:

$$\boldsymbol{\varphi}(\mathbf{x}, t, \boldsymbol{\alpha}) = \boldsymbol{R}(t, \boldsymbol{\alpha}) \cdot \mathbf{x} + \boldsymbol{T}(t, \boldsymbol{\alpha}) + \boldsymbol{u}(\mathbf{x}, t, \boldsymbol{\alpha}) + \boldsymbol{v}(\mathbf{x}, t, \boldsymbol{\alpha}) \tag{6.4}$$

Here, $\boldsymbol{R}$ and $\boldsymbol{T}$ together represent a global rigid motion with six degrees of freedom. $\boldsymbol{u}$ and $\boldsymbol{v}$ denote additional local deformable motion fields locally distorting the global motion. In order to model the behaviour of the heart, $\boldsymbol{R}$, $\boldsymbol{T}$ and $\boldsymbol{u}$ can be assumed to be periodic, and $\boldsymbol{v}$ a global, non-periodic, low-amplitude motion, for instance. Such a motion model will require interpolation schemes, and temporal B-splines [Die93] would be a possible option.

Combining a static shape Φ_0 with a dynamic warping function $\boldsymbol{\varphi}$ has several advantages: First of all, the shape reconstruction is implicitly regularised over time, since there is only one shape model. Then, the motion can be recovered directly, simplifying its later use in a tomographic reconstruction as well as enabling a direct motion regularisation. Finally, memory requirements are much lower compared to a four-dimensional grid if $\boldsymbol{\varphi}$ is properly parametrised.

6.4.2. Data Fidelity Terms

Having described a model for shape and motion, an energy functional needs to be set up that fits the reconstruction parameters Φ_0 and $\boldsymbol{\alpha}$ to the given L measured images I_l acquired at times t_l, $1 \leq l \leq L$. As has been described above, their pixels are assumed to contain intensity values in $[0, 1]$ corresponding to the probability that the associated ray hit a vessel. Later-on, the energy functional will be minimised, yielding the reconstructions of the two unknowns.

Similar to the idea of SIRT, the data fidelity terms will consider differences between synthetic forward projections and actual measurements, but errors in the shape-from-silhouette problem are also symbolic: If a ray projects onto a 'no-vessel' pixel in a projection, all positions along the ray are known not to be within the vessel tree. Vice versa, if it hits a 'vessel' pixel, it is known that at least one location along the ray is within the vessel tree. Consequently, the penalties will be constructed from false positives and false negatives in space, taking into account the projective character of the imaging device. This works in a manner similar to what was first presented by Chan and Vese [Cha01].

The first term penalises *false positives*, that is, points within Φ_0 which are reconstructed as part of the vessel tree, despite being projected to a 'no-vessel pixel'. Let $\boldsymbol{P}_l : \mathbb{R}^3 \to \mathbb{R}^2$ denote the projection operator for frame l, and

$$H(x) = \begin{cases} 0 & : \ x < 0 \\ 1 & : \ x \geq 0 \end{cases} \tag{6.5}$$

the Heaviside step function. (See [Cha01].) Then, the false positive term is:

$$E_{\mathrm{FP}}(\Phi_0, \boldsymbol{\alpha}) = \sum_{l=1}^{L} \int_{\Omega} S_{\mathrm{FP}}\Big(I_l\big(\boldsymbol{P}_l(\mathbf{x})\big)\Big) \cdot \big[1 - H\big(\Phi_0(\boldsymbol{\varphi}(\mathbf{x}, t_l, \boldsymbol{\alpha}))\big)\big] \cdot \big[1 - I_l\big(\boldsymbol{P}_l(\mathbf{x})\big)\big] \ \mathrm{d}\mathbf{x} \tag{6.6}$$

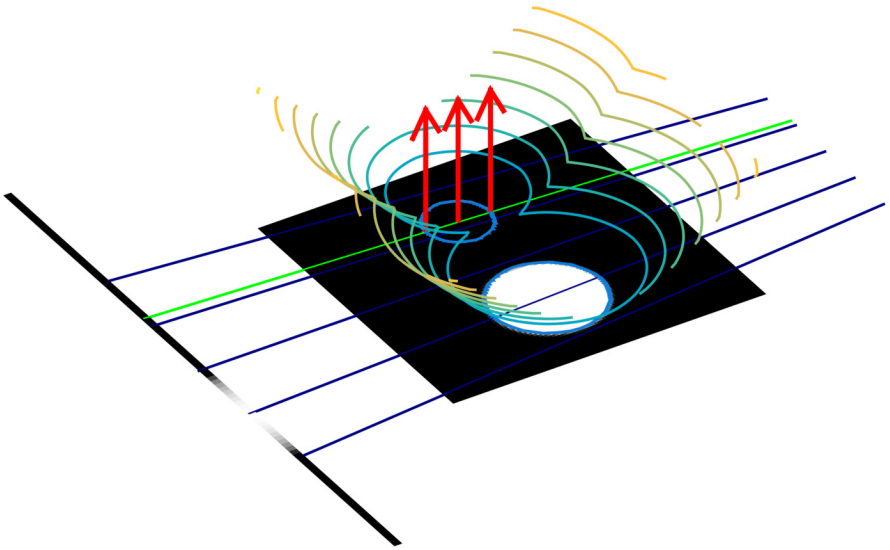

Figure 6.5.: The level-set function (coloured contour lines) describes two reconstructed blobs in this two-dimensional example. The close one (white disc with blue contour) is correct, the far one (blue contour) is a *false positive* as the respective rays (green) map into void. Consequently, the level set function needs to be increased at the respective spots (red arrows).

This expression extends over all L projection images (sum) and the entire volume of interest Ω (integral). At every such pair of a location $\mathbf{x}$ in space and its projection $\boldsymbol{P}_l(\mathbf{x})$, the product of three factors is evaluated: The first factor enables the term for projections to 'no-vessel pixels' by means of auxiliary switching function $S_{\mathrm{FP}}(i) := H\left(\frac{1}{2} - i\right)$. Consequently, the first factor is 1 for low image intensities/probabilities in the image I_l, and 0 else. Similarly, the second factor is 1 for negative values of Φ_0 'inside' of the vessel tree, and 0 for the positive values 'outside' of it. Together, the first two factors filter out the false positive reconstructions, and the third factor is the respective weighted penalty. (See fig. 6.5.)

Penalising *false negatives* works in a similar way, however, with the difference that penalties cannot be accumulated in volume space Ω. As the images are probabilistic projections, a false negative penalty can only be imposed if, and only if, no object is reconstructed along a whole ray corresponding to a high intensity 'vessel pixel'. Thus, entire rays have to be considered instead of single points, and the proposed false negative term is:

$$E_{\mathrm{FN}}(\Phi_0, \boldsymbol{\alpha}) = \sum_{l=1}^{L} \int_A S_{\mathrm{FN}}\big(I_l(\boldsymbol{p})\big) \cdot H\left(\min_{\boldsymbol{x} \in X_l(\boldsymbol{p})} \Phi_0\big(\boldsymbol{\varphi}(\boldsymbol{x}, t_l, \boldsymbol{\alpha})\big)\right) \cdot I_l\big(\boldsymbol{p}\big)\ \mathrm{d}\boldsymbol{p} \tag{6.7}$$

Here, $A \subset \mathbb{R}^2$ is the projection image space, and $X_l(\boldsymbol{p})$ denotes the set of volume points projecting onto pixel $\boldsymbol{p}$ in image I_l, that is, the ray hitting the image I_l at $\boldsymbol{p}$. Therefore, the term extends over all pixels/rays (integral) of all projection images (sum), and again evaluates a product of three factors: The first uses a switching function $S_{\mathrm{FN}}(i) := H\left(i - \frac{1}{2}\right)$ to enable the term for 'vessel pixels' only. Similarly, the second factor enables the term if the minimal

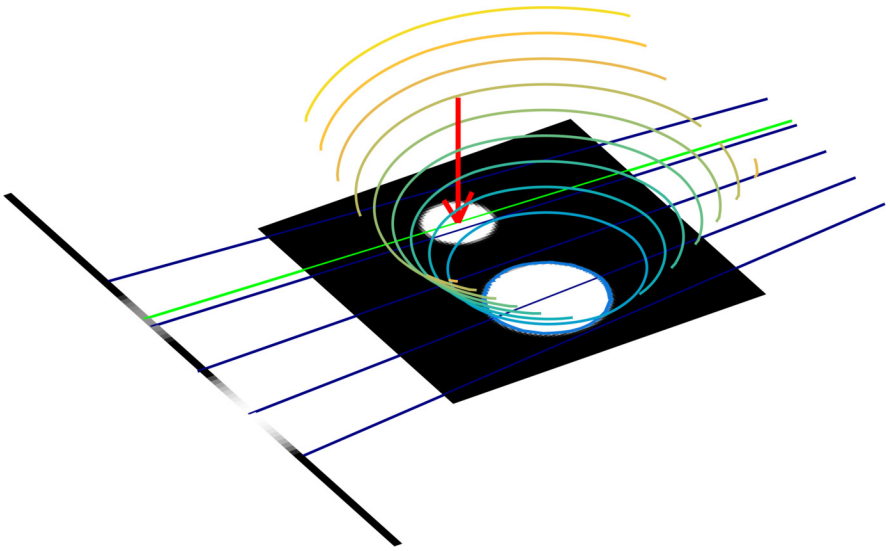

Figure 6.6.: The level-set function (coloured contour lines) describes a single reconstructed blob (near white disc with blue contour) in this example, but a second one (far white disc) is missing. The latter is a *false negative* as the respective rays (green) map into a vessel. Consequently, the level set function needs to be decreased at a single location (!) along the ray, and it is done at the relative minimum (red arrow).

level-set function value along the ray is positive, that is, if all locations along the ray are 'outside' of the reconstructed vessel tree. Together, the first two factors select the case of false negative reconstructions, and the third factor is again the respective weighted penalty. (See fig. 6.6.)

Note again that the two data terms are constructed quite differently. This is remedied by either appropriately weighting them or reformulating the false negative term to a volume integral using the co-area formula.

6.4.3. Regularisation

In terms of regularisation, only shape constraints need to be considered since the motion parameters can be inherently regularised by appropriate interpolation schemes such as B-splines with a matching number of knots. For obtaining a smooth shape reconstruction in the reference frame, a total-variation-like penalty

$$E_{\text{shape}}(\Phi_0) = \int_\Omega \delta(\Phi_0(\boldsymbol{x})) \cdot \|\nabla\Phi_0(\boldsymbol{x})\| \; \mathrm{d}\boldsymbol{x} \tag{6.8}$$

can be enforced in the immediate vicinity of the $\Phi_0 = 0$ zero-level-set as selected by the Dirac function $\delta(\cdot)$. This term favours a low surface curvature at the interface between 'inside' and 'outside', leading to a smoother vessel tree reconstruction.

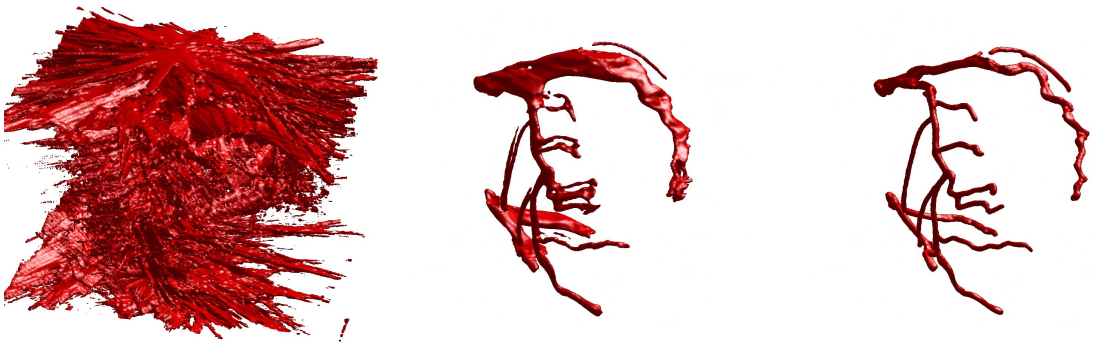

Figure 6.7.: Evolution of the static reference shape after 1, 20, and 110 iterations. Note that an approximate shape is carved out first, and that this intermediate shape may show duplicated side-branches. After further iterations, this doubled structures are merged. The input data has been obtained using the XCAT phantom [Seg99; Seg01b; Seg01a].

6.4.4. Optimisation

The data fidelity and regularisation terms (6.6)–(6.8) can be collected into a common energy functional:

$$E(\Phi_0, \boldsymbol{\alpha}) = \beta_{\text{FN}} \cdot E_{\text{FN}}(\Phi_0, \boldsymbol{\alpha}) + \beta_{\text{FP}} \cdot E_{\text{FP}}(\Phi_0, \boldsymbol{\alpha}) + \beta_{\text{shape}} \cdot E_{\text{shape}}(\Phi_0) \tag{6.9}$$

Here, the different $\beta_{\dots}$ denote weighting factors, and the reconstruction problem can be stated as follows:

$$\arg\min_{\Phi_0, \boldsymbol{\alpha}} \{E(\Phi_0, \boldsymbol{\alpha})\} \tag{6.10}$$

Optimising this system is rather complex as two sets of parameters must be computed simultaneously, namely the shape model Φ_0 and the deformation parameters $\boldsymbol{\alpha}$. The former is minimised using the variational derivative $\frac{\delta E}{\delta \Phi_0}$, the latter by calculating the gradient $\nabla_{\boldsymbol{\alpha}} E$. Computing these terms from their analytic forms involves deriving the minimum functional from equation (6.7), several numerical approximations, and a step size management during gradient descent for Φ_0 and α.

The most demanding issue to solve is the computation of E_{FN} and its derivative. It involves ray-casting for computing the minimum contained in the equation's second factor. Furthermore, updates to Φ_0 have to be applied at the respective ray-casting sample points and thus need to be extrapolated to the nearest grid locations of the discretised approximation of level-set function Φ_0. (See Keil [Kei10a] and Vogel [Vog09b] for details on the optimisation.)

6.5. Results, Conclusion and Summary

Several experiments have been conducted using phantoms and real data. For phantom data, the synthetic motion is usually rather simple, particularly periodic, and the results in this case

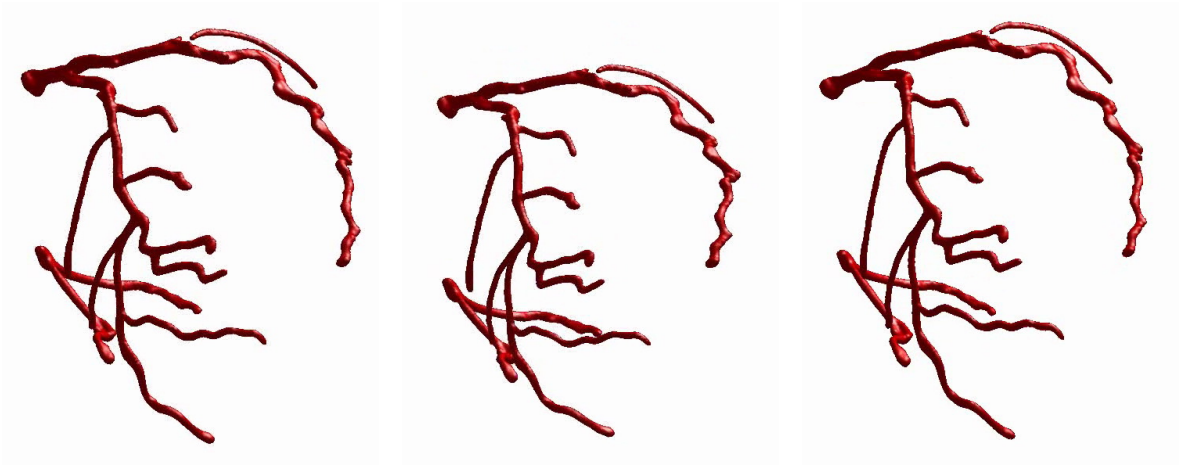

Figure 6.8.: Dynamic reconstruction result after 140 iterations. Shown are renderings of the reconstructed moving vessel tree (3D+t) after 0.0, 0.3, and 0.6 s. Note the The input data has been obtained using the XCAT phantom [Seg99; Seg01b; Seg01a].

are likely not significant in terms of judging the real performance. The probably most complex phantom experiment was done with projections of the XCAT phantom [Seg99; Seg01b; Seg01a]. (See figs. 6.7 and 6.8 for sample results; numerical results are excluded for brevity, see Keil [Kei10a] for such evaluations.)

In case of real data, it turned out that proper preprocessing of the images into vessel segmentations is a major obstacle. The clinical images typically do not show strong contrast, and the flow of the contrast agent was not sufficiently constant, at least in the few datasets that have been available. It is unclear whether the physical data acquisition can be improved, and whether doing so imposes an excessive burden onto the clinical personnel, thus preventing the use of the method in clinical scanners. It would also be interesting to see whether modern machine learning techniques yield better vessel classifications than the, from today's perspective antiquated, vessel enhancement schemes. Some early reconstructions have still been computed at the time, and the approach seems to work in general, but an accurate quantification of the performance has not been possible.

Unfortunately, the project was industry-related and needed to be concluded at a too early stage. The level-set-based dynamic reconstruction method was still included in this thesis to present thought-provoking impulses for handling motion-related inconsistencies. For this reason, a quick outline is considered to be sufficient. (For a more complete discussion including a probabilistic model, extensive results, and open research questions, see Keil [Kei10a].)

This entire chapter, particularly section 6.4 on the actual equations, is a revised and partly extended version of the original research papers [Kei09a; Kei09b].

Part III.

Interventional SPECT Imaging and Optimal Sensor Trajectories

7. Freehand and Robotic SPECT

Diagnostic tomographic scanners are designed to optimally acquire data for image reconstruction, and they are intended to be used in a dedicated radiology or nuclear medicine department. In particular, these devices are not equipped for use in operating rooms, and cannot be used for interventional imaging. This is mainly due to the massive scanning gantries which entirely surround the patient, and the relatively long scanning times required for nuclear imaging modalities. For this reason, surgeons often rely on pre-operative images which do not show the actual situation: The patient is usually in a different position, resections may have taken place, and depending on the interval between image acquisition and intervention, wound healing, digestion or similar processes may have had effects. (For details on deformable registration of datasets, see Zikic [Zik11] and Glocker [Glo11].)

On the other hand, interventional imaging is highly relevant for intervention guidance and quality control. Classical two-dimensional means are ultrasonography [Gol96] and X-ray fluoroscopy. (See section 2.4.1 for the use of X-rays in medicine.) Imaging technology has significantly advanced in this respect, and tomographic techniques such as 3D ultrasound [Fen00] and C-arm CT [Gan11] are applied in clinical practice with considerable success. (See section 6.1 for interventional tomographic cardiac imaging.) Considering the two modalities, ultrasonography is typically human-guided, and the surgeon will position the sensor manually. C-arm CT on the other hand is mechanised, and X-ray tube and detector are moved robotically. In recent years, medical robotics has been investigated intensively also for imaging. For instance, Schneider *et al.* [Sch11] proposed a robotic laparoscopic ultrasound system.

7.1. Introducing Interventional SPECT

Considering tomographic nuclear imaging, the interventional extension has been proposed rather recently. Classically, a radio-tracer was administered for pre-operative imaging, and during the intervention, a 'normal' hand-held radioactivity sensor such as a 'single-pixel' scintillation counter would be used to triangulate radioactive hotspots and to check excised tissue for radioactivity. (See section 2.4.2 for details on nuclear imaging.) In 2007, Wendler *et al.* [Wen07b] proposed to 'track' such an sensor using a optical tracking system [Kha00],

The author has contributed to some more recent developments of the freehand and robotic SPECT systems, cooperating particularly with Tobias Lasser, José Gardiazabal and Philipp Matthies, among others [Mat13; Mat14; Gar14; Las15; Gar15b]. A data acquisition scheme [Vog12; Vog13] will be discussed in chapter 8.

Figure 7.1.: The freehand SPECT system uses an optical tracking system (top left) to track position and orientation of a γ-radiation sensor (centre, on cart, with cross-shaped tracking target) which is hand-guided by a surgeon. Like this, measured counts are related to sensor perspectives, thus enabling tomographic reconstruction. *(Courtesy of José Gardiazabal.)*

thus establishing a known connection between sensor perspectives and activity counts. (See figs. 7.1 and 7.2.) Based on this data, they demonstrated successfully the first tomographically reconstructed interventional volumetric images for a phantom setup. A first clinical version followed in 2010 [Wen10b], and the term *freehand SPECT (fhSPECT)* was coined as name.

7.1.1. Medical Scenarios

Before continuing with a technical description, consider possible medical scenarios first. In this context, two aspects are relevant: First, interventional imaging is obviously not intended for whole-body acquisitions, but to monitor the situation in a confined region of interest. This situation is compatible with the proposed hand-guided mode of operation.

Second, interventional imaging needs to fit into the surgical work-flow, thus consuming as

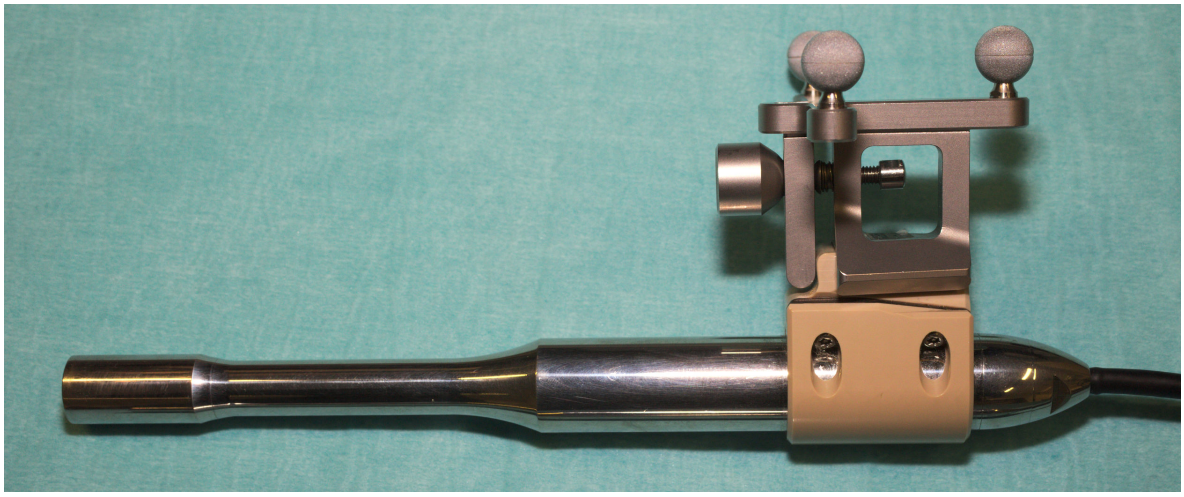

Figure 7.2.: Close-up of radiation detector with retro-reflective balls as target for optical tracking system. *(Courtesy of José Gardiazabal.)*

little time as possible. Dealing with nuclear tracers, the quality of the reconstructed images depends massively on statistically significant measurements, as usual. The radiation intensity is known to drop off exponentially with distance, and longer acquisition times will be necessary for more distant regions of interest.

Consequently, fhSPECT works best if the relevant hotspots can be expected to be close to the accessible surface. In this case, a quick, patient-specific scan will lead to useful tomographic images. In detail, primarily two interventional settings appear to be promising and have been clinically investigated.

Sentinel Lymph Nodes (SLN) Some types of cancers are known to spread along the lymph system. The first lymph node after the tumour, the *sentinel lymph node (SLN)*, has high significance in detecting metastases. An important aspect of tumour resection is thus SLN biopsy, that is, a check whether it already contains cancer cells. For this procedure, the patient is typically injected with a radioactive tracer a few hours in advance, and a planar scintigraphy is taken to ascertain the tracer uptake. During the biopsy procedure, fhSPECT three-dimensional imaging can be used to plan and guide the resection for that particular patient and control any residual radioactivity intra-operatively. Freehand SPECT has found clinical application in sentinel node biopsy for breast cancer [Sch12; Blu13], for melanoma [Rie11; Naj11] and for oral cancer [Heu12], as well as in parathyroidectomy [Rah12].

Sentinel lymph node pictures typically show distinct hotspots. The latter exhibit some contrast variations, but the picture is typically treated as pseudo-binary. (See fig. 7.3.)

Thyroid Imaging Another application is *thyroid imaging*. The thyroid is a butterfly-shaped gland of two lobes, located in the neck, at the throat. In the last decades, thyroid cancer

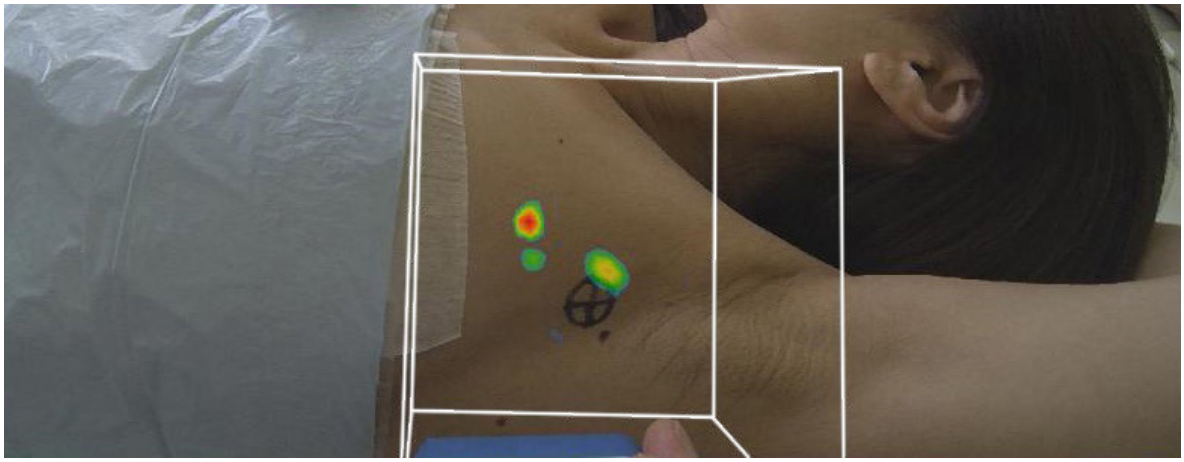

Figure 7.3.: Augmented reality view of a fhSPECT reconstruction of radio-marked lymph nodes in the axilla of a breast cancer patient. *(Courtesy of Philipp Matthies.)*

incidence rates have risen dramatically in many countries, and the reasons for the increase appear to be unclear [Fer13; Jem10; Dav06; Har95; Reg09]. It has been suggested that both, incidental detection during ultrasound examinations as well as risk factors such as radiation exposure and obesity, might be among the causes [Lee04]. Similar to other cancers, survival chances depend largely on quick and accurate staging and stratification [Sim12].

Localisation of tumours inside the thyroid is usually based on nuclear imaging, most commonly on two-dimensional scintigraphy [Grü97], but several studies have shown that volumetric visualisation based on SPECT leads to better performance [Mok00; Mar12c]. (See fig. 7.4.) Consequently, fhSPECT has also been suggested for thyroid imaging, and early phantom studies have appeared [Las15; Gar15b; Gar16]. Thyroid pictures are usually more complex than SLN images, and they require recovery of contrast, to tell apart hot and cold nodules from background. (See fig. 7.5.)

7.1.2. Fundamental Considerations

Returning to technical aspects, recall the basic setup of fhSPECT: A hand-guided radiation sensor is tracked by an optical tracking system, and counts and sensor poses are synchronously recorded. Afterwards, the two data-streams are used to reconstruct a tomographic image. Due to the probabilistic nature of nuclear decay, a statistical reconstruction technique will be employed for the last step, thus requiring measurement probabilities. (See section 4.3 for the mathematical background and section 7.2 for technical details.)

In diagnostic SPECT scanners, the gamma cameras follow a pre-determined path, and the system matrix entries giving the measurement probabilities can be obtained via known values. In freehand SPECT, however, the sensor trajectory is initially unknown and provided by the tracking system. Each position corresponds to a set of new rows of the system matrix which

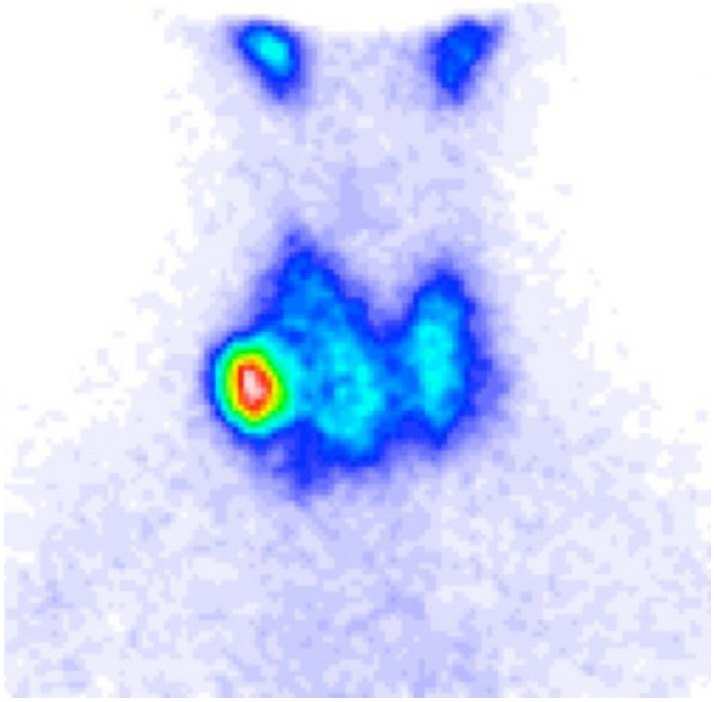

Figure 7.4.: Clinical scintigram of a thyroid patient. Note the shape of the neck and the chest, and particularly the hotspot at the thyroid. *(Courtesy of Klinikum Rechts der Isar, Nuklearmedizin.)*

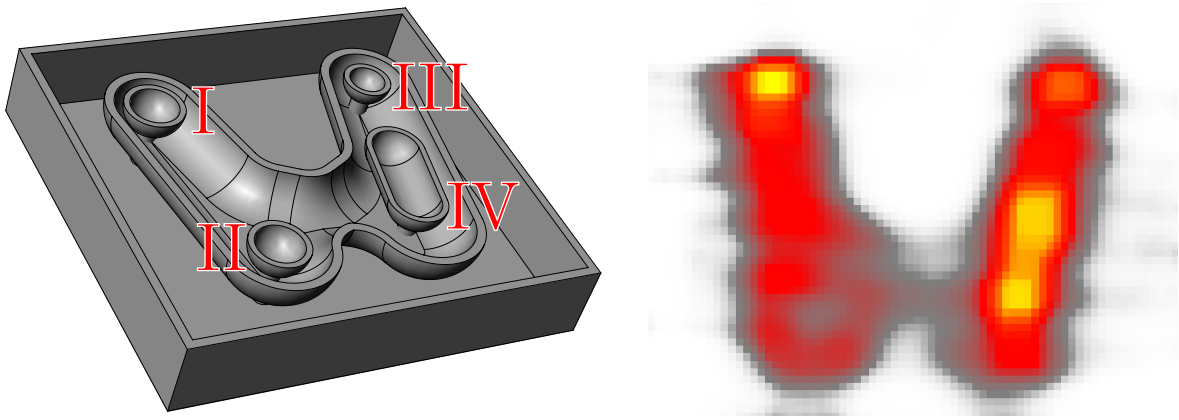

Figure 7.5.: A thyroid phantom (left) was filled with a radio-tracer, measured, and reconstructed using the fhSPECT technique (right). Chamber II of the phantom did not contain radioactivity and models a 'cold' nodule, but chambers I, III, IV were 'hot'. The large butterfly-shape chamber containing the smaller chambers I–IV was filled with less activity to model background radiation. *(Courtesy of José Gardiazabal and Tobias Lasser.)*

is implicitly stacked up along the way.

Consequently, the quality of the tomographic images depends highly on the performance of the person doing the actual scan. In general, tomographic image reconstruction does not require high counts only, but also low counts in order to carve away inactive regions. Surgeons, however, are used to triangulation, based on the characteristic sound known originally from Geiger counters.

Furthermore, tomographic reconstruction also needs as many orthogonal views on the region of interest as possible. In fact, however, many clinical settings lead to *limited angle* problems due to the confined space available. Within these bounds, the human operator of the probe needs to take care to sample the region of interest not only in a translatory sense, but also in terms of looking directions.

Additional constraints have been mentioned above: The time frame available for image acquisition is limited, and the radiation sensor must be kept in close proximity to the region of interest for optimal statistics. All these points are enforced mechanically in diagnostic scanners, but need to be met 'manually' in this case for optimal image quality.

7.2. Technical Details of Freehand SPECT (fhSPECT)

Considering the major components of the fhSPECT system, additional engineering questions arise. (For a more complete discussion, see the doctoral theses of Thomas Wendler [Wen10a] and Tobias Lasser [Las11a], and the future theses of José Gardiazabal and Philipp Matthies.)

7.2.1. Sensors

As has been mentioned above, fhSPECT originally used γ-radiation sensors available for operating room use. These devices come in different variants with respect to the target energy of the incoming γ-photons and collimation, that is the angular opening of the field of view. Typically, fhSPECT sensors would use a rather wide opening angle of around 120°, to allow for simpler coverage of the region of interest. On the other hand, this leads to blurring and problems in regions with higher background or overlapping activities.

A possible option is to replace these simple sensors with a miniaturised gamma camera [Wei00a; Wei01], thus obtaining more readings and statistically more meaningful measurements at the same time. Proposed by Matthies *et al.* [Mat13; Mat14], this has become the standard sensor for fhSPECT. (See fig. 7.6.)

7.2.2. Tracking

Knowing the location of the detector with high precision is key in tomographic reconstruction, to intersect the observations as exactly as possible. For this reason, fhSPECT typically uses an optical 'outside-in' tracking system [Kha00] to find out the position of the sensor. Following

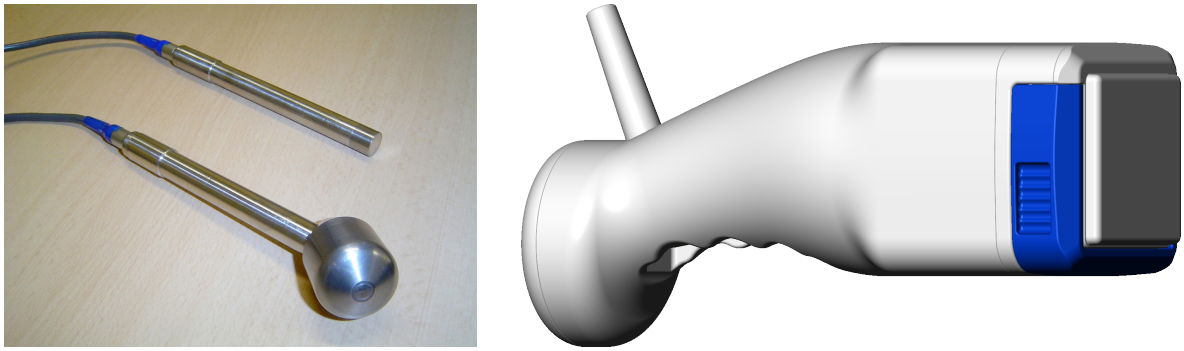

Figure 7.6.: Interventional radiation senors as used with fhSPECT: Originally, 'single-pixel' detectors (left) have been employed which provide a single scalar signal. These types of devices have been used in operating rooms before for triangulation. More recent setups usually employ a mini gamma camera (right) which provides an image of 16×16 pixels. *(Courtesy of Tobias Lasser and Philipp Matthies.)*

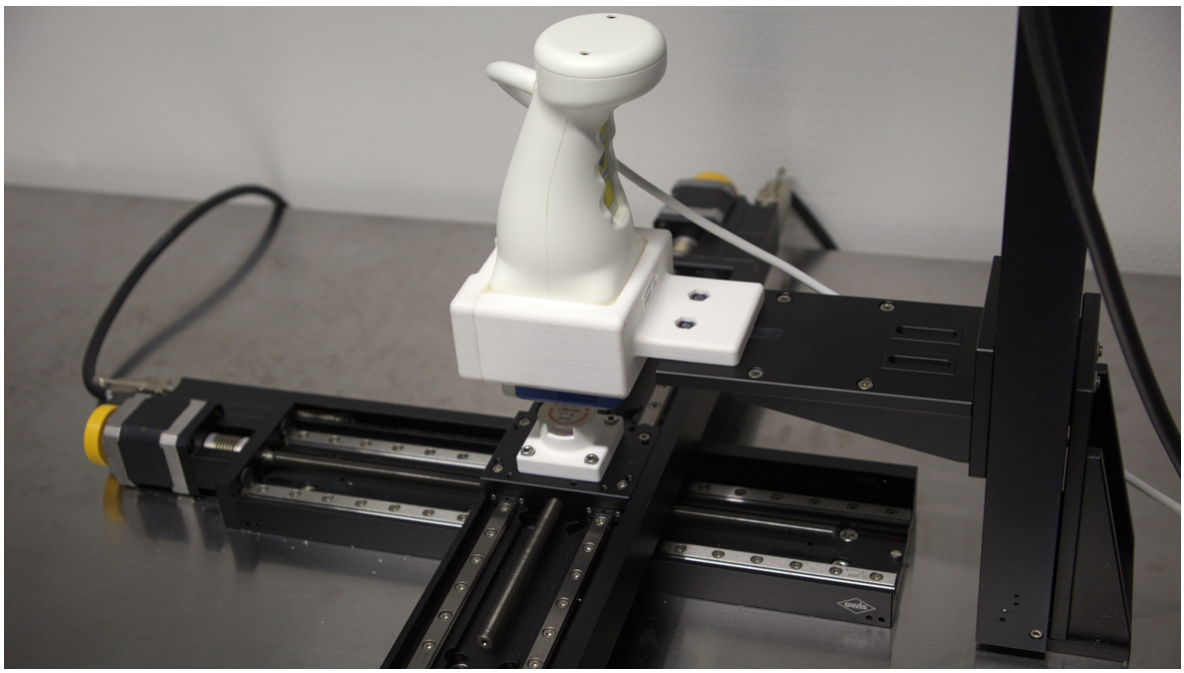

Figure 7.7.: Positioning table for sensor calibration: In order to obtain measurement probabilities, one option is to exhaustively measure the response to a point source. The latter (bottom centre, a ^{57}Co source in the white holder) is moved systematically within the field of view of the camera in x- and y-directions. Once completed, the camera is moved up in z-direction, and the process repeats. Many such measurements eventually lead to lookup tables. (See fig. 7.8.) *(Courtesy of José Gardiazabal.)*

the paradigm known from radars in flight control, an active system observes the scene from outside using optical cameras, and computes the location of a tracking target (mounted onto the sensor) consisting of retroreflective markers using stereo-vision techniques. For this to work, a direct line of sight between the over-head optical camera system and the target is required. (See Feuerstein [Feu07a] for some background on tracking systems.)

Alternatives would be mechanical or optical 'inside-out' tracking. In case of the latter, the gamma sensor is no longer tracked from outside, but computes its own location. This is usually done by mounting an additional optical camera onto the radiation sensor which observes certain markers. Using computer vision techniques, this can be done quite accurately. Of course, the approach still requires a direct line of sight, but there is more flexibility in terms of positioning the reference markers. This approach has been employed before by Rafii-Tari *et al.* [Raf11] for an ultrasound guidance system using a transducer-mounted camera to create three-dimensional panorama images relative to skin markers, and by Magaraggia *et al.* [Mag14] for a video-based solution for screw fixation guidance. Recently, Matthies *et al.* [Mat15] have proposed inside-out tracking for freehand SPECT.

In all such cases, an important point is to accurately synchronise the two data streams, photon counts and positions. Typically, the two provide data at different sampling rates and may show measurement lag. Proper calibration and synchronisation methods are thus required for optimal data acquisition. In particular, it needs to be considered that photon counts are usually integrated over certain little time frames, and the computer vision techniques employed in optical tracking systems consume time. Exploiting the ability of the gamma camera to report individual photons, Gardiazabal *et al.* [Gar15b; Gar16] have recently looked into list-mode reconstruction [Bar97; Par98; Byr01] for fhSPECT and consider the question of blurring problems associated with time-integrated counts.

7.2.3. Modeling Measurement Probabilities

As discussed in sections 4.3.1 and 7.1.2, an important ingredient of likelihood-based reconstruction are the measurement probabilities. In case of fhSPECT, these are obtained by relating the general characteristics of the radiation sensor with the perspective of this sensor onto the chosen volume of interest at a given time.

In general, there are several approaches to modelling the response characteristics of a sensor to a radiation source [Har15; Las11b]: First, one can try to find a mathematical model including exponential drop-off with distance and a restricted field of view by collimation, an approach used in the original fhSPECT system. Second, the response can be simulated based on the known mechanical design of the sensor using Monte Carlo methods. Finally, the response can be measured in long-time experiments (to avoid bias by under-sampling), leading to *lookup tables (LUTs)*.

With the introduction of gamma cameras to fhSPECT [Mat13; Mat14], the last option has

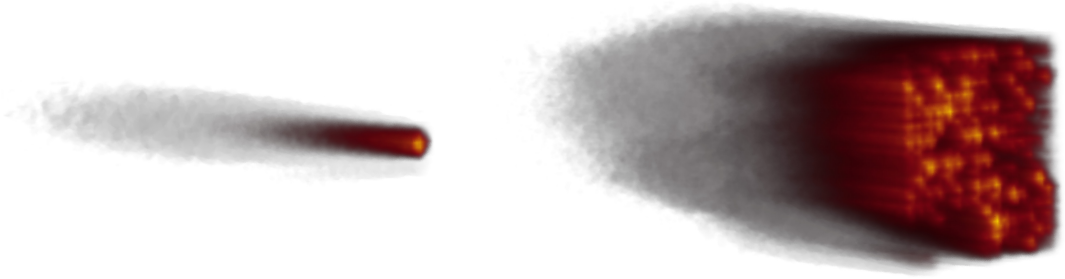

Figure 7.8.: The lookup tables (LUTs) for the mini gamma camera contain $16 \times 16 = 256$ individual pixel-wise measurement probabilities (left). Considering all sensors together, one obtains the full lookup table for the camera (right). Obviously, there are considerable differences between the individual pixels of the camera. *(Raw data by courtesy of José Gardiazabal.)*

become the standard. In order to obtain the LUTs, a ^{57}Co point source was systematically stepped through the field of view of the gamma camera, leading to highly accurate pixel-wise measurement probabilities. (See figs. 7.7 and 7.8.) Unlike mathematical models and imperfect simulations, the tables automatically describe manufacturing-related variations.

Another important aspect in nuclear imaging is attenuation correction. In fhSPECT, an accurate transmission image is usually not available, rendering patient-specific attenuation correction impossible. However, as the hotspots are expected to be close to the sensor, a typical assumption is to have a uniform attenuation. For simplicity, the reference attenuation value for water may be used to modify the LUT values which have been acquired with air between source and detector [Gar16]. This is equivalent to the typical correction approach taken in ultrasound-echography.

7.2.4. Coordinate Frames

In order to compute reconstructions, the remaining problem to solve is transforming everything into the same coordinate system. So far, the lookup tables are defined with respect to the pixel-sensors of the camera, a respective coordinate system will be referred to as $\{sensors\}$. The tracking target mounted to the camera defines another camera-relative coordinate system $\{camera\}$, and its location with respect to some world frame $\{world\}$ is reported by the tracking system as rigid transform ${}^{camera}\mathbf{T}_{world}$. The 'missing link' between the two camera-relative frames, ${}^{sensors}\mathbf{T}_{camera}$, can be established via co-calibration using a tracked pointer device [Mat13; Mat14]. Finally, the volume of interest (VOI) Ω where the radioactivity distribution needs to be reconstructed has its origin $\{voi\}$ also defined via a rigid transform ${}^{voi}\mathbf{T}_{world}$ relative to world origin $\{world\}$. (See fig. 7.9.) Technically, this is done by using the camera to position a default-sized VOI, assisted by an augmented reality view.

Consequently, to obtain the measurement probability of an event occurring at location $\mathbf{p}_{voi}$, the point is transformed into the coordinate system $\{sensors\}$ of the lookup tables by chaining

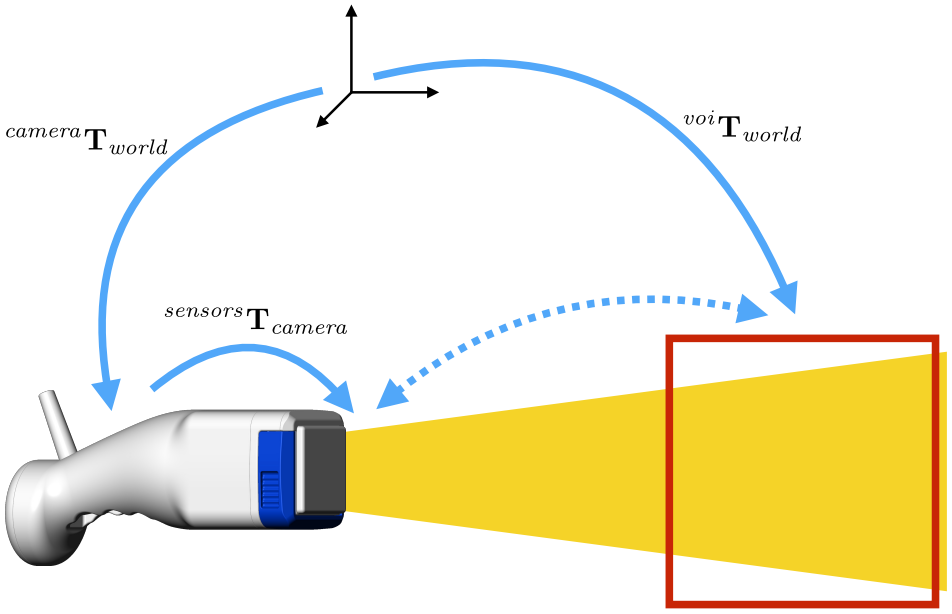

Figure 7.9.: Freehand SPECT involves several coordinate frames. In terms of reconstruction, the only interesting transformation (dotted blue double-arrow) is the one between camera pixels (lower left) and region of interest (ROI, red box, lower right), as it relates the true radioactivity distribution with the measured values reported by the camera. It is not given directly, and everything is defined relative to a world origin (black arrows, top centre) as defined by the tracking system: The world location of the camera is reported in real-time, and an additional transformation describes the hop onwards into the coordinate system of the lookup tables (yellow fan). Similarly, the ROI is defined with respect to the the world frame.

the respective transformations. With ${}^{world}\mathbf{T}_{voi} = \left({}^{voi}\mathbf{T}_{world}\right)^{-1}$:

$$\mathbf{p}_{sensors} = {}^{sensors}\mathbf{T}_{camera} \cdot {}^{camera}\mathbf{T}_{world} \cdot {}^{world}\mathbf{T}_{voi} \cdot \mathbf{p}_{voi} \tag{7.1}$$

The respective lookup tables can be read out directly at $\mathbf{p}_{sensors}$ to obtain the measurement probabilities for every pixel of the gamma camera.

7.2.5. Tomographic Imaging, Finally

Putting things together, the camera will assume a series of K poses for observing the radioactivity distribution. Using the notation defined in section 4.3.1 and denoting the first pose as $k = 0$, measurement m_j will refer to the count obtained in a specific pixel s while the camera is in a certain pose k. Defining S as the total number of sensors, $S = 256$ in case of the gamma camera, one obtains the relation $j = k \cdot S + s$.

Assume that the volume of interest Ω is discretised into I voxels. For reconstruction of coefficients, these voxels need to be related with the measurements via the measurement

probabilities encoded in the system matrix. In order to obtain its component

$$a_{ji} = \mathrm{P}[\text{ photon contributes to measurement } j \mid \text{decay event in voxel } i\ ] \tag{7.2}$$

as defined in eq. (4.30), voxel i needs to be transformed into coordinate system $\{sensors\}$ to look up the calibrated probability there. This is done by evaluating the transformation chain given in eq. (7.1) where $\mathbf{p}_{voi} = \mathbf{p}_{voi}(i)$ is set to the relative location of voxel i and ${}^{camera}\mathbf{T}_{world} = {}^{camera}\mathbf{T}_{world}(k)$ to the camera position in pose k, yielding a result $\mathbf{p}_{sensors}(i,k)$. Using $j = k \cdot S + s$, the probability is then:

$$a_{ji} = \mathrm{LUT}_s(\mathbf{p}_{sensors}(i,k)) \tag{7.3}$$

Recall that the lookup tables are defined per pixel, and LUT_s is the table for camera pixel s.

7.3. Robotic SPECT (rSPECT)

In section 7.1.2, several inherent problems of fhSPECT have been itemised that are connected to the fact that a human operator is controlling the acquisition of the images. This person is likely a medical expert, and interest in the numerical backgrounds of tomographic reconstructions cannot be presupposed. For this reason, the performance of fhSPECT will always be tightly connected to the goodwill of the user, and clinical results will only be reproducible if this is given.

For this reason, it is desirable to mechanise fhSPECT by using a robotic arm to guide the detector, in a way somewhat similar to C-arm CT. Unlike the latter, however, the detector can not be rotated around the patient at a safe distance, but it needs to move in closest proximity to the patient in order to catch as many photons as possible. This fact calls for patient-specific trajectories.

In this context, the first thing to realise is that robotics is a very complex field [Cra05; Cho05]. It is highly non-trivial to securely navigate a robotic arm with several limbs through an environment with obstacles such that there are no (self-)collisions and without the robot getting stuck in singularities. Considering the presence of a patient, severely increased security requirements apply when operating a robot in such a setting as Taylor *et al.* [Tay91] pointed out already in 1991.

For this reason, *robotic SPECT (rSPECT)* is still in its infancy, and probably will be for years to come. For now, the robot is exclusively used for preclinical phantom experiments, and path-planning is only performed to a very limited degree, such as moving between human-controlled via-points, following human-controlled trajectories, or reproducing a trajectory recorded from a human operator. In all such cases, the robot needs to be considered as 'smart holder' allowing for a certain reproducibility. A first working rSPECT setup was demonstrated by Gardiazabal *et al.* [Gar13] in 2013, following an earlier theoretical study by Bowsher *et al.* [Bow12] on a robotic multi-pinhole SPECT system. A robot was also used for

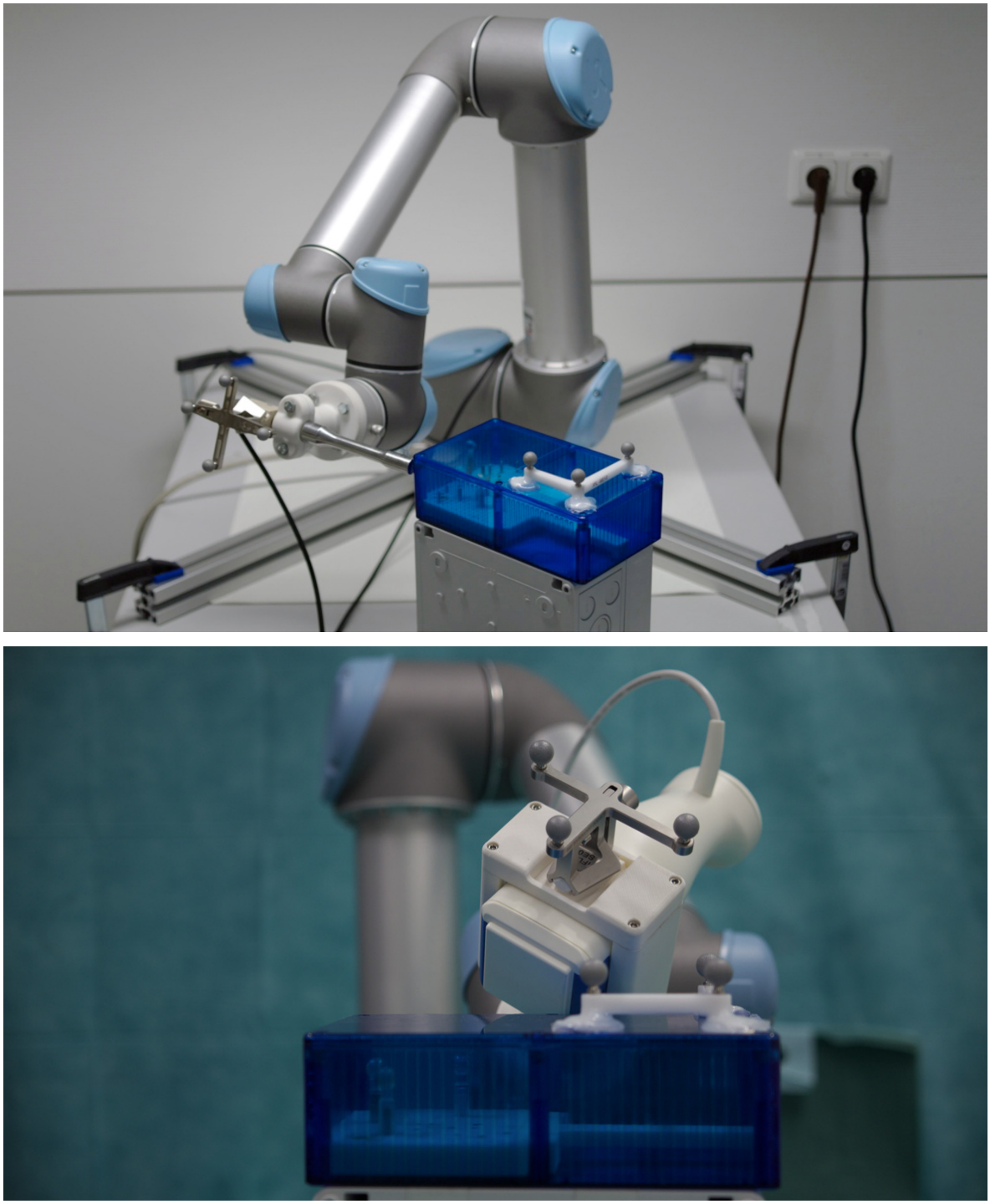

Figure 7.10.: Robotic SPECT prototypes with simple γ-radiation probe (top) and gamma-camera (bottom) mounted to the wrist of a robotic arm. For testing purposes, redundant optical tracking targets with silver-coloured retroreflective marker balls are also mounted onto the sensors. The blue box is a simple phantom containing radioactively marked spheres in a known pattern. *(Courtesy of José Gardiazabal.)*

sensor positioning in the work of Matthies *et al.* [Mat13; Mat14] which introduced the mini camera. (See fig. 7.10.) Likewise, Gardiazabal *et al.* [Gar14] used a robotic arm in a first proof-of-concept interventional SPECT-CT system where an rSPECT system and a C-arm CT were operated in a hybrid context. The only work towards real patient-specific robotic SPECT was published by the author of this thesis [Vog12; Vog13], but it only considers the specific sub-problem of picking optimal sensor poses and assumes perfect robot control. (See chapter 8 for a full discussion.)

There is yet another aspect about robotic SPECT: As mentioned in section 7.2.2, mechanical tracking could also be used to obtain the poses of the gamma camera. While requiring a mechanical connection to the camera, this tracking technique can yield highly accurate position information at very high sampling rates. Therefore, for clinical settings where human guidance is required for security reasons, a suitable robotic arm could be operated in *gravity compensation mode*, i.e. inactively self-supporting and easily yielding to external forces. A human user could thus move the camera without having to support its weight, and the system would record highly precise tracking information along the way using the results obtained by forward kinematics.

This chapter is partly based on co-authored publications, extended and revised where necessary.

8. Optimal Sensor Trajectories

Freehand and robotic SPECT both require closer consideration of the detector's trajectory. Unlike diagnostic SPECT where the path of the gamma cameras around the patient is defined by design, the trajectory in case of interventional SPECT is unknown in advance and defined only during the scan, as has been outlined in section 7.1.2. Still, the path must be chosen in a useful way, ideally leading to optimal data for tomographic reconstruction. To this avail, a human operator possibly needs to be instructed about the next poses to acquire, and a robotic system needs proper path planning anyway. In both cases, the core question is how to characterise the difference between a 'good' and a 'bad' trajectory.

8.1. Geometry in a System Matrix

Thinking in a goal-oriented way, the quality of a trajectory could be defined via the quality of the reconstructed image. Unfortunately, 'image quality' is hard to quantify [Her09, chap. 5.2], and it depends very much on the actual setting of what is being imaged for which purpose. Furthermore, it requires prior knowledge of some sort which may not be available. It is thus desirable to define the quality of an acquisition in geometrical terms only, decoupling it from the measurements.

A possible approach to do this would be to explicitly model the fields of view of the moving camera. By computing intersections, an estimate of the spatial and angular coverage could be obtained. Such a method would likely be laborious, and it would totally ignore the fact that the geometrical model has already been established for the core tomographic reconstruction problem.

Recalling the derivation of the least-squares approach in section 4.2.1, particularly eq. (4.17), it has been said that the respective linear system $\mathbf{m} \approx A\mathbf{c}$ partitions the problem into measurements $\mathbf{m}$, signal coefficients $\mathbf{c}$, and the system matrix A which contains exactly the geometrical interrelations between the two. Note that the system matrix abstracts away all the information that one would typically consider when discussing geometrical properties of a system such as basis functions, line integrals, etc. Also from a purely mathematical point of view, it is natural to look at matrix A. Solving the linear system effectively means the inversion of A (or A^TA), and one would typically consider properties such as A's *rank* or *condition* when dealing with questions about the numerical stability of the process.

The project was carried out in cooperation with Tobias Lasser in 2012 and 2013 [Vog12; Vog13].

In case of a diagnostic setup, system matrix A is defined by construction of the scanner. For an imaging system without pre-determined sensor trajectories, however, system matrix A can be thought of as being built up while measuring, potentially implicitly in a parameterised sense. Consequently, when generating a detector trajectory, it is a useful strategy to pick poses that make the linear system easier to invert in terms of a rank-like estimate.

Dealing with nuclear imaging, however, it has been said that the least-squares approach cannot be assumed, and that likelihood-based modelling is necessary. This was motivated by the fact that the measurements are considered as random variables, drawn from a Poisson distribution. (See section 4.3.1.) On the other hand, the expected measurement values as given in eq. (4.29) still obey the linear relation. Having decided to ignore the actually measured values and their randomness, it is thus entirely valid to transfer the idea to freehand and robotic SPECT: In order to compute a trajectory quality value, system matrix A and its rank-like estimates should be considered.

8.2. Evaluating Geometry with Energy Measures

Aiming at the simple comparison of different trajectories as encoded by their respective system matrices, one optimally obtains a scalar-valued energy estimate per candidate. Several such measures have been described.

8.2.1. Column Sums

Let $\widetilde{\mathbf{a}}_i = (a_{ji})$ denote the ith column vector of the system matrix A:

$$A = \begin{pmatrix} | & | & \\ \widetilde{\mathbf{a}}_1 & \widetilde{\mathbf{a}}_2 & \cdots \\ | & | & \end{pmatrix}$$

Each column vector $\widetilde{\mathbf{a}}_i$ then contains the impacts of all J measurements onto the coefficient c_i of basis function b_i. In particular, $\widetilde{\mathbf{a}}_i = \mathbf{0}$ implies that no measurement hit this basis function, and it will not be possible to compute a meaningful coefficient c_i at all. Vice versa, a high accumulated sum $h_i := \sum_j a_{ji}$ implies good coverage. For all basis functions, the individual sums can be collected into a coverage vector $\mathbf{h} = (h_i)$. Note that A has non-negative entries only.

The column sums are rather easy to compute as $\mathbf{h} = A^T\mathbf{1}$, and they can be updated incrementally while scanning. For this reason, commercial freehand SPECT systems[1] use the column sums as foundation for a user guidance scheme: The coverage vector contains a value per voxel, and a volume rendering can be computed. Presented as supportive augmented reality visualisation, the human operator will need to 'fill in' the region of interest using the

1. declipseSPECT, SurgicEye, Munich, Germany

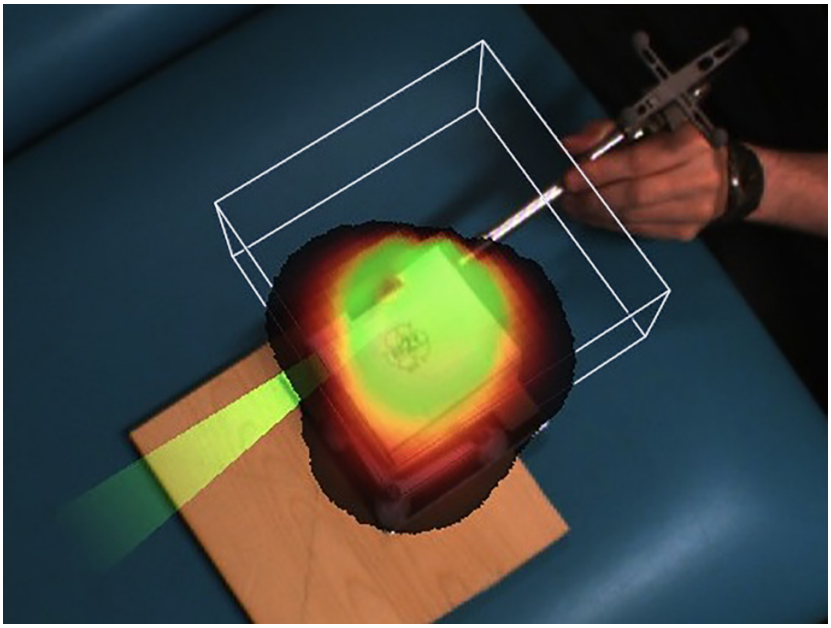

Figure 8.1.: The column sums of system matrix A lead to a vector of I components, with one value per basis function (voxel). Consequently, the column sums can be visualised in the region of interest (ROI) Ω. Freehand SPECT systems use this as foundation for an acquisition guidance system where the user is required to fill in the ROI in a kind of augmented reality drawing game. *(Courtesy of Tobias Lasser.)*

radiation detector. (See fig. 8.1.) While this visual guidance improves results significantly over no guidance [Wen10b], an experienced operator is still required for clinically useful reconstructions. The reason for this will become clear in the experiments. (See section 8.6.)

Based on the column sums, a scalar-valued energy measure can be defined via the ℓ_1-norm of the coverage vector $\mathbf{h}$:

$$\eta_C(A) := \|\mathbf{h}\|_1 = \sum_i h_i = \sum_{i,j} a_{ji} \tag{8.1}$$

Maximising η_C should thus yield a better measurement coverage of the region of interest Ω.

8.2.2. Null-Space Estimation

Assuming a null-space (kernel) vector $\widetilde{\mathbf{c}}$, that is $A\widetilde{\mathbf{c}} = \mathbf{0}$, and a vector $\mathbf{c}$ solving $A\mathbf{c} = \mathbf{m}$, an additional solution vector can be trivially generated: $A(\mathbf{c} + \widetilde{\mathbf{c}}) = \mathbf{m}$. This fact is well-known in mathematics where a matrix is defined to be invertible iff. its null-space contains the zero-vector only, thus eliminating the ambiguity. Consequently, a good trajectory will aim to reduce A's kernel to $\mathbf{0}$. (See Zeng *et al.* [Zen11] for an application with respect to SPECT.)

To estimate the null-space of A, k different approximate solutions $\widetilde{\mathbf{c}}_k$ to $A\widetilde{\mathbf{c}} = \mathbf{0}$ can be computed (using a few iterations of the conjugate gradients method, for instance) for random,

non-zero initial values. $\|\widetilde{\mathbf{c}}_k - \mathbf{0}\|_2$ should then be minimal in order for the kernel of A to be close to $\mathbf{0}$. Note that as randomised approach, the method may miss non-zero-kernel elements.

For trajectory optimisation, a scalar-valued energy measure can be defined via the maximal ℓ_2-norm of all such approximate solutions:

$$\eta_N(A) := -\max_k \|\widetilde{\mathbf{c}}_k\|_2 \tag{8.2}$$

This energy will be higher for measurement configurations with less ambiguity. However, each evaluation of this energy measure is relatively costly, as it involves solving several linear systems iteratively.

8.2.3. Singular Values

Assuming that system matrix A is explicitly known and small enough, it can be decomposed as

$$A = U \underbrace{\begin{pmatrix} \sigma_1 & & \\ & \sigma_2 & \\ & & \ddots \end{pmatrix}}_{=:\, D} V^T$$

using *singular value decomposition (SVD)*. The typical singular value spectrum of a system matrix will show some large values with low indices, and some very low values with high indices. (See fig. 8.2(a).) This shape is rather typical, and analysis of the singular value spectrum is a common tool for linear inverse problems. (See Lasser *et al.* [Las07] for optical tomography, for instance.) Even for badly conditioned matrices (caused by sub-optimal trajectories), however, there will not be a true rank deficiency, and no clear threshold to distinguish relevant from irrelevant singular values. Matrices with good condition, on the other hand, will show a very similar spectrum, only with a steeper slope.

Consequently, an energy measure needs to consider the entire spectrum, and

$$\eta_S(A) := \sum\nolimits_i \sigma_i = \|\mathrm{diag}(D)\|_1 \tag{8.3}$$

is a possible term [Vog12]. This energy value will yield higher values for better-conditioned system matrices, however, it is only useful for comparing matrices of the same size. As the number of columns equals the number of basis functions chosen (which is usually fixed beforehand), this constraint relates particularly to the number of rows; that is, the number of poses in a trajectory must be equal for the two matrices to compare.

Furthermore, computing the SVD of a large matrix is rather slow: The process consists of two steps, a transformation into bi-diagonal form using Householder transformations, followed by an *iterative* 'clean-up' to diagonal form [Gol65]. Considering the incremental nature of collecting data while moving the detector, updating the SVD after adding a single row or column to a matrix is an advantageous alternative over doing a full computation. This problem

has already been investigated in the fields of Data Mining, Latent Semantic Analysis, and also Computer Vision, and there are several approaches, depending on whether exact values are required or whether approximations suffice. Also, some applications use the dominant singular values only, and omit the smaller ones entirely.

Interested in the full spectrum, the incremental scheme suggested by Gu *et al.* [Gu94] and extended by Chetverikov *et al.* [Che10] can be used. Assuming knowledge of the current decomposition, $A = UDV_1^T$, an extended matrix A' can be preliminarily decomposed:

$$A' = \begin{pmatrix} A \\ \mathbf{a}^T \end{pmatrix} = \underbrace{\begin{pmatrix} U & \mathbf{0} \\ \mathbf{0}^T & 1 \end{pmatrix}}_{=:\, M} \underbrace{\begin{pmatrix} D & \mathbf{0} \\ \mathbf{z}^T & \zeta \end{pmatrix}}_{=:\, L} \underbrace{\begin{pmatrix} V_1^T \\ \mathbf{v}^T \end{pmatrix}}_{=:\, N^T} = \begin{pmatrix} UDV_1^T \\ \mathbf{z}^T V_1^T + \zeta \mathbf{v}^T \end{pmatrix} \tag{8.4}$$

Here, $\mathbf{z} = V_1^T \mathbf{a} \in \mathbb{R}^J$ is the projection of $\mathbf{a}$ into the subspace defined by the rows of V_1. The other unknowns, $\zeta \in \mathbb{R}$ and $\mathbf{v} \in \mathbb{R}^I$, can be solved from the equation $\mathbf{w} := \mathbf{a} - V_1 V_1^T \mathbf{a} = \zeta \mathbf{v}$ which is obtained from the last row of the decomposition of A'. If the additional vector $\mathbf{a}^T$ is linearly independent of the rows of A, $\mathbf{v}$ is orthogonal to all columns of V_1, as required. Computing the SVD of the inner – relatively small – square matrix $L \in \mathbb{R}^{(J+1)\times(J+1)}$ using standard methods yields the decomposition $L = \widetilde{U}\widetilde{D}\widetilde{V}^T$ with both, $\widetilde{U}, \widetilde{V} \in \mathrm{SO}(J+1)$ orthogonal matrices. Using this and the preliminary decomposition $A' = MLN^T$, the 'economy-sized' SVD of $A' = U'D'V_1'^T$ is given by $U' = M\widetilde{U}$, $D' = \widetilde{D}$, and $V' = N\widetilde{V}$.

For trajectory estimation, this algorithm needs to be extended in order to support the addition of linearly dependent rows [Vog12]. This situation appears to be uncommon in other settings where real-world measurements are used, but may appear when searching for additional sensor poses in a structured way. In this case, $\|\mathbf{w}\| \approx 0$ and $\zeta \approx 0$, as expected, but $\mathbf{v}$ is usually no longer orthogonal to all columns of V_1 – leading to errors in the following step $J{+}1 \to J{+}2$. This case must be detected, and $\mathbf{v}$ needs to be reinitialised by creating an orthogonal vector by means of applying the Gram-Schmidt orthogonalisation procedure to a random initial vector.

Note that these equations are valid for underdetermined systems only, as can be expected in the scenario of interventional functional imaging. Equivalent rules can be developed for overdetermined linear systems in a very similar way, but are omitted here for brevity. (See Gu *et al.* [Gu94] and Chetverikov *et al.* [Che10] for in-depth explanations and analyses.)

8.2.4. Pivoted QR

Though the most famous, the SVD is only one member out of the set of rank-revealing decompositions [Han98]. Another, considerably faster one is *pivoted QR decomposition*:

$$A = Q \underbrace{\begin{pmatrix} r_{11} & r_{12} & \cdots \\ & r_{22} & \cdots \\ & & \ddots \end{pmatrix}}_{=:\, R} P^T$$

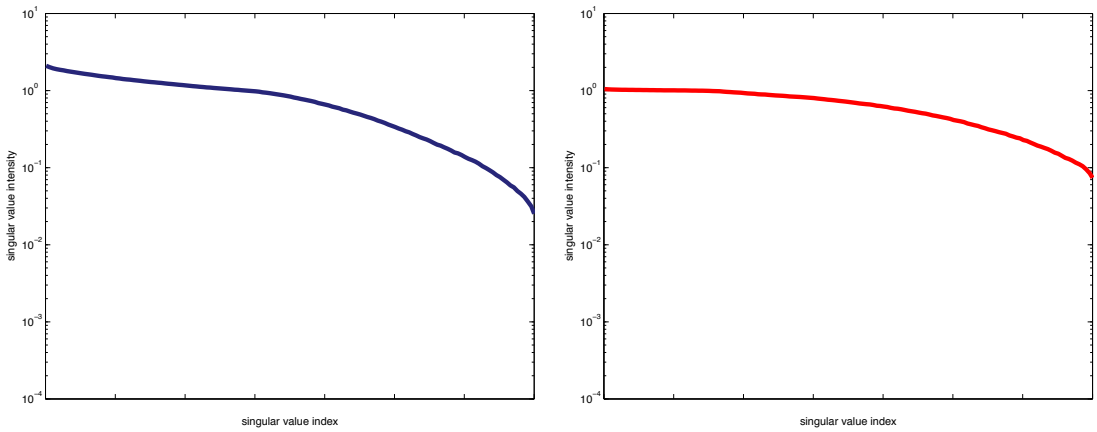

(a) SVD (b) Pivoted QR

Figure 8.2.: Two spectra of a sample system matrix: Original singular values σ_i (blue, left) as obtained via SVD, and pseudo-singular values $|r_{ii}|$ as obtained using Pivoted QR (red, right). Note the exponential scale of the vertical axis.

In this case, Q is orthogonal and P a permutation matrix (and thus also orthogonal). Not only is the structure of this decomposition very similar to the one of SVD, the spectra $\mathrm{diag}(D)$ and $|\mathrm{diag}(R)|$ are also correlated. (See fig. 8.2; a detailed mathematical description of this correlation is given by Fierro *et al.* [Fie95].)

The cost function can thus be adapted to

$$\eta_Q(A) := \sum\nolimits_i |r_{ii}| = \|\mathrm{diag}(R)\|_1 \tag{8.5}$$

and a very similar behaviour in comparison to the SVD-based measure η_S can be expected [Vog13]. (See fig. 8.3 for the energy evolution of random paths.) In contrast to SVD, however, the computation is non-iterative and thus *considerably* faster, also in comparison to the incremental scheme, and η_Q can replace η_S.

8.3. Trajectory Optimisation

Treating η_Q as efficient variant of η_S, effectively three energy measures have been described, allowing the comparison of trajectories. The column-sum- and kernel-based measures can be evaluated rather arbitrarily, but the spectrum-based measure requires matrices of the same size for meaningful results.

Usually, however, the scenario will not require to compare different given trajectories, but an optimal next destination needs to be computed. In case of robotic SPECT, this next pose can be sent to the robot's control system directly, and in case of freehand SPECT, the user could be instructed in a suitable way to move towards this location.

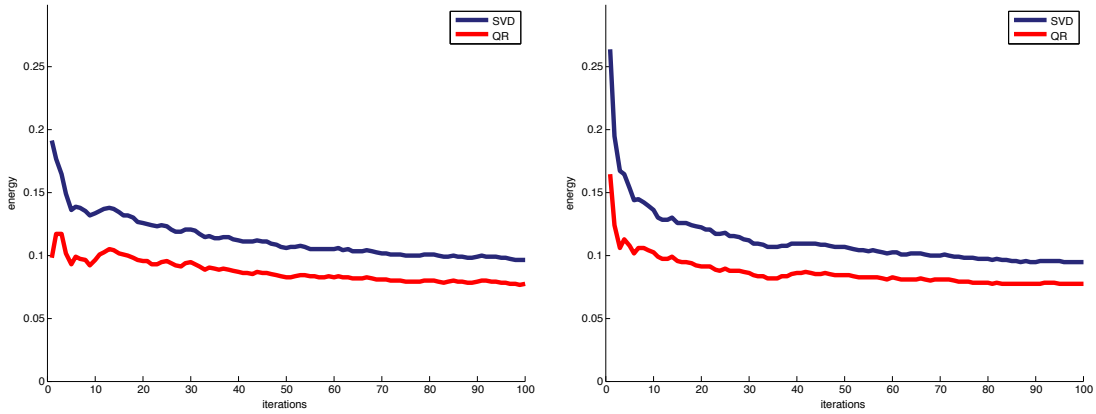

(a) Example 1 (b) Example 2

Figure 8.3.: Evolution of the SVD- (blue) and QR-based (red) energies η_S and η_Q for two random trajectories. The horizontal axis shows the number of measurements used for setting up the system matrix, that is the number of system matrix rows. The vertical axis denotes the energy value. From a certain, small number of poses onwards, the two curves behave very similarly and run almost in parallel.

For incremental real-time optimisation of the trajectory, the time required for the detector to move from a previous position to the current location $\mathbf{p}_j$ can be used for calculating the next best destination $\mathbf{p}_{j+1}$. (See fig. 8.4.) In more detail, a surface model $\mathcal{S}$ of the patient (stored as a triangle mesh) is used to describe the permissible region where the detector tip may be located. This model can be obtained interventionally, for instance by means of laser scanning, and it should include reachability limitations as posed by the particular operating room scenario. While the detector is on the way to location $\mathbf{p}_j \in \mathcal{S}$ corresponding to measurement j, the system matrix A_j containing the known measurement poses from $\mathbf{p}_1$ to $\mathbf{p}_j$ is computed. To find the next best destination $\mathbf{p}_{j+1}$ of the trajectory, candidate poses $\mathbf{p}_* \in \mathcal{S}$ on the surface model are evaluated by adding the corresponding system matrix row $\mathbf{a}_*$ to A_j and computing

$$\eta \begin{pmatrix} A_j \\ \mathbf{a}_* \end{pmatrix}$$

for one of the energy measures η. Repeating this for all triangles yields a 'measurement priority' distribution for the entire surface model. (See fig. 8.5.)

Note that the theoretically optimal extension $\mathbf{a}_*$ would be orthogonal to all previous rows. Unfortunately, the problem of finding such a most orthogonal sensor perspective is computationally not feasible, but it can be approximated well using random sampling [Str06]. Therefore, when sampling the mesh $\mathcal{S}$, each triangle of the bounding mesh is visited, and a candidate random pose $\mathbf{p}_*$ is generated within its boundary. The triangle yielding the optimal cost (that is, the highest priority for measurement) is stored, and the respective random pose

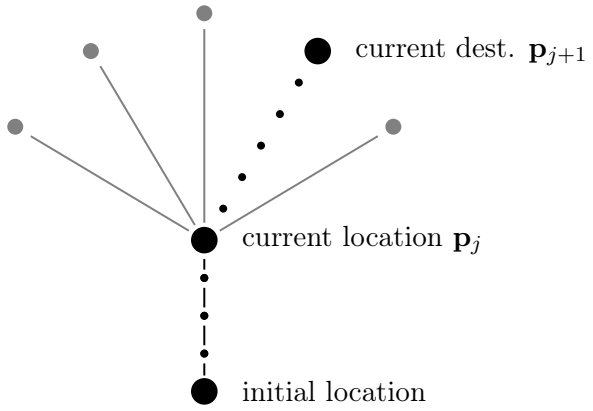

Figure 8.4.: Schematic sketch of the greedy approach: While moving from the initial to the current location, the optimization scheme tests several candidates (gray). As soon as a new destination must be picked, the best currently computed candidate is chosen. Ideally, the sampling of candidates is complete at that time, but using randomised testing allows early termination.

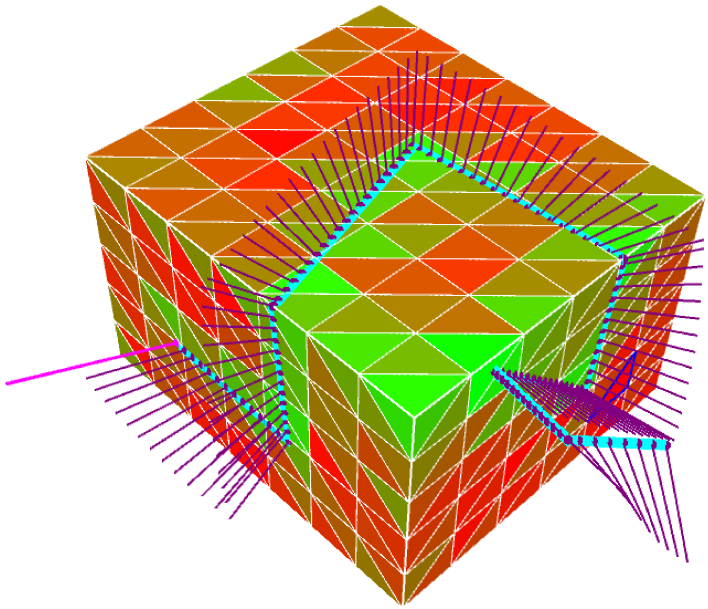

Figure 8.5.: Screenshot of the actual trajectory optimisation programme. The triangulated bounding box consists of regions where measurements could be collected (red and green). Red triangles denote planes that should be visited while sufficient measurements are already available for the green triangles; the colour is directly computed from the energy η. Note that the traversed path (cyan, with purple measurement poses) correlates to green triangles.

is taken as the next destination $\mathbf{p}_{j+1} := \mathbf{p}_*$. As soon as the detector has reached the current destination $\mathbf{p}_j$ and a sufficiently substantiated next destination $\mathbf{p}_{j+1}$ has been found, the per-triangle-costs and random poses are cleared, and the process starts again.

Apart from just optimising one of the cost functions η, it is also possible to impose additional constraints such as a certain minimal step length or reachability on the surface model $\mathcal{S}$ from $\mathbf{p}_j$. This is done by excluding poses violating one of these conditions from the optimisation process. Particularly the minimal step size is important, in order to leave enough time for planning the next step.

Note that this evaluation can be performed for several candidate poses in parallel, and it can thus be accelerated linearly by adding additional computing nodes. When visiting the triangles in a randomised order, one can also expect to obtain a significant distribution of the 'measurement priority' long before all triangles have been processed, and an early abort is possible, greedily choosing the best known candidate so far.

Also note that the paths between $\mathbf{p}_j$ and the random poses $\mathbf{p}_*$ are not considered while optimising. This is necessary for the spectrum-based energy measures, as they can only compare matrices of the same size. As soon as the next destination is fixed, however, measurements are acquired continuously while moving towards it.

8.4. Implementation Notes

Before dealing with actual results, note that the system matrix A is usually not known explicitly. (See section 4.2.1.) This fact does not present problems for the column-sum- and null-space-based measures, but it is prohibitive for the spectrum-based measures.

Even if the matrix fits into memory, the trajectory optimisation scheme requires quick computation of the energy measures. For this reason, instead of the real system matrix, it makes sense to always use a downsampled version of the original setup: The volume of interest should be discretised using considerably less voxels, all pixels of a camera should be fused into a virtual single-pixel detector with the same field of view, and the system matrix should be built up from a sparse version of the actual trajectory. The rationale behind this is that even though accuracy is lost, the general geometry will still be contained in the compressed matrix, and an optimal trajectory with respect to the compressed problem will lead to a good trajectory for the original system as well.

8.5. Experiments and Results

In order to test the proposed approach, the optimisation framework has been implemented on a 2.3 GHz Intel Core i7 quad-core portable computer with 8 GB of RAM using Boost threads for parallelisation. The candidate poses are computed using a downsampled voxel grid ($10 \times 10 \times 7$), the triangles are visited in random order, and early termination has been

used if time ran out and at least 15 % of the triangles had been evaluated. A minimal step length of 50 mm was enforced, and each position on the triangle mesh was supposed to be reachable from any other position.

The prototype implementation is thus able to generate positions in real-time for all measures (except η_N, see below), i.e. it can provide measurement poses often enough for the detector to keep moving until sufficient measurements have been acquired. (A typical computed trajectory in an early stage of the optimisation is shown in fig. 8.5).

The optimisation scheme was evaluated for all distinct energy measures η_C, η_N, η_Q in numerical simulations. Using the best energy measure η_Q, a first real experiment was also performed in a rSPECT setup where a robotic arm has been executing the optimised trajectory.

8.5.1. Trajectories

Several experiments have been performed to compare trajectories maximising the different measures. In all cases, three adjacent sides of a bounding box of size $120 \times 120 \times 87$ mm have been measured, thus simulating the limited perspectives available during a typical sentinel lymph node biopsy. The generated paths can be categorised as follows:

- *Spectrum trajectories* have been generated using the control scheme presented in this article, and attempt to optimise the QR-based measure η_Q. For the simulation experiments, such paths have been recorded to disk with a smooth interpolation between positions $\mathbf{p}_j$. (See fig. 8.6(a).)

- *Colum-sums and null-space trajectories* have been computed similarly, but instead optimising the column-sum measure η_C and the null-space measure η_N, respectively. During kernel estimation, 20 iterations of the conjugated gradients method have been run for every random initialisation.

- *Random trajectories* have been created by smoothly connecting random poses in random triangles. The same smooth interpolation as above has been used for connecting these poses. (See fig. 8.6(b).)

- *Human trajectories* have been recorded by a human expert operator in reality using an optical tracking system, and were later re-mapped to fit the surface model. The path has been enhanced further by moving the detector as close as possible to the surface model, and by using a smooth interpolation method to guarantee good coverage. This makes the human path directly comparable to the other trajectories. (See fig. 8.6(c).)

- *Grid or structured pattern trajectories* follow a simple regular motion pattern uniformly distributed on the surface, with the detector orthogonal to the bounding box. This seeks to simulate the motion pattern of inexperienced operators. (See fig. 8.6(d).)

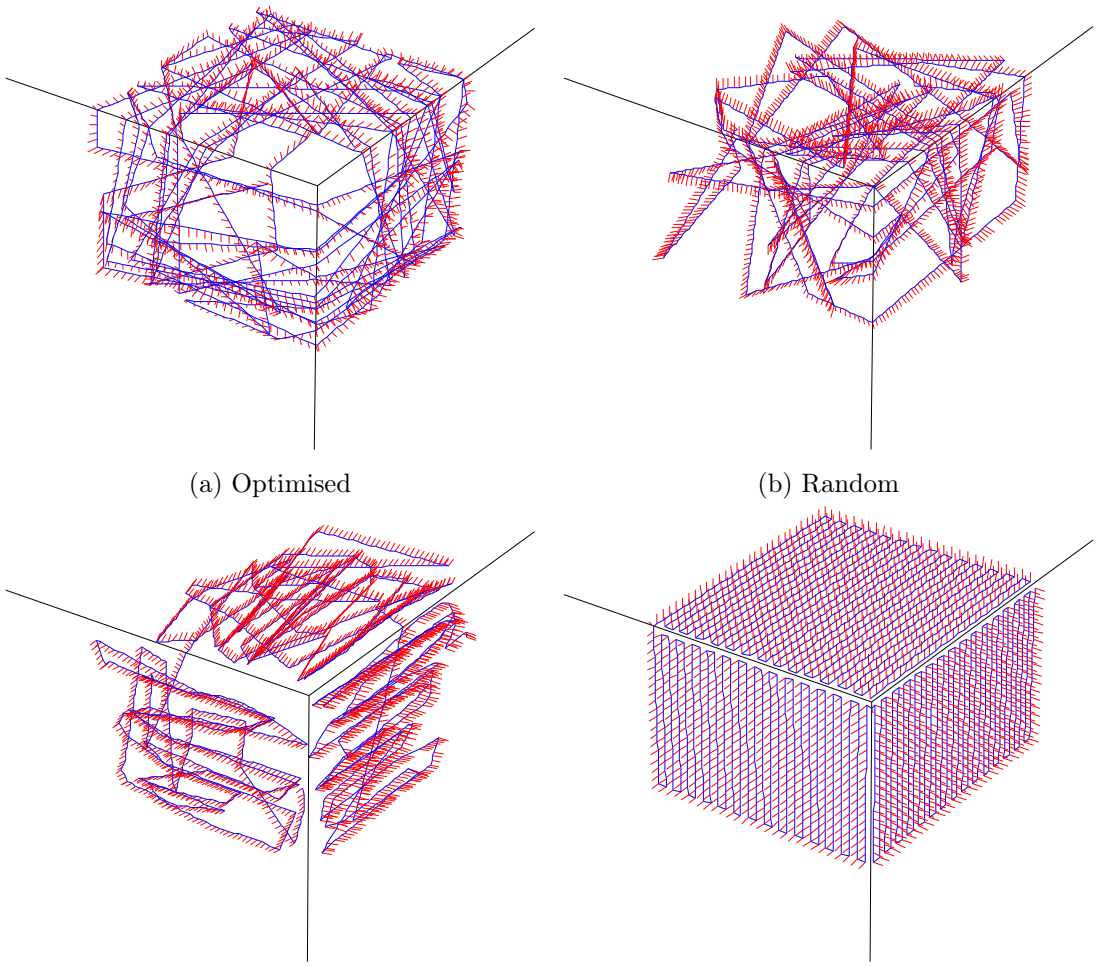

(a) Optimised (b) Random

(c) Human (d) Grid

Figure 8.6.: Sample trajectories (blue) with orientations (red). The black lines are the edges of the bounding box. The vertical axis is the z-axis, the horizontal plane is the x/y-plane. Note that the optimised path has few clusters and good coverage. At first glance, the grid path shares this property, but there are many complementary poses with only three viewing directions in total.

Each trajectory was generated to contain about 2000 measurements, corresponding to a clinically acceptable scanning time of 3–5 minutes. For the optimised and random trajectories, 10 randomised trajectories were generated per class, and the mean behaviour with standard deviations is considered in plots and when giving numbers.

8.5.2. Evolution of Optimised Energy

First, assume for the moment that the rank-motivated energy measure η_Q really prefers better-posed reconstruction problems and that such linear systems yield better reconstructions. Hence, it was checked whether the optimisation scheme really results in better numerical condition of the system matrix, and the evolution of energy values η_Q with increasing path length was compared for the sample trajectories. (See fig. 8.7.)

The optimisation scheme using η_Q (called spectrum) indeed yields the largest condition estimates for the linear problems set up from the respective trajectories, as can be expected by design of the method. More importantly, the level of the spectrum-optimised energies, including standard deviation, is considerably higher than the level of the other approaches. Only the null-space based measure is also performing better than chance level, while the more structured (among them a human expert) and state-of-the-art methods (column sums) perform below the random trajectories.

8.5.3. Numerical Simulations

Next, the assumption of better reconstruction results guaranteed by higher system matrix condition was checked using a simulated setting. Consequently, numerical phantoms showing different configurations of spherical activity hotspots were generated, and measurements were simulated using a mathematical forward acquisition model [Las07]. Neither was noise added, nor was it attempted to model nuclear statistics, in order to focus on purely trajectory-related influences on the convergence of the image reconstruction process.

Using such virtual acquisitions for the different settings, reconstructions were generated for increasing numbers of measurements, up to about 2000, thus simulating the incremental scan. The reconstructions were performed on a $71 \times 71 \times 50$ voxel grid (voxel size 1.4 mm^3), using 80 full iterations of ART with a relaxation factor of 0.1. The major difference to a real measurement – apart from nuclear statistics – is that data is only simulated at control points, and not continuously at a certain sampling rate while moving the detector.

In the resulting reconstructions, the centres of gravity of all reconstructed activity hotspots were compared with their respective ground truth locations. The centres of gravity were extracted from the reconstruction results by starting at the ground truth location and walking uphill towards a local intensity maximum. This identification method is justified as intra-operative nuclear reconstructions typically show rather simple structures with (almost convex) activity hotspots, where higher activity is usually reconstructed at the centres of the active

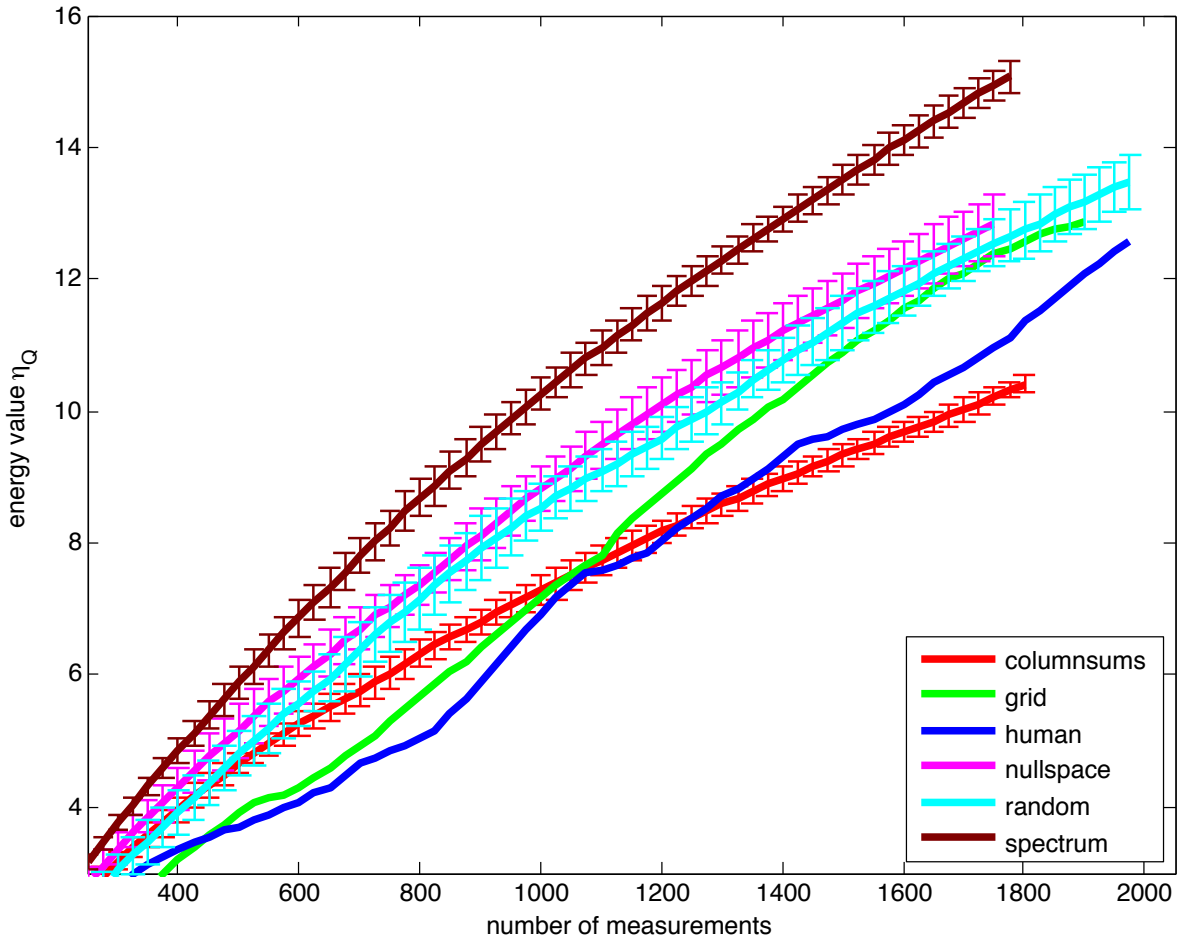

Figure 8.7.: Energies η_Q (vertical axis) over trajectory length (horizontal axis). Apart from the 'grid' and 'human' paths where only single typical examples are shown, 10 (randomised) examples have been computed per class, and the plot shows the mean curves with standard deviation. It is not surprising that more measurements (thus more system matrix rows) lead to larger energies, the decisive property is thus the growth of the curve and its relative magnitude. Here, the spectrum-based measure (maroon) clearly features fastest growth and highest value, thus yielding optimal condition for the linear problem solved during reconstruction. Only the null-space based measure (magenta) is also performing better than chance level (cyan), while the more structured (green and blue) and state-of-the-art methods (red) are inferior.

regions. In particular, this process is more robust than sphere matching or blob identification, as it does not depend on thresholding parameters.

Figure 8.8 shows the result of such an experiment with a particularly difficult configuration. There, two spherical activity hotspots with different radii (7 mm and 14 mm) have been simulated, located closely next to each other (21 mm separation). In this setting, only good trajectories yield a result where the two hotspots are distinguishable. In fact, for the column-sum-based trajectories as well as the human and grid trajectories, a separation of the hotspots was not possible. Conversely, starting at around 1000 measurements, the spectrum and null-space based as well as the random trajectories allow separation of the hotspots. The lowest mean error with lowest variance is shown by the spectrum-based method.

8.5.4. Actual Measurements

To confirm the simulation results, a first real experiment using a rSPECT setup was performed using a phantom with radioactive spheres and a robotic arm for detector movement.

A single-pixel gamma detector[2] is mounted to the wrist of an robotic arm.[3] (See fig. 8.9.) In addition to the coordinate frames obtained via forward kinematics, transformations provided by an optical tracking system[4] were used for calibration and localisation of the phantom.

The setup was used to image a box phantom containing three hollow spheres (diameter 9.86 mm) filled with a ^{99m}Tc solution with an activity of 1 MBq arranged in a triangular fashion, thus mimicking a sentinel lymph node case. (See fig. 8.10.) The trajectory optimisation software used a simple triangulated surface model of the box, accessible from three sides, and used the spectrum-based measure η_Q to generate 1665 measurement positions. The robot is fed with these measurement positions directly and moves to these poses based on inverse kinematics calculations using the triangulated surface model of the box for collision detection. The resulting data is reconstructed on a $120 \times 120 \times 60$ voxel grid (voxel size 1.25 mm^3) using 60 ML-EM iterations.

A central slice of the three-dimensional reconstruction is shown in fig. 8.10. The locations of the three hotspots are recovered with reasonable accuracy, considering that the reconstruction problem is massively underdetermined (system matrix $A \in \mathbb{R}^{1{,}665 \times 864{,}000}$). A separation of the two closer hotspots (which are separated by 15 mm) was not possible.

8.6. Discussion

The singular value decomposition of the system matrix A is a common tool to study imaging geometries [Las07]. As the singular value decomposition is costly to compute, even with

2. Crystal Photonics, Berlin, Germany

3. UR5, Universal Robots, Odense, Denmark

4. Polaris Vicra, Northern Digital, Waterloo, Canada

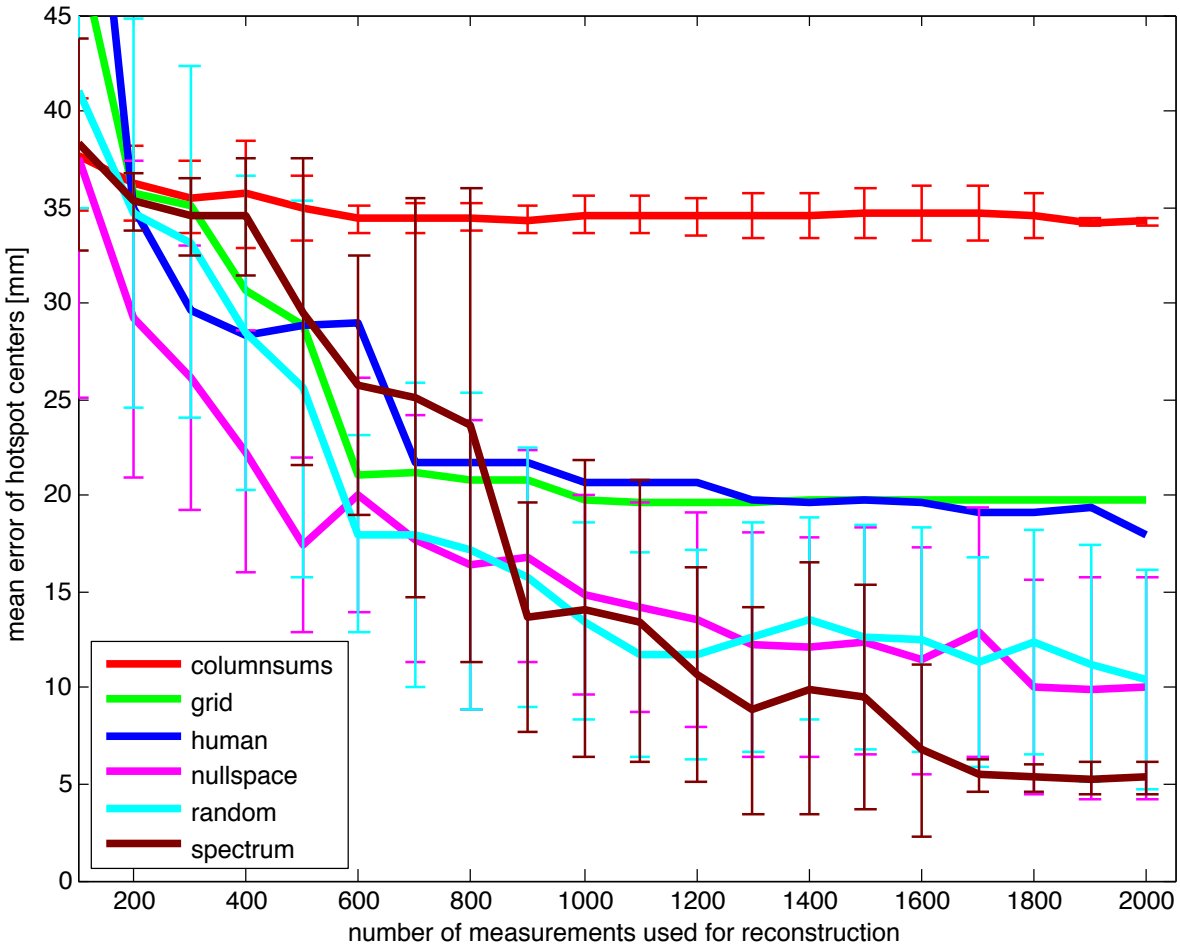

Figure 8.8.: Behaviour of error with increasing number of measurements. The vertical axis shows the mean error magnitude between the ground-truth and reconstructed centres of all activity hotspots in millimetres; the horizontal axis denotes the number of measurements being used for reconstruction. Apart from the 'grid' and 'human' paths where only single typical examples are shown, 10 (randomised) examples have been computed per class, and the graph shows the mean curves with standard deviation. Using several hundred measurements, all methods yield reconstruction results, however, the smallest error values (with small standard deviation) are obtained from the proposed spectrum-optimised paths (maroon).

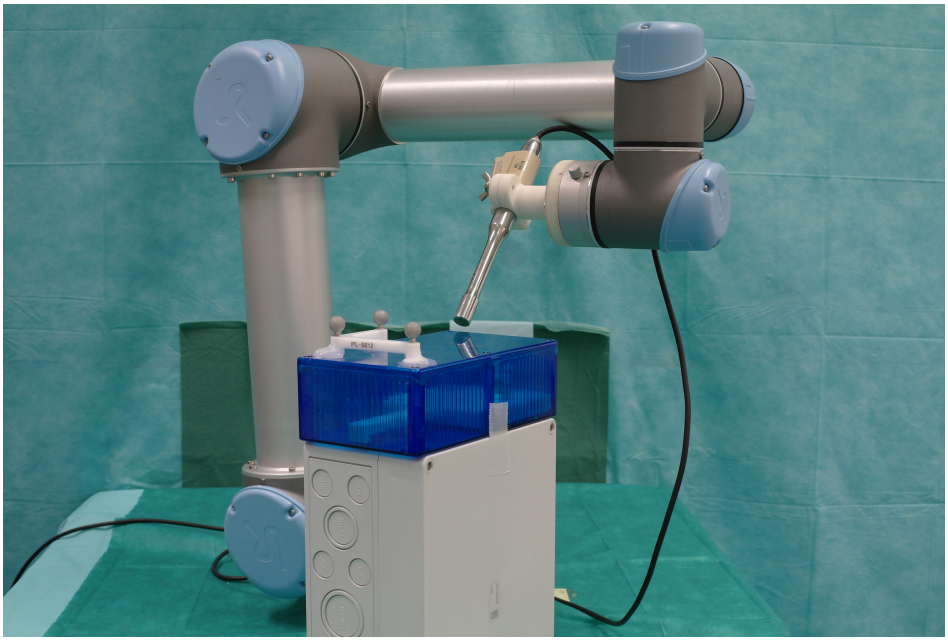

Figure 8.9.: Robotic arm with gamma detector attached to wrist. Also visible are a blue box phantom containing radioactive spheres, as well as retro-reflective marker spheres for the infrared tracking system.

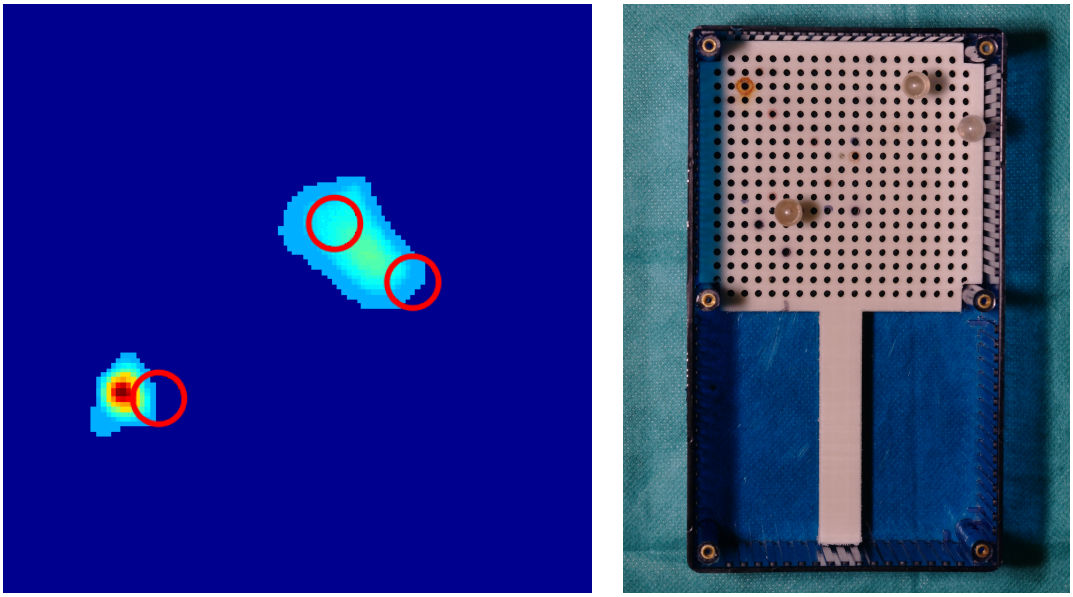

Figure 8.10.: Central slice (left) of the three-dimensional reconstruction of the radioactivity distribution in the box phantom containing three hollow spheres filled with a ^{99m}Tc solution (right). The ground truth positions of the spheres are marked by circles in red.

incremental computing schemes [Vog12], the fast, rank-revealing pivoted QR decomposition should be used instead [Vog13]. The diagonal entries of the R matrix are correlated with the singular values of A and hence also allow an evaluation of the imaging geometry. Based on this finding, the spectrum-based energy measure η_Q can be used to evaluate detector trajectories in a randomised optimisation scheme. This can also be done using other energy measures: a mathematically motivated null-space-based measure η_N, and a column-sum-based measure η_C. In order to judge the resulting trajectories, they can be compared to random trajectories as well as a structured, uniformly distributed grid trajectory and a trajectory from a human expert.

The column-sum-based trajectories allow for consistent results with low standard deviation in the 10 trial runs, but cannot improve results over a human expert or a structured grid trajectory, both of which show comparable performances. This can be explained by realising that high column-sum values can also be achieved by complementary poses instead of intersecting views: Assume a set of rows together covering every voxel exactly once:

$$\mathbf{a}_1^T = \begin{pmatrix} * & \mathbf{0} & \mathbf{0} \end{pmatrix} \tag{8.6}$$

$$\mathbf{a}_2^T = \begin{pmatrix} \mathbf{0} & * & \mathbf{0} \end{pmatrix} \tag{8.7}$$

$$\mathbf{a}_3^T = \begin{pmatrix} \mathbf{0} & \mathbf{0} & * \end{pmatrix} \tag{8.8}$$

Then, the column-sum measure can be maximised by repeating theses rows (and thus their respective sensor poses) over and over again, but the linear system will not contain more information. Instead, a rank problem will occur due to linear dependency:

$$\begin{pmatrix} * & \mathbf{0} & \mathbf{0} \\ \mathbf{0} & * & \mathbf{0} \\ * & \mathbf{0} & \mathbf{0} \\ \mathbf{0} & \mathbf{0} & * \\ \mathbf{0} & * & \mathbf{0} \end{pmatrix} = \begin{pmatrix} — & \mathbf{a}_1^T & — \\ — & \mathbf{a}_2^T & — \\ — & \mathbf{a}_1^T & — \\ — & \mathbf{a}_3^T & — \\ — & \mathbf{a}_2^T & — \end{pmatrix} \rightsquigarrow \begin{pmatrix} — & \mathbf{a}_1^T & — \\ — & \mathbf{a}_2^T & — \\ — & \mathbf{a}_3^T & — \\ — & \mathbf{0} & — \\ — & \mathbf{0} & — \end{pmatrix} \tag{8.9}$$

Obviously, ‘coverage’ in terms of column sums is to be understood as mere presence of some data, but required is ‘coverage’ in an angular sense, supporting perspectives from different directions. This leads to a worse performance in comparison to a human expert or grid trajectory which contain more intersecting views. This also fits in with clinical experience, where human experts typically acquire better images than operators relying purely on the column-sum guidance [Wen10b]. (See fig. 8.1.)

Random trajectories show high variation in reconstruction quality, but in average perform better than the human expert or the structured grid trajectory.

The null-space trajectories employ optimisation based on the system matrix condition via kernel estimation and show good results particularly in the region of up to 800 measurements. After that, their performance levels off, because of the computational complexity involved in

computing the energy measure: As the system matrix size grows, the optimisation algorithm is no longer able to visit most of the triangles and starts hitting the minimal triangle testing rate of 15 %. In fact, the average triangle sampling rate of the null-space method is 20 % over all measurement poses on the testing hardware while the column-sum- and spectrum-based methods achieve 85 % on average. The null-space method actually even violates the real-time requirement occasionally, requiring extra time to sample at least the minimal rate of 15 % of all triangles.

Finally, the spectrum based trajectories show the best performance with very low deviations, particularly for higher measurement numbers of 1700 poses and onwards. This behaviour is perfectly acceptable, as clinical data sets typically feature 2000 to 3000 measurements, corresponding to scanning times of 3–5 minutes.

8.7. Summary

This chapter has presented a set of energy measures for evaluating the numerical condition of a system matrix. Based on them, the geometry of a tomographic setting can be evaluated, and an optimisation scheme was devised to compute detector trajectories. Consisting of a series of perspectives, the respective poses can be automatically executed by a robotic arm. The feasibility of this approach was shown with a real phantom experiment, where a rSPECT setup with a robotic arm holding the detector executed the spectrum-based optimised trajectory.

Adding a robotic device to the surgical theatre is naturally a complex undertaking [Tay91]. Besides additional cost, taking up extra space and adding additional points of failure, various safety issues need to be taken care of. A simpler approach might be to instruct the human operator by projecting the computed trajectory positions directly onto the patient using a steerable laser pointer, or by using an augmented reality visualisation. While this still includes the human factor, and while it will yield less reproducible results, the incremental, real-time nature of the optimisation scheme will be able to adapt to any deviations caused by the human operator while following the computed trajectory.

The optimisation scheme requires a surface model of the patient to select the measurement poses. For the experiments presented here, the object to be scanned was a box phantom, allowing to use a simple triangulated bounding box. In a clinical setting, the bounding surface would have to be acquired for example from segmented pre-operative data or a depth model as obtained by a laser or an optical time-of-flight camera. It would even be possible to have the surgeon define a rough bounding box on-the-fly using a tracked pointing device directly on the patient, but this would give up the added detection sensitivity of having the detector as close to the surface as possible. Reachability constraints also have to be incorporated into this surface model.

While the optimisation scheme was inspired by fhSPECT, the approach only relies on principles and concepts used in general tomographic reconstruction, and is thus not limited to this

modality. Using different measurement models $\mathcal{M}_j$, the approach is also directly applicable to other tomographic modalities such as robotic C-arm CT. Used in an offline fashion, it would also be possible to optimise scanner designs.

The approach only takes into account the patient-specific surface model. It is also conceivable to add information from the actual detector measurements into the cost-function if necessary and justifiable. Note that such an approach adds the risk of adding bias into the reconstructions and potentially missing critical hotspots completely. Hence this extension would also require corresponding, registered pre-operative imaging data to ensure correct reconstructions.

Finally, among the articles published on robotic interventional SPECT so far, the work presented in this chapter needs to be considered as pioneer towards a mechanised patient-specific modality. (See section 7.3.) Still, it is a long way to go before the setup can be considered complete. In particular, the method relies on a sufficiently accurate surface model to be provided, and it only yields sensor poses, relying on the robot's control software to accurately follow the given trajectory in a secure way. Particularly the latter is a complex separate problem yet to be tackled.

This entire chapter is a combination of the original research papers [Vog12; Vog13], revised and partly extended.

Part IV.

X-ray Interferometry

9. X-ray Interferometry

Most applications of X-ray imaging limit themselves to attenuation, providing images with strong contrast between highly absorbing structures such as bones or artificially contrasted arteries, and lowly absorbing background such as tissue. From a physical point of view, however, more information can be acquired.

9.1. Imaging Concepts in Microscopy

Recalling that X-light and visible light are both forms of electromagnetic radiation at different energy levels, consider optical microscopy [Bra98] and its variants first: The direct equivalent to X-ray attenuation is 'ordinary' *bright-field microscopy* where a thin specimen is placed in a beam of light. The specimen attenuates the latter and then hits an imaging plane[1] where a transmission image can be seen showing *bright-field contrast*. (See figs. 9.1(a) and 9.2(a).) Using dyes, parts of the specimen can be coloured that would not be visible else; the same principle is employed in X-ray imaging when using radio-opaque contrast agents. (See Bardell [Bar04] for the early history of optical microscopy; the modality is popular since at least the 17^{th} century.)

A different approach is taken in *dark-field microscopy* (also *darkground microscopy*). Again, the specimen is placed in a beam of light, and while the light is attenuated as usual, some photons will be scattered away from the primary beam. If the imaging plane is set up in a way such that the main beam misses it, and only the scattered photons hit it, a *dark-field contrast* image will become visible relating effectively to the ability of the specimen to scatter light, rather than its ability to attenuate it. (See figs. 9.1(b) and 9.2(b).) This may make structures visible that are not or only barely visible in bright-field images. (See Gage [Gag20] for the history of dark-field microscopy; the modality was described already in the 17^{th} century, but it was particularly popularised after fundamental findings on microscopy by Abbe [Abb04] in the late 19^{th} century.)

The third variant is *phase-contrast microscopy* [Zer42b; Zer42a; Mar47] which exploits the wave-properties of light. The idea is that a specimen can not only attenuate the beam, it can also shift the phase of the light wave. In order to make this *phase contrast* image visible, the beam of light is effectively split up into a reference beam bypassing the specimen, and a

1. The imaging plane is to be understood in a theoretical sense. In reality, it will likely be the retina of a human eye, or photo-sensitive electronics in a digital camera.

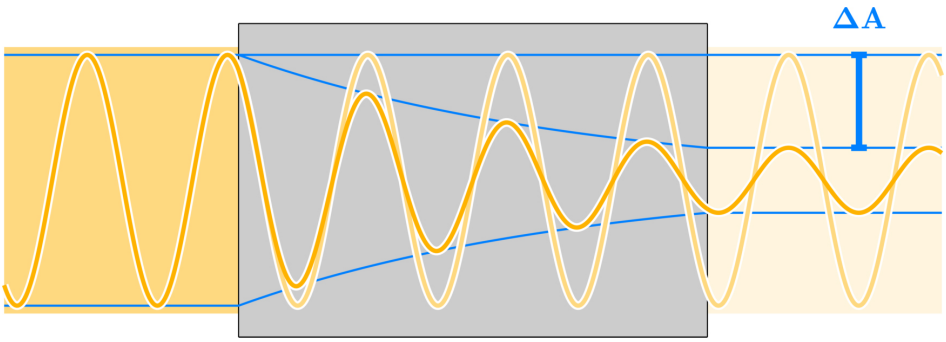

(a) Bright-field microscopy is based on the attenuation of a beam of light. Traveling through the object, the amplitude of the wave (dark yellow) is decreased following the Beer-Lambert law with respect to the reference wave (light yellow). Contrast depends on the presence of regions of different attenuation ability.

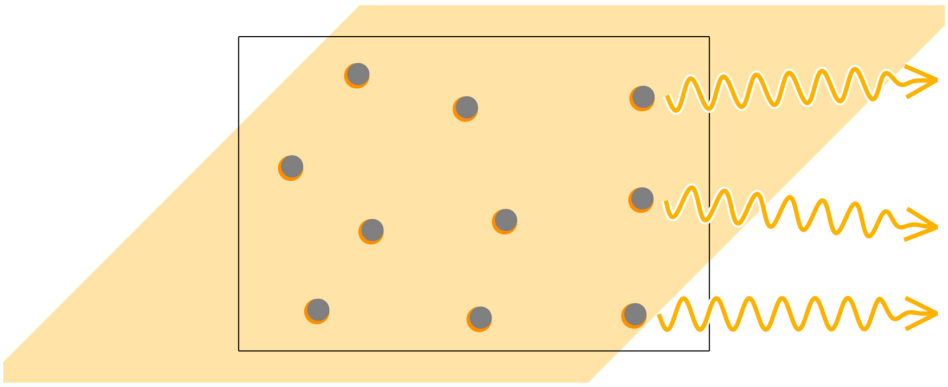

(b) Dark-field microscopy is based on photons scattered by structures in the object. The main beam of light misses the eye of the observer, leading to a black picture unless scattering structures are present which divert some of the photons into the direction of the viewer.

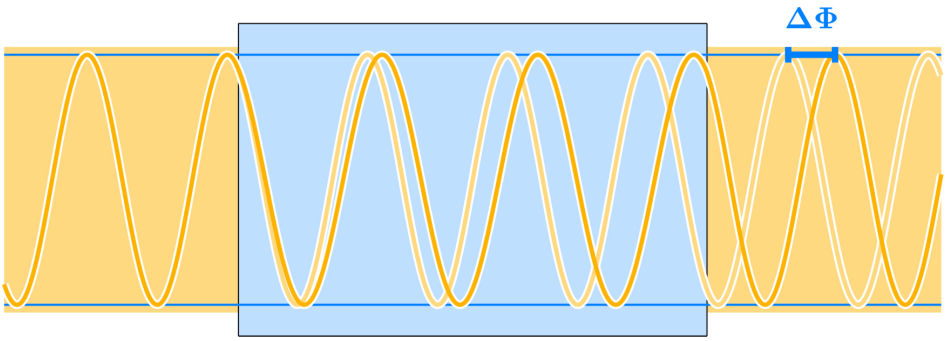

(c) Phase contrast microscopy is based on the fact that suitable transparent objects may still shift the phase of the light wave (dark yellow) with respect to the reference wave (light yellow), despite insufficient attenuation. Contrast depends on the presence of regions of different phase shifting ability.

Figure 9.1.: Microscopic imaging is based on different interaction effects between matter and a light wave, leading to different 'flavours' of image contrast: Bright-field (a), dark-field (b) and phase-contrast microscopy (c). In all cases, the observer is situated on the right-hand side.

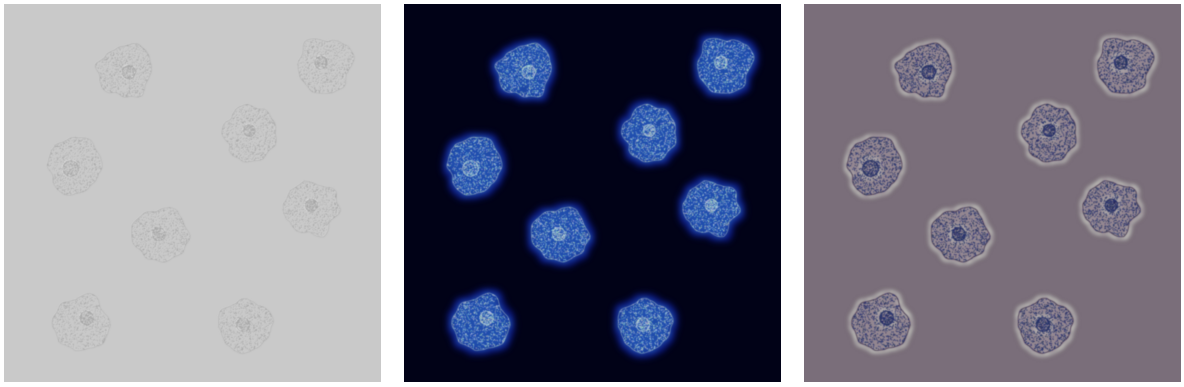

(a) Bright-field (b) Dark-field (c) Phase contrast

Figure 9.2.: Bright-field (a), dark-field (b) and phase-contrast (c) images of an unstained microscopic sample. *('Artistic' depictions based on original images of epithelial cells.*[2]*)*

scattered beam traversing it. Afterwards, the wave-shapes of the two beams can be related again to yield the phase shift. In microscopy, this is done optically by uniformly attenuating the reference beam and shifting its phase by $-90°$. Overlaying this modified reference beam with the scattered specimen beam leads to an interference image on the image plane which shows the phase contrast of the specimen. (See figs. 9.1(c) and 9.2(c).) This concept was developed by Frits Zernike [Zer35; Zer36] in the early 1930s, and he was awarded the 1953 Nobel prize in Physics [Zer53] for the discovery.

An intriguing aspect considering the different variants of microscopy is that each of them pictures a different physical property of the specimen, and they can be used complementarily. In particular, a transparent sample with minimal bright-field contrast may show considerable phase or dark-field contrast. The classical alternative technique to image a transparent sample is staining, that is the use of dyes to improve bright-field contrast by colouring. However, this approach is quite invasive and may kill the cells, thus rendering observation of living organism impossible. Complementary image signals may yield improved contrast right away, thus particularly enabling the observation of living cells. (Note that there are even more variants of microscopic contrast, like *differential interference contrast*.)

9.2. Phase Contrast and Dark-Field under X-light

Considering the advantages of the complementary imaging signals in microscopy, it would be highly beneficial to obtain the equivalent signals during clinical X-ray exams as well. Note

2. Unfortunately, it has not been possible to obtain real sample images licensed for publication, despite numerous attempts. Different universities, companies and other facilities have turned out to be unwilling or (technically or organisationally) unable to provide respective pictures. Due to the importance of the figure, sketches – though simplistic – appear to be justified.

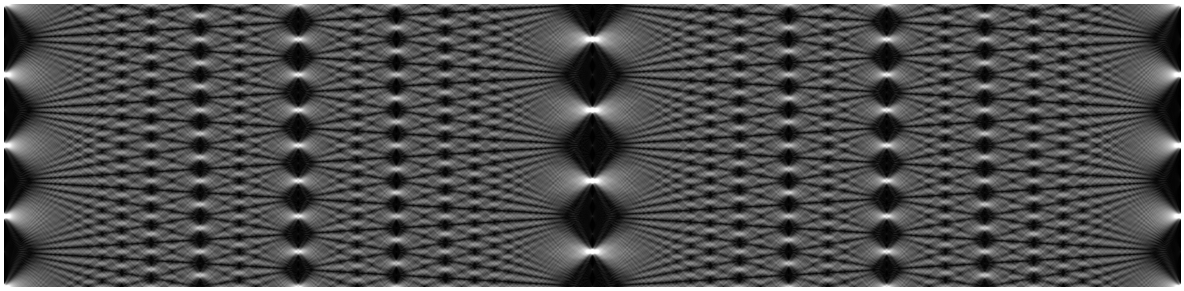

Figure 9.3.: Typical *Talbot carpet* for a simple grating. A planar wave-front is diffracted by a grating (left), leading to a characteristic interference pattern including an image of the grating.

in particular that some X-ray contrasting agents bear risks for patients with certain preconditions [Pas12; Rhe12], and it would be advantageous to have direct means of imaging body parts of low X-ray attenuation contrast, particularly soft tissue.

Unfortunately, it is not trivial to translate the concepts to X-ray imaging, particularly due to the ability of X-light to penetrate matter, and special lenses, gratings or crystals need to be used. A first crystal-based X-ray interferometer was presented by Bonse and Hart [Bon65a; Bon65b; Bon97] in 1965, and many more setups have been suggested since [Wei00b; Sta10; Cha97b; Dav96; Mia99; Thi08; Sni95; Clo99; Gro06]. For decades, these techniques were limited to research facilities as they require highly coherent (quasi-monochromatic) X-ray illumination only provided by a synchrotron or an equivalent source.[3]

Only some few years ago, Weitkamp *et al.* [Wei05] and Pfeiffer *et al.* [Pfe06] have demonstrated a novel setup for X-ray interferometry compatible with X-ray tubes, thus taking a decisive step towards clinical application. An 'ordinary' setup of X-ray tube, specimen and detector has been extended by inserting a *source grating* (G_0) directly after the tube, making the illumination sufficiently coherent, a *phase grating* (G_1) between G_0 and the specimen, and an *analyser grating* (G_2) directly in front of the detector. The latter two gratings (G_1, G_2) form an *interferometer*. (See figs. 9.4 and 9.5.)

This setup uses two well-known physical effects: The interferometer (G_1, G_2) exploits the *Talbot effect* according to which an image of a grating is repeated at a certain well-defined distance, the so-called *Talbot length*, when exposed to a quasi-monochromatic beam of light. (See fig. 9.3.) Named after Henry Fox Talbot who first described it in 1836 [Tal36], a physical and mathematical description is due to John William Strutt (Lord Rayleigh), published in 1881 [Str81]. When a second grating (G_2, analyser) of matching period is positioned at Talbot distance from the first grating (G_1, phase), and if an object distorts the wave-front in-between, extended information about the object can be obtained by observing the changing interference

3. Recently, Compact Light Sources (CLS) have attracted attention as coherent X-light source, compatible with the requirements of smaller facilities [Bec09b; Egg15]. A CLS is effectively a miniaturised synchrotron where the electron beam collides with a laser ray, thus creating quasi-monochromatic X-radiation. (See section 2.1.1, p. 15, for synchrotron radiation.)

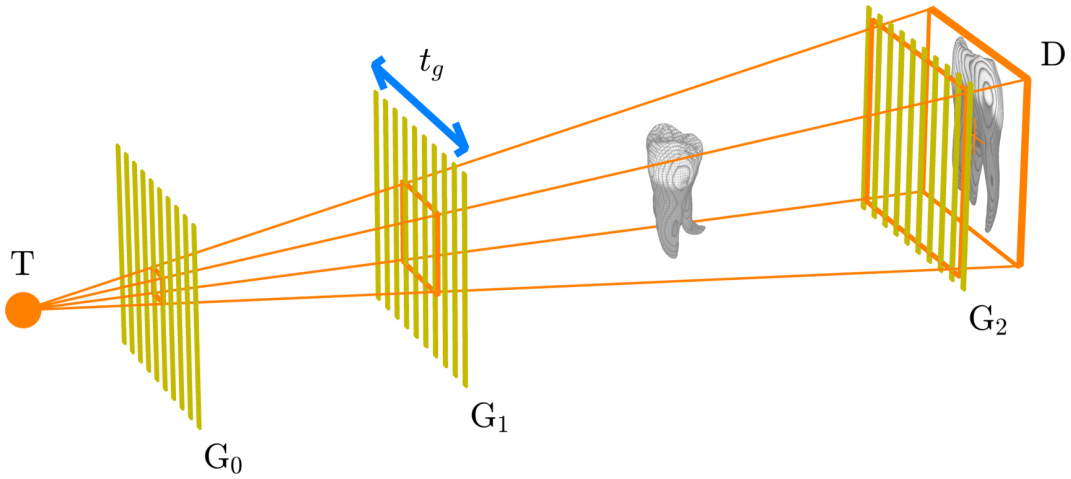

Figure 9.4.: Sketch of an X-ray grating interferometry setup. X-ray tube (T), source grating (G_0), shifting phase grating (G_1), specimen (a tooth in this sketch), static analyser grating (G_2), and detector (D).

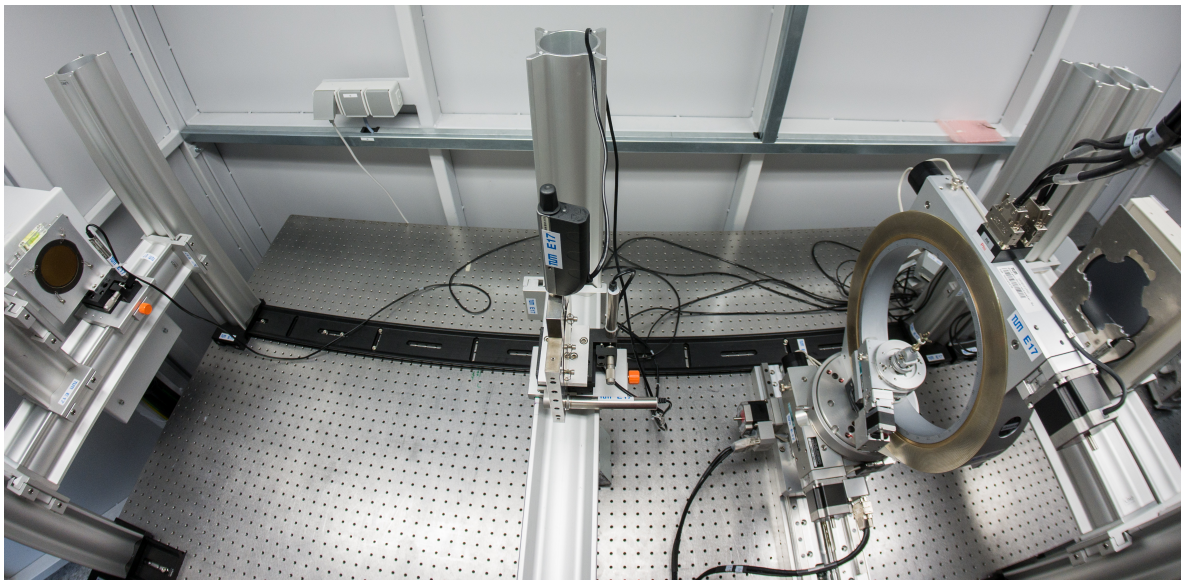

Figure 9.5.: Wide-angle view of the actual setup. From left to right: X-ray source (T) with source grating (G_0) directly in front of it, at the center the phase grating (G_1), then a Eulerian cradle with sample (S), and adjacent to it the analyser grating (G_2, in the cross-shaped holder); behind the latter the X-ray detector (D, hidden). *(Courtesy of Christoph Jud.)*

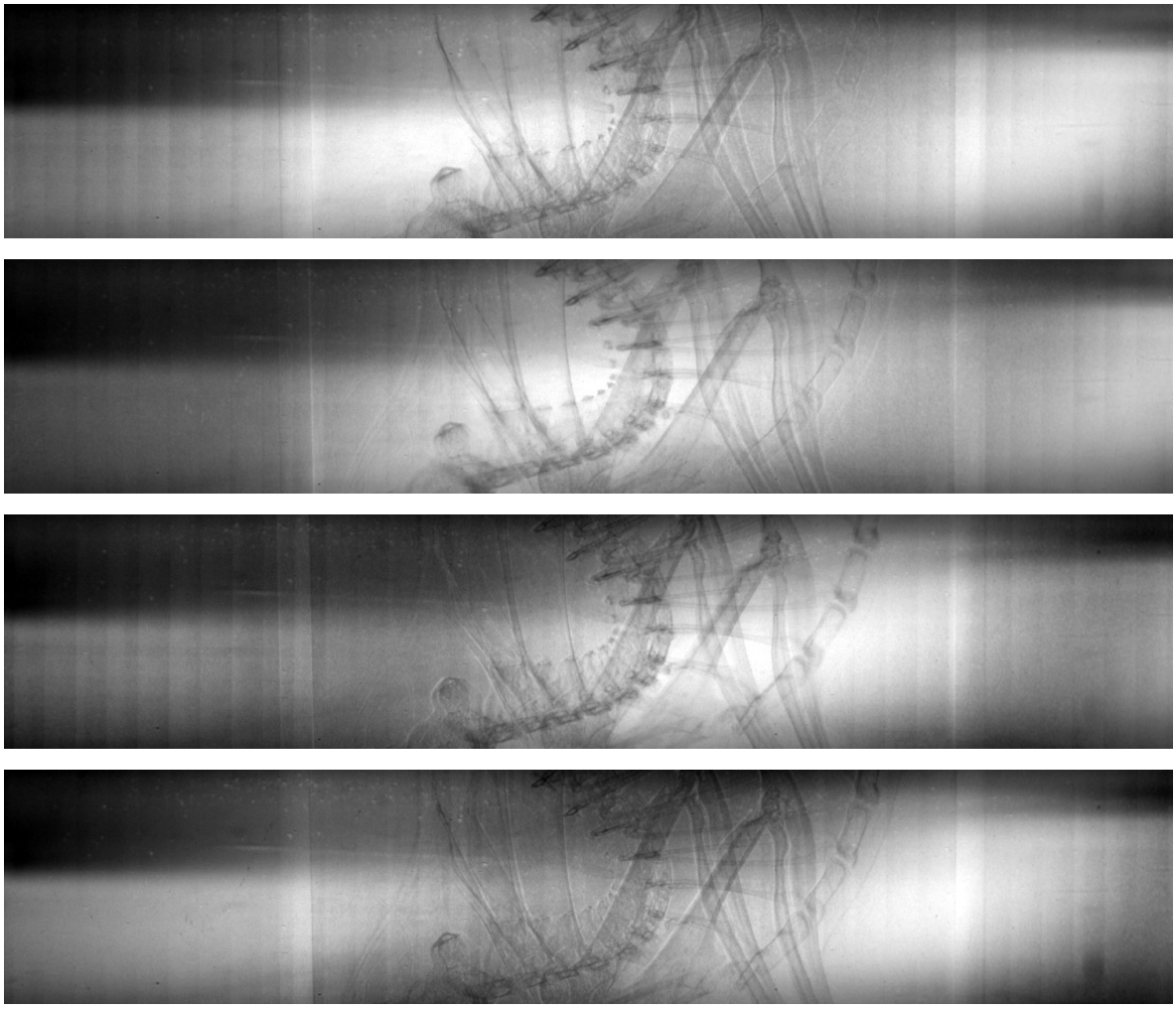

Figure 9.6.: Raw X-ray images of a mouse as obtained in a grating interferometry setup. The situation is static, but one of the gratings is shifted sideways, leading to different interference patterns. The contrast of these images has been manually improved for better visibility. *(Courtesy of Guillaume Potdevin.)*

patterns (caused by G_1's image and G_2) when one of the gratings is slightly moved sideways. This includes the object's phase shifting and scattering ability, leading to the desired image signals. Using a quasi-monochromatic X-light source such as a synchrotron, this setup can be operated directly, leading to *Talbot interferometry*.

For a polychromatic source such as an X-ray tube, the radiation must be made coherent (quasi-monochromatic) by means of the additional source grating G_0. This effect was discovered by Ernst Lau and published in 1948 [Lau48]. Again, the period of G_0 and its distance to the interferometer needs to be chosen correctly for the setup to work. The entire tube-based setup is typically referred to as *Talbot-Lau interferometer*.

In order to finally obtain the three image signals already known from microscopy for a given

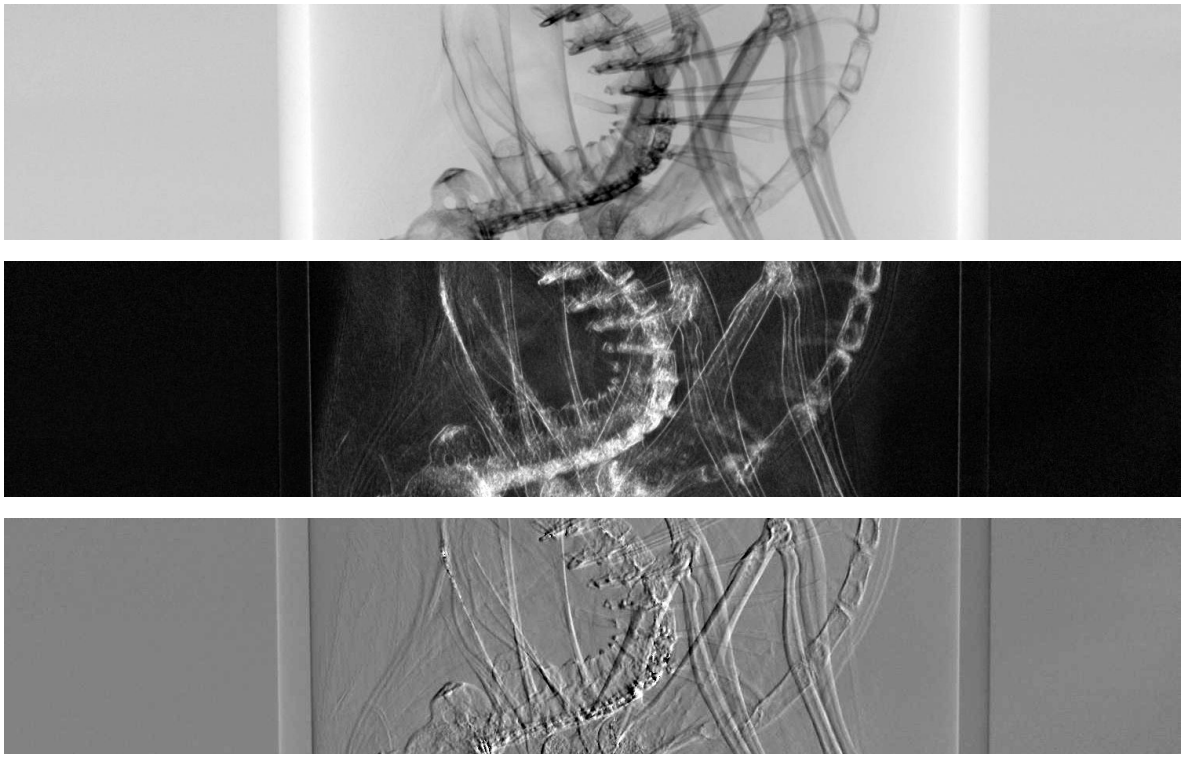

Figure 9.7.: X-ray *transmission*, *dark-field* and *differential phase contrast* image signals extracted from the raw measurements of a mouse shown in fig. 9.6. The contrast of these images has been manually improved for better visibility. *(Courtesy of Guillaume Potdevin.)*

specimen, multiple raw images are thus acquired while one of the interferometry gratings, usually G_1, is shifted sideways. As described above, the raw images will show the same situation with different interference patterns overlaid. (See fig. 9.6.) Consequently, the radiation intensity at a single static location, like a certain pixel of the detector, will change due to these patterns, and it will follow a sine-wave doing so. Comparing this wave to a reference curve at the same location without a specimen, computed from so-called *flat-field* images, yields a specific X-ray *transmission* value as usual, a *differential phase contrast* value describing the phase shift and a *dark-field* or *small angle scattering (SAXS)* component describing X-ray scattering [Pfe08]. Repeating this process for all pixels yields respective images. (See fig. 9.7.)

In more detail, considering a single static pixel $\mathbf{p}$, the two sine-shaped curves first need to be fit to the different raw intensities as obtained from the flat-field measurements and actual images showing the object. This yields a reference curve $I^r_{\mathbf{p}}(t_g)$ from the flat-field signal without the specimen, and a measurement curve $I^s_{\mathbf{p}}(t_g)$. The parameter t_g denotes the shift of the moving grating from its origin, and both interference curves use the same model [Bec10]:

$$I_{\mathbf{p}}(t_g) \approx a_0(\mathbf{p}) + a_1(\mathbf{p}) \cos\left(\frac{2\pi\ t_g}{d_2} + \phi_1(\mathbf{p})\right) \tag{9.1}$$

Consequently, each of the curves is parameterised using three magnitudes, a mean value a_0, an

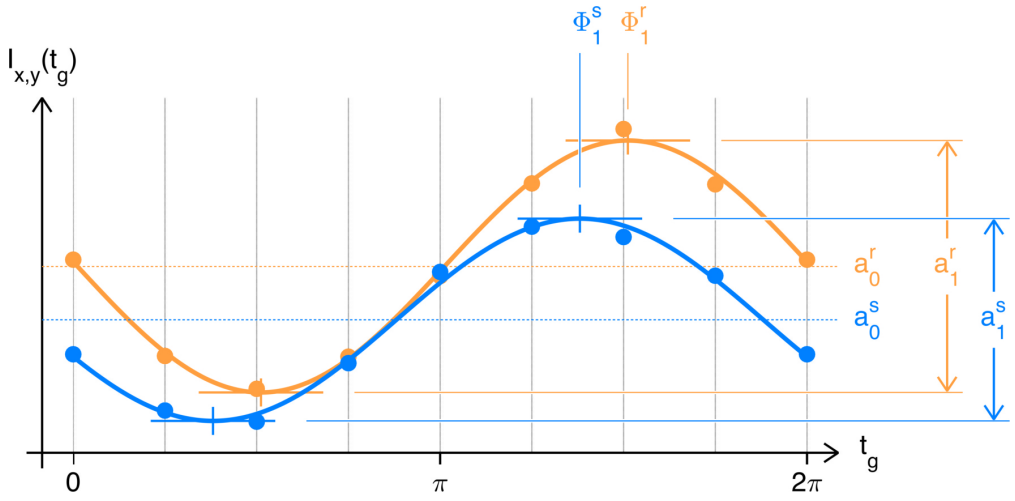

Figure 9.8.: Considering a single pixel, the fitted cosine-curve obtained from the actual measurement (blue) may differ in three aspects from the reference curve (orange) as obtained from the flat-field measurement: First, the mean value a_0 may have decreased, indicating less transmission (higher absorption). Second, the amplitude a_1 may have decreased, indicating scattering. Finally, the curves may be phase-shifted $\phi_1^r \rightsquigarrow \phi_1^s$.

amplitude a_1, and a phase shift ϕ_1. (d_2 is a setup-specific constant, see Bech *et al.* [Bec10].) Comparing the measurement interference curve with the flat-field curve, three changes may have been caused by the specimen: The mean value may have decreased, indicating less X-ray transmission, the amplitude may be smaller, indicating X-ray scattering, and phase-shift may occur. (See figs. 9.8 and 9.9.) Consequently, the transmission for pixel $\mathbf{p}$ can be defined as

$$T(\mathbf{p}) = \frac{a_0^s(\mathbf{p})}{a_0^r(\mathbf{p})}, \tag{9.2}$$

the respective scattering value as

$$V(\mathbf{p}) = \frac{a_1^s(\mathbf{p})}{a_0^s(\mathbf{p})} \frac{a_0^r(\mathbf{p})}{a_1^r(\mathbf{p})}, \tag{9.3}$$

and finally the differential phase contrast value as

$$\nabla_x \phi(\mathbf{p}) = \frac{d_2}{\lambda d} \left(\phi_1^s(\mathbf{p}) - \phi_1^r(\mathbf{p})\right). \tag{9.4}$$

(λ and d denote further setup-specific constants, see Bech *et al.* [Bec10].)

Based on this method, the different image signals can be obtained in a rather simple setup, compared to a synchrotron. Note, however, that several issues still need to be solved before clinical imaging of living patients is possible: First of all, the gratings are rather small, thus requiring small samples. Second, due to the stepping procedure and the additional attenuation caused by the analyser grating between specimen and detector, the radiation exposure at the sample is considerably higher than in a comparable 'ordinary' setup without gratings.

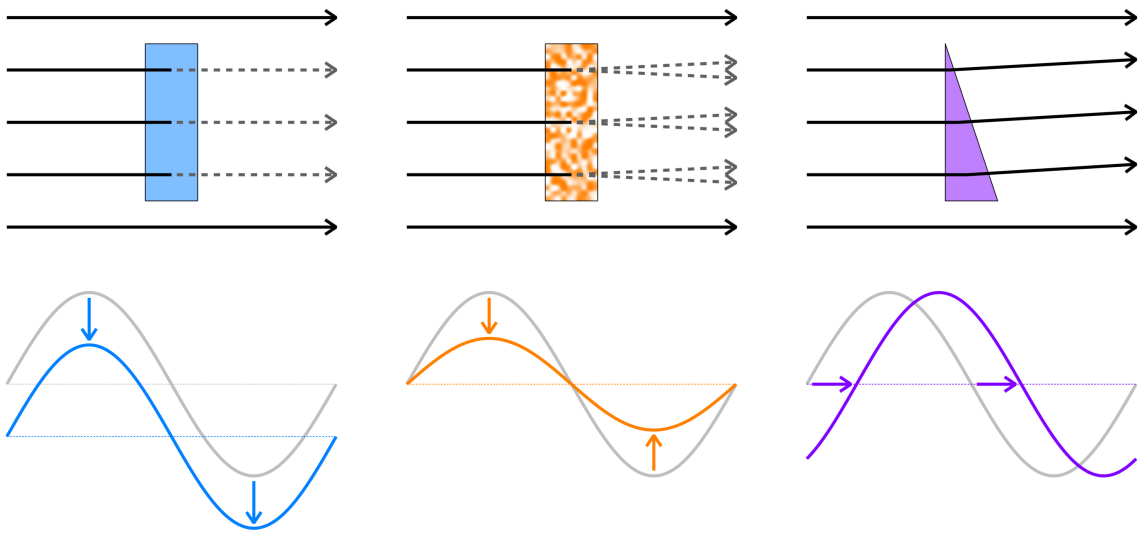

(a) Attenuation (b) Dark-field (c) Differential phase contrast

Figure 9.9.: X-ray attenuation leads to a reduced mean of the interference curve (a), X-ray scattering to a smaller amplitude (b), and a phase shift of the X-ray wave maps directly into a phase shift of the interference curve (c). *(Inspired by Andreas Malecki.)*

9.3. Tomographic Imaging

An obvious extension of X-ray interferometry leads to tomographic imaging. In order to do this, the stepping procedure as described above needs to be done for every relevant perspective. Of course, the transmission signal can be reconstructed as usual, after conversion into line integrals by application of the negative logarithm. (See fig. 9.10(a).)

9.3.1. Phase Contrast

For phase contrast, it must be considered that the signal is differential with respect to the stepping direction of the phase grating. Consequently, the forward model for the signal requires a differentiation operator. Defining a phase shift map $\mu_\mathrm{P}(\mathbf{x})$ (equivalent to the attenuation map $\mu(\mathbf{x})$ used in 'classical' CT), the forward model [Bec09a, chap. 3.2.2] is again based on a line integral:

$$p_j = -\frac{\partial}{\partial \hat{\mathbf{t}}_j} \int_{L_j} \mu_\mathrm{P}(\mathbf{x}) \, \mathrm{d}\mathbf{x} \tag{9.5}$$

Here, p_j denotes the jth differential phase contrast measurement, L_j the line of the respective ray, and $\hat{\mathbf{t}}_j \in \mathbb{R}^3$ is the normalised sensitivity direction, orthogonal to the grating lines and parallel to the surfaces of the – mutually parallel – gratings. In order to reconstruct images, several options exist. First, the phase contrast images can be numerically integrated and reconstructed as normal line-integral data. Second, filtered back-projection can be modified to use a special filter for integration in Fourier space [Bec09a, chap. 3.2.2]. Finally, a least-

squares-problem can be defined that includes an additional differentiation operator D:

$$\mathbf{p} = D\ A\ \mathbf{c} \tag{9.6}$$

Here, $\mathbf{p} = (p_j)$ denotes the vector containing all differential phase contrast measurements, and A is the usual system matrix as used for the transmission signal. Note that in this case, the coefficients relate to an approximated phase-shifting signal μ_P, of course.

As expected, a tomographic reconstruction of the phase contrast shows improved soft-tissue contrast [McD09]. (See fig. 9.10(c).) For this reason, tomographic phase-contrast reconstructions have become quite popular since the first demonstrations [Mom95; Mom96; Pfe07b; Pfe07a; Bec09c; Don10], and they continue to be an active field of research.[4] Examples with promising results are mammography [Sta11; Wil14], particularly the non-invasive discrimination of malign and benign tumours [Wan14] based on micro-calcifications, and ex-vivo imaging of plaques caused by Alzheimer's disease [Pin12]. Note, however, that there is still a largely unsolved problem, the issue of *phase wrapping* [Hah13]: Whenever the phase signal exceeds 2π, the value will be wrapped back into $[0, 2\pi)$. This happens at spots with high phase contrast, for instance bones. At these locations, a value too low will be used for reconstruction, leading to streak artefacts. (See fig. 9.10(c).)

9.3.2. Dark-Field

Considering the dark-field signal, a straight-forward tomographic reconstruction yields a volumetric representation of the respective X-ray scattering magnitudes. An appropriate forward model resembling the Beer-Lambert law as given in eqs. (2.1) and (3.1), respectively, is [Bec09a]:

$$d_j = \exp\left[-\int_{L_j} \mu_\mathrm{D}(\mathbf{x})\ \mathrm{d}\mathbf{x}\right] \tag{9.7}$$

Here, d_j denotes the jth dark-field measurement, L_j the line of the respective ray, and $\mu_\mathrm{D}(\mathbf{x})$ the scattering distribution over the volume of interest. After applying the negative logarithm, the signal can thus be reconstructed as usual. (See fig. 9.10(b).)

The tomographic dark-field reconstructions of this kind can be of practical value when isotropic scattering is of interest. Previous studies have shown its potential for lung and breast imaging [Yar13; And05; Sid11], micro-bubble contrast agents [Arf10] and material

4. While there are fierce proponents of grating interferometry (GI) for medical X-ray imaging, others have expressed considerable doubt about the technique and whether it will have any impact on clinical practice. For instance, Raupach *et al.* [Rau11; Rau12] – representing a major manufacturer of clinical scanners holding respective patents [Bau06; Hem08, among others] – conclude from theoretical studies that GI outperforms 'normal' attenuation CT only for very small voxel sizes. At the same time, due to different noise characteristics, they claim that the radiation dose required in that case is prohibitively large. Based on that relation, they compute a break-even point where GI becomes useful and conclude that only some few mammography applications may benefit at all. In particular, they rule out GI for whole-body-imaging.

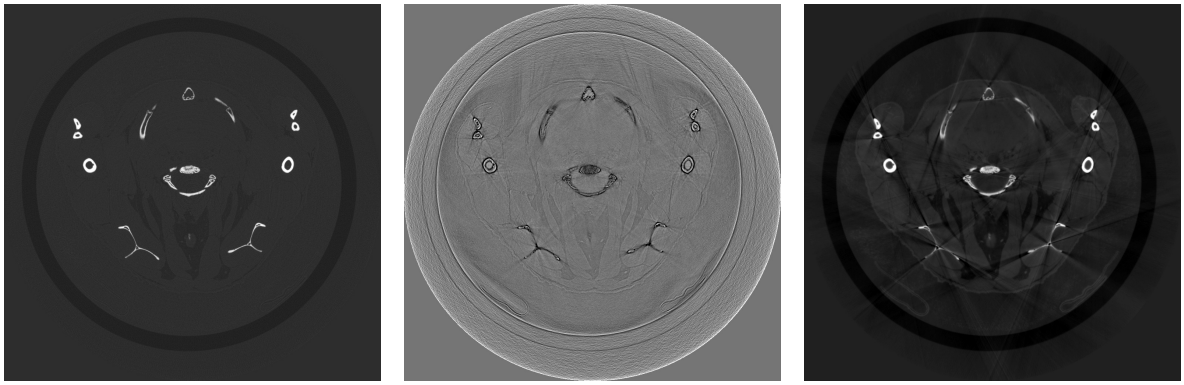

(a) Attenuation (b) Dark-field (c) Differential phase contrast

Figure 9.10.: Two-dimensional sample reconstruction of a mouse. Attenuation (a), scattering (b), and phase contrast (c). Note the considerably improved soft-tissue comparing (a) and (c), but also the streak artefacts caused by phase wrapping in the last case. *(Courtesy of Guillaume Potdevin.)*

testing [Rev11]. In all these cases, dark-field reconstructions have been shown to provide contrast where the other two signals, phase-contrast and absorption, only yield poor results.

This chapter is partly based on co-authored publications, extended and revised where necessary.

10. Directional Dark-field and Scattering Tensors

An important property of the dark-field signal has not been discussed yet: The signal depends on the relative alignment of the small structures within the specimen causing the scattering and the direction of the grating lines [Jen10a; Jen10b]. Consequently, when turning the specimen around the viewing direction (rather than the tomographic axis), the signal will change depending on the angle. Based on such data, a two-dimensional *vector radiograph* can be reconstructed that shows the main scattering orientations, for instance using colour coding, in a two-dimensional projection. Thus, the image hints at the tiny structures causing the scattering effect. (See figs. 10.1 and 10.2.) This method has been shown to yield promising results for the analysis of bone structure [Pot12; Sch14], for instance.

Consequently, the isotropic scattering volume reconstructed as explained in section 9.3.2 can be considered as some kind of scattering average that can be seen from all directions. In particular, it does not capture the full information contained in the dark-field projections. Tomographic reconstruction of the anisotropic component of the dark-field signal is thus a highly interesting problem, but is has not yet gained much attention. Only recently, Malecki *et al.* [Mal14; Mal13a] have presented *tensor-valued tomographic reconstruction*, thus taking directional scattering information into account. The method uses a full directional sampling of the dark-field signal as input data: In addition to the usual tomographic axis, the sample is also rotated around the other two axes using an Eulerian cradle. Assuming a *Gaussian scattering model* [Jen10b], the authors present a first mathematical model and a specialised SART-based reconstruction algorithm, thus obtaining the first scattering tensor reconstructions. Informally speaking, inspired by the shape of a three-dimensional Gaussian, they obtain an ellipsoid at every voxel, and its size and shape hints at the structure of the specimen at this location. In particular, plate-like scattering ellipsoids hint at fibre- or tube-like structures. (See fig. 10.3.)

The only other work on X-ray scattering tensor reconstruction has recently been presented by Bayer *et al.* [Bay14]. In contrast to the aforementioned approach, this group uses the single tomographic axis of rotation only and relies on extended mathematical modelling. In particular, they do not reconstruct full scattering tensors, but projections of fibre directions onto the tomographic plane, and thus a stack of two-dimensional projections rather than a volume of three-dimensional shapes.

Tomographically reconstructing tensor-valued data, that is a shape per location, is generally

This project was carried out in cooperation with Tobias Lasser, Matthias Wieczorek, Florian Schaff, Andreas Fehringer and Christoph Jud in 2014 and 2015 [Vog15a; Vog15b].

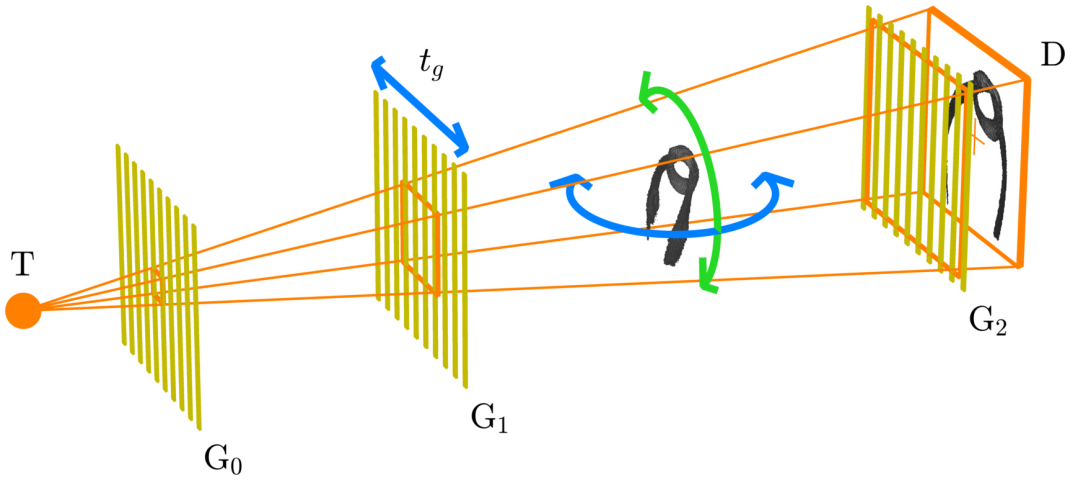

Figure 10.1.: For vector radiography, the sample is rotated around the viewing direction (green arrow). For tomographic reconstruction of scattering directions, the sample is *additionally* rotated around the other axes (green *and* blue arrows), yielding an almost complete angular sampling.

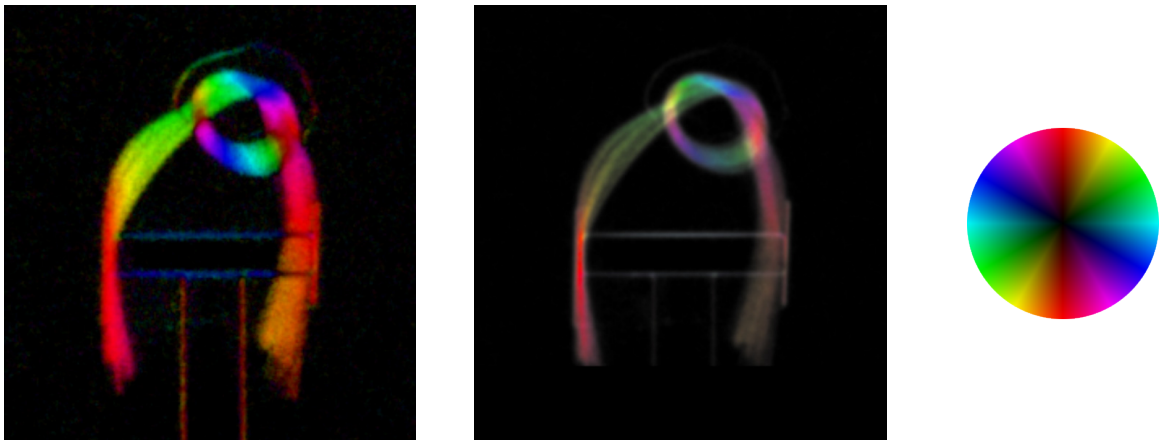

(a) (b) (c)

Figure 10.2.: X-ray vector radiography sample pictures of a knot made from a bunch of carbon fibres. (See section 10.6 and fig. 10.9(a).) Turning the sample around the viewing direction and observing the scattering signal allows to extract information about the fibre directions from two-dimensional projections. Note that the carbon fibers are too small to be resolved directly, but their scattering effect becomes clearly visible. The figure shows two different colouring schemes for the same sample in (a) and (b), and a colour direction indicator in (c). *(Courtesy of Florian Schaff.)*

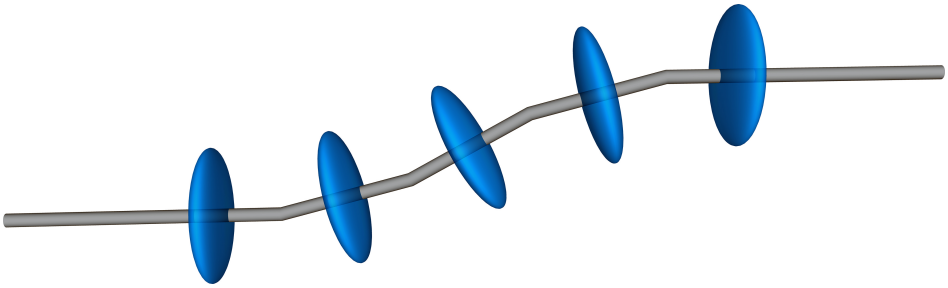

Figure 10.3.: Expected X-ray scattering (blue ellipsoids) at fibre- or tube-like structures (grey). Vice versa, the smallest half-axes of reconstructed scattering ellipsoids will later be interpreted as fibre directions for visualisation.

rather uncommon. Another well-known tensor-based imaging modality is diffusion tensor magnetic resonance imaging (DTI) [Le 86; Fil09]. (See section 3.4.2.) Only visualisation techniques [Con99] are shared with this modality.

The approach of Malecki *et al.* has been improved by the author of this thesis, and several algorithmic improvements have been presented [Vog15b; Vog15a]. Among them are, most importantly, a novel, more generic description for solving X-ray tensor tomography (XTT) problems, and two ways to enforce tensor-shapes during reconstruction.

10.1. A Forward Model for Anisotropic Scattering

Scattering is not a scalar entity (as X-ray attenuation is), but a tensor-valued one, that is a three-dimensional shape per location. This requires a more complicated mathematical model.

Malecki *et al.* [Mal14; Mal13a] propose to consider a finite set of K pre-defined, normalised, well-distributed *sampling directions* $\hat{\epsilon}_k \in \mathbb{R}^3$ rather than a tensor. Here, and in the remainder of the chapter, the 'hat' will be used to denote normalised vectors, that is $\|\hat{\epsilon}_k\|_2 = 1 \; \forall k = 1, \ldots, K$. For each of these $\hat{\epsilon}_k$ and every voxel $\mathbf{x}_i$, a corresponding *scattering coefficient* $\zeta_k(\mathbf{x}_i) \in \mathbb{R}$ will be reconstructed, and the tensor itself can later be approximated by voxel-wise fitting of tensor descriptions to these 'bouquets' of weighted directions. (This entire process is sketched for a single voxel in fig. 10.4, a visual account of a larger region is given in fig. 10.5.) Note that the exact orientation of the sampling directions is rather arbitrary, and the choice does not require any knowledge about the expected reconstruction outcome. The sampling directions are just auxiliary, virtual entities, allowing to avoid an explicit description of the scattering tensor at a given location by considering its projection onto a finite set of well-distributed reference directions instead. They are chosen from a single hemisphere only, as the scattering tensors are supposed to be symmetric.

Based on this approach, Malecki *et al.* derive a forward model for X-ray scattering [Bec10;

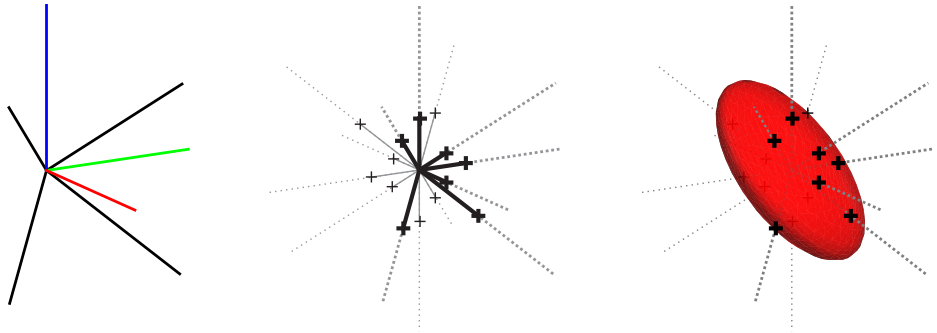

(a) Sampling directions (b) Coefficients (c) Ellipsoid fit

Figure 10.4.: Sampling directions, and ellipsoid fitting for a single voxel. Usually, $K = 13$ directions are used for reconstruction, but in this sketch, $K = 7$ for clarity. They consist of the standard base vectors – red, green, blue in (a) for x, y, z, respectively – and diagonals – black. For a given voxel $\mathbf{x}$, reconstruction yields a scattering coefficient $\zeta_k(\mathbf{x})$ for every sampling direction $\hat{\epsilon}_k$. These are indicated by bold black marks in (b), and they are mirrored to the other hemisphere along the negative sampling direction, yielding the small black marks. Finally, an ellipsoid can be fitted to that scaled, mirrored 'bouquet' afterwards (c).

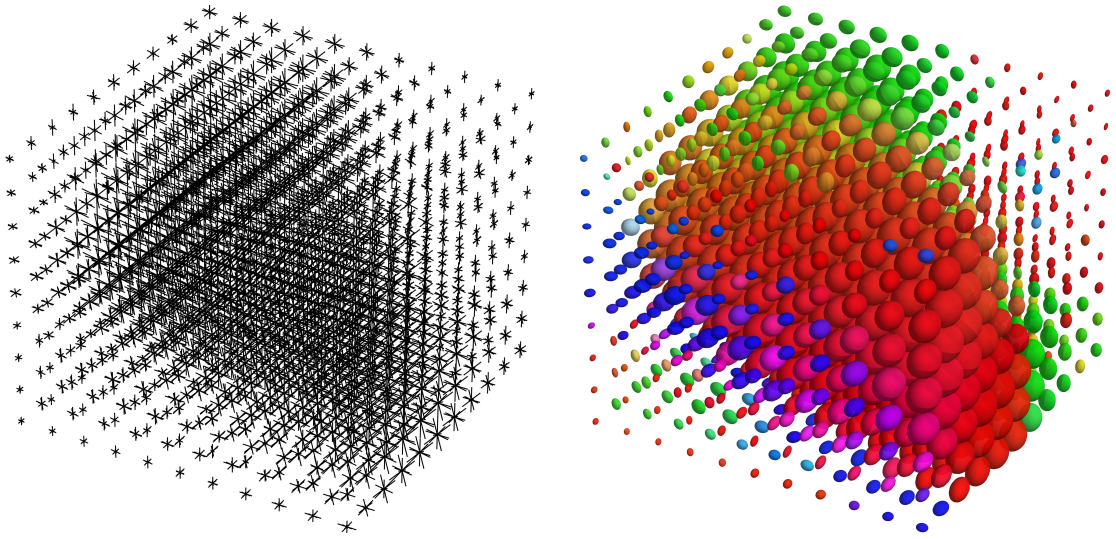

(a) Scaled sampling vectors (b) Ellipsoids with axes

Figure 10.5.: Different variants of the same data, a downsampled detail from an actual result. Reconstruction is performed in terms of scaling the sampling directions (a), the scattering tensors are obtained by retrospectively fitting ellipsoids in a voxel-wise fashion (b). The colours indicate the directions of the smallest half-axes, see fig. 10.8(a).

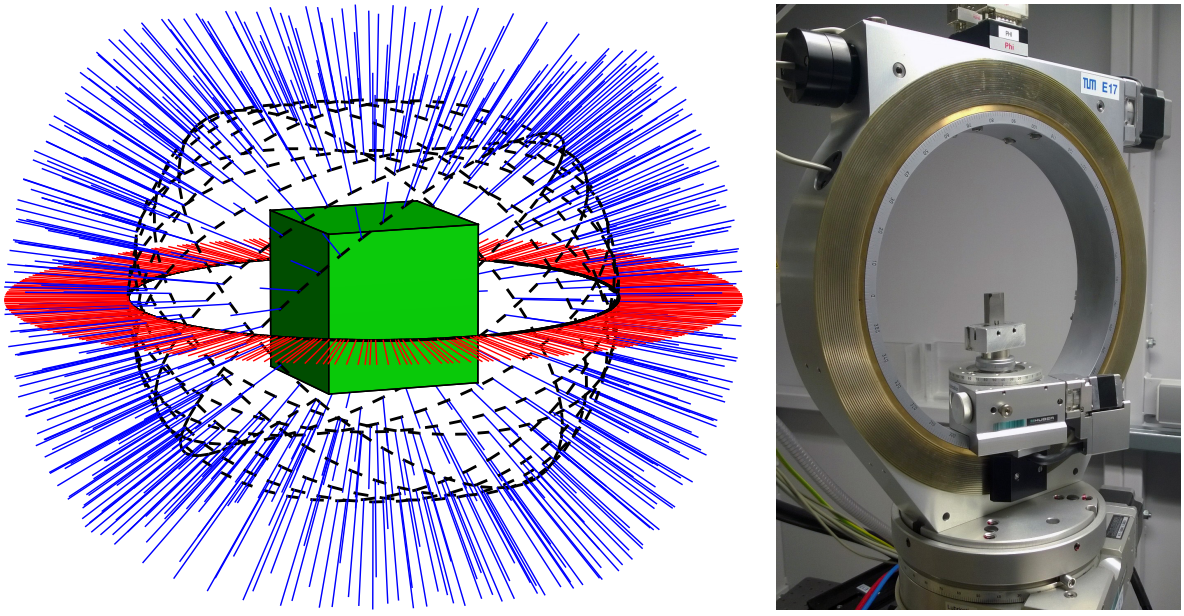

Figure 10.6.: Viewing directions and Eulerian cradle. Only the perspectives marked by red lines are in the 'normal' viewing plane as used in standard CT applications. Blue lines mark additional off-plane perspectives. The dashed black line indicates the trajectory of the X-ray source-detector "camera" around the green cube, representing a specimen. The coverage gaps are due to limitations imposed by the Eulerian cradle. *(Photo of the cradle by courtesy of Florian Schaff.)*

Rev12; Mal13b], extending the isotropic model given in eq. (9.7):

$$d_j = \exp\left[-\int_{L_j} \sum_k \left\langle |\hat{\mathbf{l}}_j \times \hat{\epsilon}_k|(\zeta_k(\mathbf{x})\hat{\epsilon}_k), \hat{\mathbf{t}}_j \right\rangle^2 \, \mathrm{d}\mathbf{x}\right] \tag{10.1}$$

Here, $d_j \in \mathbb{R}$ denotes the jth scalar *dark-field measurement*,[1] and L_j the corresponding ray with normalised direction $\hat{\mathbf{l}}_j \in \mathbb{R}^3$. As has been defined for eq. (9.5), the normalised *sensitivity direction* $\hat{\mathbf{t}}_j \in \mathbb{R}^3$ is orthogonal to the grating lines and parallel to the surfaces of the – mutually parallel – gratings, and thus depends on the perspective during measurement j.

Considering eq. (10.1) in more detail, the true scattering measurement at every voxel $\mathbf{x}$ along the ray is generally modelled as finite sum of K measurements along the pre-defined sampling directions $\hat{\epsilon}_k$. For every such summand, two things need to be taken into account: Scattering must be possible to occur at all, considering the normalised direction $\hat{\mathbf{l}}_j$ of the incoming X-ray with respect to $\hat{\epsilon}_k$. This fact is modelled by the magnitude of the cross-product $|\cdot \times \cdot|$, thus excluding head-on views. Furthermore, if scattering occurs, only components

1. As usual, despite acquiring two-dimensional projections, individual pixels are treated as independent measurements with corresponding rays. Index $j = 1, \ldots, J$ extends over all pixels of all projection images hence.

along the normalised sensitivity direction $\hat{\mathbf{t}}_j$ contribute to the measurement as modelled by the scalar product $\langle \cdot, \cdot \rangle$ [Rev12; Mal13b]. Vice versa, in order to have a good sampling of the scattering tensors, more than just the usual tomographic scanning perspectives are taken into consideration while scanning. (See fig. 10.6.)

Returning to eq. (10.1), factoring out the (unknown) *squared scattering coefficients* $\eta_k(\mathbf{x}) := \zeta_k(\mathbf{x})^2$ from the squared scalar product and defining the weight factor

$$v_{kj} := (|\hat{\mathbf{l}}_j \times \hat{\epsilon}_k| \langle \hat{\epsilon}_k, \hat{\mathbf{t}}_j \rangle)^2 \tag{10.2}$$

yields a formulation very similar to the *Radon transform* as defined in section 4.1.1:

$$-\ln\ d_j \ = \ \int_{L_j} \sum_k v_{kj} \cdot \eta_k(\mathbf{x})\ \mathrm{d}\mathbf{x} \tag{10.3}$$

$$= \ \sum_k v_{kj} \int_{L_j} \eta_k(\mathbf{x})\ \mathrm{d}\mathbf{x} \tag{10.4}$$

Note that the factors defined in eq. (10.2) are independent of the unknowns, and can thus be precomputed for more efficient reconstruction.

10.2. Tomographic Reconstruction of Tensors

Obviously, eq. (10.4) is a weighted sum of line integrals. In particular, in a discretised setting, it can be rewritten as scalar product

$$m_j \ = \ -\ln\ d_j \ = \ \sum_k v_{kj}\ \langle \mathbf{a}_j, \boldsymbol{\eta}_k \rangle \ = \ \sum_k v_{kj}\ \mathbf{a}_j^T\ \boldsymbol{\eta}_k \tag{10.5}$$

where $\boldsymbol{\eta}_k \in \mathbb{R}^I$ is the vector of the squared coefficients for the kth sampling direction for all voxels (again, I is the number of voxels). As has been done before, $\mathbf{a}_j$ denotes the *system matrix* row for measurement j, and is thus part of the 'standard' matrix as used for an equivalent attenuation reconstruction. Recall that this vector contains geometric information about the arrangement of X-ray source, specimen and sensor during measurement j, an information already included abstractly in eq. (10.4) as ray L_j. Let $A = (\mathbf{a}_j)$, $A \in \mathbb{R}^{J \times I}$, again denote the entire system matrix describing *all* J line integrals. Furthermore, let $D_k = \mathrm{diag}(v_{k1}, v_{k2}, \dots)$ denote a diagonal scaling matrix containing the weighting factors from eq. (10.2) for sampling direction k. Then, using eq. (10.5) and defining the measurement vector $\mathbf{m} = (m_j) = (-\ln\ d_j)$, a huge linear system can be derived:

$$\mathbf{m} \ = \ \begin{pmatrix} v_{11}\mathbf{a}_1^T \\ v_{12}\mathbf{a}_2^T \\ \vdots \\ v_{1J}\mathbf{a}_J^T \end{pmatrix} \boldsymbol{\eta}_1 \ + \ \begin{pmatrix} v_{21}\mathbf{a}_1^T \\ v_{22}\mathbf{a}_2^T \\ \vdots \\ v_{2J}\mathbf{a}_J^T \end{pmatrix} \boldsymbol{\eta}_2 \ + \ \cdots \ + \ \begin{pmatrix} v_{K1}\mathbf{a}_1^T \\ v_{K2}\mathbf{a}_2^T \\ \vdots \\ v_{KJ}\mathbf{a}_J^T \end{pmatrix} \boldsymbol{\eta}_K \tag{10.6}$$

$$= \begin{pmatrix} v_{11} & & & \\ & v_{12} & & \\ & & \ddots & \\ & & & v_{1J} \end{pmatrix} \begin{pmatrix} \mathbf{a}_1^T \\ \mathbf{a}_2^T \\ \vdots \\ \mathbf{a}_J^T \end{pmatrix} \boldsymbol{\eta}_1 + \begin{pmatrix} v_{21} & & & \\ & v_{22} & & \\ & & \ddots & \\ & & & v_{2J} \end{pmatrix} \begin{pmatrix} \mathbf{a}_1^T \\ \mathbf{a}_2^T \\ \vdots \\ \mathbf{a}_J^T \end{pmatrix} \boldsymbol{\eta}_2 + \cdots \tag{10.7}$$

$$= D_1\, A\, \boldsymbol{\eta}_1 + D_2\, A\, \boldsymbol{\eta}_2 + \cdots + D_K\, A\, \boldsymbol{\eta}_K = \sum_k D_k\, A\, \boldsymbol{\eta}_k \tag{10.8}$$

$$= (D_1\, A,\ D_2\, A,\ \ldots,\ D_K\, A) \begin{pmatrix} \boldsymbol{\eta}_1 \\ \boldsymbol{\eta}_2 \\ \vdots \\ \boldsymbol{\eta}_K \end{pmatrix} \tag{10.9}$$

$$\equiv H\mathbf{s} \tag{10.10}$$

This linear system has K times as many unknowns than the corresponding system for computing a 'traditional' tomographic attenuation reconstruction: The original system matrix A is of size $J \times I$, and H is of size $J \times IK$. Recall that in practical settings, that is when reconstructing a sufficiently sized three-dimensional volume, the system matrix A is already far too large to fit into computer memory, and *projector* software is typically used that simulates the ray instead of handling the matrix directly, thus computing the entries of A on the fly [Feh14].

When reconstructing scattering tensors, it is desirable to use existing software infrastructure that has been put into place for other tomographic reconstruction scenarios rather than solving eq. (10.10) directly. Consequently, in their original work, Malecki *et al.* suggest a specially crafted variant of SART [And84; Sør14] for reconstructing the unknown squared coefficients $\boldsymbol{\eta}_k$. (See section 4.2.4 for the original algorithm.)

Using eq. (10.5), however, a much more generic approach can be taken [Vog15a], supporting arbitrary iterative solvers such as particularly the better-behaving method of Conjugate Gradients (CG) [Hes52; She94]. (See section 4.2.5 for the original algorithm.) Let $x_1 = \textbf{approximate}(A, b, x_0)$ denote an auxiliary function running a *few* iterations of an iterative linear solver, thus very approximately 'solving' the linear system $Ax = b$. Then, an iterative algorithm solving the tensor reconstruction problem (10.5) can be defined: A single iteration q essentially consists of 'approximately solving' K modified linear systems

$$(D_k \cdot A)\, \mathbf{t}_k^{(q)} = \widetilde{\mathbf{m}}_k^{(q-1)} \tag{10.11}$$

for each sampling direction k using function **approximate** as previously defined, where right-hand side vector

$$\widetilde{\mathbf{m}}_k^{(q-1)} = \mathbf{m} - \sum_{l \neq k} D_l \cdot A \cdot \boldsymbol{\eta}_l^{(q-1)} \tag{10.12}$$

denotes a *reduced measurement vector* relevant for sampling direction k, based on the estimates $\boldsymbol{\eta}_l^{(q-1)}$ of the previous iteration, and $\mathbf{t}_k^{(q)}$ an intermediate, temporary vector. The latter is then

used to compute the current iterate via relaxation as

$$\boldsymbol{\eta}_k^{(q)} = \frac{K-1}{K}\,\boldsymbol{\eta}_k^{(q-1)} + \frac{1}{K}\,\mathbf{t}_k^{(q)}\ . \tag{10.13}$$

Altogether, this proposed approach can be thought of as simultaneously solving K linear systems in an interleaved sense. (See alg. 10.1 for the entire proposed generic tensor reconstruction approach.) Note that the scattering coefficients need to be extracted after reconstruction of all $\boldsymbol{\eta}_k$ by component-wise application of the square root:

$$\zeta_k(\mathbf{x}) = \sqrt{|\eta_k(\mathbf{x})|} \tag{10.14}$$

Using the absolute magnitude of η_k is a valid security measure, considering the symmetry of the tensors.

$\eta_k^{(0)} = \mathbf{0}\ \forall k$
for iterations q **do**
  for sampling directions $k \in \{1, \dots, K\}$ **do**
    $WFP_k = D_k \cdot A \cdot \boldsymbol{\eta}_k^{(q-1)}$ {pre-compute weighted forward projections}
  end for

  for sampling directions $k \in \{1, \dots, K\}$ **do**
    $RHS = \mathbf{m} - \sum_{l \neq k} WFP_l$ {compute right-hand side}
    $TEMP = \textbf{approximate}(D_k \cdot A, RHS, \boldsymbol{\eta}_k^{(q-1)})$ {run a single solver iteration}

    $\lambda = 1/K$ {update coefficients with relaxation}
    $\boldsymbol{\eta}_k^{(q)} = (1-\lambda)\,\boldsymbol{\eta}_k^{(q-1)} + \lambda\, TEMP$
  end for

  ... {optionally enforce constraints here}
end for

Algorithm 10.1: Generic tomographic X-ray tensor reconstruction. A denotes the system matrix describing the imaging process, D_k a scaling matrix containing weighting factors as defined in Eq. (10.2). $\mathbf{m}$ is the measurement vector, and $\boldsymbol{\eta}_k^{(q)}$ a vector containing the qth iterate of the voxel-wise squared scattering coefficients corresponding to sampling direction k. **approximate** is a function running a few iterations of an arbitrary iterative linear solver.

10.3. Ellipsoid Fitting

After reconstruction, that is after executing several iterations as described in section 10.2, voxel-wise scattering coefficients ζ_k for the sampling vectors $\hat{\epsilon}_k$ have been recovered. Malecki *et al.* propose to fit ellipsoids to these weighted vectors in order to obtain voxel-wise

tensors. In particular, they use an iterative ellipsoid fitter [Li04], apparently intended for rather degenerate cases where ellipsoids need to be matched to just a couple of ill-distributed sample points.

However, the sampling locations are well-distributed, and *principal component analysis (PCA)* [Pea01; Hot33; Bis06] can be used instead of the iterative approach [Vog15a], thus saving considerable computation time. (See fig. 10.4.)

In more detail, at every voxel $\mathbf{x}_i$, a set of $2K$ direction vectors

$$S_i := \{\pm\sqrt{|\eta_1(\mathbf{x}_i)|}\cdot\hat{\epsilon}_1,\ \pm\sqrt{|\eta_2(\mathbf{x}_i)|}\cdot\hat{\epsilon}_2,\ \dots\} \tag{10.15}$$

$$= \{\pm\zeta_1(\mathbf{x}_i)\cdot\hat{\epsilon}_1,\ \pm\zeta_2(\mathbf{x}_i)\cdot\hat{\epsilon}_2,\ \dots\} \tag{10.16}$$

can be defined by scaling the normalised sampling directions $\hat{\epsilon}_k$ with the positive and negative reconstructed corresponding coefficients $\zeta_k(\mathbf{x}_i) = |\eta_k(\mathbf{x}_i)|^{1/2}$. Again, this is due to the symmetry of the scattering tensors. Note that the mean of this set trivially equals $\mathbf{0}$. Let $C_i \in \mathbb{R}^{3\times3}$ denote the *covariance* matrix of S_i. Then, its *eigen-decomposition*

$$V_i \cdot \Lambda_i = C_i \cdot V_i \tag{10.17}$$

yields a diagonal matrix $\Lambda_i \in \mathbb{R}^{3\times3}$ containing the three *eigenvalues* $\lambda_{i,1}$, $\lambda_{i,2}$, $\lambda_{i,3}$ of the set's covariance matrix C_i, and an orthogonal matrix $V_i \in O(3) \subset \mathbb{R}^{3\times3}$ containing the corresponding mutually orthonormal *eigenvectors* $\mathbf{v}_{i,1}$, $\mathbf{v}_{i,2}$, $\mathbf{v}_{i,3}$ as column vectors.

Let $\overline{\eta}_i = \sum_k |\eta_k(\mathbf{x}_i)|/K$ denote the average squared scattering magnitude at voxel $\mathbf{x}_i$, and $\overline{\lambda}_i = (|\lambda_{i,1}| + |\lambda_{i,2}| + |\lambda_{i,3}|)/3$ the corresponding average eigenvalue magnitude. Define a *size correction* factor $\sigma_i := \overline{\eta}_i/\overline{\lambda}_i$ for scaling the statistically defined ellipsoid to the point set S. Then, the scattering ellipsoid at voxel $\mathbf{x}_i$ is defined by half-axis lengths $r_{i,1} = [\sigma_i\lambda_{i,1}]^{1/2}$, $r_{i,2} = [\sigma_i\lambda_{i,2}]^{1/2}$, $r_{i,3} = [\sigma_i\lambda_{i,3}]^{1/2}$ with respect to the orthonormal basis formed by vectors $\mathbf{v}_{i,1}$, $\mathbf{v}_{i,2}$, $\mathbf{v}_{i,3}$.

10.4. Constraint Enforcement

As it will turn out in the experiments, unconstrained reconstruction of the scattering coefficients yields useful but noisy results. Instead of just fitting ellipsoids retrospectively, it makes sense to enforce ellipsoidal shapes during reconstruction. (See section 4.4 for constraint enforcement in general.) Therefore, the scattering coefficients should be post-processed at the end of *every* iteration as indicated in the last comment of alg. 10.1, thus forcing them to evolve in the vicinity of the manifold of ellipsoid-shaped tensors [Vog15a].

10.4.1. Hard Ellipsoid Constraint

An obvious approach to reach this aim is to fit ellipsoids after every iteration, and to project the reconstructed squared coefficients $\boldsymbol{\eta}_k$ onto them [Vog15a]. This method will be referred to as *hard ellipsoid constraint* as the coefficients will really be forced into ellipsoidal shapes.

In detail, after the computation of all squared coefficients $\boldsymbol{\eta}_k^{(q)}$ in iteration q, every voxel $\mathbf{x}_i$ is visited, and an ellipsoid is fitted as described in section 10.3, thus obtaining a coordinate frame $V_i = [\mathbf{v}_{i,1}, \mathbf{v}_{i,2}, \mathbf{v}_{i,3}] \in \mathbb{R}^{3\times3}$ and corresponding half-axes $r_{i,1}, r_{i,2}, r_{i,3} \in \mathbb{R}$. Then, the reconstructed coefficients $\boldsymbol{\eta}_k^{(q)}$ are replaced with the projections of the respective normalised sampling directions $\hat{\epsilon}_k$ onto this ellipsoid.

In detail, to do this for every sampling direction k and voxel $\mathbf{x}_i$, first rotate the (by design normalised) vector into the ellipsoid's coordinate frame, thus obtaining a unit vector $[x_{i,k},\ y_{i,k},\ z_{i,k}]^T = V_i^T \hat{\epsilon}_k$. By definition, the scaled vector $\sigma_{i,k} \cdot [x_{i,k},\ y_{i,k},\ z_{i,k}]^T$, $\sigma_{i,k} \in \mathbb{R}$, resides on the surface of the ellipsoid if

$$\sigma_{i,k}{}^2 \left[\left(\frac{x_{i,k}}{r_{i,1}} \right)^2 + \left(\frac{y_{i,k}}{r_{i,2}} \right)^2 + \left(\frac{z_{i,k}}{r_{i,3}} \right)^2 \right] = 1. \tag{10.18}$$

This equation can simply be solved for $\sigma_{i,k}{}^2$, and considering that squared coefficients are reconstructed, the correctly projected coefficients are

$$\boldsymbol{\eta}_{i,k}^{(q)} = \sigma_{i,k}{}^2 \tag{10.19}$$

for all voxels $\mathbf{x}_i$ and directions k. (See fig. 10.7(a) for a sketch.)

10.4.2. Soft Ellipsoid Constraint

Alternatively, a softer variant favouring ellipsoids but allowing some more freedom can be used. Essentially, this is done by smoothing the K direction coefficients per voxel, over the ellipsoid [Vog15a]. Consequently, this approach will be referred to as *soft ellipsoid constraint*. Note that still only individual voxels and their K coefficients are considered; a neighbourhood is not taken into account as one would do for smoothness constraints in regularised X-ray attenuation reconstruction. (See section 4.6 for a general discussion of regularisation.)

In detail, first compute the pair-wise absolute scalar products between all K normalised sampling directions, and obtain a matrix $S \in [0,1]^{K\times K}$, $S_{k,l} = |\langle \hat{\epsilon}_k, \hat{\epsilon}_l \rangle|$. In order to increase the influence of more similar sampling directions, additionally apply a Gaussian and obtain a matrix $G \in \mathbb{R}^{K\times K}$, $G_{k,l} = \exp[-(S_{k,l}-1)^2/2\mu]$ with some selectable variance μ. The larger μ is chosen, the higher will be the influence of the smoothing.

To process coefficient k, a matching convolution kernel can be defined by normalising the kth row of G to a sum of 1, denoted as $\mathbf{g}_k^T$, $\sum_l [\mathbf{g}_k^T]_l = 1$. Collecting all K coefficients into a vector, the regularised kth value for voxel $\mathbf{x}_i$ computes as

$$\boldsymbol{\eta}_{i,k}^{(q)} = \langle \mathbf{g}_k^T, [\boldsymbol{\eta}_{i,1}^{(q)}, \ldots, \boldsymbol{\eta}_{i,K}^{(q)}] \rangle. \tag{10.20}$$

In other words, this approach can be considered as angle-dependent Gaussian smoothing of the squared coefficients $\eta_k(\mathbf{x}_i)$ over all directions k for every individual voxel $\mathbf{x}_i$. (The smoothing kernel is illustrated in fig. 10.7(b).)

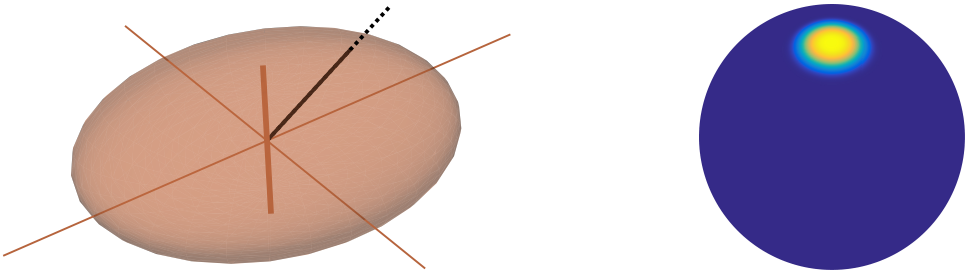

(a) Hard constraint (b) Soft constraint

Figure 10.7.: Constraint enforcement. In both cases, the reconstructed coefficients are forced to be close to the manifold of valid ellipsoids while iterating. The hard constraint (a) projects back onto ellipsoids directly, where a – in this toy example exaggerated – scattering coefficient (dotted black line) is shortened appropriately (solid black line). The soft constraint smoothes the coefficients with respect to the other sampling directions of the *same* voxel respecting the angular relation, thus favouring ellipsoids in a relaxed sense. This is done using a Gaussian smoothing kernel based on the scalar product as shown in (b), ranging between 0 (blue) and 1 (yellow), before normalisation.

10.5. Visualisation

A last, vital point for X-ray tensor tomography is a proper visualisation of the results. This is of particular importance as the voxel-wise tensors can not be accurately shown using rendering techniques intended for scalar-valued data [Eng06; Eng04]. Apart from plotting the ellipsoids themselves, a prominent option is to visualise derived shapes.

Interested in fibre- and tube-like structures, an obvious choice is a *streamline* visualisation [Vog15a] based on the classical *Runge-Kutta method (RK4)* [Run95; Kut01; Edw07]. This metaphor is well-known in the field of diffusion-tensor magnetic resonance imaging (DTI) [Con99; Fil09; Ten02], and commonly referred to as *tractography*. As sketched in fig. 10.3, plate-like ellipsoids hint at fibres in the direction of the smallest half-axes. Then, RK4 can be employed to trace streamlines along these smallest half-axes, adapted to account for the symmetric, 'bidirectional' nature of ellipsoid axes (compared to a vector field). This is done by inverting directions queried from the raw ellipsoid axes whenever the scalar product with the direction of an incoming fibre is negative, i.e. new directions are chosen to continue the streamline in forward direction. (See alg. 10.2.) Furthermore, colour coding is used to give cues about the orientation of these fibres. (See fig. 10.8 for an example.)

Note that the streamlines do not necessarily correspond to real fibres, and there is no intention for this to be the case. The streamlines are to be interpreted as scattering visualisation, however, using a model which is likely similar to the invisible structure.

for steps $q = 1, ..., N$ **do**
  $\mathbf{p}_1 = \mathbf{s}^{(q-1)}$, $\mathbf{d}_1 = \mathbf{direction}(\mathbf{p}_1)$ {set first intermediate point, obtain direction}
  if $\|\mathbf{d}_1\| < T$ **then**
    terminate {enforce to move in relevant regions only}
  end if
  if $\langle \mathbf{d}_1, \mathbf{d}^{(q-1)} \rangle < 0$ **then**
    $\mathbf{d}_1 = -\mathbf{d}_1$ {invert direction to follow the reference direction}
  end if

  $\mathbf{p}_2 = \mathbf{s}^{(q-1)} + \frac{1}{2}\ H\ \mathbf{d}_1$ {compute second intermediate point, obtain direction}
  $\mathbf{d}_2 = \mathbf{direction}(\mathbf{p}_2)$
  ... {perform the two checks as above}
  $\mathbf{p}_3 = \mathbf{s}^{(q-1)} + \frac{1}{2}\ H\ \mathbf{d}_2$ {compute third intermediate point, obtain direction}
  ... {perform the two checks as above}
  $\mathbf{p}_4 = \mathbf{s}^{(q-1)} + H\ \mathbf{d}_3$ {compute fourth intermediate point, obtain direction}
  ... {perform the two checks as above}

  $\mathbf{d}^{(q)} = \frac{1}{6}(\mathbf{d}_1 + 2\ \mathbf{d}_2 + 2\ \mathbf{d}_3 + \mathbf{d}_4)$ {compute complete direction}
  ... {perform the two checks as above}
  $\mathbf{s}^{(q)} = \mathbf{s}^{(q-1)} + H\ \mathbf{d}^{(q)}$ {compute next streamline point}
end for

... {process or visualise streamline $\mathbf{s}^{(0)}, ..., \mathbf{s}^{(N)}$}

Algorithm 10.2: Streamline tracing using RK4. The method $\mathbf{direction}(\mathbf{x})$ denotes a lookup function yielding the appropriate smallest ellipsoid half-axis at a given voxel $\mathbf{x} \in \mathbb{R}^3$. In the reference implementation, this was simply done by a nearest-neighbour lookup. The point $\mathbf{s}^{(0)}$ is a streamline seed-point, and $\mathbf{d}^{(0)} = \mathbf{direction}(\mathbf{s}^{(0)})$ the corresponding initial fibre direction. The seed-points are chosen from a regular grid where the reconstructed smallest half-axes exceed a certain threshold T. Spacing of the seed-points, step size H, threshold T, fibre-length N and similar parameters are chosen intuitively to optimise the visual result. Once the given algorithm terminates, it is repeated for the same seed-point $\mathbf{s}^{(0)}$, this time following the opposite direction $\mathbf{d}^{(0)} = -\mathbf{direction}(\mathbf{s}^{(0)})$.

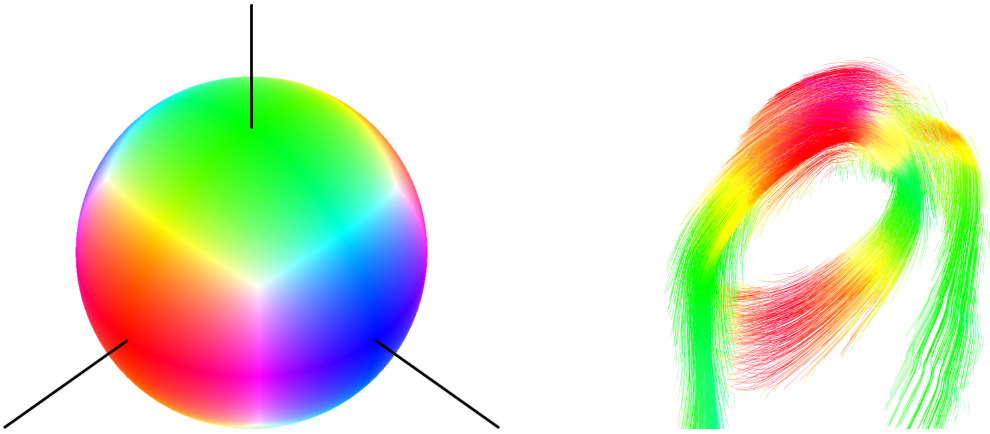

(a) (b)

Figure 10.8.: Streamline visualisation and colour coding. Colours sampled from a sphere (a) are used to give visual cues about the orientation of the 'fibres'. Note that the colour ball is symmetric with respect to the x-y-, x-z-, and y-z-planes. In a sample picture of the carbon knot (b), looking down from a slightly elevated perspective, vertically (green), horizontally (red) and obliquely (orange and yellow) oriented parts can be easily distinguished.

10.6. Experiments and Results

The reconstruction algorithm has been implemented within *CampRecon* [Wie14], a C++ framework for solving linear inverse problems. The discrete integration along lines $A\mathbf{x}$ and its adjoint $A^T\mathbf{b}$ are approximated roughly via intersections between ray and pixels using projector software as proposed by Siddon [Sid85], employing the GPU-based X-ray projector developed by Fehringer *et al.* [Feh14] in OpenCL. All experiments have been run on a computer with dual Intel Xeon E5-2687W processors and a Nvidia Tesla K20 accelerator.

In general, reconstructions of three datasets have been computed, the carbon *'knot'*, a knotted bunch of carbon fibres embedded in hot glue, the tree *'branch'*, a short piece of raw wood, and a *'tooth'*. (Photographs of the samples are given in fig. 10.9.) X-ray images of all samples have been acquired in an experimental setup. (See fig. 9.5.) 732 projections of 321×321 pixels have been used for the *knot*, 551 projections of 301×301 pixels for the *branch*, and 902 projections of 701×701 pixels for the tooth, with trajectories resembling the one shown in fig. 10.6.

All samples were measured at an acceleration voltage of 60 kVp. Eight phase steps were recorded per projection with a flat panel detector[2] with pixel pitch of 127 μm. The exposure time was 1 s per phase step. A $\pi/2$ phase grating for the design energy of 45 kV composed of 8 μm high Ni lines and period of 5 μm was used. The two other gratings were absorption gratings with 170 μm high Au lines and a period of 10 μm. The interferometer was symmetric

2. Varian, Palo Alto, USA

(a) Knot (b) Branch (c) Tooth

Figure 10.9.: Photographs of the samples. Knot (a), branch (b), and tooth (c). *(Photos of the* knot *and the tree* branch *by courtesy of Andreas Malecki and Christoph Jud.)*

with both inter-grating distances being 92.7 cm.

Each of the datasets was reconstructed without constraint enforcement, with hard, and with soft ellipsoid enforcement, each time with $K = 13$ sampling directions. In all cases, 100 iterations of alg. 10.1 have been executed and no other stopping criterion was in force. A single iteration of CG was used as function **approximate**. Note that this corresponds to a single Landweber step with respect to the sub-problem. For the soft constraint, an experimentally established smoothing variance of $\mu = 0.1$ was generally used, unless stated otherwise. Reconstruction times are about 1.75 hours for the *branch* (251^3 voxels), 2 hours for the *knot* (201^3 voxels), and 15.5 hours for the *tooth* ($301 \times 501 \times 291$ voxels). Relating the number of voxels with the input projections, it is clear that the linear system $\mathbf{m} = H\mathbf{s}$ as defined in eq. (10.10) is underdetermined in all experiments. The ratios of measurements to unknowns are 24.3 % for the *branch*, 70.4 % for the *knot*, and 77.7 % for the *tooth*, respectively.

Furthermore, a reconstruction of the *knot* produced with the original SART-variant proposed by Malecki *et al.* has been obtained for comparison.

10.6.1. Numerical Behaviour

In order to check the behaviour of the three algorithm variants (unconstrained, soft, and hard ellipsoid constraint), the normalised residual norms

$$r^{(q)} := \|\mathbf{m} - \sum_k D_k \cdot A \cdot \boldsymbol{\eta}_k^{(q)}\|_2 \;/\; \|\mathbf{m}\|_2 \tag{10.21}$$

have been computed for iterations $q \in \{1, \ldots, 100\}$, and also the normalised mean updates

$$\Delta^{(q)} := \operatorname*{mean}_k \|\boldsymbol{\eta}_k^{(q)} - \boldsymbol{\eta}_k^{(q-1)}\|_2 \;/\; \|\boldsymbol{\eta}_k^{(q)}\|_2. \tag{10.22}$$

Sample plots of these sequences for the *knot* and the tree *branch* are given in fig. 10.10 and 10.11. There, the curves for both measures flatten out with increasing number of iter-

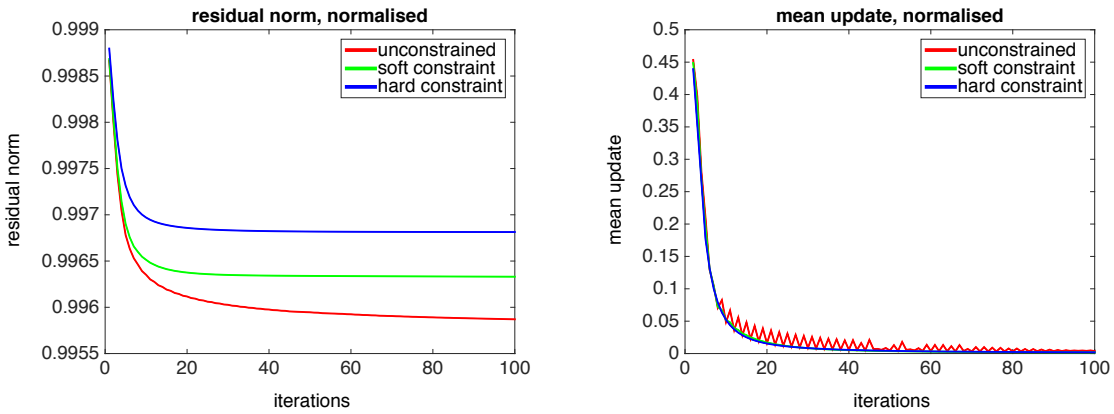

Figure 10.10.: Behaviour of the algorithm for the *knot*. The plots show the normalised residual norm $r^{(q)}$ as defined in eq. (10.21) over iterations q (left) and the normalised mean update $\Delta^{(q)}$ as defined in eq. (10.22) over iterations q (right). The unconstrained version yields smaller residuals, but the updates are noisy.

ations. The unconstrained variant tends to reach a smaller residual norm, while the update norms appear to oscillate. Vice versa, the constrained variants show larger residual norms, but smooth updates. For other datasets, similar curves can be obtained.

10.6.2. Comparison with State of Art

Next, in order to compare the new method with the original SART-based approach of Malecki *et al.*, compare an unconstrained reconstruction of the *knot* was compared with a reference result. (See fig. 10.12.) As Malecki's results can not be considered as ground truth, a visual comparison is considered sufficient.

10.6.3. Knot

Fig. 10.13 shows volume renderings of raw scattering coefficients relating to a single sampling direction, but for the three different constraint enforcement schemes. Most importantly, the unconstrained version shows considerable streak artefacts, and the constrained versions do not, hinting at a beneficial behaviour of constraint enforcement.

Fig. 10.14 shows streamline visualisations of the *knot*. As can be seen, enforcing the two constraints yields *visually* smoother fibres that are more densely packed. Again, note that these fibres visualise the scattering ellipsoids, and are not to be considered reconstructions of the raw carbon fibres.

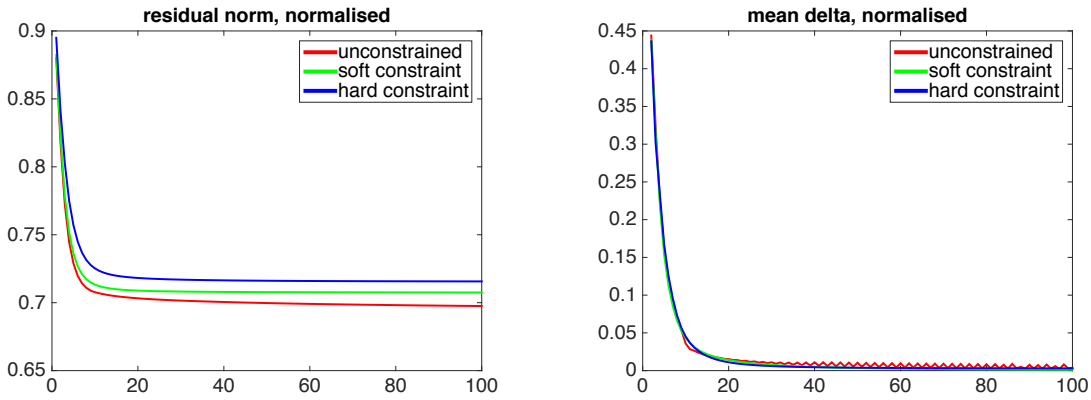

Figure 10.11.: Behaviour of the algorithm for the tree *branch*. Again, the plots show the normalised residual norm $r^{(q)}$ as defined in eq. (10.21) over iterations q (left) and the normalised mean update $\Delta^{(q)}$ as defined in eq. (10.22) over iterations q (right), and yet again, the unconstrained version yields smaller residuals, but the updates are noisy.

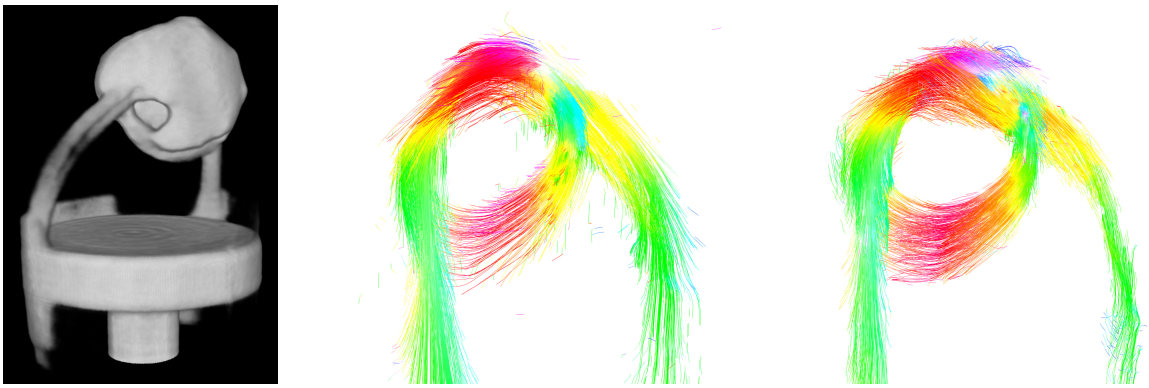

(a) Attenuation (b) Malecki's reconstruction (c) Novel reconstruction

Figure 10.12.: Comparison of attenuation reconstruction (a), Malecki's tensor reconstruction (b), and an (unconstrained) tensor reconstruction following the proposed approach (c). The first image is included for reference, to show that scattering data is of a considerably different nature than usual attenuation reconstructions. The two scattering reconstructions are largely equivalent, considering the different algorithms with different parameters.

(a) Unconstrained (b) Soft constraint ($\mu = 0.10$) (c) Hard constraint

Figure 10.13.: Volume renderings of the *knot*'s scattering coefficients for sampling direction $\hat{\epsilon}_k = [0, 0, 1]^T$. The unconstrained reconstruction (a) shows strong streak artefacts, the two constrained versions (b) and (c) are much clearer.

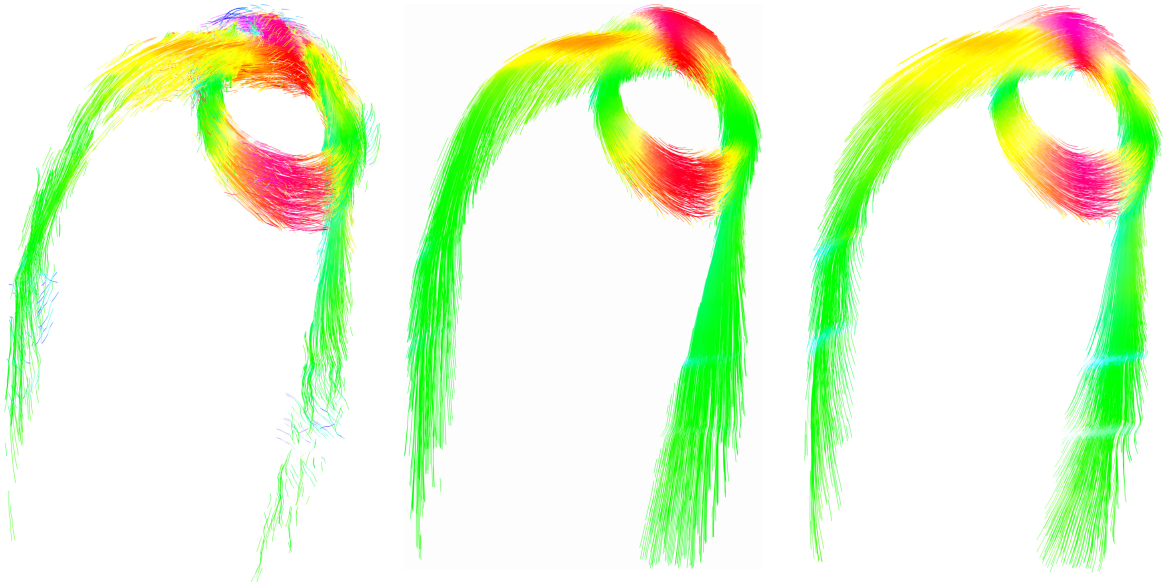

(a) Unconstrained (b) Soft constraint ($\mu = 0.10$) (c) Hard constraint

Figure 10.14.: Streamline visualisation of the *knot*'s scattering ellipsoids. The streamlines are supposed to follow the directions of the carbon fibres, see fig. 10.9(a), but are not intended to accurately reconstruct individual fibres. The unconstrained version (a) shows noise, the two constrained versions (b) and (c) are visually considerably smoother. The 'waves' in the lower right appear to be additional scattering caused by the sample holder.

10.6.4. Branch

Fig. 10.15 shows streamline visualisations of the *branch*. For this dataset, enforcing ellipsoid constraints has even more prominent effects. Considering the structure of wood, scattering will be caused primarily by the tiny vessels transporting water towards the leaves. That is, streamlines are supposed to run mainly in parallel to the axes of the branches. In the unconstrained case, reconstruction of scattering along the main branch fails almost entirely, but the constrained versions are able to recover more reasonable scattering streamlines there.

This time, the smoothing parameter μ was also modified for the soft constraint. In particular, a 'combing' effect can be observed for stronger constraint enforcement where streamlines are nicely aligned to each other, but 'combed' away from their expected location. (See the side branches in fig. 10.15(d).) On the other side, a smaller value of μ will increase the amount of noise but cause the reconstruction to stay closer to the data. Especially the side branches appear to benefit from a smaller parameter, as the 'combing' effect is considerably reduced, and the main branch still reconstructs properly.

10.6.5. Tooth

The reconstruction results of the *tooth* are given in fig. 10.18. This sample is particularly intriguing: Teeth generally consist of a hard crown of highly mineralised enamel, and a root covered by cementum. Below these layers, the core of the tooth consists of dentine and, embedded within, the pulp chamber containing living tissue, blood vessels and nerves. Dentine is a fibrous material and less mineralised than enamel. Tiny dentinal tubules (about 2 μm in diameter) are passing through it in radial direction, between pulp chamber and the surface (but not through the enamel). These tubules are generally not visible in X-ray attenuation reconstructions of usual resolution, due to their small size. (See fig. 10.16.)

Despite this, however, the scattering caused by them can be measured and reconstructed. Note that the results in fig. 10.18 have been masked using the reconstruction of the attenuation signal. This is necessary as the contents of the pulp chamber, relicts of the tissue, cause considerable isotropic scattering themselves – clearly visible as distinct black region in the scattering projection in fig. 10.17(c).

The influence of constraint enforcement is similar to the one observed for the other samples. However, at the lower parts of the roots, the soft constraint also yields streamlines caused by pulp chamber scattering.

10.7. Discussion

As shown in the first experiments, the proposed reconstruction algorithm apparently shows reasonable numerical behaviour in terms of the energy measures. Plots similar to the ones shown in fig. 10.10 can be produced for all experiments that have been conducted so far. Note

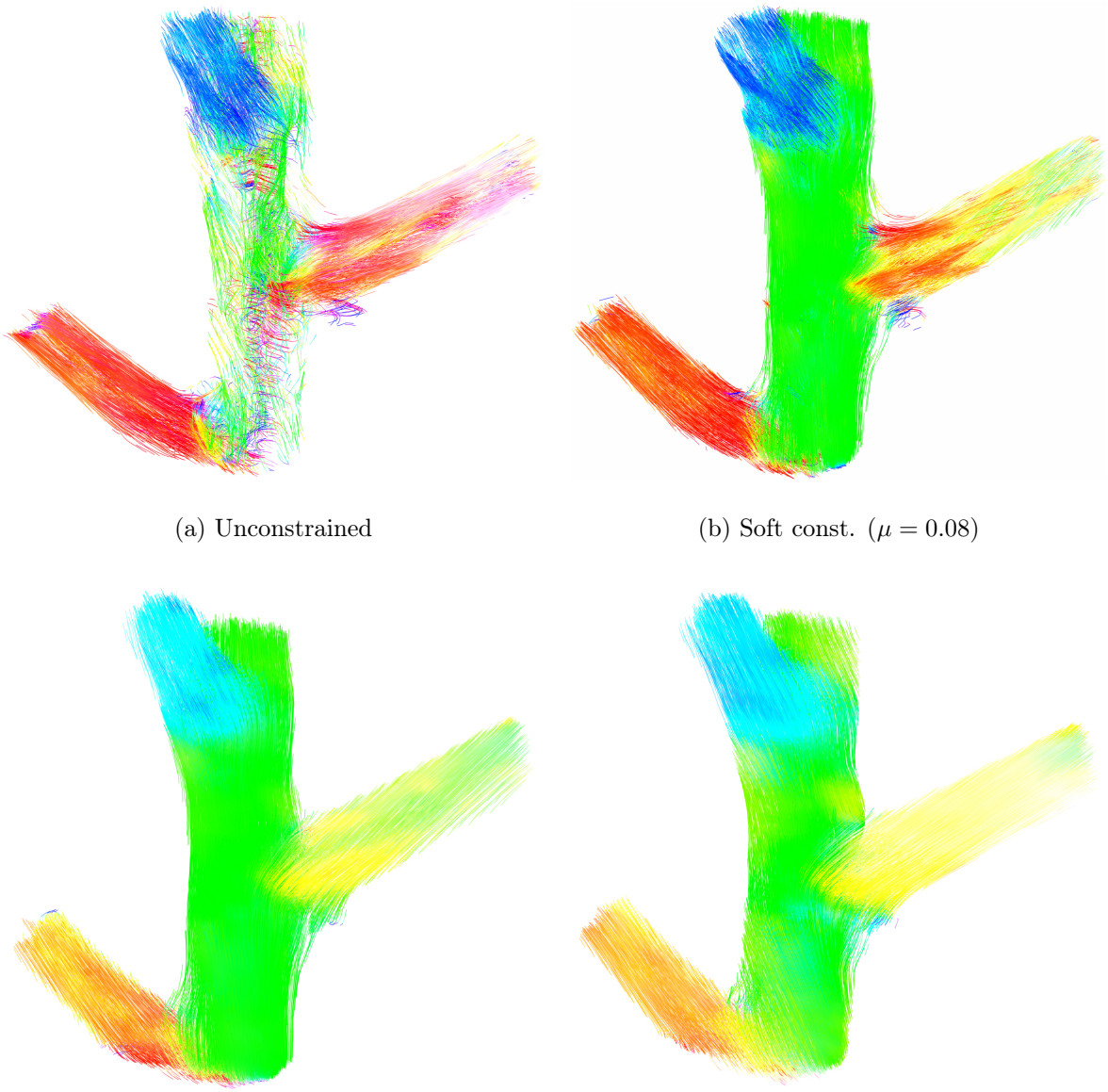

(a) Unconstrained

(b) Soft const. ($\mu = 0.08$)

(c) Soft const. ($\mu = 0.10$)

(d) Hard constraint

Figure 10.15.: Streamline visualisation of the *branch*. Scattering is supposed to be caused by the tiny tubular vessels embedded in wood that transport water towards the leaves. The streamlines are thus expected to run mainly in parallel to the individual branches. The unconstrained version (a) fails to recover useful scattering along the main branch. The lightly constrained versions (b) and (c) show more reasonable scattering there. The hard constraint (d) overshoots and produces wavy patterns along the main branch, and introduces a 'combing' effect for the other branches. The latter can already be seen in (c).

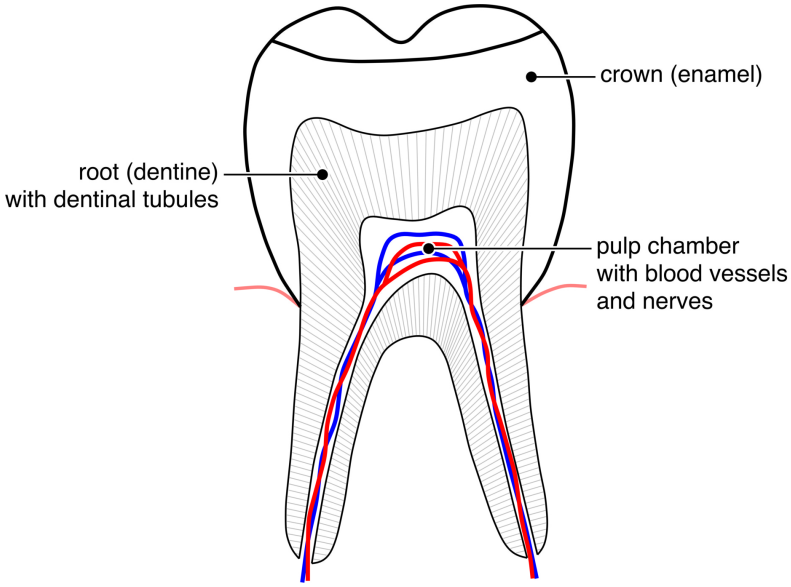

Figure 10.16.: A tooth consists of a root of dentine covered by cementum, and a crown of enamel. The pulp chamber is situated within the dentine, and it contains blood vessels and nerves. Tiny tubular structures, the dentinal tubules, are passing through the dentine in roughly radial direction. The latter are usually not visible in images of standard resolution.

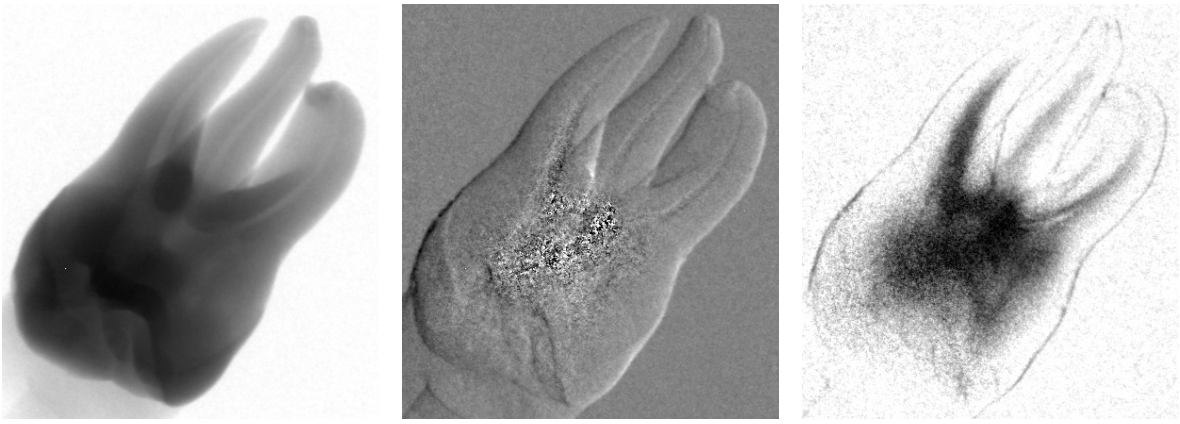

(a) Transmission (b) Phase contrast (c) Dark-field

Figure 10.17.: Three image signals for a sample perspective of the *tooth*: Transmission, phase contrast and dark-field. Note the strong isotropic scattering in the vicinity of the pulp chamber, visible as distinct black region in (c). The contrast of these images has been manually improved for better visibility, and the images have been cropped. The structure in the lower-left quadrant is the sample holder.

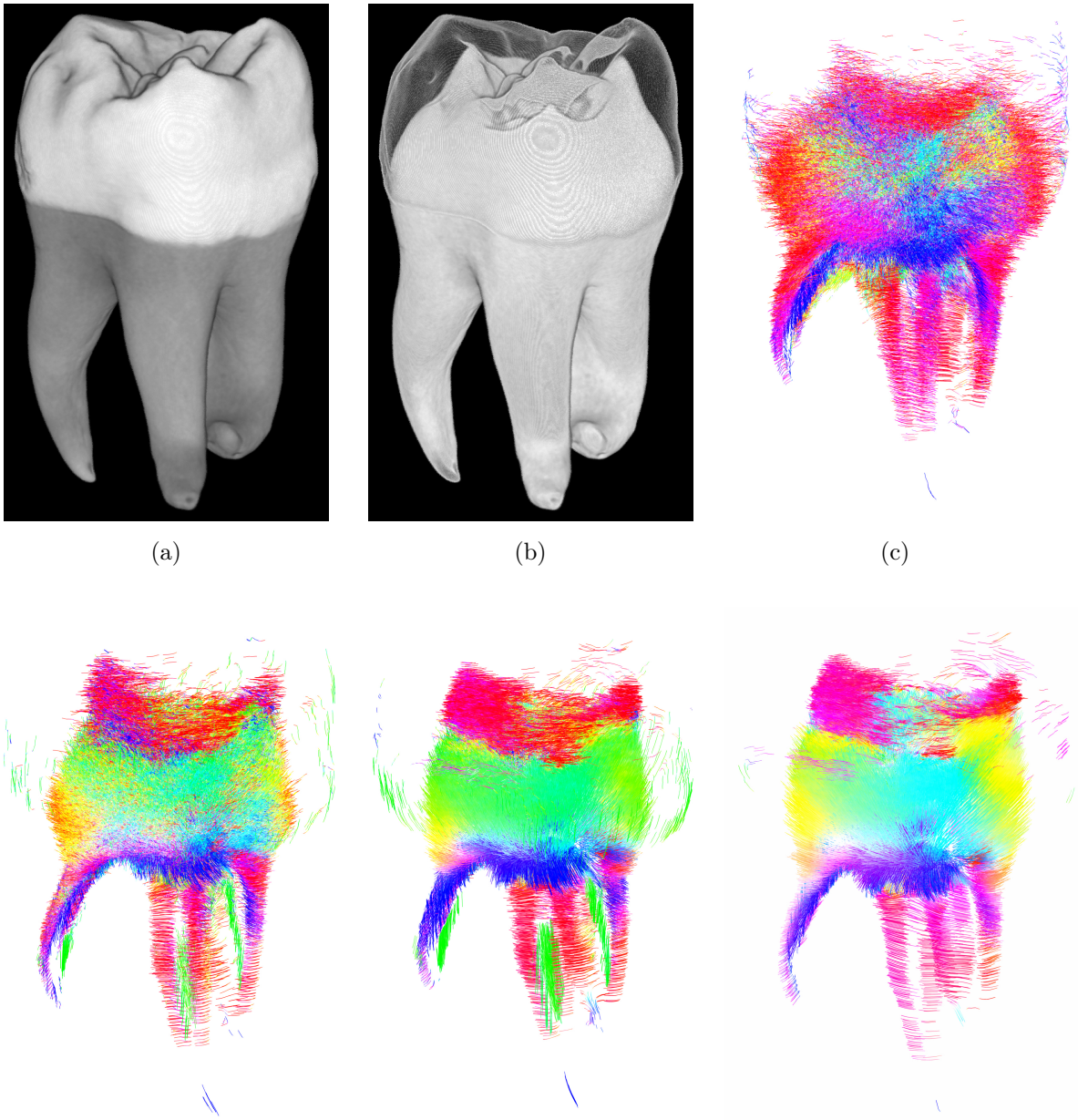

(a) (b) (c)

(d) (e) (f)

Figure 10.18.: Reconstruction results of the *tooth*. Volume rendering of X-ray *attenuation* (a) showing enamel (white) and dentine (gray). Equivalent *attenuation* volume rendering showing dentine only (b). Scattering streamlines obtained without constraint (c), with soft constraint with $\mu = 0.08$ (d) and $\mu = 0.10$ (e), and with hard constraint (f). Scattering is caused by dentinal tubules, tiny structures in radial direction, as indicated by the streamlines. The pulp chamber was obtained by masking.

that these plots only provide hints that the iteration does not become unstable, they neither indicate image quality nor do they prove convergence.

Comparing with the state of art, the unconstrained variant of the new algorithm yields a result quite similar to Malecki's original SART-modification, considering the different nature and parameters of the two methods.

The constrained variants of the new method have been shown to produce considerably less artefacts and visually smoother, non-oscillating updates. As most notable example, the main branch of the wood sample apparently requires some kind of constraint enforcement, to push the reconstruction towards a reasonable result. On the other side, exaggerated constraint enforcement may lead to new artefacts, particularly unexpected wavy patterns or 'combed' directions, as can also be seen for the tree *branch* sample, for instance. It appears that constraint enforcement is necessary, but its influence must be limited. It seems that soft constraint enforcement with a conservatively chosen parameter μ is the most promising approach.

In general, a remarkable feature of X-ray tensor tomography is that scattering effects caused by sub-voxel-sized structures can be recovered, thus giving insight into the microstructure. Considering the experiments presented above, this holds for both, the vessels in the branch, and the dentinal tubules in the tooth. Of course, highly important future work[3] will be an exact correlation of X-ray scattering results with suitable high-resolution pictures of the samples, through μCT or microscopy, for instance.

An important consequence of the work is that the forward model using sampling directions as given in eq. (10.1) and expecting ellipsoids appears not to be entirely correct, despite yielding useful results. This conclusion needs to be drawn from the fact that, even after flattening out, the residual norms are still rather large, particularly for the knot, and from the fact that stronger constraint enforcement causes the results to deteriorate, showing the 'combing' patterns as described. From the perspective of the author of this thesis, three possible conditions are conceivable: First, the model including the sampling directions is sufficiently correct itself, but the assumption of a Gaussian scattering model and ellipsoids, respectively, is too simple to describe the scattering effect. As the reconstruction itself is agnostic of assuming ellipsoids, however, the problem should have been solved by weaker constraint enforcement in this case. Second, the $K = 13$ sampling directions may be chosen too sparsely, thus improperly modelling particularly the forward projection. Third, the entire model may only partially describe the dark-field signal, and additional effects should be considered in the model. Considering the visual quality of the reconstructions, the author of this thesis tends toward the latter explanation. For this reason, the approach should be reconsidered from both, a mathematical as well as a physical perspective. In particular, it will be interesting to see an integrated forward model based on a proper manifold-based ellipsoid description as proposed by Wieczorek *et al.* [Wie15b].

3. Christoph Jud has conducted extensive such studies, especially on a tooth, and a detailed article will appear.

Considering the proposed algorithm alone, many further interesting mathematical questions are still open and will need to be tackled in future work. As pointed out by Per Christian Hansen, it should be possible to position the proposed algorithm in the context of other, well-established solution algorithms, such as column-based block iterative algorithms [Sør14], for the huge system defined in eq. (10.10). Particularly interesting will be an investigation of two points: First, the algorithm computes the weighted forward projections WFP_k based on the previous iterates, and thus exclusively uses the previous state to update the solution. This decision has been made from an engineering perspective, and to avoid bias towards the scattering coefficients that are processed earlier. From a mathematical point of view, however, it may be beneficial to only use the previous state where necessary and the already known current state where possible. The second question is the dependence on the exact choice of function **approximate**. In this context, it will also be useful to attempt to solve the original linear system directly. More advanced mathematical topics include an investigation of the convergence, and the influence of the constraint enforcement schemes onto it. Finally, another important open question is inter-voxel regularisation such as total variation minimisation, and an interesting scheme has already been demonstrated by Wieczorek *et al.* [Wie15b].

10.8. Summary

A new processing chain [Vog15a; Vog15b] for X-ray tensor tomography has been described. In particular, a generic formulation for solving the inverse problem using arbitrary linear solvers has been detailed, firmly based on the forward model and avoiding the tight coupling to SART, along with constraint enforcement schemes improving the reconstructions considerably. Furthermore, a way for quick recovery of the ellipsoids and streamline visualisation for scattering tensors has been demonstrated.

Tensor reconstruction of X-ray scattering in general may be a promising technique. As seen in the experiments, it is possible to visualise effects caused by sub-voxel structures, thus allowing detailed insight that is infeasible when using attenuation information only. A lot of work still needs to go into X-ray tensor tomography, besides the theoretical questions mentioned above: At this point, the mechanical design of the setup requires small samples, and the radiation exposure is considerable. The latter is due to both the large number of acquisitions (more perspectives, more acquisitions per perspective), and the additional absorption caused by the interferometer grating between sample and detector, thus requiring higher radiation at the specimen in order to obtain good detector readings. Nevertheless, application in ex-vivo imaging or material testing is well within reach today, and improvements are subject of active research.

This chapter is based on co-authored publications, extended and revised where necessary.

Part V.

Conclusion and Appendix

11. Summary and Closing Words

This thesis has attempted to first present a general overview over the tomographic reconstruction problem, including a quick description of the historical development, physical and technical principles, and mathematical approaches to invert the measurement process in order to obtain sectional images. Then, three projects attempting to solve problems going 'beyond' the classical setting have been discussed: A scheme compensating for motion, an approach towards finding optimal sensor trajectories in real time for an interventional imaging setting, and finally, the reconstruction of scattering tensors from the X-ray dark-field (or small angle scattering) signal. These projects are selected from the work done by the author during his studies, and appendix A lists the remaining ones for completeness.

The first two projects both relate to interventional imaging modalities. In our time, diagnostic scanners have reached a fantastic quality, and computers have become fast enough to work gainfully with this data. Interventional imaging on the other hand still provides ample space for improvement. Some such techniques are rather mature, like externally applied ultrasound echography or X-ray angiography, and are used in clinical practice. Others such as robotic ultrasound or the modality discussed in this thesis, freehand/robotic SPECT, are rather young and still require many problems to be solved. In general, the challenge is to acquire images in a setting that is not as well-defined and carefully engineered as in the diagnostic cases, leaving space and time to the surgeons. The author is confident that interventional imaging will see many more applications in the future, closely interleaved with the work-flow of the surgeons.

Probably of a more radical nature is the development of novel imaging modalities, and the third project falls into this category. X-ray grating interferometry has laid the foundation for revolutionary imaging devices yielding information yet again orthogonal to the images provided by the existing modalities. Some problems have already been solved so far, and many more lie still ahead, waiting to be tackled, and cooperation between many different communities is required to bring the respective scanners into clinics, eventually making phase contrast and (directional) dark field imaging available to practitioners.

In both cases, once the pending issues are solved and the modalities become fully accessible, a second layer of challenges will unfold: Computer scientists have made many different suggestions for post-processing and exploiting pictures in the past, and diligently continue to propose further ones. For instance, employing state-of-the-art machine learning techniques, objects can be identified, extensive statistical data can be collected, or even diagnoses can

be suggested. It will be thrilling to see the impact of novel signals, and how they affect the performance (and thus the role) of computers in medicine.

A. Additional Projects and Cooperations

Besides the major projects described above, the author has had the opportunity to work on additional projects over the years.

Medical Augmented Reality (Marco Feuerstein, Tobias Reichl, Thomas Wendler)

During 2006 and 2007, the author has contributed to several medical augmented reality projects. Core responsibility was spatial and temporal calibration of tracked ultrasound probes. That is the computation of both, the rigid transform relating the tracking target and the ultrasound image, and the temporal offset between tracking updates and ultrasound image formation. Both pieces of information are essential to fuse ultrasound images with data provided by other synchronised sources. The results were subsequently used for different applications, among them navigation for radio-frequency needle ablation [Alc07], laparoscopic imaging [Feu07b; Feu08; Feu09] and hand-held nuclear imaging [Wen07a; Wen08].

Quality Estimation for Non-Linear Optimisation (Ruxandra Lasowski, Martin Brokate, Christian Clason, Selim Benhimane)

In 2008, the author has supported a project seeking registration of a two-dimensional tomographic slice into a three-dimensional volumetric dataset [Las08b; Las08a]. Due to the extreme ill-posedness of this problem, a unique optimum can not be expected. Aim of the author's work [Vog08] was to characterise the cost function potential around the supposed optimum, to identify similarly 'optimal' alternative solutions, and to devise a visualisation scheme involving all possible solution candidates.

Multi-Organ Segmentation (Kensaku Mori, Takayuki Kitasaka, Makiko Sakashita, Yasuhito Suenaga, Andreas Keil, Marco Feuerstein)

In 2007, the author has had the great opportunity to spend some time in Japan, working on a project on automatic multi-organ segmentation employing expectation maximisation [Vog09a].

Interventional Freehand and Robotic SPECT (Tobias Lasser, José Gardiazabal, Philipp Matthies, Thomas Wendler)

Besides path planning for rSPECT as described in chapter 8, the author has contributed to other aspects of freehand and robotic SPECT, particularly the introduction of miniaturised gamma-cameras [Mat13; Mat14], development of an interventional SPECT/CT system

by combination with angiography [Gar14], novel tracking [Mat15], and list-mode reconstruction [Gar15a; Gar15b; Las15; Gar16].

Tomographic Reconstruction, Curvelets and Manifolds for XTT (Tobias Lasser, Matthias Wieczorek)

As part of a group focusing on tomographic reconstruction, the author has had the chance to contribute to other projects of respective nature. Among them are the development of a reconstruction framework [Wie14], regularised reconstruction via sparse curvelet coefficients [Wie15a; Wie13], a more advanced physical model for XTT (as opposed to the one used in chapter 10) considering the manifold of scattering tensors [Wie15b], and streak reduction for dynamic PET [Che12b].

Multispectral Imaging (Alexandru Duliu)

Besides tomographic reconstruction, the author had the opportunity to also work on a project dealing with multispectral imaging for dermatology. In particular, contributions have been made for nevi tracking [Vog14] and denoising of multispectral images [Dul15].

Cell Classification (Darko Zikic)

During 2013, the author has enjoyed an internship in the United Kingdom where work was done on automatic identification of cancer cells in microscopic images by means of randomised forests. (Unpublished.)

(Co-)Authored Publications

Journal Articles

[Gar16] José **Gardiazabal**, Philipp **Matthies**, Jakob **Vogel**, Benjamin **Frisch**, Nassir **Navab**, Sibylle I. **Ziegler** and Tobias **Lasser**. 'Freehand Mini Gamma Camera Reconstructions of the Thyroid using List-Mode'. In: *Medical Physics* (2016). **(In revision.)** (Cited on pp. 104, 108, 109, 178)

[Vog15a] Jakob **Vogel**, Florian **Schaff**, Andreas **Fehringer**, Christoph **Jud**, Matthias **Wieczorek**, Franz **Pfeiffer** and Tobias **Lasser**. 'Constrained X-ray tensor tomography reconstruction'. In: *Optics Express* 23.12 (June 2015), pp. 15134–15151. (Cited on pp. 149, 151, 155, 157–159, 171)
DOI: 10.1364/OE.23.015134

[Wie15a] Matthias **Wieczorek**, Jürgen **Frikel**, Jakob **Vogel**, Elena **Eggl**, Felix **Kopp**, Peter B. **Noël**, Franz **Pfeiffer**, Laurent **Demaret** and Tobias **Lasser**. 'X-ray Computed Tomography using Curvelet Sparse Regularization'. In: *Medical Physics* 42.4 (Apr. 2015), pp. 1555–1565. (Cited on pp. 77, 80, 178)
DOI: 10.1118/1.4914368

[Mat14] Philipp **Matthies**, José **Gardiazabal**, Aslı **Okur**, Jakob **Vogel**, Nassir **Navab** and Tobias **Lasser**. 'Mini gamma cameras for intra-operative nuclear tomographic reconstruction'. In: *Medical Image Analysis* 18.8 (Dec. 2014), pp. 1329–1336. (Cited on pp. 101, 106, 108, 109, 113, 177)
DOI: 10.1016/j.media.2014.04.009

[Vog13] Jakob **Vogel**, Tobias **Lasser**, José **Gardiazabal** and Nassir **Navab**. 'Trajectory optimization for intra-operative nuclear tomographic imaging'. In: *Medical Image Analysis* 17.7 (Oct. 2013), pp. 723–731. (Cited on pp. 101, 113, 115, 120, 131, 133)
DOI: 10.1016/j.media.2013.04.009

[Feu09] Marco **Feuerstein**, Tobias **Reichl**, Jakob **Vogel**, Joerg **Traub** and Nassir **Navab**. 'Magneto-Optical Tracking of Flexible Laparoscopic Ultrasound: Model-Based Online Detection and Correction of Magnetic Tracking Errors'. In: *IEEE Transactions on Medical Imaging* 28.6 (June 2009), pp. 951–967. (Cited on p. 177)
DOI: 10.1109/TMI.2008.2008954

[Feu08] Marco **Feuerstein**, Tobias **Reichl**, Jakob **Vogel**, Joerg **Traub** and Nassir **Navab**. 'New approaches to online estimation of electromagnetic tracking errors for laparoscopic ultrasonography'. In: *Computer Aided Surgery* 13.5 (Sept. 2008), pp. 311–323. (Cited on p. 177)
DOI: 10.3109/10929080802310002

Conference Proceedings

[Dul15] Alexandru **Duliu**, Jakob **Vogel**, Claudia Dorina **Samoilescu**, Tobias **Lasser** and Nassir **Navab**. 'Illumination Compensation for High-Resolution Multispectral Image Mosaicing of Heritage Paintings'. In: *Proceedings of Digital Heritage International Congress*. Vol. 1. **(Oral presentation.)** Sept. 2015, pp. 191–198. (Cited on p. 178)
DOI: 10.1109/DigitalHeritage.2015.7413871

[Gar15a] José **Gardiazabal**, Benjamin **Frisch**, Philipp **Matthies**, Jakob **Vogel**, Sibylle I. **Ziegler**, Nassir **Navab** and Tobias **Lasser**. 'List-Mode Reconstruction for Continuous Freehand SPECT Acquisitions'. In: *IEEE Nuclear Science Symposium and Medical Imaging Conference*. Oct. 2015. (Cited on p. 178)

[Gar15b] José **Gardiazabal**, Jakob **Vogel**, Philipp **Matthies**, Matthias **Wieczorek**, Benjamin **Frisch**, Nassir **Navab**, Sibylle I. **Ziegler** and Tobias **Lasser**. 'Fully 3D thyroid imaging with mini gamma cameras'. In: *Proceedings of International Meeting on Fully Three-Dimensional Image Reconstruction in Radiology and Nuclear Medicine (Fully3D)*. June 2015. (Cited on pp. 101, 104, 108, 178)
URL: http://www.fully3d.org/Fully3D_Proceedings_2015.pdf (Visited on 5th July 2015)

[Las15] Tobias **Lasser**, José **Gardiazabal**, Matthias **Wieczorek**, Philipp **Matthies**, Jakob **Vogel**, Benjamin **Frisch** and Nassir **Navab**. 'Towards 3D thyroid imaging using robotic mini gamma cameras'. In: *Bildverarbeitung für die Medizin*. Informatik aktuell. Mar. 2015, pp. 498–503. (Cited on pp. 101, 104, 178)
DOI: 10.1007/978-3-662-46224-9_85

[Mat15] Philipp **Matthies**, Benjamin **Frisch**, Jakob **Vogel**, Tobias **Lasser**, Michael **Friebe** and Nassir **Navab**. 'Inside-Out Tracking for Flexible Hand-held Nuclear Tomographic Imaging'. In: *IEEE Nuclear Science Symposium and Medical Imaging Conference*. Oct. 2015. (Cited on pp. 108, 178)

[Vog15b] Jakob **Vogel**, Matthias **Wieczorek**, Christoph **Jud**, Florian **Schaff**, Franz **Pfeiffer** and Tobias **Lasser**. 'X-ray Tensor Tomography Reconstruction'. In: *Proceedings of International Meeting on Fully Three-Dimensional Image Reconstruction in Radiology and Nuclear Medicine (Fully3D)*. **(Oral presentation.)** June 2015. (Cited on pp. 149, 151, 171)
URL: http://www.fully3d.org/Fully3D_Proceedings_2015.pdf (Visited on 5th July 2015)

[Wie15b] Matthias **Wieczorek**, Jakob **Vogel**, Andreas **Weinmann**, Christoph **Jud**, Florian **Schaff**, Franz **Pfeiffer**, Maximilian **Baust** and Tobias **Lasser**. 'Total Variation Regularization for X-Ray Tensor Tomography'. In: *Proceedings of International Meeting on Fully Three-Dimensional Image Reconstruction in Radiology and Nuclear Medicine (Fully3D)*. June 2015. (Cited on pp. 170, 171, 178)
URL: http://www.fully3d.org/Fully3D_Proceedings_2015.pdf (Visited on 5th July 2015)

[Gar14] José **Gardiazabal**, Marco **Esposito**, Philipp **Matthies**, Aslı **Okur**, Jakob **Vogel**, Silvan **Kraft**, Benjamin **Frisch**, Tobias **Lasser** and Nassir **Navab**. 'Towards personalized interventional SPECT-CT imaging'. In: *Medical Image Computing and Computer-Assisted Intervention (MICCAI)*. Vol. 8673. Lecture Notes in Computer Science. Sept. 2014, pp. 504–511. (Cited on pp. 101, 113, 178)
DOI: 10.1007/978-3-319-10404-1_63

[Vog14] Jakob **Vogel**, Alexandru **Duliu**, Yuji **Oyamada**, José **Gardiazabal**, Tobias **Lasser**, Mahzad **Ziai**, Rüdiger **Hein** and Nassir **Navab**. 'Towards Robust Identification and Tracking of Nevi in Sparse Photographic Time Series'. In: *Medical Imaging 2014. Computer-Aided Diagnosis*. Vol. 9035. Proc. SPIE. Mar. 2014, p. 90353D. (Cited on p. 178)
DOI: 10.1117/12.2043788

[Mat13] Philipp **Matthies**, Kanishka **Sharma**, Aslı **Okur**, José **Gardiazabal**, Jakob **Vogel**, Tobias **Lasser** and Nassir **Navab**. 'First use of mini gamma cameras for intra-operative robotic SPECT reconstruction'. In: *Medical Image Computing and Computer-Assisted Intervention (MICCAI)*. Vol. 8149. Lecture Notes in Computer Science. Sept. 2013, pp. 163–170. (Cited on pp. 101, 106, 108, 109, 113, 177)
DOI: 10.1007/978-3-642-40811-3_21

[Wie13] Matthias **Wieczorek**, Jürgen **Frikel**, Jakob **Vogel**, Franz **Pfeiffer**, Laurent **Demaret** and Tobias **Lasser**. 'Curvelet sparse regularization for differential phase-contrast X-ray imaging'. In: *Proceedings of International Meeting on Fully Three-Dimensional Image Reconstruction in Radiology and Nuclear Medicine (Fully3D)*. June 2013. (Cited on p. 178)
URL: http://www.fully3d.org/Fully3D2013Proceedings.pdf (Visited on 5th July 2015)

[Che12b] Xiaoyin **Cheng**, Jun **Liu**, Jakob **Vogel**, Zhen **Liu**, Nassir **Navab**, Sibylle I. **Ziegler** and Kuangyu **Shi**. 'Time-Activity Curve based Sinogram Decomposition for Streak Artifacts Reduction in Dynamic PET Reconstruction'. In: *Proceedings of IEEE Medical Imaging Conference*. Oct. 2012. (Cited on p. 178)

[Vog12] Jakob **Vogel**, Tobias **Reichl**, José **Gardiazabal**, Nassir **Navab** and Tobias **Lasser**. 'Optimization of Acquisition Geometry for Intra-operative Tomographic Imaging'. In: *Medical Image Computing and Computer-Assisted Intervention (MICCAI)*. Vol. 7512. Lecture Notes in Computer Science. **(Oral presentation.)** Oct. 2012, pp. 42–49. (Cited on pp. 101, 113, 115, 118, 119, 131, 133)
DOI: 10.1007/978-3-642-33454-2_6

[Kei09a] Andreas **Keil**, Jakob **Vogel**, Günter **Lauritsch** and Nassir **Navab**. 'Dynamic Cone Beam Reconstruction Using a New Level Set Formulation'. In: *Medical Image Computing and Computer-Assisted Intervention (MICCAI)*. Vol. 5762. Lecture Notes in Computer Science. Sept. 2009, pp. 389–397. (Cited on pp. 87, 89, 90, 97)
DOI: 10.1007/978-3-642-04271-3_48

[Kei09b] Andreas **Keil**, Jakob **Vogel**, Günter **Lauritsch** and Nassir **Navab**. 'Dynamic Cone-Beam Reconstruction Using a Variational Level Set Formulation'. In: *Proceedings of International Meeting on Fully Three-Dimensional Image Reconstruction in Radiology and Nuclear Medicine (Fully3D)*. Sept. 2009, pp. 319–322. (Cited on pp. 87, 90, 97)
URL: http://www.fully3d.org/2009/3D09Proceedings.pdf (Visited on 5th July 2015)

[Las08a] Ruxandra **Lasowski**, Selim **Benhimane**, Jakob **Vogel**, Tobias F. **Jakob**, Christoph J. **Zech**, Christoph **Trumm**, Martin **Brokate** and Nassir **Navab**. 'Adaptive Visualization Using the Annealing M-estimator'. In: *Bildverarbeitung für die Medizin*. Informatik aktuell. Apr. 2008, pp. 348–352. (Cited on p. 177)
DOI: 10.1007/978-3-540-78640-5_70

[Las08b] Ruxandra **Lasowski**, Selim **Benhimane**, Jakob **Vogel**, Tobias F. **Jakobs**, Christoph J. **Zech**, Christoph **Trumm**, Christian **Clason** and Nassir **Navab**. 'Adaptive visualization for needle guidance in RF Liver Ablation: Taking organ deformation into account'. In: *Medical Imaging 2008. Visualization, Image-guided Procedures, and Modeling*. Vol. 6918. Proc. SPIE. Mar. 2008, 69180A. (Cited on p. 177)
DOI: 10.1117/12.769847

[Wen08] Thomas **Wendler**, Joerg **Traub**, Tobias **Lasser**, Marco **Feuerstein**, Jakob **Vogel**, Sibylle I. **Ziegler** and Nassir **Navab**. 'Combined ultrasound and gamma probe imaging for examination of thyroid nodules'. In: *Journal of Nuclear Medicine*. Vol. 49. Supplement 1, Meeting Abstracts. May 2008, 69P. (Cited on p. 177)
URL: http://jnm.snmjournals.org/content/49/supplement_1/69P.2.abstract (Visited on 5th July 2015)

[Alc07] Claudio **Alcérreca**, Jakob **Vogel**, Marco **Feuerstein** and Nassir **Navab**. 'A New Approach to Ultrasound Guided Radio-Frequency Needle Placement'. In: *Bildverarbeitung für die Medizin*. Informatik aktuell. Mar. 2007, pp. 26–30. (Cited on p. 177)
DOI: 10.1007/978-3-540-71091-2_6

[Feu07b] Marco **Feuerstein**, Tobias **Reichl**, Jakob **Vogel**, Armin **Schneider**, Hubertus **Feussner** and Nassir **Navab**. 'Magneto-optic Tracking of a Flexible Laparoscopic Ultrasound Transducer for Laparoscope Augmentation'. In: *Medical Image Computing and Computer-Assisted Intervention (MICCAI)*. Vol. 4791. Lecture Notes in Computer Science. Oct. 2007, pp. 458–466. (Cited on p. 177)
DOI: 10.1007/978-3-540-75757-3_56

[Wen07a] Thomas **Wendler**, Marco **Feuerstein**, Joerg **Traub**, Tobias **Lasser**, Jakob **Vogel**, Farhad **Daghighian**, Sibylle I. **Ziegler** and Nassir **Navab**. 'Real-Time Fusion of Ultrasound and Gamma Probe for Navigated Localization of Liver Metastases'. In: *Medical Image Computing and Computer-Assisted Intervention (MICCAI)*. Vol. 4792. Lecture Notes in Computer Science. Oct. 2007, pp. 252–260. (Cited on p. 177)
DOI: 10.1007/978-3-540-75759-7_31

Patent

[Kei10b] Andreas **Keil**, Jakob **Vogel**, Günter **Lauritsch** and Nassir **Navab**. 'Method for visualising structures in a body, in particular in the body of a patient'. Patent EP 2,187,353. May 2010. (Cited on p. 87)
URL: http://worldwide.espacenet.com/publicationDetails/biblio?CC=EP&NR=2187353 (Visited on 5th July 2015)

Other

[Wie14] Matthias **Wieczorek**, Jakob **Vogel** and Tobias **Lasser**. *CampRecon — a software framework for linear inverse problems*. Tech. rep. TUM-I1401. Technische Universität München, 2014. (Cited on pp. 161, 178)
URL: https://mediatum.ub.tum.de/node?id=1191442 (Visited on 5th July 2015)

References

[Abb04] Ernst Karl **Abbe**. *Abhandlungen über die Theorie des Mikroskops [Treatises on the Theory of the Microscope]*. Vol. 1. Gesammelte Abhandlungen [Collected Treatises]. Jena: Gustav Fischer, 1904. (Cited on p. 137)
URL: http://books.google.de/books?id=ezTQAAAAMAAJ (Visited on 13th July 2015)

[Abr96] Herbert L. **Abrams**. 'Cardiac Radiology'. In: *A History of the Radiological Sciences: Diagnosis*. Ed. by Raymond **Gagliardi** and Bruce L. **McClennan**. 1996. Chap. 10, pp. 254–269. (Cited on pp. 22, 87)
URL: http://www.arrs.org/Publications/HRS.aspx (Visited on 19th May 2015)

[Ach06a] Stephan **Achenbach**. 'Computed Tomography Coronary Angiography'. In: *Journal of the American College of Cardiology* 48.10 (Nov. 2006), pp. 1919–1928. (Cited on pp. 87, 89)
DOI: 10.1016/j.jacc.2006.08.012

[Ach06b] Stephan **Achenbach**. *Half-Scan vs. Multi-Segment Reconstruction for Computed Tomography Coronary Angiography. Considerations on the effects on image quality*. Tech. rep. A91CT-00352-12C1-7600. Forchheim: Siemens AG, Medical Solutions, Computed Tomography, Dec. 2006. (Cited on pp. 87, 89)

[Ahn03] Sangtae **Ahn** and Jeffrey A. **Fessler**. 'Globally Convergent Image Reconstruction for Emission Tomography Using Relaxed Ordered Subsets Algorithms'. In: *IEEE Transactions on Medical Imaging* 22.5 (May 2003), pp. 613–626. (Cited on pp. 67, 70, 76)
DOI: 10.1109/TMI.2003.812251

[All51] Herbert C. **Allen**, Raymond L. **Libby** and Benedict **Cassen**. 'The Scintillation Counter in Clinical Studies of Human Thyroid Physiology Using I^{131}'. In: 11.5 (May 1951), pp. 492–511. (Cited on pp. 21, 24)
DOI: 10.1210/jcem-11-5-492

[Amb36] Victor A. **Ambartsumian**. 'On the Derivation of the Frequently Function of Space Velocities of the Stars from the Observed Radial Velocities'. In: *Monthly Notices of the Royal Astronomical Society* 96.3 (Jan. 1936), pp. 172–178. (Cited on p. 81)
DOI: 10.1093/mnras/96.3.172

[Amb73] James **Ambrose**. 'Computerized transverse axial scanning (tomography): Part 2. Clinical application'. In: *British Journal of Radiology* 46.552 (Dec. 1973), pp. 1023–1047. (Cited on p. 35)
DOI: 10.1259/0007-1285-46-552-1023

[Amb80] Victor A. **Ambartsumian**. 'On Some Trends in the Development of Astrophysics'. In: *Annual Review of Astronomy and Astrophysics* 18 (Sept. 1980), pp. 1–14. (Cited on p. 81)
DOI: 10.1146/annurev.aa.18.090180.000245

[And05] Masami **Ando**, Katsuhito **Yamasaki**, Fukai **Toyofuku**, Hiroshi **Sugiyama**, Chiho **Ohbayashi**, Gang **Li**, Lin **Pan**, Xiaoming **Jiang**, Wanwisa **Pattanasiriwisawa**, Daisuke **Shimao**, Eiko **Hashimoto**, Tatsuro **Kimura**, Masazumi **Tsuneyoshi**, Ei **Ueno**, Kenji **Tokumori**, Anton **Maksimenko**, Yoshiharu **Higashida** and Masatsugu **Hirano**. 'Attempt at Visualizing Breast Cancer with X-ray Dark Field Imaging'. In: *Japanese Journal of Applied Physics* 44.4L (Apr. 2005), pp. L528–L531. (Cited on p. 146)
DOI: 10.1143/JJAP.44.L528

[And33] Carl David **Anderson**. 'The Positive Electron'. In: *Physical Review* 43 (Mar. 1933), pp. 491–494. (Cited on p. 40)
DOI: 10.1103/PhysRev.43.491

[And36] Carl David **Anderson**. *The production and properties of positrons*. Nobel Lecture. Dec. 1936. (Cited on p. 41)
URL: http://www.nobelprize.org/nobel_prizes/physics/laureates/1936/anderson-lecture.pdf (Visited on 5th July 2015)

[And84] Anders H. **Andersen** and Avinash C. **Kak**. 'Simultaneous Algebraic Reconstruction Technique (SART): A superior implementation of the ART algorithm'. In: *Ultrasonic Imaging* 6.1 (Jan. 1984), pp. 81–94. (Cited on pp. 60, 155)
DOI: 10.1177/016173468400600107

[Ang61] Hal O. **Anger**. 'Radiation Image Device'. Patent US 3,011,057. Nov. 1961. (Cited on pp. 21, 24)
URL: http://worldwide.espacenet.com/publicationDetails/biblio?CC=US&NR=3011057 (Visited on 5th July 2015)

[Ang67] Hal O. **Anger**, D. C. **Price** and P. E. **Yost**. 'Transverse-Section Tomography with the Scintillation Camera'. In: *Journal of Nuclear Medicine* 8.4 (Apr. 1967), p. 314. (Cited on p. 39)
URL: http://jnm.snmjournals.org/content/8/4/261.full.pdf+html (Visited on 5th July 2015)

[Arf10] F. **Arfelli**, L. **Rigon** and R. H. **Menk**. 'Microbubbles as x-ray scattering contrast agents using analyzer-based imaging'. In: *Physics in Medicine and Biology* 55.6 (Feb. 2010), pp. 1643–1658. (Cited on p. 146)
DOI: 10.1088/0031-9155/55/6/008

[Bae17] Carlo **Baese**. 'Method of, and Apparatus for, the Localization of Foreign Objects in, and the Radio-therapic Treatment of, the Human Body by the X-rays'. Patent GB 100,491. July 1917. (Cited on p. 30)
URL: http://worldwide.espacenet.com/publicationDetails/biblio?CC=GB&NR=100491 (Visited on 5th July 2015)

[Bar03] S. Serge **Barold**. 'Willem Einthoven and the Birth of Clinical Electrocardiography a Hundred Years Ago'. In: *Cardiac Electrophysiology Review* 7.1 (Jan. 2003), pp. 99–104. (Cited on p. 88)
DOI: 10.1023/A:1023667812925

[Bar04] David **Bardell**. 'The invention of the microscope'. In: *BIOS* 75.2 (May 2004), pp. 78–84. (Cited on p. 137)
DOI: 10.1893/0005-3155(2004)75<78:TIOTM>2.0.CO;2

[Bar17] Charles Glover **Barkla**. 'On X-rays and the Theory of Radiation'. In: *Philosophical Transactions of the Royal Society of London. A* 217.549–560 (Aug. 1917), pp. 315–360. (Cited on p. 14)
DOI: 10.1098/rsta.1918.0009

[Bar20] Charles Glover **Barkla**. *Characteristic Röntgen Radiation*. Nobel Lecture. June 1920. (Cited on p. 14)
URL: http://www.nobelprize.org/nobel_prizes/physics/laureates/1917/barkla-lecture.pdf (Visited on 5th July 2015)

[Bar80] Roland **Barthes**. *La chambre claire [The bright room]. Note sur la photographie [Note about photography]*. Paris: Gallimard, 1980. ISBN: 978-2070205417. (Cited on p. 6)

[Bar81] Harrison H. **Barrett** and William **Swindell**. 'Theory of Random Processes'. In: *Radiological Imaging. The Theory of Image Formation, Detection, and Processing*. San Diago: Academic Press, 1981. Chap. 3, pp. 62–116. (Cited on p. 65)
DOI: 10.1016/B978-0-08-057230-7.50010-X

[Bar94] Richard **Barrett**, Michael **Berry**, Tony F. **Chan**, James **Demmel**, June **Donato**, Jack **Dongarra**, Victor **Eijkhout**, Roldan **Pozo**, Charles **Romine** and Henk van der **Vorst**. *Templates for the Solution of Linear Systems. Building Blocks for Iterative Methods*. Philadelphia: SIAM, 1994. ISBN: 978-0898713282. (Cited on pp. 57, 58, 63)
DOI: 10.1137/1.9781611971538

[Bar97] Harrison H. **Barrett**, Timothy **White** and Lucas C. **Parra**. 'List-mode likelihood'. In: *Journal of the Optical Society of America A* 14.11 (Nov. 1997), pp. 2914–2923. (Cited on pp. 65, 66, 108)
DOI: 10.1364/JOSAA.14.002914

[Bau06] Joachim **Baumann**, Manfred **Schuster**, Jörg **Freudenberger**, Eckhard **Hempel**, Martin **Hoheisel**, Thomas **Mertelmeier**, Stefan **Popescu** and Martin **Engelhardt**. 'Fokus-Detektor-Anordnung zur Erzeugung von Phasenkontrast-Röntgenaufnahmen und Verfahren hierzu [Focus-detector-setup for the acquisition of phase contrast X-ray images and respective method]'. Patent EP 1,803,398. Aug. 2006. (Cited on p. 146)
URL: http://worldwide.espacenet.com/publicationDetails/biblio?CC=EP&NR=1803398 (Visited on 8th July 2015)

[Bay14] Florian L. **Bayer**, Shiyang **Hu**, Andreas **Maier**, Thomas **Weber**, Gisela **Anton**, Thilo **Michel** and Christian P. **Riess**. 'Reconstruction of scalar and vectorial components in X-ray dark-field tomography'. In: *Proceedings of the National Academy of Sciences of the United States of America* 111.35 (Sept. 2014), pp. 12699–12704. (Cited on p. 149)
DOI: 10.1073/pnas.1321080111

[Bec01] Antoine Henri **Becquerel**. 'The Radio-Activity of Matter'. In: *Nature* 63.1634 (Feb. 1901), pp. 396–398. (Cited on p. 18)
DOI: 10.1038/063396d0

[Bec03] Antoine Henri **Becquerel**. *On radioactivity, a new property of matter*. Nobel Lecture. Dec. 1903. (Cited on p. 18)
URL: http://www.nobelprize.org/nobel_prizes/physics/laureates/1903/becquerel-lecture.pdf (Visited on 5th July 2015)

[Bec09a] Martin **Bech**. 'X-ray imaging with a grating interferometer'. PhD thesis. Copenhagen: University of Copenhagen, Faculty of Science, May 2009. (Cited on pp. 145, 146)
URL: http://www.nbi.ku.dk/english/research/phd_theses/phd_theses_2009/martin_bech/Martin_Bech_July09.pdf (Visited on 6th July 2015)

[Bec09b] Martin **Bech**, Oliver **Bunk**, Christian **David**, Ronald **Ruth**, Jeff **Rifkin**, Rod **Loewen**, Robert **Feidenhans'l** and Franz **Pfeiffer**. 'Hard X-ray phase-contrast imaging with the Compact Light Source based on inverse Compton X-rays'. In: *Journal of Synchrotron Radiation* 16.1 (Jan. 2009), pp. 43–47. (Cited on p. 140)
DOI: 10.1107/S090904950803464X

[Bec09c] Martin **Bech**, Torben H. **Jensen**, Robert **Feidenhans'l**, Oliver **Bunk**, Christian **David** and Franz **Pfeiffer**. 'Soft-tissue phase-contrast tomography with an x-ray tube source'. In: *Physics in Medicine and Biology* 54.9 (May 2009), pp. 2747–2753. (Cited on p. 146)
DOI: 10.1088/0031-9155/54/9/010

[Bec09d] Amir **Beck** and Marc **Teboulle**. 'A Fast Iterative Shrinkage-Thresholding Algorithm for Linear Inverse Problems'. In: *SIAM Journal on Imaging Sciences* 2.1 (2009), pp. 183–202. (Cited on p. 79)
DOI: 10.1137/080716542

[Bec10] Martin **Bech**, Oliver **Bunk**, Tilman **Donath**, Robert **Feidenhans'l**, Christian **David** and Franz **Pfeiffer**. 'Quantitative x-ray dark-field computed tomography'. In: *Physics in Medicine and Biology* 55.18 (Sept. 2010), pp. 5529–5539. (Cited on pp. 143, 144, 151)
DOI: 10.1088/0031-9155/55/18/017

[Bec96a] Antoine Henri **Becquerel**. 'Sur les radiations émises par phosphorescence [On rays emitted by phosphorescence]'. In: *Comptes Rendus Hebdomadaires des Séances de l'Académie des Sciences* 122 (Feb. 1896), pp. 420–421. (Cited on p. 18)
URL: http://catalogue.bnf.fr/ark:/12148/cb343481087 (Visited on 5th July 2015)

[Bec96b] Antoine Henri **Becquerel**. 'Sur les radiations invisibles émises par les corps phosphorescents [On invisible rays emitted by phosphorescent bodies]'. In: *Comptes Rendus Hebdomadaires des Séances de l'Académie des Sciences* 122 (Mar. 1896), pp. 501–503. (Cited on p. 18)
URL: http://catalogue.bnf.fr/ark:/12148/cb343481087 (Visited on 5th July 2015)

[Bec96c] Antoine Henri **Becquerel**. 'Sur quelques propriétés nouvelles des radiations invisibles émises par divers corps phosphorescents [On some new properties of the invisible rays emitted by different phosphorescent bodies]'. In: *Comptes Rendus Hebdomadaires des Séances de l'Académie des Sciences* 122 (Mar. 1896), pp. 559–564. (Cited on p. 18)
URL: http://catalogue.bnf.fr/ark:/12148/cb343481087 (Visited on 5th July 2015)

[Bec96d] Antoine Henri **Becquerel**. 'Sur les radiations invisibles émises par les sels d'uranium [On the invisible rays emitted by uranium salts]'. In: *Comptes Rendus Hebdomadaires des Séances de l'Académie des Sciences* 122 (Mar. 1896), pp. 689–694. (Cited on p. 18)
URL: http://catalogue.bnf.fr/ark:/12148/cb343481087 (Visited on 5th July 2015)

[Bec96e] Antoine Henri **Becquerel**. 'Sur les propriétés différentes des radiations invisibles émises par les sels d'uranium, et du rayonnement de la paroi anticathodique d'un tube de Crookes [On the different properties of the invisible rays emitted by uranium salts, and of the radiation of the anticathodic wall of a Crookes tube]'. In: *Comptes Rendus Hebdomadaires des Séances de l'Académie des Sciences* 122 (Mar. 1896), pp. 762–767. (Cited on p. 18)
URL: http://catalogue.bnf.fr/ark:/12148/cb343481087 (Visited on 5th July 2015)

[Bec96f] Antoine Henri **Becquerel**. 'Émission de radiations nouvelles par l'uranium métallique [Emission of new rays by metallic uranium]'. In: *Comptes Rendus Hebdomadaires des Séances de l'Académie des Sciences* 122 (May 1896), pp. 1086–1088. (Cited on p. 18)
URL: http://catalogue.bnf.fr/ark:/12148/cb343481087 (Visited on 5th July 2015)

[Bee52] August **Beer**. 'Bestimmung der Absorption des rothen Lichts in farbigen Flüssigkeiten [Determination of the absorption of red light in coloured liquids]'. In: *Annalen der Physik und Chemie* 162.5 (1852), pp. 78–88. (Cited on p. 17)
DOI: 10.1002/andp.18521620505

[Ber01] Leonard **Berlin**. 'Radiation-Induced Skin Injuries and Fluoroscopy'. In: *American Journal of Roentgenology* 177.1 (July 2001), pp. 21–25. (Cited on p. 25)
DOI: 10.2214/ajr.177.1.1770021

[Bey00] Thomas **Beyer**, David W. **Townsend**, Tony **Brun**, Paul E. **Kinahan**, Martin **Charron**, Raymond **Roddy**, Jeff **Jerin**, John **Young**, Larry **Byars** and Ronald **Nutt**. 'A Combined PET/CT Scanner for Clinical Oncology'. In: *Journal of Nuclear Medicine* 41.8 (Aug. 2000), pp. 1369–1379. (Cited on p. 43)
URL: http://jnm.snmjournals.org/content/41/8/1369.full.pdf+html (Visited on 5th July 2015)

[BfS15a] **Bundesamt für Strahlenschutz**. *Das Mammographie-Screening-Programm in Deutschland [The Mammography Screening Programme in Germany]*. Website. Mar. 2015. (Cited on p. 27)
URL: http://www.bfs.de/de/ion/medizin/diagnostik/roentgen/Mammographie.html (Visited on 21st May 2015)

[BfS15b] **Bundesamt für Strahlenschutz**. *Röntgendiagnostik: Häufigkeit und Strahlenexposition [X-ray Diagnostics: Frequency and Radiation Exposure]*. Website. Apr. 2015. (Cited on p. 27)
URL: http://www.bfs.de/de/ion/medizin/diagnostik/roentgen/haeufigkeit_strahlenexposition.html (Visited on 21st May 2015)

[Bis05] Franco **Bistolfi**. 'Alessandro Vallebona (1899-1987) – Ricordo di un grande Radiologo e del suo contributo allo sviluppo delle scienze radiologiche [Alessandro Vallebona (1899-1987) – Memory of a Great Radiologist and of His Contribution to the Development of the Radiologic Sciences]'. In: *Fisica in Medicina* 2 (Apr. 2005), pp. 115–123. (Cited on p. 30)
URL: http://www.fisicamedica.it/aifm/periodico/2005/2005_2_Fisica_in_Medicina.pdf (Visited on 23rd May 2015)

[Bis06] Christopher M. **Bishop**. 'Principal Components Analysis'. In: *Pattern Recognition and Machine Learning*. New York: Springer, 2006. Chap. 12.1. ISBN: 978-0387310732. (Cited on p. 157)

[Bla96] William H. **Blahd**. 'Ben Cassen and the Development of the Rectilinear Scanner'. In: *Seminars in Nuclear Medicine* 26.3 (1996), pp. 165–170. (Cited on pp. 21, 24)
DOI: 10.1016/S0001-2998(96)80021-3

[Blo06] Christophe **Blondel**, Grégoire **Malandain**, Régis **Vaillant** and Nicholas **Ayache**. 'Reconstruction of Coronary Arteries from a Single Rotational X-ray Projection Sequence'. In: *IEEE Transactions on Medical Imaging* 25.5 (May 2006), pp. 653–663. (Cited on p. 89)
DOI: 10.1109/TMI.2006.873224

[Blo98] Peter **Blomgren** and Tony F. **Chan**. 'Color TV. Total Variation Methods for Restoration of Vector-Valued Images'. In: *IEEE Transactions on Image Processing* 7.3 (Mar. 1998), pp. 304–309. (Cited on p. 73)
DOI: 10.1109/83.661180

[Blu09] Moritz **Blume**, Andreas **Keil**, Nassir **Navab** and Magdalena **Rafecas**. 'Blind Motion Compensation for Positron-Emission-Tomography'. In: *Medical Imaging 2009. Physics of Medical Imaging*. Vol. 7258. Proc. SPIE. Mar. 2009, 72580T. (Cited on p. 92)
DOI: 10.1117/12.811118

[Blu13] Christina **Bluemel**, Andreas **Schnelzer**, Aslı **Okur**, Alexandra **Ehlerding**, Stefan **Paepke**, Klemens **Scheidhauer** and Marion **Kiechle**. 'Freehand SPECT for image-guided sentinel lymph node biopsy in breast cancer'. In: *European Journal of Nuclear Medicine and Molecular Imaging* 40.11 (Oct. 2013), pp. 1656–1661. (Cited on p. 103)
DOI: 10.1007/s00259-013-2473-0

[Boc00] Moshe **Bocher**, Adi **Balan**, Yodphat **Krausz**, Yigal **Shrem**, Albert **Lonn**, Michael **Wilk** and Roland **Chisin**. 'Gamma camera-mounted anatomical X-ray tomography: Technology, system characteristics and first images'. In: *European Journal of Nuclear Medicine* 27.6 (June 2000), pp. 619–627. (Cited on p. 43)
DOI: 10.1007/s002590050555

[Boc06] H. B. A. **Bockwinkel**. 'Over de Voortplanting van Licht in een Twee-Assig Kristal rondom een Middelpunt van Trilling [On the Propagation of Light in a Biaxial Crystal about a Midpoint of Oscillation]'. In: *Verslag van de Gewone Vergaderingen der Wis- en Natuurkundige Afdeeling*. Vol. 14. Amsterdam: Koninklijke Akademie van Wetenschappen, Jan. 1906, pp. 636–651. (Cited on p. 81)
URL: https://archive.org/details/p2verslagvandege14akad (Visited on 30th June 2015)

[Boc22] André Edmond Marie **Bocage**. 'Procédé et dispositifs de radiographie sur plaque en mouvement [Method of and Apparatus for Radiography on a Moving Plate]'. Patent FR 536,464. May 1922. (Cited on p. 30)
URL: https://depatisnet.dpma.de/DepatisNet/depatisnet?action=pdf&docid=FR000000536464A (Visited on 5th July 2015)

[Bon65a] Ulrich **Bonse** and M. **Hart**. 'An X-Ray Interferometer'. In: *Applied Physics Letters* 6.8 (Apr. 1965), pp. 155–156. (Cited on p. 140)
DOI: 10.1063/1.1754212

[Bon65b] Ulrich **Bonse** and M. **Hart**. 'An X-Ray Interferometer with Long Separated Interfering Beam Paths'. In: *Applied Physics Letters* 7.4 (Aug. 1965), pp. 99–100. (Cited on p. 140)
DOI: 10.1063/1.1754330

[Bon97] Ulrich **Bonse**. 'Interferometry'. In: *Röntgen Centennial. X-rays in Natural and Life Sciences*. Ed. by Axel **Haase**, Gottfried **Landwehr** and Eberhard **Umbach**. Singapore: World Scientific, 1997, pp. 521–537. ISBN: 978-9810230852. (Cited on p. 140)

[Bou29] Pierre **Bouguer**. *Essai d'Optique sur la Gradation de la Lumière [Essay on Optics about the Gradation of Light]*. Paris, 1729. (Cited on p. 17)
URL: http://books.google.com/books?id=JNkTAAAAQAAJ (Visited on 5th July 2015)

[Bou33] Albert **Bouwers**. 'X-ray Tube'. Patent US 1,893,759. Jan. 1933. (Cited on p. 12)
URL: http://worldwide.espacenet.com/publicationDetails/biblio?CC=US&NR=1893759 (Visited on 5th July 2015)

[Bow12] J. **Bowsher**, S. **Yan**, J. **Roper**, W. **Giles** and F. **Yin**. 'TU-A-BRA-01: A Robotic Multi-Pinhole SPECT System for Onboard and Other Region-Of-Interest Imaging'. In: *Medical Physics* 39.6 (June 2012), pp. 3887–3888. (Cited on p. 111)
DOI: 10.1118/1.4735869

[Boy11] Stephen **Boyd**, Neal **Parikh**, Eric **Chu**, Borja **Peleato** and Jonathan **Eckstein**. 'Distributed Optimization and Statistical Learning via the Alternating Direction Method of Multipliers'. In: *Foundations and Trends in Machine Learning* 3.1 (July 2011), pp. 1–122. (Cited on p. 79)
DOI: 10.1561/2200000016

[Bra55] Ronald N. **Bracewell** and J. A. **Roberts**. 'Aerial Smoothing in Radio Astronomy'. In: *Australian Journal of Physics* 7.4 (1955), pp. 615–640. (Cited on p. 81)
DOI: 10.1071/PH540615

[Bra56] Ronald N. **Bracewell**. 'Strip Integration in Radio Astronomy'. In: *Australian Journal of Physics* 9.2 (1956), pp. 198–217. (Cited on pp. 49, 81)
DOI: 10.1071/PH560198

[Bra67] Ronald N. **Bracewell** and A. C. **Riddle**. 'Inversion of Fan-Beam Scans in Radio Astronomy'. In: *Astrophysical Journal* 150 (Nov. 1967), pp. 427–434. (Cited on pp. 49, 52, 81)
DOI: 10.1086/149346

[Bra96] Hermann **Braus**. 'Ueber Photogramme von Metallinjectionen mittelst Röntgen-Strahlen [About Photograms of Metal Injections by Means of X-rays]'. In: *Anatomischer Anzeiger* 11.21 (1896), pp. 625–629. (Cited on pp. 22, 23)
URL: http://digi.ub.uni-heidelberg.de/diglit/braus1896 (Visited on 5th July 2015)

[Bra98] Savile **Bradbury** and Brian **Bracegirdle**. *Introduction to Light Microscopy*. Oxford: BIOS Scientific Publishers, June 1998. ISBN: 978-1859961216. (Cited on p. 137)

[Bre52] Henri **Breuil**. *Quatre cents siècles d'art pariétal [40'000 years of parietal art]*. Montignac, 1952. (Cited on p. 3)

[Bri00] William L. **Briggs**, Van Emden **Hensen** and Steve F. **McCormick**. *A Multigrid Tutorial*. Second edition. Philadelphia: SIAM, 2000. ISBN: 978-0898714623. (Cited on pp. 57, 58)
DOI: 10.1137/1.9780898719505

[Bro53] Gordon L. **Brownell** and William H. **Sweet**. 'Localization of Brain Tumors with Positron Emitters'. In: *Nucleonics* 11 (1953), pp. 40–45. (Cited on p. 41)

[Bro95a] Percy **Brown**. 'American Martyrs to Radiology: Clarence Madison Dally (1865–1904)'. In: *American Journal of Roentgenology* 164.1 (Jan. 1995), pp. 237–239. (Cited on p. 25)
DOI: 10.2214/ajr.164.1.7998548

[Bro95b] Percy **Brown**. 'American Martyrs to Radiology: Elizabeth Fleischman Ascheim (1859–1905)'. In: *American Journal of Roentgenology* 164.2 (Feb. 1995), pp. 497–499. (Cited on pp. 22, 25)
DOI: 10.2214/ajr.164.2.7839997

[Bro95c] Percy **Brown**. 'American Martyrs to Radiology: Mihran Krikor Kassabian (1870–1910)'. In: *American Journal of Roentgenology* 164.5 (May 1995), pp. 1285–1289. (Cited on p. 25)
DOI: 10.2214/ajr.164.5.7717249

[Bro99] Gordon L. **Brownell**. *A History of Positron Imaging*. Lecture. Oct. 1999. (Cited on p. 41)
URL: http://neurosurgery.mgh.harvard.edu/docs/PEThistory.pdf (Visited on 20th May 2015)

[Bry84] D. J. **Bryant**, J. A. **Payne**, D. N. **Firmin** and D. B. **Longmore**. 'Measurement of Flow with NMR Imaging Using a Gradient Pulse and Phase Difference Technique'. In: *Journal of Computer Assisted Tomography* 8.4 (Aug. 1984), pp. 588–593. (Cited on p. 45)
URL: http://journals.lww.com/jcat/Fulltext/1984/08000/Measurement_of_Flow_with_NMR_Imaging_Using_a.2.aspx (Visited on 8th July 2015)

[Bud74] Thomas F. **Budinger** and Grant T. **Gullberg**. *Three-Dimensional Reconstruction in Nuclear Medicine by Iterative Least-Squares and Fourier Transform Techniques*. Tech. rep. Berkeley: University of California, Jan. 1974. (Cited on p. 39)
URL: https://inis.iaea.org/search/search.aspx?orig_q=RN:5124834 (Visited on 20th June 2015)

[Bud97] Thomas F. **Budinger**. 'Physical Characteristics and Relative Merits of Ten Medical Imaging Technologies'. In: *Röntgen Centennial. X-rays in Natural and Life Sciences*. Ed. by Axel **Haase**, Gottfried **Landwehr** and Eberhard **Umbach**. Singapore: World Scientific, 1997, pp. 173–206. ISBN: 978-9810230852. (Cited on pp. 44, 45)

[Bug09] E. **Buglova** and R. **Martinčič**, eds. *The Radiological Accident in Nueva Aldea*. Vienna: International Atomic Energy Agency, 2009. ISBN: 978-9201030092. (Cited on p. 28)
URL: http://www-pub.iaea.org/books/IAEABooks/8117/The-Radiological-Accident-in-Nueva-Aldea (Visited on 5th July 2015)

[Buz08] Thorsten M. **Buzug**. *Computed Tomography*. Berlin: Springer, 2008. (Cited on pp. 14, 17, 18, 20, 21, 30, 35, 37, 47, 49, 50, 52, 58, 59, 66)
DOI: 10.1007/978-3-540-39408-2

[Byr01] Charles **Byrne**. 'Likelihood Maximization for List-Mode Emission Tomographic Image Reconstruction'. In: *IEEE Transactions on Medical Imaging* 20.10 (Oct. 2001), pp. 1084–1092. (Cited on pp. 66, 108)
DOI: 10.1109/42.959305

[Byr02] Charles **Byrne**. 'Iterative oblique projection onto convex sets and the split feasibility problem'. In: *Inverse Problems* 18.2 (Apr. 2002), pp. 441–453. (Cited on p. 60)
DOI: 10.1088/0266-5611/18/2/310

[Can02] Emmanuel J. **Candès** and David L. **Donoho**. 'Recovering Edges in Ill-Posed Inverse Problems. Optimality of Curvelet Frames'. In: *Annals of Statistics* 30.3 (June 2002), pp. 784–842. (Cited on p. 77)
DOI: 10.1214/aos/1028674842

[Can06] Emmanuel J. **Candès**, Justin K. **Romberg** and Terence **Tao**. 'Stable Signal Recovery from Incomplete and Inaccurate Measurements'. In: *Communications on Pure and Applier Mathematics* 59.8 (Aug. 2006), pp. 1207–1223. (Cited on p. 76)
DOI: 10.1002/cpa.20124

[Can78] F. **Cannizzaro**, G. **Greco**, S. **Rizzo** and E. **Sinagra**. 'Results of the Measurements Carried Out in Order to Verify the Validity of the Poisson-Exponential Distribution in Radioactive Decay Events'. In: *International Journal of Applied Radiation and Isotopes* 29.11 (Nov. 1978), pp. 649–652. (Cited on p. 65)
DOI: 10.1016/0020-708X(78)90101-1

[Can98] Emmanuel J. **Candès**. 'Ridgelets. Theory and Applications'. PhD thesis. Stanford: Stanford University, Department of Statistics, Aug. 1998. (Cited on p. 77)
URL: http://statweb.stanford.edu/~candes/papers/Thesis.ps.gz (Visited on 5th July 2015)

[Car02] Émile **Cartailhac**. 'Les cavernes ornées de dessins. La grotte d'Altamira, Espagne. «Mea culpa» d'un sceptique. [The caves decorated with paintings. The cave of Altamira, Spain. 'Mea culpa' of a sceptic.]' In: *L'Anthropologie* 13 (1902), pp. 348–354. (Cited on p. 3)
URL: http://catalogue.bnf.fr/ark:/12148/cb343482075 (Visited on 4th Sept. 2015)

[Car03] Émile **Cartailhac** and Henri **Breuil**. 'Les peintures préhistoriques de la grotte d'Altamira à Santillane (Espagne) [The prehistoric paintings in the cave of Altamira in Santillane (Spain)]'. In: *Comptes rendus des séances de l'Académie des Inscriptions et Belles-lettres* 256 (1903), pp. 256–264. (Cited on p. 3)
URL: http://www.persee.fr/web/revues/home/prescript/revue/crai (Visited on 4th Sept. 2015)

[Cas49] Benedict **Cassen**, Larry **Curtis** and Clifford W. **Reed**. *A Sensitive Directional Gamma-ray Detector*. Tech. rep. 49. UCLA, 1949. (Cited on pp. 21, 24)

[Cas50] Benedict **Cassen**, Larry **Curtis** and Clifford W. **Reed**. 'A Sensitive Directional Gamma-ray Detector'. In: *Nucleonics* 6 (1950), pp. 78–80. (Cited on pp. 21, 24)

[Cen01a] Yair **Censor**, Dan **Gordon** and Rachel **Gordon**. 'BICAV. A Block-Iterative Parallel Algorithm for Sparse Systems With Pixel-Related Weighting'. In: *IEEE Transactions on Medical Imaging* 20.10 (Oct. 2001), pp. 1050–1060. (Cited on p. 60)
DOI: 10.1109/42.959302

[Cen01b] Yair **Censor**, Dan **Gordon** and Rachel **Gordon**. 'Component averaging. An efficient iterative parallel algorithm for large and sparse unstructured problems'. In: *Parallel Computing* 27.6 (May 2001), pp. 777–808. (Cited on p. 60)
DOI: 10.1016/S0167-8191(00)00100-9

[Cen83] Yair **Censor**, Paul P. B. **Eggermont** and Dan **Gordon**. 'Strong Underrelaxation in Kaczmarz's Method for Inconsistent Systems'. In: *Numerische Mathematik* 41.1 (Feb. 1983), pp. 83–92. (Cited on p. 59)
DOI: 10.1007/BF01396307

[Cha01] Tony F. **Chan** and Luminita A. **Vese**. 'Active Contours Without Edges'. In: *IEEE Transactions on Image Processing* 10.2 (Feb. 2001), pp. 266–277. (Cited on p. 93)
DOI: 10.1109/83.902291

[Cha11] Antonin **Chambolle** and Thomas **Pock**. 'A First-Order Primal-Dual Algorithm for Convex Problems with Applications to Imaging'. In: *Journal of Mathematical Imaging and Vision* 40.1 (May 2011), pp. 120–145. (Cited on p. 79)
DOI: 10.1007/s10851-010-0251-1

[Cha22] Jean-François **Champollion**. *Lettre à M. Dacier relative à l'alphabet des hiéroglyphes phonétiques [Letter to M. Dacier concerning the alphabet of the phonetic hieroglyphs]*. Paris: Firmin-Didot, 1822. (Cited on p. 3)
URL: http://catalogue.bnf.fr/ark:/12148/cb377454716 (Visited on 4th Sept. 2015)

[Cha38] Henri **Chaoul** and Gustav **Grossmann**. 'Verfahren und Einrichtung zur röntgenographischen Darstellung einer planparallelen Körperschicht [Method of and Apparatus for Röntgenographically Acquiring a Plane-Parallel Section of the Body]'. Patent DE 658,784. Mar. 1938. (Cited on p. 30)
URL: http://worldwide.espacenet.com/publicationDetails/biblio?CC=DE&NR=658784 (Visited on 5th July 2015)

[Cha97a] Antonin **Chambolle** and Pierre-Louis **Lions**. 'Image recovery via total variation minimization and related problems'. In: *Numerische Mathematik* 76.2 (Apr. 1997), pp. 167–188. (Cited on pp. 73, 76)
DOI: 10.1007/s002110050258

[Cha97b] D. **Chapman**, W. **Thomlinson**, R. E. **Johnston**, D. **Washburn**, E. **Pisano**, N. **Gmür**, Z. **Zhong**, R. **Menk**, F. **Arfelli** and D. **Sayers**. 'Diffraction enhanced x-ray imaging'. In: *Physics in Medicine and Biology* 42.11 (Nov. 1997), pp. 2015–2025. (Cited on p. 140)
DOI: 10.1088/0031-9155/42/11/001

[Cha99] Tony F. **Chan**, Gene H. **Golub** and Pep **Mulet**. 'A nonlinear primal-dual method for total variation-based image restoration'. In: *SIAM Journal on Scientific Computing* 20.6 (1999), pp. 1964–1977. (Cited on p. 79)
DOI: 10.1137/S1064827596299767

[Che01] Scott Shaobing **Chen**, David L. **Donoho** and Michael A. **Saunders**. 'Atomic Decomposition by Basis Pursuit'. In: *SIAM Review* 43.1 (2001), pp. 129–159. (Cited on p. 78)
DOI: 10.1137/S003614450037906X

[Che06] Simon R. **Cherry** and Magnus **Dahlbom**. *PET: Physics, Instrumentation, and Scanners*. Ed. by Michael E. **Phelps**. New York: Springer, 2006. ISBN: 978-0387323022. (Cited on pp. 41, 42)
DOI: 10.1007/0-387-34946-4

[Che10] Dmitry **Chetverikov** and Attila **Axt**. 'Approximation-free Running SVD and its Application to Motion Detection'. In: *Pattern Recognition Letters* 31.9 (July 2010), pp. 891–897. (Cited on p. 119)
DOI: 10.1016/j.patrec.2009.12.031

[Che12a] Yuxiang **Chen**, Thomas **Hrabe**, Stefan **Pfeffer**, Olivier **Pauly**, Diana **Mateus**, Nassir **Navab** and Friedrich **Förster**. 'Detection and Identification of Macromolecular Complexes in Cryo-Electron Tomograms using Support Vector Machines'. In: *IEEE International Symposium on Biomedical Imaging (ISBI)*. May 2012, pp. 1373–1376. (Cited on p. 46)
DOI: 10.1109/ISBI.2012.6235823

[Che12c] Simon R. **Cherry**, James A. **Sorenson** and Michael E. **Phelps**. *Physics in Nuclear Medicine*. Fourth edition. Philadelphia: Saunders, 2012. ISBN: 978-1416051985. (Cited on pp. 21, 24)
DOI: 10.1016/B978-1-4160-5198-5.00033

[Che71] David A. **Chesler**. 'Three-Dimensional Activity Distribution from Multiple Positron Scintigraphs'. In: *Journal of Nuclear Medicine* 12.6 (June 1971), pp. 347–348. (Cited on p. 42)
URL: http://jnm.snmjournals.org/content/12/6/334.full.pdf+html (Visited on 5th July 2015)

[Che73a] David A. **Chesler**. 'Positron Tomography and Three-Dimensional Reconstruction Technique'. In: *Tomographic Imaging in Nuclear Medicine*. Ed. by Gerald S. **Freedman**. New York: The Society of Nuclear Medicine, 1973, pp. 176–183. (Cited on p. 42)

[Che73b] David A. **Chesler**, Jr. Bernard **Hoop** and Gordon L. **Brownell**. 'Transverse Section Imaging of Myocardium with $^{13}NH_4$'. In: *Journal of Nuclear Medicine* 14.8 (Aug. 1973), p. 623. (Cited on p. 42)
URL: http://jnm.snmjournals.org/content/14/8/619.full.pdf+html (Visited on 5th July 2015)

[Chi35] Ole **Chievitz** and George Charles **Hevesy**. 'Radioactive Indicators in the Study of Phosphorus Metabolism in Rats'. In: *Nature* 136.3445 (Nov. 1935), pp. 754–755. (Cited on p. 24)
DOI: 10.1038/136754a0

[Cho05] Howie **Choset**, Kevin M. **Lynch**, Seth **Hutchinson**, George **Kantor**, Wolfram **Burgard**, Lydia E. **Kavraki** and Sebastian **Thrun**. *Principles of Robot Motion. Theory, Algorithms, and Implementations*. Cambridge: MIT Press, 2005. ISBN: 978-0262033275. (Cited on p. 111)

[Chr24a] Jens Anton **Christiansen**, George Charles **Hevesy** and Svend **Lomholt**. 'Recherches, par une méthode radiochimique, sur la circulation du bismuth dans l'organisme [Studies, by a radiochemical method, on the circulation of bismuth in the organism]'. In: *Comptes Rendus Hebdomadaires des Séances de l'Académie des Sciences* 178 (Apr. 1924), pp. 1324–1326. (Cited on p. 24)
URL: http://catalogue.bnf.fr/ark:/12148/cb343481087 (Visited on 5th July 2015)

[Chr24b] Jens Anton **Christiansen**, George Charles **Hevesy** and Svend **Lomholt**. 'Recherches, par une méthode radiochimique, sur la circulation du plomb dans l'organisme [Studies, by a radiochemical method, about the circulation of lead in the organism]'. In: *Comptes Rendus Hebdomadaires des Séances de l'Académie des Sciences* 179 (July 1924), pp. 291–293. (Cited on p. 24)
URL: http://catalogue.bnf.fr/ark:/12148/cb343481087 (Visited on 5th July 2015)

[Clo99] P. **Cloetens**, W. **Ludwig**, J. **Baruchel**, D. **Van Dyck**, J. **Van Landuyt**, J. P. **Guigay** and M. **Schlenker**. 'Holotomography. Quantitative phase tomography with micrometer resolution using hard synchrotron radiation x rays'. In: *Applied Physics Letters* 75.19 (Nov. 1999), pp. 2912–2914. (Cited on p. 140)
DOI: 10.1063/1.125225

[Col48] John W. **Coltman**. 'Fluoroscopic Image Brightening by Electronic Means'. In: *Radiology* 51.3 (Sept. 1948), pp. 359–367. (Cited on p. 20)
DOI: 10.1148/51.3.359

[Com23] Arthur Holly **Compton**. 'A Quantum Theory of the Scattering of X-rays by Light Elements'. In: *Physical Review* 21.5 (May 1923), pp. 483–502. (Cited on p. 15)
DOI: 10.1103/PhysRev.21.483

[Com27] Arthur Holly **Compton**. *X-rays as a branch of optics*. Nobel Lecture. Dec. 1927. (Cited on p. 15)
URL: http://www.nobelprize.org/nobel_prizes/physics/laureates/1927/compton-lecture.pdf (Visited on 5th July 2015)

[Con99] Thomas E. **Conturo**, Nicolas F. **Lori**, Thomas S. **Cull**, Erbil **Akbudak**, Abraham Z. **Snyder**, Joshua S. **Shimony**, Robert C. **McKinstry**, Harold **Burton** and Marcus E. **Raichle**. 'Tracking neuronal fiber pathways in the living human brain'. In: *Proceedings of the National Academy of Sciences of the United States of America* 96.18 (Aug. 1999), pp. 10422–10427. (Cited on pp. 151, 159)
DOI: 10.1073/pnas.96.18.10422

[Coo16] William David **Coolidge**. 'Vacuum-tube'. Patent US 1,203,495. Oct. 1916. (Cited on p. 11)
URL: http://worldwide.espacenet.com/publicationDetails/biblio?CC=US&NR=1203495 (Visited on 5th July 2015)

[Coo17] William David **Coolidge**. 'X-ray apparatus'. Patent US 1,215,116. Feb. 1917. (Cited on p. 12)
URL: http://worldwide.espacenet.com/publicationDetails/biblio?CC=US&NR=1215116 (Visited on 5th July 2015)

[Coo86] James K. **Cooper**. 'Electrocardiography 100 Years Ago'. In: *New England Journal of Medicine* 315.7 (Aug. 1986), pp. 461–464. (Cited on p. 88)
DOI: 10.1056/NEJM198608143150722

[Cor63] Allan M. **Cormack**. 'Representation of a Function by Its Line Integrals, with Some Radiological Applications. Part I'. In: *Journal of Applied Physics* 34.9 (Sept. 1963), pp. 2722–2727. (Cited on pp. 35, 50, 82)
DOI: 10.1063/1.1729798

[Cor64] Allan M. **Cormack**. 'Representation of a Function by Its Line Integrals, with Some Radiological Applications. Part II'. In: *Journal of Applied Physics* 35.10 (Oct. 1964), pp. 2908–2913. (Cited on pp. 35, 50, 82)
DOI: 10.1063/1.1713127

[Cor73] Allan M. **Cormack**. 'Reconstruction of Densities from their Projections, with Applications in Radiological Physics'. In: *Physics in Medicine and Biology* 18.2 (Mar. 1973), pp. 195–207. (Cited on p. 82)
DOI: 10.1088/0031-9155/18/2/003

[Cor79] Allan M. **Cormack**. *Early Two-Dimensional Reconstruction and Recent Topics Stemming from it*. Nobel Lecture. Dec. 1979. (Cited on p. 35)
URL: http://www.nobelprize.org/nobel_prizes/medicine/laureates/1979/cormack-lecture.pdf (Visited on 5th July 2015)

[Cor82] Allan M. **Cormack**. 'Computed Tomography. Some History and Recent Developments'. In: *Computed Tomography*. Ed. by Lawrence A. **Shepp**. Vol. 27. Proceedings of Symposia in Applied Mathematics. Providence: American Mathematical Society, 1982, pp. 35–42. (Cited on pp. 81, 82)
DOI: 10.1090/psapm/027

[Cra05] John J. **Craig**. *Introduction to Robotics. Mechanics and Control*. Third edition. Upper Saddle River: Pearson Education, 2005. ISBN: 978-8178084510. (Cited on p. 111)

[Cra36] H. **Cramér** and H. **Wold**. 'Some Theorems on Distribution Functions'. In: *Journal of the London Mathematical Society* 11.4 (Oct. 1936), pp. 290–294. (Cited on p. 81)
DOI: 10.1112/jlms/s1-11.4.290

[Cre06] Daniel **Cremers**. 'Dynamical Statistical Shape Priors for Level Set-Based Tracking'. In: *IEEE Transactions on Pattern Analysis and Machine Intelligence* 28.8 (Aug. 2006), pp. 1262–1273. (Cited on p. 91)
DOI: 10.1109/TPAMI.2006.161

[Cro79] William **Crookes**. 'On the Illumination of Lines of Molecular Pressure, and the Trajectory of Molecules'. In: *Philosophical Transactions of the Royal Society of London* 170 (1879), pp. 135–164. (Cited on pp. 9, 11)
DOI: 10.1098/rstl.1879.0065

[Cur03] Marie Skłodowska **Curie**. *Recherches sur les Substances Radioactives [Research on the Radioactive Substances]*. Paris, 1903. (Cited on p. 18)
URL: http://visualiseur.bnf.fr/ark:/12148/bpt6k624839 (Visited on 5th July 2015)

[Cur05] Pierre **Curie**. *Radioactive substances, especially radium*. Nobel Lecture. June 1905. (Cited on p. 18)
URL: http://www.nobelprize.org/nobel_prizes/physics/laureates/1903/pierre-curie-lecture.pdf (Visited on 5th July 2015)

[Cur21] Marie Skłodowska **Curie**. *La Radiologie et La Guerre [Radiology and the War]*. Paris, 1921. (Cited on pp. 22, 25)
URL: http://visualiseur.bnf.fr/ark:/12148/bpt6k67970j (Visited on 5th July 2015)

[Cur34] Irène **Curie** and Frédéric **Joliot**. 'Un nuouveau type de radioactivité [A new type of radioactivity]'. In: *Comptes Rendus Hebdomadaires des Séances de l'Académie des Sciences* 198 (Jan. 1934), pp. 254–256. (Cited on p. 41)
URL: http://catalogue.bnf.fr/ark:/12148/cb343481087 (Visited on 5th July 2015)

[Cur38] Ève **Curie**. *Madame Curie*. Paris: Gallimard, 1938. (Cited on p. 25)
URL: https://archive.org/details/madamecurie035051mbp (Visited on 5th July 2015)

[Cur48] Samuel Crowe **Curran** and W. R. **Baker**. 'Photoelectric Alpha-Particle Detector'. In: *Review of Scientific Instruments* 19.2 (1948), p. 116. (Cited on p. 21)
DOI: 10.1063/1.1741210

[Cur49] Samuel Crowe **Curran** and John Drummond **Craggs**. *Counting Tubes: Theory and Applications*. New York: Academic Press, 1949. (Cited on p. 21)
URL: http://catalog.hathitrust.org/Record/001485199 (Visited on 5th July 2015)

[Cur98] Pierre **Curie**, Marie Skłodowska **Curie** and G. **Bémont**. 'Sur une nouvelle substance fortement radioactive contenue dans la pechblende [On a new heavily radio-active substance contained in pitchblende]'. In: *Comptes Rendus Hebdomadaires des Séances de l'Académie des Sciences* 127 (Dec. 1898), pp. 1215–1217. (Cited on p. 18)
URL: http://catalogue.bnf.fr/ark:/12148/cb343481087 (Visited on 5th July 2015)

[Dar45] Charles **Darwin**. *Journal of Researches into the Natural History and Geology of the countries visited during the voyage of* H.M.S. Beagle *round the world*. Second edition. London: Murray, 1845. (Cited on p. 6)

[Dau04] Ingrid **Daubechies**, Michel **Defrise** and Christine de **Mol**. 'An Iterative Thresholding Algorithm for Linear Inverse Problems with a Sparsity Constraint'. In: *Communications on Pure and Applied Mathematics* 57.11 (Nov. 2004), pp. 1413–1457. (Cited on p. 78)
DOI: 10.1002/cpa.20042

[Dav06] Louise **Davies** and H. Gilbert **Welch**. 'Increasing Incidence of Thyroid Cancer in the United States, 1973–2002'. In: *Journal of the American Medical Association* 295.18 (May 2006), pp. 2164–2167. (Cited on p. 104)
DOI: 10.1001/jama.295.18.2164

[Dav96] T. J. **Davis** and A. W. **Stevenson**. 'Direct measure of the phase shift of an x-ray beam'. In: *Journal of the Optical Society of America A* 13.6 (June 1996), pp. 1193–1198. (Cited on p. 140)
DOI: 10.1364/JOSAA.13.001193

[Daw13] M. Joan **Dawson**. *Paul Lauterbur and the Invention of MRI*. MIT Press, 2013. ISBN: 978-0262316712. (Cited on p. 45)
URL: http://ieeexplore.ieee.org/servlet/opac?bknumber=6642229 (Visited on 21st June 2015)

[De 93] Alvaro R. **De Pierro**. 'On the Relation Between the ISRA and the EM Algorithm for Positron Emission Tomography'. In: *IEEE Transactions on Medical Imaging* 12.2 (June 1993), pp. 328–333. (Cited on p. 66)
DOI: 10.1109/42.232263

[De 95] Alvaro R. **De Pierro**. 'A Modified Expectation Maximization Algorithm for Penalized Likelihood Estimation in Emission Tomography'. In: *IEEE Transactions on Medical Imaging* 14.1 (Mar. 1995), pp. 132–137. (Cited on p. 66)
DOI: 10.1109/42.370409

[Dea07] Stanley R. **Deans**. *The Radon Transform and Some of Its Applications*. Mineola: Dover, 2007. ISBN: 978-0486462417. (Cited on pp. 44–47, 49, 50, 52, 54, 81, 82)

[Def12] Michel **Defrise**, Ahmadreza **Rezaei** and Johan **Nuyts**. 'Time-of-flight PET data determine the attenuation sinogram up to a constant'. In: *Physics in Medicine and Biology* 57.4 (Feb. 2012), pp. 885–899. (Cited on p. 43)
DOI: 10.1088/0031-9155/57/4/885

[Def14] Michel **Defrise**, Ahmadreza **Rezaei** and Johan **Nuyts**. 'Transmission-less attenuation correction in time-of-flight PET: Analysis of a discrete iterative algorithm'. In: *Physics in Medicine and Biology* 59.4 (Feb. 2014), pp. 1073–1095. (Cited on p. 43)
DOI: 10.1088/0031-9155/59/4/1073

[Def88] Michel **Defrise**. 'Possible Criteria for Choosing the Number of Iterations in Some Iterative Reconstruction Methods'. In: *Mathematics and Computer Science in Medical Imaging*. Ed. by MaxA. **Viergever** and Andrew **Todd-Pokropek**. Vol. 39. NATO ASI Series. Springer, 1988, pp. 293–303. (Cited on p. 70)
DOI: 10.1007/978-3-642-83306-9_13

[Dem77] Arthur P. **Dempster**, Nan M. **Laird** and Donald B. **Rubin**. 'Maximum Likelihood from Incomplete Data via the EM Algorithm'. In: *Journal of the Royal Statistical Society B* 39.1 (1977), pp. 1–38. (Cited on p. 66)
URL: http://www.jstor.org/stable/2984875 (Visited on 27th June 2015)

[Des04] Benoit **Desjardins** and Ella A. **Kazerooni**. 'ECG-Gated Cardiac CT'. In: *American Journal of Roentgenology* 182.4 (Apr. 2004), pp. 993–1010. (Cited on p. 89)
DOI: 10.2214/ajr.182.4.1820993

[Des05] R. D. **Deslattes**, E. G. **Kessler Jr.**, P. **Indelicato**, L. de **Billy**, E. **Lindroth**, J. **Anton**, J. S. **Coursey**, D. J. **Schwab**, C. **Chang**, R. **Sukumar**, K. **Olsen** and R. A. **Dragoset**. *X-ray Transition Energies (version 1.2)*. Website. Gaithersburg: National Institute of Standards and Technology (NIST), 2005. (Cited on p. 14)
URL: http://physics.nist.gov/XrayTrans (Visited on 22nd Apr. 2015)

[Die93] Paul **Dierckx**. *Curve and Surface Fitting with Splines*. Monographs on Numerical Analysis. Oxford: Oxford University Press, Apr. 1993. ISBN: 978-0198534402. (Cited on p. 93)

[Dij84] P. van **Dijk**. 'Direct Cardiac NMR Imaging of Heart Wall and Blood Flow Velocity'. In: *Journal of Computer Assisted Tomography* 8.3 (June 1984), pp. 429–436. (Cited on p. 45)
URL: http://journals.lww.com/jcat/Abstract/1984/06000/Direct_Cardiac_NMR_Imaging_of_Heart_Wall_and_Blood.12.aspx (Visited on 8th July 2015)

[Din79] Kris A. **Dines** and R. Jeffrey **Lytle**. 'Computerized Geophysical Tomography'. In: *Proceedings of the IEEE* 67.7 (July 1979), pp. 1065–1073. (Cited on p. 82)
DOI: 10.1109/PROC.1979.11390

[Dir28] Paul Adrien Maurice **Dirac**. 'The Quantum Theory of the Electron'. In: *Proceedings of the Royal Society of London. A* 117.778 (Feb. 1928), pp. 610–624. (Cited on p. 40)
DOI: 10.1098/rspa.1928.0023

[Dir33] Paul Adrien Maurice **Dirac**. *Theory of electrons and positrons*. Nobel Lecture. Dec. 1933. (Cited on p. 41)
URL: http://www.nobelprize.org/nobel_prizes/physics/laureates/1933/dirac-lecture.pdf (Visited on 5th July 2015)

[DiS96] David J. **DiSantis**. 'Pioneer Practitioners'. In: *A History of the Radiological Sciences: Diagnosis*. Ed. by Raymond **Gagliardi** and Bruce L. **McClennan**. 1996. Chap. 3, pp. 47–57. (Cited on p. 22)
URL: http://www.arrs.org/Publications/HRS.aspx (Visited on 19th May 2015)

[Dob03] James T. **Dobbins** III and Devon J. **Godfrey**. 'Digital x-ray tomosynthesis: current state of the art and clinical potential'. In: *Physics in Medicine and Biology* 48.19 (Oct. 2003), R65–R106. (Cited on p. 30)
DOI: 10.1088/0031-9155/48/19/R01

[Dod96] Gerald D. **Dodd** Jr. and Richard H. **Gold**. 'Mammography'. In: *A History of the Radiological Sciences: Diagnosis*. Ed. by Raymond **Gagliardi** and Bruce L. **McClennan**. 1996. Chap. 13, pp. 319–343. (Cited on p. 27)
URL: http://www.arrs.org/Publications/HRS.aspx (Visited on 19th May 2015)

[Don03] David L. **Donoho** and Michael **Elad**. 'Optimally sparse representation in general (nonorthogonal) dictionaries via ℓ_1 minimization'. In: *Proceedings of the National Academy of Sciences of the United States of America* 100.5 (Mar. 2003), pp. 2197–2202. (Cited on p. 73)
DOI: 10.1073/pnas.0437847100

[Don06] David L. **Donoho**. 'For Most Large Underdetermined Systems of Linear Equations the Minimal ℓ_1-norm Solution Is Also the Sparsest Solution'. In: *Communications on Pure and Applied Mathematics* 59.6 (June 2006), pp. 797–829. (Cited on p. 73)
DOI: 10.1002/cpa.20132

[Don10] Tilman **Donath**, Franz **Pfeiffer**, Oliver **Bunk**, Christian **Grünzweig**, Eckhard **Hempel**, Stefan **Popescu**, Peter **Vock** and Christian **David**. 'Toward Clinical X-ray Phase-Contrast CT. Demonstration of Enhanced Soft-Tissue Contrast in Human Specimen'. In: *Investigative Radiology* 45.7 (July 2010), pp. 445–452. (Cited on p. 146)
DOI: 10.1097/RLI.0b013e3181e21866

[Don95] David L. **Donoho**. 'De-Noising by Soft-Thresholding'. In: *IEEE Transactions on Information Theory* 41.3 (May 1995), pp. 613–627. (Cited on p. 78)
DOI: 10.1109/18.382009

[Dow99] Betsy A. **Dowd**, Graham H. **Campbell**, Robert B. **Marr**, Vivek V. **Nagarkar**, Sameer V. **Tipnis**, Lisa **Axe** and D. Peter **Siddons**. 'Developments in synchrotron x-ray computed microtomography at the National Synchrotron Light Source'. In: *Developments in X-Ray Tomography II*. Vol. 3772. Proc. SPIE. Sept. 1999, pp. 224–236. (Cited on pp. 15, 50)
DOI: 10.1117/12.363725

[Due97] Eckhart **Duehmke**. 'Present Status of Radiotherapy in Clinical Practice'. In: *Röntgen Centennial. X-rays in Natural and Life Sciences*. Ed. by Axel **Haase**, Gottfried **Landwehr** and Eberhard **Umbach**. Singapore: World Scientific, 1997, pp. 143–172. ISBN: 978-9810230852. (Cited on p. 27)

[Duf00] Jacalyn **Duffin** and Charles R. R. **Hayter**. 'Baring the Sole: The Rise and Fall of the Shoe-Fitting Fluoroscope'. In: *Isis* 91.2 (June 2000), pp. 260–282. (Cited on p. 27)
URL: http://www.jstor.org/stable/236916 (Visited on 5th July 2015)

[Dut13] Joyita **Dutta**, Sangtae **Ahn** and Quanzheng **Li**. 'Quantitative Statistical Methods for Image Quality Assessment'. In: *Theranostics* 3.10 (2013), pp. 741–756. (Cited on p. 70)
DOI: 10.7150/thno.6815

[Eck92] Jonathan **Eckstein** and Dimitri P. **Bertsekas**. 'On the Douglas-Rachford splitting method and the proximal point algorithm for maximal monotone operators'. In: *Mathematical Programming* 55.1–3 (Apr. 1992), pp. 293–318. (Cited on p. 79)
DOI: 10.1007/BF01581204

[Edh77] Paul **Edholm**. 'Tomogram Reconstruction Using an Opticophotographic Method'. In: *Acta Radiologica* 18.1 (Jan. 1977), pp. 126–144. (Cited on pp. 33, 35)
DOI: 10.1177/028418517701800116

[Edi07] Thomas Alva **Edison**. 'Fluorescent Electric Lamp'. Patent US 865,367. Sept. 1907. (Cited on p. 20)
URL: http://worldwide.espacenet.com/publicationDetails/biblio?CC=US&NR=865367 (Visited on 5th July 2015)

[Edw07] C. Henry **Edwards** and David E. **Penney**. 'Differential Equations'. In: Pearson, 2007. Chap. 4.3. ISBN: 978-0136054252. (Cited on p. 159)
URL: http://wps.prenhall.com/wps/media/objects/4559/4668829/chapt4/proj4.3A/proj4-3A.pdf (Visited on 5th July 2015)

[Egg15] Elena **Eggl**, Simone **Schleede**, Martin **Bech**, Klaus **Achterhold**, Roderick **Loewen**, Ronald D. **Ruth** and Franz **Pfeiffer**. 'X-ray phase-contrast tomography with a compact laser-driven synchrotron source'. In: *Proceedings of the National Academy of Sciences of the United States of America* 112.18 (May 2015), pp. 5567–5572. (Cited on p. 140)
DOI: 10.1073/pnas.1500938112

[Egg81] Paul P. B. **Eggermont**, Gabor T. **Herman** and Arnold **Lent**. 'Iterative Algorithms for Large Partitioned Linear Systems, with Applications to Image Reconstruction'. In: *Linear Algebra and Its Applications* 40 (Oct. 1981), pp. 37–67. (Cited on p. 71)
DOI: 10.1016/0024-3795(81)90139-7

[Ein05] Albert **Einstein**. 'Über einen die Erzeugung und Verwandlung des Lichtes betreffenden heuristischen Gesichtspunkt [On a Heuristic Viewpoint Concerning the Production and Transformation of Light]'. In: *Annalen der Physik* 322.6 (1905). § 8, pp. 132–148. (Cited on p. 15)
DOI: 10.1002/andp.19053220607

[Eis96] Ronald L. **Eisenberg**. 'Early Developments in X-ray Equipment'. In: *A History of the Radiological Sciences: Diagnosis*. Ed. by Raymond **Gagliardi** and Bruce L. **McClennan**. 1996. Chap. 4, pp. 58–86. (Cited on p. 10)
URL: http://www.arrs.org/Publications/HRS.aspx (Visited on 19th May 2015)

[Ela07] Michael **Elad**, Peyman **Milanfar** and Ron **Rubinstein**. 'Analysis versus synthesis in signal priors'. In: *Inverse Problems* 23.3 (June 2007), pp. 947–968. (Cited on p. 78)
DOI: 10.1088/0266-5611/23/3/007

[Eng00] Heinz Werner **Engl**, Martin **Hanke** and Günther **Neubauer**. *Regularization of Inverse Problems*. Dordrecht: Kluwer Academic, 2000. ISBN: 978-0792341574. (Cited on p. 70)

[Eng04] Klaus **Engel**, Markus **Hadwiger**, Joe M. **Kniss**, Aaron E. **Lefohn**, Christof **Rezk-Salama** and Daniel **Weiskopf**. 'Real-Time Volume Graphics'. In: *ACM SIGGRAPH 2004* Course Note 28 (2004). (Cited on pp. 29, 159)
DOI: 10.1145/1103900.1103929

[Eng06] Klaus **Engel**, Markus **Hadwiger**, Joe M. **Kniss**, Christof **Rezk-Salama** and Daniel **Weiskopf**. *Real-Time Volume Graphics*. Wellesley, 2006. ISBN: 978-1568812663. (Cited on pp. 29, 159)
URL: http://www.real-time-volume-graphics.org (Visited on 16th May 2015)

[Erd99a] Hakan **Erdoğan**. 'Statistical Image Reconstruction Algorithms Using Paraboloidal Surrogates for PET Transmission Scans'. PhD thesis. Ann Arbor: University of Michigan, 1999. (Cited on p. 67)
URL: http://web.eecs.umich.edu/~fessler/student/diss/99,erdogan.pdf (Visited on 23rd June 2015)

[Erd99b] Hakan **Erdoğan** and Jeffrey A. **Fessler**. 'Ordered subsets algorithms for transmission tomography'. In: *Physics in Medicine and Biology* 44.11 (Nov. 1999), pp. 2835–2851. (Cited on pp. 67, 76)
DOI: 10.1088/0031-9155/44/11/311

[Eve96] Ronald G. **Evens**. 'Computed Tomography'. In: *A History of the Radiological Sciences: Diagnosis*. Ed. by Raymond **Gagliardi** and Bruce L. **McClennan**. 1996. Chap. 16, pp. 402–411. (Cited on p. 35)
URL: http://www.arrs.org/Publications/HRS.aspx (Visited on 19th May 2015)

[Feh14] Andreas **Fehringer**, Tobias **Lasser**, Irene **Zanette**, Peter B. **Noël** and Franz **Pfeiffer**. 'A versatile tomographic forward- and backprojection approach on Multi-GPUs'. In: *Medical Imaging 2014. Image Processing*. Vol. 9034. Proc. SPIE. Mar. 2014, 90344F. (Cited on pp. 155, 161)
DOI: 10.1117/12.2043860

[Fel84] L. A. **Feldkamp**, L. C. **Davis** and J. W. **Kress**. 'Practical cone-beam algorithm'. In: *Journal of the Optical Society of America A* 1.6 (June 1984), pp. 612–619. (Cited on p. 54)
DOI: 10.1364/JOSAA.1.000612

[Fen00] Aaron **Fenster** and Donal B. **Downey**. 'Three-Dimensional Ultrasound Imaging'. In: *Annual Review of Biomedical Engineering* 2 (Aug. 2000), pp. 457–475. (Cited on p. 101)
DOI: 10.1146/annurev.bioeng.2.1.457

[Fer13] J. **Ferlay**, E. **Steliarova-Foucher**, J. **Lortet-Tieulent**, S. **Rosso**, J. W. W. **Coebergh**, H. **Comber**, D. **Forman** and F. **Bray**. 'Cancer incidence and mortality patterns in Europe: Estimates for 40 countries in 2012'. In: *European Journal of Cancer* 49.6 (Apr. 2013), pp. 1374–1403. (Cited on p. 104)
DOI: 10.1016/j.ejca.2012.12.027

[Fer96] Ernest J. **Ferris** and Max L. **Baker**. 'Vascular and Interventional Radiology'. In: *A History of the Radiological Sciences: Diagnosis*. Ed. by Raymond **Gagliardi** and Bruce L. **McClennan**. 1996. Chap. 11, pp. 270–288. (Cited on pp. 22, 87)
URL: http://www.arrs.org/Publications/HRS.aspx (Visited on 19th May 2015)

[Fes00] Jeffrey A. **Fessler**. 'Statistical Image Reconstruction Methods for Transmission Tomography'. In: *Medical Image Processing and Analysis*. Ed. by Milan **Sonka** and J. Michael **Fitzpatrick**. Vol. 2. Handbook of Medical Imaging. Bellingham: SPIE, 2000. Chap. 1, pp. 1–70. (Cited on pp. 66–68)
DOI: 10.1117/3.831079.ch1

[Fes99] Jeffrey A. **Fessler** and Scott D. **Booth**. 'Conjugate-Gradient Preconditioning Methods for Shift-Variant PET Image Reconstruction'. In: *IEEE Transactions on Image Processing* 8.5 (May 1999), pp. 688–699. (Cited on p. 63)
DOI: 10.1109/83.760336

[Feu07a] Marco **Feuerstein**. 'Augmented Reality in Laparoscopic Surgery. New Concepts for Intraoperative Multimodal Imaging'. PhD thesis. München: Technische Universität München, Department of Computer Science, Oct. 2007. (Cited on p. 108)
URL: http://nbn-resolving.de/urn/resolver.pl?urn:nbn:de:bvb:91-diss-20070619-622737-1-8 (Visited on 4th July 2015)

[Fie95] Ricardo D. **Fierro** and Per Christian **Hansen**. 'Accuracy of TSVD solutions computed from rank-revealing decompositions'. In: *Numerische Mathematik* 70.4 (June 1995), pp. 453–471. (Cited on p. 120)
DOI: 10.1007/s002110050128

[Fil09] Aaron **Filler**. 'Magnetic Resonance Neurography and Diffusion Tensor Imaging: Origins, History, and Clinical Impact of the First 50 000 Cases with an Assessment of Efficacy and Utility in a Prospective 5000-Patient Study Group'. In: *Neurosurgery* 65.4 (2009), A29–A43. (Cited on pp. 45, 151, 159)
DOI: 10.1227/01.NEU.0000351279.78110.00

[Fin03] David V. **Finch**. 'The Attenuated X-Ray Transform. Recent Developments'. In: *Inside Out. Inverse Problems and Applications*. Ed. by Gunther **Uhlmann**. Cambridge: Cambridge University Press, 2003, pp. 47–66. (Cited on p. 54)
URL: http://math.oregonstate.edu/~finch/papers/attenpost.pdf (Visited on 23rd June 2015)

[Fle64] R. **Fletcher** and C. M. **Reeves**. 'Function minimization by conjugate gradients'. In: *Computer Journal* 7.2 (1964), pp. 149–154. (Cited on p. 69)
DOI: 10.1093/comjnl/7.2.149

[For89] A. R. **Formiconi**, A. **Pupi** and A. **Passeri**. 'Compensation of spatial system response in SPECT with conjugate gradient reconstruction technique'. In: *Physics in Medicine and Biology* 34.1 (Jan. 1989), pp. 69–84. (Cited on p. 63)
DOI: 10.1088/0031-9155/34/1/007

[Fou22] Jean Baptiste Joseph **Fourier**. *Théorie analytique de la chaleur [Analytical Theory of Heat]*. Paris: Firmin Didot, 1822. (Cited on pp. 49, 76)
URL: https://archive.org/details/thorieanalytiq00four (Visited on 24th June 2015)

[Fra05] Jean-Sébastien **Franco** and Edmond **Boyer**. 'Fusion of Multi-View Silhouette Cues Using a Space Occupancy Grid'. In: *IEEE International Conference on Computer Vision (ICCV)* 2 (Oct. 2005), pp. 1747–1753. (Cited on p. 91)
DOI: 10.1109/ICCV.2005.105

[Fra06] Joachim **Frank**, ed. *Electron Tomography. Methods for Three-Dimensional Visualization of Structures in the Cell*. Second edition. New York: Springer, 2006. (Cited on p. 46)
DOI: 10.1007/978-0-387-69008-7

[Fra42] Gabriel **Frank**. 'X-ray Apparatus'. Patent US 2,281,931. May 1942. (Cited on pp. 32, 33, 48, 50, 82)
URL: http://worldwide.espacenet.com/publicationDetails/biblio?CC=US&NR=2281931 (Visited on 5th July 2015)

[Fra98] Alejandro F. **Frangi**, Wiro J. **Niessen**, Koen L. **Vincken** and Max A. **Viergever**. 'Multiscale Vessel Enhancement Filtering'. In: *Medical Image Computing and Computer-Assisted Intervention (MICCAI)*. Lecture Notes in Computer Science 1496 (Oct. 1998), pp. 130–137. (Cited on p. 91)
DOI: 10.1007/BFb0056195

[Fri13] Jürgen **Frikel**. 'Sparse Regularization in Limited Angle Tomography'. In: *Applied and Computational Harmonic Analysis* 34.1 (Jan. 2013), pp. 117–141. (Cited on p. 77)
DOI: 10.1016/j.acha.2012.03.005

[Gag20] Simon Henry **Gage**. 'Modern Dark-Field Microscopy and the History of Its Development'. In: *Transactions of the American Microscopical Society* 39.2 (Apr. 1920), pp. 95–141. (Cited on p. 137)
DOI: 10.2307/3221838

[Gal10] Galileo **Galilei**. *Sidereus Nuncius [Sidereal Messenger]*. Venezia, Mar. 1610. (Cited on p. 6)
URL: http://moro.imss.fi.it/lettura/LetturaWEB.DLL?AZIONE=APRITESTO&TESTO=E_Y&VOL=3 (Visited on 4th Sept. 2015)

[Gan11] A. **Ganguly**, A. **Fieselmann**, M. **Marks**, J. **Rosenberg**, J. **Boese**, Y. **Deuerling-Zheng**, M. **Straka**, G. **Zaharchuck**, R. **Bammer** and R. **Fahrig**. 'Cerebral CT Perfusion Using an Interventional C-Arm Imaging System. Cerebral Blood Flow Measurements'. In: *American Journal of Neuroradiology* 32.8 (2011), pp. 1525–1531. (Cited on p. 101)
DOI: 10.3174/ajnr.A2518

[Gar13] José **Gardiazabal**, Tobias **Reichl**, Aslı **Okur**, Tobias **Lasser** and Nassir **Navab**. 'First flexible robotic intra-operative nuclear imaging for image-guided surgery'. In: *Information Processing in Computer-Assisted Interventions (IPCAI)*. Vol. 7915. Lecture Notes in Computer Science. June 2013, pp. 81–90. (Cited on p. 111)
DOI: 10.1007/978-3-642-38568-1_9

[Gei28] Hans Wilhelm **Geiger** and Walther **Müller**. 'Elektronenzählrohr zur Messung schwächster Aktivitäten [Electron counting tube for the measurement of weakest radioactivities]'. In: *Naturwissenschaften* 16.31 (Aug. 1928), pp. 617–618. (Cited on p. 21)
DOI: 10.1007/BF01494093

[Gem85] Stuart **Geman** and D. E. **McClure**. 'Bayesian image analysis. An application to single photon emission tomography'. In: *Proceedings of the American Statistical Association. Statistical Computing Section*. 1985, pp. 12–18. (Cited on p. 74)
URL: http://www.dam.brown.edu/people/geman/Homepage/Image%20processing,%20image%20analysis,%20Markov%20random%20fields,%20and%20MCMC/1985GemanMcClureASA.pdf (Visited on 29th June 2015)

[Ges15] Senatsverwaltung für **Gesundheit und Soziales** der Stadt Berlin. *Neuer Röntgenbus zur TBC-Untersuchung der Flüchtlinge im Einsatz [New mobile X-ray unit for tuberculosis screening of refugees in use]*. Invitation to media event. July 2015. (Cited on p. 27)
URL: https://www.berlin.de/sen/gessoz/presse/pressemitteilungen/2015/pressemitteilung.339661.php (Visited on 16th Sept. 2015)

[Gil72] Peter **Gilbert**. 'Iterative Methods for the Three-dimensional Reconstruction of an Object from Projections'. In: *Journal of Theoretical Biology* 36.1 (July 1972), pp. 105–117. (Cited on p. 59)
DOI: 10.1016/0022-5193(72)90180-4

[Glo11] Benjamin M. **Glocker**. 'Random Fields for Image Registration'. PhD thesis. München: Technische Universität München, Department of Computer Science, June 2011. (Cited on p. 101)
URL: http://nbn-resolving.de/urn/resolver.pl?urn:nbn:de:bvb:91-diss-20110609-997270-1-5 (Visited on 3rd July 2015)

[Goe08] Johann Wolfgang von **Goethe**. *Faust. Der Tragödie erster Teil [Faust: The First Part of the Tragedy]*. Tübingen: Cotta, 1808. (Cited on p. 9)
URL: http://www.nbn-resolving.org/urn/resolver.pl?urn=urn:nbn:de:kobv:b4-200905191726 (Visited on 4th Sept. 2015)

[Goe26] Otto **Goetze**. 'Method of and Apparatus for Producing Sharp Röntgen Images'. Patent US 1,590,971. June 1926. (Cited on p. 12)
URL: http://worldwide.espacenet.com/publicationDetails/biblio?CC=US&NR=1590971 (Visited on 5th July 2015)

[Gol09] Tom **Goldstein** and Stanley **Osher**. 'The Split Bregman Method for L1-Regularized Problems'. In: *SIAM Journal on Imaging Sciences* 2.2 (2009), pp. 323–343. (Cited on p. 79)
DOI: 10.1137/080725891

[Gol65] Gene H. **Golub** and William **Kahan**. 'Calculating the Singular Values and Pseudo-Inverse of a Matrix'. In: *SIAM Journal on Numerical Analysis* 2.2 (1965), pp. 205–224. (Cited on p. 118)
DOI: 10.1137/0702016

[Gol96] Barry B. **Goldberg**, Raymond **Gramiak** and Atis K. **Freimanis**. 'Ultrasonography'. In: *A History of the Radiological Sciences: Diagnosis*. Ed. by Raymond **Gagliardi** and Bruce L. **McClennan**. 1996. Chap. 17, pp. 412–442. (Cited on pp. 44, 101)
URL: http://www.arrs.org/Publications/HRS.aspx (Visited on 19th May 2015)

[Goo96] Philip C. **Goodman**. 'Roentgenology of the Abdomen'. In: *A History of the Radiological Sciences: Diagnosis*. Ed. by Raymond **Gagliardi** and Bruce L. **McClennan**. 1996. Chap. 8, pp. 173–194. (Cited on p. 22)
URL: http://www.arrs.org/Publications/HRS.aspx (Visited on 19th May 2015)

[Gor70] Richard **Gordon**, Robert **Bender** and Gabor T. **Herman**. 'Algebraic Reconstruction Techniques (ART) for Three-dimensional Electron Microscopy and X-ray Photography'. In: *Journal of Theoretical Biology* 29.3 (Dec. 1970), pp. 471–481. (Cited on p. 58)
DOI: 10.1016/0022-5193(70)90109-8

[Gou01] Yann **Gousseau** and Jean-Michel **Morel**. 'Are Natural Images of Bounded Variation?' In: *SIAM Journal on Mathematical Analysis* 33.3 (2001), pp. 634–648. (Cited on pp. 73, 76)
DOI: 10.1137/S0036141000371150

[Gre90a] Peter J. **Green**. 'Bayesian Reconstructions from Emission Tomography Data Using a Modified EM Algorithm'. In: *IEEE Transactions on Medical Imaging* 9.1 (Mar. 1990), pp. 84–93. (Cited on pp. 74–76)
DOI: 10.1109/42.52985

[Gre90b] Peter J. **Green**. 'On Use of the EM for Penalized Likelihood Estimation'. In: *Journal of the Royal Statistical Society B* 52.3 (1990), pp. 443–452. (Cited on p. 76)
URL: http://www.jstor.org/stable/2345668 (Visited on 23rd June 2015)

[Gri96] N. Thorne **Griscom**. 'Pediatric Radiology'. In: *A History of the Radiological Sciences: Diagnosis*. Ed. by Raymond **Gagliardi** and Bruce L. **McClennan**. 1996. Chap. 14, pp. 344–367. (Cited on p. 27)
URL: http://www.arrs.org/Publications/HRS.aspx (Visited on 19th May 2015)

[Gro06] A. **Groso**, R. **Abela** and Marco **Stampanoni**. 'Implementation of a fast method for high resolution phase contrast tomography'. In: *Optics Express* 14.18 (Sept. 2006), pp. 8103–8110. (Cited on p. 140)
DOI: 10.1364/OE.14.008103

[Gro38] Gustav **Grossmann**. 'Method of and Apparatus for Making Radiographs More Particularly of Body Sections'. Patent US 2,110,953. Mar. 1938. (Cited on p. 30)
URL: http://worldwide.espacenet.com/publicationDetails/biblio?CC=US&NR=2110953 (Visited on 5th July 2015)

[Grü97] Frank **Grünwald**, Christian **Menzel**, Hans **Bender**, Holger **Palmedo**, Petra **Willkomm**, Jürgen **Ruhlmann**, Tom **Frankson** and Hans-Jürgen **Biersack**. 'Comparison of ^{18}FDG-PET with ^{131}Iodine and ^{99m}Tc-Sestamibi Scintigraphy in Differentiated Thyroid Cancer'. In: *Thyroid* 7.3 (June 1997), pp. 327–335. (Cited on p. 104)
DOI: 10.1089/thy.1997.7.327

[Gu94] Ming **Gu** and Stanley C. **Eisenstat**. *A Stable and Fast Algorithm for Updating the Singular Value Decomposition*. Research Report RR-966. New Haven: Yale University, 1994. (Cited on p. 119)
URL: http://www.cs.yale.edu/publications/techreports/tr966.pdf (Visited on 3rd July 2015)

[Guo07] Kanghui **Guo** and Demetrio **Labate**. 'Optimally Sparse Multidimensional Representation Using Shearlets'. In: *SIAM Journal on Mathematical Analysis* 39.1 (2007), pp. 298–318. (Cited on p. 77)
DOI: 10.1137/060649781

[Gut73] Frederick **Guthrie**. 'On a new Relation between Heat and Electricity'. In: *Proceedings of the Royal Society of London* 21 (Feb. 1873), pp. 168–169. (Cited on p. 11)
DOI: 10.1098/rspl.1872.0037

[Haa11] Alfred **Haar**. 'Zur Theorie der orthogonalen Funktionensysteme [On the Theory of Orthogonal Systems of Functions]'. In: *Mathematische Annalen* 71.1 (Mar. 1911), pp. 38–53. (Cited on p. 77)
DOI: 10.1007/BF01456927

[Had02] Jacques **Hadamard**. 'Sur les Problèmes aux Dérivées Partielles et Leur Signification Physique [On Partial Differential Problems and Their Physical Significance]'. In: *Princeton University Bulletin* 13.4 (Apr. 1902), pp. 49–52. (Cited on p. 47)
URL: http://hdl.handle.net/2027/chi.095582186 (Visited on 22nd June 2015)

[Hah13] Dieter **Hahn**, Pierre **Thibault**, Andreas **Fehringer**, Martin **Bech**, Peter B. **Noël** and Franz **Pfeiffer**. 'Bone artifact reduction in differential phase-contrast CT'. In: *Proceedings of International Meeting on Fully Three-Dimensional Image Reconstruction in Radiology and Nuclear Medicine (Fully3D)*. June 2013. (Cited on p. 146)
URL: http://www.fully3d.org/Fully3D2013Proceedings.pdf (Visited on 5th July 2015)

[Hak14] Zahi N. **Hakim**. *Antique X-Ray Tubes and Accessories*. Website. Dec. 2014. (Cited on pp. 11, 20, 25)
URL: http://www.earlytubes.com (Visited on 21st Apr. 2015)

[Han08] Eberhard **Hansis**, Dirk **Schäfer**, Olaf **Dössel** and Michael **Grass**. 'Projection-based Motion Compensation for Gated Coronary Artery Reconstruction from Rotational X-ray Angiograms'. In: *Physics in Medicine and Biology* 53.14 (July 2008), pp. 3807–3820. (Cited on p. 89)
DOI: 10.1088/0031-9155/53/14/007

[Han87] Per Christian **Hansen**. 'The Truncated SVD as a Method for Regularization'. In: *BIT Numerical Mathematics* 27.4 (Dec. 1987), pp. 534–553. (Cited on p. 57)
DOI: 10.1007/BF01937276

[Han98] Per Christian **Hansen**. *Rank-Deficient and Discrete Ill-Posed Problems. Numerical Aspects of Linear Inversion*. Philadelphia: SIAM, 1998. (Cited on pp. 72, 75, 119)
DOI: 10.1137/1.9780898719697

[Har04] Richard **Hartley** and Andrew **Zisserman**. *Multiple View Geometry in Computer Vision*. Second edition. Cambridge: Cambridge University Press, Mar. 2004. ISBN: 978-0521540513. (Cited on p. 57)

[Har15] Alexander **Hartl**, Dzhoshkun I. **Shakir**, Tobias **Lasser**, Sibylle I. **Ziegler** and Nassir **Navab**. 'Detection models for freehand SPECT reconstruction'. In: *Physics in Medicine and Biology* 60.3 (Feb. 2015), pp. 1031–1046. (Cited on p. 108)
DOI: 10.1088/0031-9155/60/3/1031

[Har65] P. V. **Harper**, R. N. **Beck**, D. E. **Charleston**, B. **Brunsden** and K. A. **Lathrop**. 'The Three Dimensional Mapping and Display of Radioisotope Distributions'. In: *Journal of Nuclear Medicine* 6.5 (May 1965), p. 332. (Cited on p. 39)
URL: http://jnm.snmjournals.org/content/6/5/325.full.pdf+html (Visited on 5th July 2015)

[Har95] H. R. **Harach** and E. D. **Williams**. 'Childhood thyroid cancer in England and Wales'. In: *British Journal of Cancer* 72.3 (Sept. 1995), pp. 777–783. (Cited on p. 104)
DOI: 10.1038/bjc.1995.410

[Has96] E. **Haschek** and O. Th. **Lindenthal**. 'Ein Beitrag zur praktischen Verwertung der Photographie nach Röntgen [A Contribution to the Practical Use of the Photography According to Röntgen]'. In: *Wiener Klinische Wochenschrift* 9.4 (Jan. 1896), p. 63. (Cited on p. 22)

[Hau96] Arthur G. **Haus** and Johne E. **Cullinan**. 'Recording the Image'. In: *A History of the Radiological Sciences: Diagnosis*. Ed. by Raymond **Gagliardi** and Bruce L. **McClennan**. 1996. Chap. 5, pp. 87–107. (Cited on p. 19)
URL: http://www.arrs.org/Publications/HRS.aspx (Visited on 19th May 2015)

[Hay96] Tamara Miner **Haygood** and Stanley P. **Bohrer**. 'Skeletal Radiology'. In: *A History of the Radiological Sciences: Diagnosis*. Ed. by Raymond **Gagliardi** and Bruce L. **McClennan**. 1996. Chap. 6, pp. 108–130. (Cited on p. 22)
URL: http://www.arrs.org/Publications/HRS.aspx (Visited on 19th May 2015)

[Hei27] Werner **Heisenberg**. 'Über den anschaulichen Inhalt der quantentheoretischen Kinematik und Mechanik [On the Perceptual Content of Quantum Theoretical Kinematics and Mechanics]'. In: *Zeitschrift für Physik* 43.3–4 (1927), pp. 172–198. (Cited on p. 4)
DOI: 10.1007/BF01397280

[Hei96] E. Robert **Heitzman** Jr. and Reginald **Greene**. 'Chest Radiology'. In: *A History of the Radiological Sciences: Diagnosis*. Ed. by Raymond **Gagliardi** and Bruce L. **McClennan**. 1996. Chap. 7, pp. 131–172. (Cited on pp. 22, 27)
URL: http://www.arrs.org/Publications/HRS.aspx (Visited on 19th May 2015)

[Hel67] Hermann von **Helmholtz**. 'Von den Wahrnehmungen im Allgemeinen [About Perception in General]'. In: *Handbuch der Physiologischen Optik [Handbook of Physiological Optics]*. Vol. 3. Leipzig, 1867. (Cited on p. 3)
URL: https://archive.org/details/handbuchderphysi00helm (Visited on 15th May 2015)

[Hel99] Sigurdur **Helgason**. *The Radon Transform*. Second edition. Springer, 1999. ISBN: 978-1475714630. (Cited on pp. 47, 82)
DOI: 10.1007/978-1-4757-1463-0

[Hem08] Eckhard **Hempel**, Martin **Hoheisel**, Stefan **Popescu**, Christian **David**, Tilman **Donath** and Franz **Pfeiffer**. 'Röntgen-CT-System zur Röntgen-Phasenkontrast- und/oder Röntgen-Dunkelfeld-Bildgebung [X-ray CT system for X-ray phase contrast and/or X-ray dark-field imaging]'. Patent EP 2,168,488. Sept. 2008. (Cited on p. 146)
URL: http://worldwide.espacenet.com/publicationDetails/biblio?CC=EP&NR=2168488 (Visited on 8th July 2015)

[Her00] Friedrich Wilhelm (William) **Herschel**. 'Experiments on the Refrangibility of the Invisible Rays of the Sun'. In: *Philosophical Transactions of the Royal Society of London* 90 (1800), pp. 284–292. (Cited on p. 9)
DOI: 10.1098/rstl.1800.0015

[Her09] Gabor T. **Herman**. *Fundamentals of Computerized Tomography*. Second edition. London: Springer, 2009. (Cited on pp. 17, 30, 35, 47, 49, 50, 52, 54, 55, 59, 60, 82, 115)
DOI: 10.1007/978-1-84628-723-7

[Her78] Gabor T. **Herman**, Arnold **Lent** and Peter H. **Lutz**. 'Relaxation Methods for Image Reconstruction'. In: *Communications of the ACM* 21.2 (Feb. 1978), pp. 152–158. (Cited on p. 59)
DOI: 10.1145/359340.359351

[Her87] Heinrich Rudolf **Hertz**. 'Über sehr schnelle electrische Schwingungen [On very rapid electric oscillations]'. In: *Annalen der Physik* 267.7 (1887), pp. 421–448. (Cited on p. 9)
DOI: 10.1002/andp.18872670707

[Her93] Gabor T. **Herman** and Lorraine B. **Meyer**. 'Algebraic Reconstruction Techniques Can Be Made Computationally Efficient'. In: *IEEE Transactions on Medical Imaging* 12.3 (Sept. 1993), pp. 600–609. (Cited on p. 59)
DOI: 10.1109/42.241889

[Hes52] Magnus R. **Hestenes** and Eduard **Stiefel**. 'Methods of Conjugate Gradients for Solving Linear Systems'. In: *Journal of Research of the National Bureau of Standards* 49.6 (Dec. 1952), pp. 409–436. (Cited on pp. 61, 155)
DOI: 10.6028/jres.049.044

[Heu12] D. A. **Heuveling**, K. H. **Karagozoglu**, A. van **Schie**, S. van **Weert**, A. van **Lingen** and R. de **Bree**. 'Sentinel node biopsy using 3D lymphatic mapping by freehand SPECT in early stage oral cancer. A new technique'. In: *Clinical Otolaryngology* 37.1 (Feb. 2012), pp. 89–90. (Cited on p. 103)
DOI: 10.1111/j.1749-4486.2011.02427.x

[Hev36] George Charles **Hevesy**, Kaj Ulrik **Linderstrøm-Lang** and Carsten Erik **Olsen**. 'Atomic Dynamics of Plant Growth'. In: *Nature* 137.3454 (Jan. 1936), pp. 66–67. (Cited on p. 24)
DOI: 10.1038/137066a0

[Hev44] George de **Hevesy**. *Some applications od isotopic indicators*. Nobel Lecture. Dec. 1944. (Cited on p. 24)
URL: http://www.nobelprize.org/nobel_prizes/chemistry/laureates/1943/hevesy-lecture.pdf (Visited on 5th July 2015)

[Hof76] Edward J. **Hoffman**, Michael E. **Phelps**, Nizar A. **Mullani**, Carol S. **Higgins** and Michel M. **Ter-Pogossian**. 'Design and Performance Characteristics of a Whole-Body Positron Transaxial Tomograph'. In: *Journal of Nuclear Medicine* 17.6 (June 1976), pp. 493–502. (Cited on p. 42)
URL: http://jnm.snmjournals.org/content/17/6/493.full.pdf+html (Visited on 5th July 2015)

[Hol30] Gilles **Holst**. 'Method of and Apparatus for Obtaining Photographic Images from Primary Actinic Images'. Patent GB 326,200. Mar. 1930. (Cited on p. 20)
URL: http://worldwide.espacenet.com/publicationDetails/biblio?CC=GB&NR=326200 (Visited on 5th July 2015)

[Hol34] Gilles **Holst**, Jan Hendrik de **Boer**, Marten Cornelis **Teves** and Cornelis Frederik **Veenemans**. 'An Apparatus for the Transformation of Light of Long Wavelength into Light of Short Wavelength'. In: *Physica* 1.1–6 (Feb. 1934), pp. 297–305. (Cited on p. 20)
DOI: 10.1016/S0031-8914(34)90036-7

[Hot33] Harold **Hotelling**. 'Analysis of a complex of statistical variables into principal components'. In: *Journal of Educational Psychology* 24.6 (Sept. 1933), pp. 417–441. (Cited on p. 157)
DOI: 10.1037/h0071325

[Hou73a] Godfrey N. **Hounsfield**. 'Computerized transverse axial scanning (tomography): Part 1. Description of system'. In: *British Journal of Radiology* 46.552 (Dec. 1973), pp. 1016–1022. (Cited on p. 35)
DOI: 10.1259/0007-1285-46-552-1016

[Hou73b] Godfrey N. **Hounsfield**. 'Method and Apparatus for Measuring X- or γ-Radiation Absorption or Transmission at Plural Angles and Analyzing the Data'. Patent US 3,778,614. Dec. 1973. (Cited on pp. 60, 82)
URL: http://worldwide.espacenet.com/publicationDetails/biblio?CC=US&NR=3778614 (Visited on 5th July 2015)

[Hou79] Godfrey N. **Hounsfield**. *Computed Medical Imaging*. Nobel Lecture. Dec. 1979. (Cited on p. 35)
URL: http://www.nobelprize.org/nobel_prizes/medicine/laureates/1979/hounsfield-lecture.pdf (Visited on 5th July 2015)

[Hra08] Maja **Hrabak**, Ranka **Stern Padovan**, Marko **Kralik**, David **Ozretic** and Kristina **Potocki**. 'Nikola Tesla and the Discovery of X-rays'. In: *RadioGraphics* 28.4 (July 2008), pp. 1189–1192. (Cited on p. 10)
DOI: 10.1148/rg.284075206

[Huc96] Michael S. **Huckman** and Donald A. **Stewart**. 'Neuroradiology'. In: *A History of the Radiological Sciences: Diagnosis*. Ed. by Raymond **Gagliardi** and Bruce L. **McClennan**. 1996. Chap. 12, pp. 289–318. (Cited on p. 22)
URL: http://www.arrs.org/Publications/HRS.aspx (Visited on 19th May 2015)

[Hud94] H. Malcom **Hudson** and Richard S. **Larkin**. 'Accelerated Image Reconstruction Using Ordered Subsets of Projection Data'. In: *IEEE Transactions on Medical Imaging* 13.4 (Dec. 1994), pp. 601–609. (Cited on p. 71)
DOI: 10.1109/42.363108

[Hun51] Lloyd P. **Hunter** and Richard L. **Longini**. 'Image Intensifier'. Patent US 2,555,545. June 1951. (Cited on p. 20)
URL: http://worldwide.espacenet.com/publicationDetails/biblio?CC=US&NR=2555545 (Visited on 5th July 2015)

[Huy90] Christiaan **Huygens**. *Traité de la lumière [Treatise on light]*. Leiden, 1690. (Cited on p. 9)
URL: http://books.google.com/books?id=X9PKaZlChggC (Visited on 5th July 2015)

[ISO 4993] **ISO** 4993. *Steel and iron castings – Radiographic inspection*. 2009. (Cited on p. 28)
URL: https://www.iso.org/obp/ui/#iso:std:iso:4993 (Visited on 15th May 2015)

[ISO 5579] **ISO** 5579. *Non-destructive testing – Radiographic testing of metallic materials using film and X- or gamma rays – Basic rules*. 2013. (Cited on p. 28)
URL: https://www.iso.org/obp/ui/#iso:std:iso:5579 (Visited on 15th May 2015)

[Jaf01] Stéphane **Jaffard**, Yves **Meyer** and Robert D. **Ryan**. *Wavelets. Tools for Science and Technology*. Philadelphia: SIAM, 2001. ISBN: 978-0898714487. (Cited on pp. 55, 77)
DOI: 10.1137/1.9780898718119

[Jem10] Ahmedin **Jemal**, Rebecca **Siegel**, Jiaquan **Xu** and Elizabeth M. **Ward**. 'Cancer Statistics, 2010'. In: *CA: A Cancer Journal for Clinicians* 60.5 (Sept. 2010), pp. 277–300. (Cited on p. 104)
DOI: 10.3322/caac.20073

[Jen10a] Torben H. **Jensen**, Martin **Bech**, Oliver **Bunk**, Tilman **Donath**, Christian **David**, Robert **Feidenhans'l** and Franz **Pfeiffer**. 'Directional x-ray dark-field imaging'. In: *Physics in Medicine and Biology* 55.12 (June 2010), p. 3317. (Cited on p. 149)
DOI: 10.1088/0031-9155/55/12/004

[Jen10b] Torben Haugaard **Jensen**, Martin **Bech**, Irene **Zanette**, Timm **Weitkamp**, Christian **David**, Hans **Deyhle**, Simon **Rutishauser**, Elena **Reznikova**, Jürgen **Mohr**, Robert **Feidenhans'l** and Franz **Pfeiffer**. 'Directional x-ray dark-field imaging of strongly ordered systems'. In: *Physical Review B* 82.21 (Dec. 2010), p. 214103. (Cited on p. 149)
DOI: 10.1103/PhysRevB.82.214103

[Joh34] Fritz **John**. 'Bestimmung einer Funktion aus ihren Integralen über gewisse Mannigfaltigkeiten [Determination of a Function from Its Integrals over Certain Manifolds]'. In: *Mathematische Annalen* 109.1 (Dec. 1934), pp. 488–520. (Cited on p. 81)
DOI: 10.1007/BF01449151

[Jør11] Jakob H. **Jørgensen**, Tobias L. **Jensen**, Per Christian **Hansen**, Søren H. **Jensen**, Emil Y. **Sidky** and Xiaochuan **Pan**. 'Accelerated gradient methods for total-variation-based CT image reconstruction'. In: *Proceedings of International Meeting on Fully Three-Dimensional Image Reconstruction in Radiology and Nuclear Medicine (Fully3D)*. July 2011. (Cited on p. 73)
URL: http://arxiv.org/pdf/1105.4002.pdf (Visited on 5th July 2015)

[Jor81] Camille **Jordan**. 'Sur la série de Fourier [On the Fourier series]'. In: *Comptes Rendus Hebdomadaires des Séances de l'Académie des Sciences* 92 (Jan. 1881), pp. 228–230. (Cited on p. 72)
URL: http://catalogue.bnf.fr/ark:/12148/cb343481087 (Visited on 5th July 2015)

[Kac37] Stefan **Kaczmarz**. 'Angenäherte Auflösung von Systemen linearer Gleichungen [Approximate Solution of Systems of Linear Equations]'. In: *Bulletin International de l'Académie Polonaise des Sciences et des Lettres. Classe des Sciences Mathématiques et Naturelles. Série A, Sciences Mathématiques* 35 (June 1937), pp. 355–357. (Cited on p. 58)
URL: http://jasonstockmann.com/Jason_Stockmann/Welcome_files/kaczmarz_english_translation_1937.pdf (Visited on 23rd June 2015)

[Kah96a] David **Kahn**. 'Ancestral Voices'. In: *The Codebreakers*. Second edition. New York: Scribner, 1996, 895ff. ISBN: 978-0684831305. (Cited on p. 3)

[Kah96b] David **Kahn**. 'Messages from Outer Space'. In: *The Codebreakers*. Second edition. New York: Scribner, 1996, 938ff. ISBN: 978-0684831305. (Cited on p. 4)

[Kak87] Avinash C. **Kak** and Malcolm **Slaney**. *Principles of Computerized Tomographic Imaging*. New York: IEEE, 1987. ISBN: 978-0879421984. (Cited on pp. 17, 39, 44, 45, 47, 49, 50, 52, 54, 58–60)
URL: http://www.slaney.org/pct/index.html (Visited on 5th July 2015)

[Kal90] Willi A. **Kalender**, Wolfgang **Seissler**, Ernst **Klotz** and Peter **Vock**. 'Spiral Volumetric CT with Single-Breath-Hold Technique, Continuous Transport and Continuous Scanner Rotation'. In: *Radiology* 176.1 (July 1990), pp. 181–183. (Cited on p. 37)
DOI: 10.1148/radiology.176.1.2353088

[Kas00] Mihran Kirkor **Kassabian**. 'X-ray as an Irritant'. In: *American X-ray Journal* 7.4 (Oct. 1900), pp. 784–786. (Cited on p. 25)
URL: https://archive.org/details/americanxrayjour7819unse (Visited on 5th July 2015)

[Kas01] Mihran Kirkor **Kassabian**. 'Technique of X-ray Work'. In: *American X-ray Journal* 8.3 (Mar. 1901), pp. 867–875. (Cited on p. 19)
URL: https://archive.org/details/americanxrayjour7819unse (Visited on 5th July 2015)

[Kas03] Mihran Kirkor **Kassabian**. 'Instantaneous Skiagraphy'. In: *American X-ray Journal* 12.2 (Feb. 1903), pp. 41–44. (Cited on p. 19)
URL: https://archive.org/details/americanxrayjour1213unse (Visited on 5th July 2015)

[Kas88] Michael **Kass**, Andrew **Witkin** and Demetri **Terzopoulos**. 'Snakes. Active Contour Models'. In: *International Journal of Computer Vision* 1.4 (Jan. 1988), pp. 321–331. (Cited on p. 90)
DOI: 10.1007/BF00133570

[Kau87] Linda **Kaufman**. 'Implementing and Accelerating the EM Algorithm for Positron Emission Tomography'. In: *IEEE Transactions on Medical Imaging* 6.1 (Mar. 1987), pp. 37–51. (Cited on p. 69)
DOI: 10.1109/TMI.1987.4307796

[Kau93] Linda **Kaufman**. 'Maximum Likelihood, Least Squares, and Penalized Least Squares for PET'. In: *IEEE Transactions on Medical Imaging* 12.2 (June 1993), pp. 200–214. (Cited on pp. 69, 75)
DOI: 10.1109/42.232249

[Kei10a] Andreas **Keil**. 'Dynamic Variational Level Sets for Cardiac 4D Reconstruction'. PhD thesis. München: Technische Universität München, Department of Computer Science, Sept. 2010. (Cited on pp. 87, 90, 96, 97)
URL: http://nbn-resolving.de/urn/resolver.pl?urn:nbn:de:bvb:91-diss-20100916-978584-1-3 (Visited on 1st July 2015)

[Kes12] Elizabeth A. **Kessler**. *Picturing the Cosmos. Hubble Space Telescope Images and the Astronomical Sublime*. University of Minnesota Press, 2012. ISBN: 978-0816679577. (Cited on p. 7)

[Kha00] Rasool **Khadem**, Clement C. **Yeh**, Mohammad **Sadeghi-Tehrani**, Michael R. **Bax**, Jeremy A. **Johnson**, Jacqueline **Nerney Welch**, Eric P. **Wilkinson** and Ramin **Shahidi**. 'Comparative Tracking Error Analysis of Five Different Optical Tracking Systems'. In: *Computer Aided Surgery* 5.2 (2000), pp. 98–107. (Cited on pp. 101, 106)
DOI: 10.3109/10929080009148876

[Kie34] Jean **Kieffer**. 'X-ray Device and Method of Technique'. Patent US 1,954,321. Apr. 1934. (Cited on p. 30)
URL: http://worldwide.espacenet.com/publicationDetails/biblio?CC=US&NR=1954321 (Visited on 5th July 2015)

[Koe01a] Titus R. **Koenig**, Detlev **Wolff**, Fred A. **Mettler** and Louis K. **Wagner**. 'Skin Injuries from Fluoroscopically Guided Procedures'. In: *American Journal of Roentgenology* 177.1 (July 2001), pp. 3–11. (Cited on p. 27)
DOI: 10.2214/ajr.177.1.1770003

[Koe01b] Titus R. **Koenig**, Fred A. **Mettler** and Louis K. **Wagner**. 'Skin Injuries from Fluoroscopically Guided Procedures'. In: *American Journal of Roentgenology* 177.1 (July 2001), pp. 13–20. (Cited on p. 27)
DOI: 10.2214/ajr.177.1.1770013

[Kol15a] Taha S. **Koltukluoglu**, Christian **Binter**, Christine **Tanner**, Sven **Hirsch**, Sebastian **Kozerke**, Gábor **Székely** and Aymen **Laadhari**. 'A Partial Domain Approach to Enable Aortic Flow Simulation without Turbulent Modeling'. In: *Medical Image Computing and Computer-Assisted Intervention (MICCAI)*. Lecture Notes in Computer Science 9350 (Oct. 2015), pp. 544–551. (Cited on p. 45)
DOI: 10.1007/978-3-319-24571-3_65

[Kol15b] Taha S. **Koltukluoglu**, Sven **Hirsch**, Christian **Binter**, Sebastian **Kozerke**, Gábor **Székely** and Aymen **Laadhari**. 'A Robust Comparison Approach of Velocity Data between MRI and CFD based on Divergence-Free Space Projection'. In: *International Symposium on Biomedical Imaging (ISBI)*. Apr. 2015, pp. 1393–1397. (Cited on p. 45)
DOI: 10.1109/ISBI.2015.7164136

[Kol95] Th. M. **Koller**, G. **Gerig**, Gábor **Székely** and D. **Dettwiler**. 'Multiscale Detection of Curvilinear Structures in 2-D and 3-D Image Data'. In: *International Conference on Computer Vision* (June 1995), pp. 864–869. (Cited on p. 91)
DOI: 10.1109/ICCV.1995.466846

[Kop57] H. **Kopp**. 'Radiation Damaga Caused by Shoe-Fitting Fluoroscope'. In: *British Medical Journal* 5057 (Dec. 1957), pp. 1344–1345. (Cited on p. 27)
DOI: 10.1136/bmj.2.5057.1344

[Kuh63] David E. **Kuhl** and Roy Q. **Edwards**. 'Image Separation Radioisotope Scanning'. In: *Radiology* 80.4 (Apr. 1963), pp. 653–662. (Cited on p. 39)
DOI: 10.1148/80.4.653

[Kuh66] David E. **Kuhl**, John **Hale** and Walter L. **Eaton**. 'Transmission Scanning: A Useful Adjunct to Conventional Emission Scanning for Accurately Keying Isotope Deposition to Radiographic Anatomy'. In: *Radiology* 87.2 (Aug. 1966), pp. 278–284. (Cited on pp. 35, 43)
DOI: 10.1148/87.2.278

[Kut01] Martin Wilhelm **Kutta**. 'Beitrag zur näherungsweisen Integration totaler Differentialgleichungen [Contribution to the Approximate Integration of Total Differential Equations]'. In: *Zeitschrift für Mathematik und Physik* 46.4 (1901), pp. 435–453. (Cited on p. 159)
URL: https://archive.org/details/zeitschriftfrma12runggoog (Visited on 5th July 2015)

[Lag97] Joseph Louis **Lagrange**. *Théorie des Fonctions Analytiques [Theory of the Analytical Functions]*. Paris: Imprimerie de la République, 1797. (Cited on p. 72)
URL: https://archive.org/details/theoriedesfoncti00lagr (Visited on 28th June 2015)

[Lal95] David S. **Lalush** and Benjamin M. W. **Tsui**. 'The Importance of Preconditioners in Fast Poisson-based Iterative Reconstruction Algorithms for SPECT'. In: *IEEE Nuclear Science Symposium and Medical Imaging Conference* 3 (Oct. 1995), pp. 1326–1330. (Cited on p. 63)
DOI: 10.1109/NSSMIC.1995.500248

[Lam60] Johann Heinrich **Lambert**. *Photometria sive de Mensura et Gradibus Luminis, Colorum et Umbrae [Photometry, or on Measuring and the Gradations of Light, Colours and Shades]*. Augsburg, 1760, p. 391. (Cited on p. 17)
URL: http://books.google.com/books?id=JdkTAAAAQAAJ (Visited on 5th July 2015)

[Lan51] L. **Landweber**. 'An Iteration Formula for Fredholm Integral Equations of the First Kind'. In: *American Journal of Mathematics* 73.3 (July 1951), pp. 615–624. (Cited on p. 59)
DOI: 10.2307/2372313

[Lan61] Henry J. **Landau** and Henry O. **Pollak**. 'Prolate Spheroidal Wave Functions, Fourier Analysis and Uncertainty — II'. In: *Bell System Technical Journal* 40.1 (Jan. 1961), pp. 65–84. (Cited on p. 50)
DOI: 10.1002/j.1538-7305.1961.tb03977.x

[Lan62] Henry J. **Landau** and Henry O. **Pollak**. 'Prolate Spheroidal Wave Functions, Fourier Analysis and Uncertainty — III. The Dimension of the Space of Essentially Time- and Band-Limited Signals'. In: *Bell System Technical Journal* 41.4 (July 1962), pp. 1295–1336. (Cited on p. 50)
DOI: 10.1002/j.1538-7305.1962.tb03279.x

[Lan90] Kenneth **Lange**. 'Convergence of EM Image Reconstruction Algorithms with Gibbs Smoothing'. In: *IEEE Transactions on Medical Imaging* 9.4 (Dec. 1990), pp. 439–446. (Cited on p. 74)
DOI: 10.1109/42.61759

[Lan95] Kenneth **Lange** and Jeffrey A. **Fessler**. 'Globally convergent algorithms for maximum a posteriori transmission tomography'. In: *IEEE Transactions on Image Processing* 4.10 (Oct. 1995), pp. 1430–1438. (Cited on p. 66)
DOI: 10.1109/83.465107

[Lan97] Gottfried **Landwehr**. 'Wilhelm Conrad Röntgen and the Beginning of Modern Physics'. In: *Röntgen Centennial. X-rays in Natural and Life Sciences*. Ed. by Axel **Haase**, Gottfried **Landwehr** and Eberhard **Umbach**. Singapore: World Scientific, 1997, pp. 3–23. ISBN: 978-9810230852. (Cited on pp. 9, 10, 22)

[Las07] Tobias **Lasser** and Vasilis **Ntziachristos**. 'Optimization of 360° Projection Fluorescence Molecular Tomography'. In: *Medical Image Analysis* 11.4 (Aug. 2007), pp. 389–399. (Cited on pp. 118, 126, 128)
DOI: 10.1016/j.media.2007.04.003

[Las11a] Tobias **Lasser**. 'Tomographic Reconstruction Methods for Optical and Intra-operative Functional Imaging'. PhD thesis. München: Technische Universität München, Department of Computer Science, June 2011. (Cited on pp. 39, 42, 45, 106)
URL: http://nbn-resolving.de/urn/resolver.pl?urn:nbn:de:bvb:91-diss-20110609-1002052-1-4 (Visited on 1st July 2015)

[Las11b] Tobias **Lasser**, Sibylle I. **Ziegler** and Nassir **Navab**. 'Freehand SPECT in low uptake situations'. In: *Medical Imaging 2011. Physics of Medical Imaging*. Vol. 7961. Proc. SPIE. Mar. 2011, 79611Z. (Cited on p. 108)
DOI: 10.1117/12.877552

[Lau03] Paul C. **Lauterbur**. *All Science is Interdisciplinary. From Magnetic Moments to Molecules to Men*. Nobel Lecture. Dec. 2003. (Cited on p. 44)
URL: http://www.nobelprize.org/nobel_prizes/medicine/laureates/2003/lauterbur-lecture.pdf (Visited on 5th July 2015)

[Lau15] Béatrice **Lauby-Secretan**, Chiara **Scoccianti**, Dana **Loomis**, Lamia **Benbrahim-Tallaa**, Véronique **Bouvard**, Franca **Bianchini** and Kurt **Straif**. 'Breast-Cancer Screening – Viewpoint of the IARC Working Group'. In: *New England Journal of Medicine* (June 2015). (Cited on p. 27)
DOI: 10.1056/NEJMsr1504363

[Lau48] Ernst **Lau**. 'Beugungserscheinungen an Doppelrastern'. In: *Annalen der Physik* 437.7–8 (1948), pp. 417–423. (Cited on p. 142)
DOI: 10.1002/andp.19484370709

[Lau73] Paul C. **Lauterbur**. 'Image Formation by Induced Local Interactions: Examples Employing Nuclear Magnetic Resonance'. In: *Nature* 242.5394 (Mar. 1973), pp. 190–191. (Cited on p. 44)
DOI: 10.1038/242190a0

[Le 86] Denis **Le Bihan**, Eric **Breton**, Denis **Lallemand**, Philippe **Grenier**, Emmanuel **Cabanis** and Maurice **Laval-Jeantet**. 'MR Imaging of Intravoxel Incoherent Motions. Application to Diffusion and Perfusion in Neurologic Disorders'. In: *Radiology* 161.2 (Nov. 1986), pp. 401–407. (Cited on pp. 45, 151)
DOI: 10.1148/radiology.161.2.3763909

[Lee04] Laurence **Leenhardt**, Pascale **Grosclaude** and Laurence **Chérié-Challine**. 'Increased Incidence of Thyroid Carcinoma in France: A True Epidemic or Thyroid Nodule Management Effects? Report from the French Thyroid Cancer Committee'. In: *Thyroid* 14.12 (Dec. 2004), pp. 1056–1060. (Cited on p. 104)
DOI: 10.1089/thy.2004.14.1056

[Lev67] Hilde **Levi**. 'George de Hevesy: 1 August 1885 – 5 July 1966'. In: *Nuclear Physics. A* 98.1 (May 1967), pp. 1–24. (Cited on p. 24)
DOI: 10.1016/0375-9474(67)90894-9

[Lev76] Hilde **Levi**. 'George Hevesy and His Concept of Radioactive Indicators – In Retrospect'. In: *European Journal of Nuclear Medicine* 1.1 (1976), pp. 3–10. (Cited on p. 24)
DOI: 10.1007/BF00253259

[Lev87] Emanuel **Levitan** and Gabor T. **Herman**. 'A Maximum A Posteriori Probability Expectation Maximization Algorithm for Image Reconstruction in Emission Tomography'. In: *IEEE Transactions on Medical Imaging* 6.3 (Sept. 1987), pp. 185–192. (Cited on p. 75)
DOI: 10.1109/TMI.1987.4307826

[Li04] Qingde **Li** and John G. **Griffiths**. 'Least Squares Ellipsoid Specific Fitting'. In: *Proceedings of Geometric Modeling and Processing*. 2004, pp. 335–340. (Cited on p. 157)
DOI: 10.1109/GMAP.2004.1290055

[Lin10] Daniel J. **Lingenfelter** and Jeffrey A. **Fessler**. 'Augmented Lagrangian methods for penalized likelihood reconstruction in emission tomography'. In: *IEEE Nuclear Science Symposium and Medical Imaging Conference* (Oct. 2010), pp. 3288–3291. (Cited on p. 80)
DOI: 10.1109/NSSMIC.2010.5874413

[Lit96] Jesse T. **Littleton** and Marie Lou **Durizch Littleton**. 'Conventional Tomography'. In: *A History of the Radiological Sciences: Diagnosis*. Ed. by Raymond **Gagliardi** and Bruce L. **McClennan**. 1996. Chap. 15, pp. 368–401. (Cited on p. 30)
URL: http://www.arrs.org/Publications/HRS.aspx (Visited on 19th May 2015)

[Lot00] Gerhard **Lottes** and Otmar **Schober**. 'Zur Geschichte der Nuklearmedizin – eine chronologische Darstellung der Ursprünge aus Naturwissenschaft, Technik und Medizin [On the History of Nuclear Medicine – a Chronological Presentation of the Origins in Natural Sciences, Engineering and Medicine]'. In: *Zeitschrift für Medizinische Physik* 10.4 (2000), pp. 225–234. (Cited on p. 24)
DOI: 10.1016/S0939-3889(15)70285-0

[Low27] Jacob J. **Lowe**. 'Method and Means for Visually Determining the Fit of Footwear'. Patent US 1,614,988. Jan. 1927. (Cited on p. 27)
URL: http://worldwide.espacenet.com/publicationDetails/biblio?CC=US&NR=1614988 (Visited on 5th July 2015)

[Lučo5] Vladan **Lučić**, Friedrich **Förster** and Wolfgang **Baumeister**. 'Structural Studies by Electron Tomography. From Cells to Molecules'. In: *Annual Review of Biochemistry* 74 (July 2005), pp. 833–865. (Cited on p. 46)
DOI: 10.1146/annurev.biochem.73.011303.074112

[Mag14] Jessica **Magaraggia**, Gerhard **Kleinszig**, Wei **Wei**, Markus **Weiten**, Rainer **Graumann**, Elli **Angelopoulou** and Joachim **Hornegger**. 'On the accuracy of a video-based drill-guidance solution for orthopedic and trauma surgery. Preliminary results'. In: *Medical Imaging 2014. Robotic Interventions, and Modeling*. Vol. 9036. Proc. SPIE. Mar. 2014, p. 903610. (Cited on p. 108)
DOI: 10.1117/12.2043508

[Mah14] James **Mahaffey**. *Atomic Accidents. A History of Nuclear Meltdowns and Disasters from the Ozark Mountains to Fukushima*. New York: Pegasus Books, 2014. ISBN: 978-1605986807. (Cited on p. 10)

[Mal13a] Andreas **Malecki**. 'X-Ray Tensor Tomography'. PhD thesis. München: Technische Universität München, Department of Physics, June 2013. (Cited on pp. 149, 151)
URL: http://nbn-resolving.de/urn/resolver.pl?urn:nbn:de:bvb:91-diss-20130822-1156401-0-3 (Visited on 1st July 2015)

[Mal13b] Andreas **Malecki**, Guillaume **Potdevin**, Thomas **Biernath**, Elena **Eggl**, Eduardo **Grande Garcia**, Thomas **Baum**, Peter B. **Noël**, Jan S. **Bauer** and Franz **Pfeiffer**. 'Coherent Superposition in Grating-Based Directional Dark-Field Imaging'. In: *PLoS ONE* 8.4 (2013), e61268. (Cited on pp. 153, 154)
DOI: 10.1371/journal.pone.0061268

[Mal14] Andreas **Malecki**, Guillaume **Potdevin**, Thomas **Biernath**, Elena **Eggl**, Konstantin **Willer**, Tobias **Lasser**, Jens **Maisenbacher**, Jens **Gibmeier**, Alexander **Wanner** and Franz **Pfeiffer**. 'X-ray tensor tomography'. In: *Europhysics Letters* 105.3 (Feb. 2014), p. 38002. (Cited on pp. ii, iv, 149, 151)
DOI: 10.1209/0295-5075/105/38002

[Man03] Peter **Mansfield**. *Snap-Shot MRI*. Nobel Lecture. Dec. 2003. (Cited on p. 44)
URL: http://www.nobelprize.org/nobel_prizes/medicine/laureates/2003/mansfield-lecture.pdf (Visited on 5th July 2015)

[Mar12a] Michael **Markl**, Alex **Frydrychowicz**, Sebastian **Kozerke**, Mike **Hope** and Oliver **Wieben**. '4D Flow MRI'. In: *Journal of Magnetic Resonance Imaging* 36.5 (Nov. 2012), pp. 1015–1036. (Cited on p. 45)
DOI: 10.1002/jmri.23632

[Mar12b] Federica **Marone** and Marco **Stampanoni**. 'Regridding reconstruction algorithm for real-time tomographic imaging'. In: *Journal of Synchrotron Radiation* 19.6 (Nov. 2012), pp. 1029–1037. (Cited on pp. 15, 50)
DOI: 10.1107/S0909049512032864

[Mar12c] Yasuhiro **Maruoka**, Koichiro **Abe**, Shingo **Baba**, Takuro **Isoda**, Hirofumi **Sawamoto**, Yoshitaka **Tanabe**, Masayuki **Sasaki** and Hiroshi **Honda**. 'Incremental Diagnostic Value of SPECT/CT with ^{131}I Scintigraphy after Radioiodine Therapy in Patients with Well-differentiated Thyroid Carcinoma'. In: *Radiology* 265.3 (Dec. 2012), pp. 902–909. (Cited on p. 104)
DOI: 10.1148/radiol.12112108

[Mar47] Louis C. **Martin**. 'Phase-Contrast Methods in Microscopy'. In: *Nature* 159.4051 (June 1947), pp. 827–830. (Cited on p. 137)
DOI: 10.1038/159827a0

[Mar84] Andrew **Markoe**. 'Fourier Inversion of the Attenuated X-Ray Transform'. In: *SIAM Journal on Mathematical Analysis* 15.4 (July 1984), pp. 718–722. (Cited on p. 54)
DOI: 10.1137/0515055

[Max65] James Clerk **Maxwell**. 'A Dynamical Theory of the Electromagnetic Field'. In: *Philosophical Transactions of the Royal Society of London* 155 (1865), pp. 459–512. (Cited on p. 9)
DOI: 10.1098/rstl.1865.0008

[McD09] Samuel Alan **McDonald**, Federica **Marone**, Christoph **Hintermüller**, Gordan **Mikuljan**, Christian **David**, Franz **Pfeiffer** and Marco **Stampanoni**. 'Advanced phase-contrast imaging using a grating interferometer'. In: *Journal of Synchrotron Radiation* 16.4 (July 2009), pp. 562–572. (Cited on p. 146)
DOI: 10.1107/S0909049509017920

[Mea96] Thomas F. **Meaney**. 'Magnetic Resonance Imaging'. In: *A History of the Radiological Sciences: Diagnosis*. Ed. by Raymond **Gagliardi** and Bruce L. **McClennan**. 1996. Chap. 19, pp. 470–482. (Cited on p. 45)
URL: http://www.arrs.org/Publications/HRS.aspx (Visited on 19th May 2015)

[Mer98] Pierre **Mercier**. 'André Bocage et la tomographie ou la vie d'un homme qui aurait dû être illustre [André Bocage and tomography or the life of a man who should have been famous]'. In: *Histoire des Sciences Médicales* 32.2 (Apr. 1998), pp. 169–173. (Cited on p. 30)
URL: http://www.biusante.parisdescartes.fr/sfhm/hsm/HSMx1998x032x002/HSMx1998x032x002x0169.pdf (Visited on 23rd May 2015)

[Met53] Wolfgang **Metzger**. *Gesetze des Sehens [Laws of Seeing]*. Zweite Auflage. Frankfurt: Kramer, 1953. ISBN: 978-3880744929. (Cited on p. 4)

[Mia99] Jianwei **Miao**, Pambos **Charalambous**, Janos **Kirz** and David **Sayre**. 'Extending the methodology of X-ray crystallography to allow imaging of micrometre-sized non-crystalline specimens'. In: *Nature* 400.6742 (July 1999), pp. 342–344. (Cited on p. 140)
DOI: 10.1038/22498

[Mok00] Detlef **Moka**, Eberhard **Voth**, Markus **Dietlein**, Antonio **Larena-Avellaneda** and Harald **Schicha**. 'Technetium 99m-MIBI-SPECT. A highly sensitive diagnostic tool for localization of parathyroid adenomas'. In: *Surgery* 128.1 (July 2000), pp. 29–35. (Cited on p. 104)
DOI: 10.1067/msy.2000.107066

[Mol71] Abraham André **Moles**. *Informationstheorie und ästhethische Wahrnehmung [Information theory and aesthetic perception]*. (Originally "*Théorie de l'information et perception esthétique*", 1958). Köln: DuMont Schauberg, 1971. ISBN: 978-3770105267. (Cited on p. 7)

[Mom95] Atsushi **Momose**, Tohoru **Takeda** and Yuji **Itai**. 'Phase-contrast x-ray computed tomography for observing biological specimens and organic materials'. In: *Review of Scientific Instruments* 66.2 (Feb. 1995), pp. 1434–1436. (Cited on p. 146)
DOI: 10.1063/1.1145931

[Mom96] Atsushi **Momose**, Tohoru **Takeda**, Yuji **Itai** and Keiichi **Hirano**. 'Phase-contrast X-ray computed tomography for observing biological soft tissues'. In: *Nature Medicine* 2.4 (Apr. 1996), pp. 473–475. (Cited on p. 146)
DOI: 10.1038/nm0496-473

[Mor82] Paul R. **Moran**. 'A Flow Velocity Zeugmatographic Interlace for NMR Imaging in Humans'. In: *Magnetic Resonance Imaging* 1.4 (1982), pp. 197–203. (Cited on p. 45)
DOI: 10.1016/0730-725X(82)90170-9

[Mov06] Babak **Movassaghi**, Dirk **Schaefer**, Michael **Grass**, Volker **Rasche**, Onno **Wink**, Joel A. **Garcia**, James Y. **Chen**, John C. **Messenger** and John D. **Carroll**. '3D Reconstruction of Coronary Stents in Vivo Based on Motion Compensated X-Ray Angiograms'. In: *Medical Image Computing and Computer-Assisted Intervention (MICCAI)*. Lecture Notes in Computer Science 4191 (Oct. 2006), pp. 177–184. (Cited on p. 89)
DOI: 10.1007/11866763_22

[Mul27] Hermann Joseph **Muller**. 'Artificial Transmutation of the Gene'. In: *Science* 66.1699 (July 1927), pp. 84–87. (Cited on p. 26)
DOI: 10.1126/science.66.1699.84

[Mum94] Erkan Ü. **Mumcuoğlu**, Richard **Leahy**, Simon R. **Cherry** and Zhenyu **Zhou**. 'Fast Gradient-Based Methods for Bayesian Reconstruction of Transmission and Emission PET Images'. In: *IEEE Transactions on Medical Imaging* 13.4 (Dec. 1994), pp. 687–701. (Cited on p. 63)
DOI: 10.1109/42.363099

[Naj11] Shetha **Naji**, Amir **Tadros**, Joerg **Traub** and Ciaran **Healy**. 'Case report: Improving the speed and accuracy of melanoma sentinel node biopsy with 3D intra-operative imaging'. In: *Journal of Plastic, Reconstructive and Aesthetic Surgery* 64.12 (Dec. 2011), pp. 1712–1715. (Cited on p. 103)
DOI: 10.1016/j.bjps.2011.05.011

[Nat01a] Frank **Natterer**. 'Inversion of the attenuated Radon transform'. In: *Inverse Problems* 17.1 (Feb. 2001), pp. 113–119. (Cited on p. 54)
DOI: 10.1088/0266-5611/17/1/309

[Nat01b] Frank **Natterer**. *The Mathematics of Computerized Tomography*. Philadelphia: SIAM, 2001. (Cited on p. 47)
DOI: 10.1137/1.9780898719284

[Nat01c] Frank **Natterer** and Frank **Wübbeling**. *Mathematical Methods in Image Reconstruction*. Philadelphia: SIAM, 2001. (Cited on pp. 47, 49)
DOI: 10.1137/1.9780898718324

[Nat86] Frank **Natterer**. *The Mathematics of Computerized Tomography*. Stuttgart: Teubner, 1986. (Cited on pp. 47, 49, 50, 52, 54, 59)
DOI: 10.1007/978-3-663-01409-6

[New04] Isaac **Newton**. *Opticks or a Treatise of the Reflexions, Refractions, Inflexions and Colours of Light*. London, 1704. (Cited on p. 9)
URL: http://gallica.bnf.fr/ark:/12148/bpt6k3362k (Visited on 5th July 2015)

[Ntz05] Vasilis **Ntziachristos**, Jorge **Ripoll**, Lihong V. **Wang** and Ralph **Weissleder**. 'Looking and listening to light. The evolution of whole-body photonic imaging'. In: *Nature Biotechnology* 23.3 (Mar. 2005), pp. 313–320. (Cited on p. 45)
DOI: 10.1038/nbt1074

[Nut02] Ronald **Nutt**. 'The History of Positron Emission Tomography'. In: *Molecular Imaging and Biology* 4.1 (Jan. 2002), pp. 11–26. (Cited on p. 42)
DOI: 10.1016/S1095-0397(00)00051-0

[NYT04] 'C. M. Dally Dies a Martyr to Science'. In: *The New York Times* (Oct. 1904), p. 16. (Cited on p. 25)
URL: http://query.nytimes.com/gst/abstract.html?res=9501EEDF123BE733A25757C0A9669D946597D6CF (Visited on 19th May 2015)

[NYW03] 'Edison Fears Hidden Perils of the X-Rays'. In: *New York World* (Aug. 1903), p. 1. (Cited on p. 25)
URL: https://web.archive.org/web/20140307181654/http://home.gwi.net/~dnb/read/edison/edison_xrays.htm (Visited on 19th May 2015)

[Oga90] Seiji **Ogawa**, T. M. **Lee**, A. R. **Kay** and D. W. **Tank**. 'Brain magnetic resonance imaging with contrast dependent on blood oxygenation'. In: *Proceedings of the National Academy of Sciences of the United States of America* 87.24 (Dec. 1990), pp. 9868–9872. (Cited on p. 45)
URL: http://www.pnas.org/content/87/24/9868.abstract (Visited on 21st June 2015)

[Old61] William H. **Oldendorf**. 'Isolated Flying Spot Detection of Radiodensity Discontinuities – Displaying the Internal Structural Pattern of a Complex Object'. In: *IRE Transactions on Bio-Medical Electronics* 8.1 (Jan. 1961), pp. 68–72. (Cited on pp. 35, 82)
DOI: 10.1109/TBMEL.1961.4322854

[Old63] William H. **Oldendorf**. 'Radiant Energy Apparatus for Investigating Selected Areas of the Interior of Objects Obscured by Dense Material'. Patent US 3,106,640. Oct. 1963. (Cited on pp. 35, 82)
URL: http://worldwide.espacenet.com/publicationDetails/biblio?CC=US&NR=3106640 (Visited on 5th July 2015)

[Osh88] Stanley **Osher** and James A. **Sethian**. 'Fronts Propagating with Curvature Dependent Speed. Algorithms Based on Hamilton-Jacobi Formulations'. In: *Journal of Computational Physics* 79.1 (Nov. 1988), pp. 12–49. (Cited on p. 90)
DOI: 10.1016/0021-9991(88)90002-2

[OSu85] John D. **O'Sullivan**. 'A Fast Sinc Function Gridding Algorithm for Fourier Inversion in Computer Tomography'. In: *IEEE Transactions on Medical Imaging* 4.4 (Dec. 1985), pp. 200–207. (Cited on p. 50)
DOI: 10.1109/TMI.1985.4307723

[Pan99] V. Y. **Panin**, G. L. **Zeng** and G. T. **Gullberg**. 'Total Variation Regulated EM Algorithm'. In: *IEEE Transactions on Nuclear Science* 46.6 (Dec. 1999), pp. 2202–2210. (Cited on p. 73)
DOI: 10.1109/23.819305

[Par98] Lucas **Parra** and Harrison H. **Barrett**. 'List-Mode Likelihood. EM Algorithm and Image Quality Estimation Demonstrated on 2-D PET'. In: *IEEE Transactions on Medical Imaging* 17.2 (Apr. 1998), pp. 228–235. (Cited on pp. 66, 108)
DOI: 10.1109/42.700734

[Pas12] Jeffrey J. **Pasternak** and Eric E. **Williamson**. 'Clinical Pharmacology, Uses, and Adverse Reactions of Iodinated Contrast Agents. A Primer for the Non-radiologist'. In: *Mayo Clinic Proceedings* 87.4 (Apr. 2012), pp. 390–402. (Cited on p. 140)
DOI: 10.1016/j.mayocp.2012.01.012

[Pat96] Dennis D. **Patton**. 'Röntgen and the Discovery'. In: *A History of the Radiological Sciences: Diagnosis*. Ed. by Raymond **Gagliardi** and Bruce L. **McClennan**. 1996. Chap. 2, pp. 30–46. (Cited on p. 10)
URL: http://www.arrs.org/Publications/HRS.aspx (Visited on 19th May 2015)

[Pea01] Karl **Pearson**. 'On Lines and Planes of Closes Fit to Systems of Points in Space'. In: *Philosophical Magazine*. 6th ser. 2.11 (1901), pp. 559–572. (Cited on p. 157)
DOI: 10.1080/14786440109462720

[Pen93] William B. **Pennebaker** and Joan L. **Mitchell**. *JPEG. Still Image Data Compression Standard*. Springer, 1993. ISBN: 978-0442012724. (Cited on p. 77)

[Per73] B. John **Perry** and C. **Bridges**. 'Computerized transverse axial scanning (tomography): Part 3. Radiation dose considerations'. In: *British Journal of Radiology* 46.552 (Dec. 1973), pp. 1048–1051. (Cited on p. 35)
DOI: 10.1259/0007-1285-46-552-1048

[Pfe06] Franz **Pfeiffer**, Timm **Weitkamp**, Oliver **Bunk** and Christian **David**. 'Phase retrieval and differential phase-contrast imaging with low-brilliance X-ray sources'. In: *Nature Physics* 2.4 (Apr. 2006), pp. 258–261. (Cited on p. 140)
DOI: 10.1038/nphys265

[Pfe07a] Franz **Pfeiffer**, Oliver **Bunk**, Christian **David**, Martin **Bech**, G. **Le Duc**, A. **Bravin** and P. **Cloetens**. 'High-resolution brain tumor visualization using three-dimensional x-ray phase contrast tomography'. In: *Physics in Medicine and Biology* 52.23 (Dec. 2007), pp. 6923–6930. (Cited on p. 146)
DOI: 10.1088/0031-9155/52/23/010

[Pfe07b] Franz **Pfeiffer**, C. **Kottler**, Oliver **Bunk** and Christian **David**. 'Hard X-Ray Phase Tomography with Low-Brilliance Sources'. In: *Physical Review Letters* 98.10 (Mar. 2007), p. 108105. (Cited on p. 146)
DOI: 10.1103/PhysRevLett.98.108105

[Pfe08] Franz **Pfeiffer**, Martin **Bech**, Oliver **Bunk**, P. **Kraft**, E. F. **Eikenberry**, Ch. **Brönnimann**, C. **Grünzweig** and Christian **David**. 'Hard-X-ray dark-field imaging using a grating interferometer'. In: *Nature Materials* 7.2 (Feb. 2008), pp. 134–137. (Cited on p. 143)
DOI: 10.1038/nmat2096

[Phe75] Michael E. **Phelps**, Edward J. **Hoffman**, Nizar A. **Mullani** and Michel M. **Ter-Pogossian**. 'Application of Annihilation Coincidence Detection to Transaxial Reconstruction Tomography'. In: *Journal of Nuclear Medicine* 16.3 (Mar. 1975), pp. 210–224. (Cited on p. 42)
URL: http://jnm.snmjournals.org/content/16/3/210.full.pdf+html (Visited on 5th July 2015)

[Phe76] Michael E. **Phelps**, Edward J. **Hoffman**, Nizar A. **Mullani**, Carol S. **Higgins** and Michel M. **Ter-Pogossian**. 'Design Considerations for a Positron Emission Transaxial Tomograph (PETT III)'. In: *IEEE Transactions on Nuclear Science* 23.1 (Feb. 1976), pp. 516–522. (Cited on p. 42)
DOI: 10.1109/TNS.1976.4328298

[Phi62] David L. **Phillips**. 'A Technique for the Numerical Solution of Certain Integral Equations of the First Kind'. In: *Journal of the ACM* 9.1 (Jan. 1962), pp. 84–97. (Cited on p. 72)
DOI: 10.1145/321105.321114

[Pin12] B. R. **Pinzer**, M. **Cacquevel**, P. **Modregger**, Samuel Alan **McDonald**, J. C. **Bensadoun**, Thomas **Thuering**, P. **Aebischer** and Marco **Stampanoni**. 'Imaging brain amyloid deposition using grating-based differential phase contrast tomography'. In: *NeuroImage* 61.4 (July 2012), pp. 1336–1346. (Cited on p. 146)
DOI: 10.1016/j.neuroimage.2012.03.029

[Pol96a] Howard M. **Pollack**. 'Uroradiology'. In: *A History of the Radiological Sciences: Diagnosis*. Ed. by Raymond **Gagliardi** and Bruce L. **McClennan**. 1996. Chap. 9, pp. 195–253. (Cited on p. 22)
URL: http://www.arrs.org/Publications/HRS.aspx (Visited on 19th May 2015)

[Pol96b] Myron **Pollycove**. 'Nuclear Medicine'. In: *A History of the Radiological Sciences: Diagnosis*. Ed. by Raymond **Gagliardi** and Bruce L. **McClennan**. 1996. Chap. 18, pp. 443–469. (Cited on pp. 24, 38)
URL: http://www.arrs.org/Publications/HRS.aspx (Visited on 19th May 2015)

[Pop72] Karl R. **Popper**. *Objective Knowledge. An Evolutionary Approach*. Oxford: Clarendon Press, 1972. ISBN: 978-0198750246. (Cited on pp. 4, 5)

[Pot12] Guillaume **Potdevin**, Andreas **Malecki**, Thomas **Biernath**, Martin **Bech**, Torben H. **Jensen**, Robert **Feidenhans'l**, Irene **Zanette**, Timm **Weitkamp**, Johannes **Kenntner**, Jürgen **Mohr**, Paul **Roschger**, Michael **Kerschnitzki**, Wolfgang **Wagermaier**, Klaus **Klaushofer**, Peter **Fratzl** and Franz **Pfeiffer**. 'X-ray vector radiography for bone micro-architecture diagnostics'. In: *Physics in Medicine and Biology* 57.11 (June 2012), pp. 3451–3461. (Cited on p. 149)
DOI: 10.1088/0031-9155/57/11/3451

[Pre85] William Henry **Preece**. 'On a Peculiar Behaviour of Glow-Lamps When Raised to High Incandescence'. In: *Proceedings of the Royal Society of London* 38 (Mar. 1885), pp. 219–230. (Cited on p. 11)
DOI: 10.1098/rspl.1884.0093

[Prü06] Marcus **Prümmer**, L. **Wigström**, J. **Hornegger**, Jan **Boese**, Günter **Lauritsch**, Norbert **Strobel** and Rebecca **Fahrig**. 'Cardiac C-arm CT: Efficient Motion Correction for 4D-FBP'. In: *IEEE Nuclear Science Symposium and Medical Imaging Conference* 4 (Oct. 2006), pp. 2620–2628. (Cited on p. 89)
DOI: 10.1109/NSSMIC.2006.354444

[Pul96] Ivan Pavlovich **Puluj**. 'On Kathode Rays'. In: *Proceedings of the Physical Society of London* 14 (Mar. 1896), p. 178. (Cited on p. 9)
DOI: 10.1088/1478-7814/14/1/315

[R96] S. J. **R.** 'Some Effects of the X-Rays on the Hands'. In: *Nature* 54.1409 (Oct. 1896), p. 621. (Cited on p. 25)
DOI: 10.1038/054621b0

[Rad07] Johann **Radon**. 'On the Determination of Functions From Their Integrals Along Certain Manifolds'. In: *The Radon Transform and Some of Its Applications*. Ed. by Stanley R. **Deans**. Trans. by R. **Lohner**. Mineola: Dover, 2007, pp. 204–217. ISBN: 978-0486462417. (Cited on pp. 48, 81)

[Rad17] Johann **Radon**. 'Über die Bestimmung von Funktionen durch ihre Integralwerte längs gewisser Mannigfaltigkeiten [On the Determination of Functions From Their Integral Values Along Certain Manifolds]'. In: *Berichte über die Verhandlungen der Königlich Sächsischen Gesellschaft der Wissenschaften zu Leipzig* 69 (Apr. 1917), pp. 262–277. (Cited on pp. 48, 49, 81)
URL: http://people.csail.mit.edu/bkph/courses/papers/Exact_Conebeam/Radon_Deutsch_1917.pdf (Visited on 23rd June 2015)

[Rad86] Johann **Radon**. 'On the Determination of Functions From Their Integral Values Along Certain Manifolds'. Trans. by P. C. **Parks**. In: *IEEE Transactions on Medical Imaging* 5.4 (Dec. 1986), pp. 170–176. (Cited on pp. 48, 81)
DOI: 10.1109/TMI.1986.4307775

[Raf11] Hedyeh **Rafii-Tari**, Purang **Abolmaesumi** and Robert **Rohling**. 'Panorama ultrasound for guiding epidural anesthesia: a feasibility study'. In: *Information Processing in Computer-Assisted Interventions (IPCAI)*. Vol. 6689. Lecture Notes in Computer Science. June 2011, pp. 179–189. (Cited on p. 108)
DOI: 10.1007/978-3-642-21504-9_17

[Rah12] Kambiz **Rahbar**, Mario **Colombo-Benkmann**, Christina **Haane**, Christian **Wenning**, Alexis **Vrachimis**, Matthias **Weckesser** and Otmar **Schober**. 'Intraoperative 3-D mapping of parathyroid adenoma using freehand SPECT'. In: *EJNMMI Research* 2 (Sept. 2012), p. 51. (Cited on p. 103)
DOI: 10.1186/2191-219X-2-51

[Ram71] G. N. **Ramachandran** and A. V. **Lakshminarayanan**. 'Three-dimensional Reconstruction from Radiographs and Electron Micrographs. Application of Convolutions instead of Fourier Transforms'. In: *Proceedings of the National Academy of Sciences of the United States of America* 68.9 (Sept. 1971), pp. 2236–2240. (Cited on p. 52)
URL: http://www.pnas.org/content/68/9/2236.abstract (Visited on 23rd June 2015)

[Rat05] Yogesh **Rathi**, Namrata **Vaswani**, Allen **Tannenbaum** and Anthony **Yezzi**. 'Particle Filtering for Geometric Active Contours with Application to Tracking Moving and Deforming Objects'. In: *IEEE Computer Society Conference on Computer Vision and Pattern Recognition (CVPR)* 2 (June 2005), pp. 2–9. (Cited on p. 91)
DOI: 10.1109/CVPR.2005.271

[Rau11] Rainer **Raupach** and Thomas G. **Flohr**. 'Analytical evaluation of the signal and noise propagation in x-ray differential phase-contrast computed tomography'. In: *Physics in Medicine and Biology* 56.7 (Apr. 2011), pp. 2219–2244. (Cited on p. 146)
DOI: 10.1088/0031-9155/56/7/020

[Rau12] Rainer **Raupach** and Thomas G. **Flohr**. 'Performance evaluation of x-ray differential phase contrast computed tomography (PCT) with respect to medical imaging'. In: *Medical Physics* 39.8 (Aug. 2012), pp. 4761–4774. (Cited on p. 146)
DOI: 10.1118/1.4736529

[RBB15] **Radio Berlin-Brandenburg**. *Berlin untersucht Flüchtlinge künftig auch im Röntgenbus [Berlin to examine refugees also in mobile X-ray unit]*. July 2015. (Cited on p. 27)
URL: http://www.rbb-online.de/politik/thema/fluechtlinge/berlin/roentgenbus-lageso-fluechtlinge-tuberkulose.html (Visited on 16th Sept. 2015)

[Reg09] Antonia **Rego-Iraeta**, Luisa F. **Pérez-Méndez**, Beatriz **Mantinan** and Ricardo V. **Garcia-Mayor**. 'Time Trends for Thyroid Cancer in Northwestern Spain: True Rise in the Incidence of Micro and Larger Forms of Papillary Thyroid Carcinoma'. In: *Thyroid* 19.4 (Apr. 2009), pp. 333–340. (Cited on p. 104)
DOI: 10.1089/thy.2008.0210

[Rén52] A. **Rényi**. 'On Projections of Probability Distributions'. In: *Acta Mathematica Academiae Scientiarum Hungarica* 3.3 (Sept. 1952), pp. 131–142. (Cited on p. 81)
DOI: 10.1007/BF02022515

[Rev11] V. **Revol**, I. **Jerjen**, C. **Kottler**, P. **Schütz**, R. **Kaufmann**, T. **Lüthi**, U. **Sennhauser**, U. **Straumann** and C. **Urban**. 'Sub-pixel porosity revealed by x-ray scatter dark field imaging'. In: *Journal of Applied Physics* 110.4 (Aug. 2011), p. 044912. (Cited on p. 147)
DOI: 10.1063/1.3624592

[Rev12] V. **Revol**, C. **Kottler**, R. **Kaufmann**, A. **Neels** and A. **Dommann**. 'Orientation-selective X-ray dark field imaging of ordered systems'. In: *Journal of Applied Physics* 112 (2012), p. 114903. (Cited on pp. 153, 154)
DOI: 10.1063/1.4768525

[Rhe12] Connie M. **Rhee**, Ishir **Bhan**, Erik K. **Alexander** and Steven M. **Brunelli**. 'Association Between Iodinated Contrast Media Exposure and Incident Hyperthyroidism and Hypothyroidism'. In: *Archives of Internal Medicine* 172.2 (Jan. 2012), pp. 153–159. (Cited on p. 140)
DOI: 10.1001/archinternmed.2011.677

[Ric79] Paul G. **Richards**. 'Theoretical Seismic Wave Propagation'. In: *Reviews of Geophysics and Space Physics* 17.2 (Apr. 1979), pp. 312–328. (Cited on p. 82)
DOI: 10.1029/RG017i002p00312

[Rie11] A. **Rieger**, J. **Saeckl**, B. **Belloni**, R. **Hein**, Aslı **Okur**, Klemens **Scheidhauer**, Thomas **Wendler**, Joerg **Traub**, H. **Friess** and Marc E. **Martignoni**. 'First Experiences with Navigated Radio-Guided Surgery Using Freehand SPECT'. In: *Case Reports in Oncology* 4.2 (Aug. 2011), pp. 420–425. (Cited on p. 103)
DOI: 10.1159/000330273

[Rit06] Johann Wilhelm **Ritter**. 'Bemerkungen zu Herschel's neueren Untersuchungen über das Licht [Remarks about Herschel's newer studies on light]'. In: *Physisch-Chemische Abhandlungen in chronologischer Folge [Physical-chemical treatises in chronological order]*. Vol. 2. Leipzig: Reclam, 1806, pp. 81–107. (Cited on p. 9)
URL: http://books.google.com/books?id=Wmc5AAAAcAAJ (Visited on 5th July 2015)

[Rob73] J. S. **Robertson**, R. B. **Marr**, M. **Rosenblum**, V. **Radeka** and Y. L. **Yamamoto**. '32-Crystal Positron Transverse Section Detector'. In: *Tomographic Imaging in Nuclear Medicine*. Ed. by Gerald S. **Freedman**. New York: The Society of Nuclear Medicine, 1973, pp. 142–153. (Cited on p. 41)

[Roh09] Christopher **Rohkohl**, Günter **Lauritsch**, Marcus **Prümmer**, Jan **Boese** and Joachim **Hornegger**. 'Towards 4-D Cardiac Reconstruction without ECG and Motion Periodicity using C-arm CT'. In: *Proceedings of International Meeting on Fully Three-Dimensional Image Reconstruction in Radiology and Nuclear Medicine (Fully3D)*. Sept. 2009, pp. 323–326. (Cited on p. 90)
URL: http://www.fully3d.org/2009/3D09Proceedings.pdf (Visited on 5th July 2015)

[Roh12] Christopher **Rohkohl**. 'Motion Estimation and Compensation for Interventional Cardiovascular Image Reconstruction'. PhD thesis. Erlangen: Friedrich-Alexander-Universität Erlangen-Nürnberg, Dec. 2012. (Cited on p. 90)
URL: http://nbn-resolving.de/urn/resolver.pl?urn:nbn:de:bvb:29-opus-22150 (Visited on 1st July 2015)

[Rol03] William Herbert **Rollins**. *Notes on X-Light*. Boston, 1903. (Cited on pp. 12, 26)
URL: https://archive.org/details/notesonxlight00roll (Visited on 5th July 2015)

[Rön95] Wilhelm Conrad **Röntgen**. 'Über eine neue Art von Strahlen [On a New Kind of Rays]'. In: *Sitzungsberichte der Physikalisch-Medizinischen Gesellschaft in Würzburg* 137 (Dec. 1895), pp. 132–141. (Cited on pp. 9, 10, 19, 23)
URL: http://www.nbn-resolving.org/urn/resolver.pl?urn=urn:nbn:de:kobv:b4-200905194973 (Visited on 5th July 2015)

[Rön96] Wilhelm Conrad **Röntgen**. 'On a New Kind of Rays'. In: *Nature* 53.1369 (Jan. 1896), pp. 274–276. (Cited on pp. 9, 10, 19)
DOI: 10.1038/053274b0

[Rud92] Leonid I. **Rudin**, Stanley **Osher** and Emad **Fatemi**. 'Nonlinear total variation based noise removal algorithms'. In: *Physica D: Nonlinear Phenomena* 6.1–4 (Nov. 1992), pp. 259–268. (Cited on pp. 72, 73, 76)
DOI: 10.1016/0167-2789(92)90242-F

[Run10] Philipp Otto **Runge**. *Die Farbenkugel [The Colour Sphere]*. Hamburg, 1810. (Cited on p. 6)

[Run95] Carl **Runge**. 'Über die numerische Auflösung von Differentialgleichungen [About Numerically Solving Differential Equations]'. In: *Mathematische Annalen* 46.2 (June 1895), pp. 167–178. (Cited on p. 159)
DOI: 10.1007/BF01446807

[Rut03] Ernest **Rutherford**. 'The Magnetic and Electric Deviation of the easily absorbed Rays from Radium'. In: *Philosophical Magazine*. 6th ser. 5.26 (Feb. 1903), pp. 177–187. (Cited on p. 18)
DOI: 10.1080/14786440309462912

[Rut08a] Ernest **Rutherford**. *The Chemical Nature of the Alpha Particles from Radioactive Substances*. Nobel Lecture. Dec. 1908. (Cited on p. 18)
URL: http://www.nobelprize.org/nobel_prizes/chemistry/laureates/1908/rutherford-lecture.html (Visited on 5th July 2015)

[Rut08b] Ernest **Rutherford** and Hans Wilhelm **Geiger**. 'An Electrical Method of Counting the Number of α-Particles from Radio-active Substances'. In: *Proceedings of the Royal Society of London. A* 81.546 (Aug. 1908), pp. 141–161. (Cited on p. 21)
DOI: 10.1098/rspa.1908.0065

[Rut14] Ernest **Rutherford** and Edward Neville da Costa **Andrade**. 'The Wave-Length of the Soft γ-Rays from Radium B'. In: *Philosophical Magazine*. 6th ser. 27.161 (1914), pp. 854–868. (Cited on p. 18)
DOI: 10.1080/14786440508635156

[Rut99] Ernest **Rutherford**. 'Uranium Radiation and the Electrical Conduction produced by it'. In: *Philosophical Magazine*. 5th ser. 47.284 (1899), pp. 109–163. (Cited on p. 18)
DOI: 10.1080/14786449908621245

[Saa03] Yousef **Saad**. *Iterative Methods for Sparse Linear Systems*. Second edition. Philadelphia: SIAM, 2003. ISBN: 978-0898715347. (Cited on pp. 57, 59)
URL: http://www-users.cs.umn.edu/~saad/books.html (Visited on 25th June 2015)

[San80] Marcelino **Sanz de Sautuola**. *Breves apuntes sobre algunos objetos prehistóricos de la provincia de Santander [Short notes about some prehistoric objects in the province of Santander]*. Santander, 1880. (Cited on p. 3)
URL: http://www.europeana.eu/portal/record/91956/u__fulletsAB_5302.html (Visited on 4th Sept. 2015)

[Sch06] Dirk **Schäfer**, Jörn **Borgert**, Volker **Rasche** and Michael **Grass**. 'Motion-Compensated and Gated Cone Beam Filtered Back-Projection for 3-D Rotational X-Ray Angiography'. In: *IEEE Transactions on Medical Imaging* 25.7 (July 2006), pp. 898–906. (Cited on p. 89)
DOI: 10.1109/TMI.2006.876147

[Sch07] Jörg D. **Schoenen**. *Medizinisches ABC-Manual [Medical ABC-Manual]*. Website. Feb. 2007. (Cited on p. 27)
URL: http://www.j-schoenen.de/abc-manual/ (Visited on 4th May 2015)

[Sch11] Caitlin **Schneider**, Julian **Guerrero**, Christopher **Nguan**, Robert **Rohling** and Septimiu **Salcudean**. 'Intra-operative "Pick-Up" Ultrasound for Robot Assisted Surgery with Vessel Extraction and Registration. A Feasibility Study'. In: *Information Processing in Computer-Assisted Interventions (IPCAI)*. Vol. 6689. Lecture Notes in Computer Science. June 2011, pp. 122–132. (Cited on p. 101)
DOI: 10.1007/978-3-642-21504-9_12

[Sch12] Andreas **Schnelzer**, Alexandra **Ehlerding**, Christina **Blümel**, Aslı **Okur**, Klemens **Scheidhauer**, Stefan **Paepke** and Marion **Kiechle**. 'Showcase of Intraoperative 3D Imaging of the Sentinel Lymph Node in a Breast Cancer Patient using the New Freehand SPECT Technology'. In: *Breast Care* 7.6 (Dec. 2012), pp. 484–486. (Cited on p. 103)
DOI: 10.1159/000345472

[Sch14] Florian **Schaff**, Andreas **Malecki**, Guillaume **Potdevin**, Elena **Eggl**, Peter B. **Noël**, Thomas **Baum**, Eduardo **Grande Garcia**, Jan S. **Bauer** and Franz **Pfeiffer**. 'Correlation of X-Ray Vector Radiography to Bone Micro-Architecture'. In: *Scientific Reports* 4 (Jan. 2014), p. 3695. (Cited on p. 149)
DOI: 10.1038/srep03695

[Seg01a] William Paul **Segars**. 'Development of a New Dynamic NURBS-Based Cardiac-Torso (NCAT) Phantom'. PhD thesis. Chapel Hill: University of North Carolina, May 2001. (Cited on pp. 96, 97)

[Seg01b] William Paul **Segars**, David S. **Lalush** and Benjamin M. W. **Tsui**. 'Modeling Respiratory Mechanics in the MCAT and Spline-Based MCAT Phantoms'. In: *IEEE Transactions on Nuclear Science* 48.1 (Feb. 2001), pp. 89–97. (Cited on pp. 96, 97)
DOI: 10.1109/23.910837

[Seg99] William Paul **Segars**, David S. **Lalush** and Benjamin M. W. **Tsui**. 'A Realistic Spline-Based Dynamic Heart Phantom'. In: *IEEE Transactions on Nuclear Science* 46.3 (June 1999), pp. 503–506. (Cited on pp. 96, 97)
DOI: 10.1109/23.775570

[Set99] James A. **Sethian**. *Level Set Methods and Fast Marching Methods. Evolving Interfaces in Computational Geometry, Fluid Mechanics, Computer Vision, and Materials Science*. Second Edition. Cambridge Monographs on Applied and Computational Mathematics. New York: Cambridge University Press, Aug. 1999. ISBN: 978-0521645577. (Cited on p. 90)

[Sha97] Y. **Shao**, S. R. **Cherry**, K. **Farahani**, R. **Slates**, R. W. **Silverman**, K. **Meadors**, A. **Bowery**, S. **Siegel**, P. K. **Marsden** and P. B. **Garlick**. 'Development of a PET Detector System Compatible with MRI/NMR Systems'. In: *IEEE Transaction on Nuclear Science* 44.3 (June 1997), pp. 1167–1171. (Cited on p. 45)
DOI: 10.1109/23.596982

[She82] Lawrence A. **Shepp** and Yehuda **Vardi**. 'Maximum Likelihood Reconstruction for Emission Tomography'. In: *IEEE Transactions on Medical Imaging* 1.2 (Oct. 1982), pp. 113–122. (Cited on p. 66)
DOI: 10.1109/TMI.1982.4307558

[She94] Jonathan Richard **Shewchuk**. *An Introduction to the Conjugate Gradient Method Without the Agonizing Pain*. Edition $1\frac{1}{4}$. Pittsburgh: Carnegie Mellon University, Aug. 1994. (Cited on pp. 61, 63, 64, 69, 155)
URL: http://www.cs.cmu.edu/~quake-papers/painless-conjugate-gradient.pdf (Visited on 5th July 2015)

[Sid11] S. **Sidhu**, G. **Falzon**, S. A. **Hart**, J. G. **Fox**, R. A. **Lewis** and K. K. W. **Siu**. 'Classification of breast tissue using a laboratory system for small-angle x-ray scattering (SAXS)'. In: *Physics in Medicine and Biology* 56.21 (Oct. 2011), pp. 6779–6791. (Cited on p. 146)
DOI: 10.1088/0031-9155/56/21/002

[Sid85] Robert L. **Siddon**. 'Fast calculation of the exact radiological path for a three-dimensional CT array'. In: *Medical Physics* 12.2 (1985), pp. 252–255. (Cited on pp. 57, 161)
DOI: 10.1118/1.595715

[Sim12] Edgar P. **Simard**, Elizabeth M. **Ward**, Rebecca **Siegel** and Ahmedin **Jemal**. 'Cancers with increasing incidence trends in the United States: 1999 through 2008'. In: *CA: A Cancer Journal for Clinicians* 62.2 (Mar. 2012), pp. 118–128. (Cited on p. 104)
DOI: 10.3322/caac.20141

[Sle61] David S. **Slepian** and Henry O. **Pollak**. 'Prolate Spheroidal Wave Functions, Fourier Analysis and Uncertainty — I'. In: *Bell System Technical Journal* 40.1 (Jan. 1961), pp. 43–63. (Cited on p. 50)
DOI: 10.1002/j.1538-7305.1961.tb03976.x

[Sle64] David S. **Slepian**. 'Prolate Spheroidal Wave Functions, Fourier Analysis and Uncertainty — IV. Extensions to Many Dimensions; Generalized Prolate Spheroidal Functions'. In: *Bell System Technical Journal* 43.6 (Nov. 1964), pp. 3009–3057. (Cited on p. 50)
DOI: 10.1002/j.1538-7305.1964.tb01037.x

[Slu86] A. van der **Sluis** and H. A. van der **Vorst**. 'The Rate of Convergence of Conjugate Gradients'. In: *Numerische Mathematik* 48.5 (Sept. 1986), pp. 543–560. (Cited on pp. 61, 63)
DOI: 10.1007/BF01389450

[Slu90] A. van der **Sluis** and H. A. van der **Vorst**. 'SIRT- and CG-Type Methods for the Iterative Solution of Sparse Linear Least-Squares Problems'. In: *Linear Algebra and Its Applications* 130 (Mar. 1990), pp. 257–302. (Cited on pp. 60, 63)
DOI: 10.1016/0024-3795(90)90215-X

[Smi77] Kennan T. **Smith**, Donald C. **Solomon** and Sheldon L. **Wagner**. 'Practical and mathematical aspects of the problem of reconstructing objects from radiographs'. In: *Bulletin of the American Mathematical Society* 83.6 (Nov. 1977), pp. 1227–1270. (Cited on p. 49)
DOI: 10.1090/S0002-9904-1977-14406-6

[Sni95] A. **Snigirev**, I. **Snigireva**, V. **Kohn**, S. **Kuznetsov** and I. **Schelokov**. 'On the possibilities of x-ray phase contrast microimaging by coherent high-energy synchrotron radiation'. In: *Review of Scientific Instruments* 66.12 (Dec. 1995), pp. 5486–5492. (Cited on p. 140)
DOI: 10.1063/1.1146073

[Son77] Susan **Sontag**. *On Photography*. New York, 1977. ISBN: 978-0713911282. (Cited on p. 6)

[Sør14] Hans Henrik B. **Sørensen** and Per Christian **Hansen**. 'Multicore Performance of Block Algebraic Iterative Reconstruction Methods'. In: *SIAM Journal of Scientific Computing* 36.5 (2014), pp. C524–C546. (Cited on pp. 59, 60, 155, 171)
DOI: 10.1137/130920642

[Sta10] Marco **Stampanoni**, Rajmund **Mokso**, Federica **Marone**, Joan **Vila-Comamala**, Sergey **Gorelick**, Pavel **Trtik**, Konstantin **Jefimovs** and Christian **David**. 'Phase-contrast tomography at the nanoscale using hard x rays'. In: *Physical Review B* 81.14 (Apr. 2010), p. 140105. (Cited on p. 140)
DOI: 10.1103/PhysRevB.81.140105

[Sta11] Marco **Stampanoni**, Zhentian **Wang**, Thomas **Thüring**, Christian **David**, Ewald **Roessl**, Mafalda **Trippel**, Rahel A. **Kubik-Huch**, Gad **Singer**, Michael K. **Hohl** and Nik **Hauser**. 'The First Analysis and Clinical Evaluation of Native Breast Tissue Using Differential Phase-Contrast Mammography'. In: *Investigative Radiology* 46.12 (Dec. 2011), pp. 801–806. (Cited on p. 146)
DOI: 10.1097/RLI.0b013e31822a585f

[Ste04] Gabriele **Steidl**, Joachim **Weickert**, Thomas **Brox**, Pavel **Mrázek** and Martin **Welk**. 'On the Equivalence of Soft Wavelet Shrinkage, Total Variation Diffusion, Total Variation Regularization, and SIDEs'. In: *SIAM Journal on Numerical Analysis* 42.2 (2004), pp. 686–713. (Cited on p. 77)
DOI: 10.1137/S0036142903422429

[Sti52] Eduard **Stiefel**. 'Über einige Methoden der Relaxationsrechnung [On Some Methods of the Relaxation Technique]'. In: *Zeitschrift für angewandte Mathematik und Physik* 3.1 (Jan. 1952), pp. 1–33. (Cited on p. 61)
DOI: 10.1007/BF02080981

[Str06] Thomas **Strohmer** and Roman **Vershynin**. 'A Randomized Solver for Linear Systems with Exponential Convergence'. In: *Approximation, Randomization, and Combinatorial Optimization. Algorithms and Techniques*. Vol. 4110. Lecture Notes in Computer Science. Springer, Aug. 2006, pp. 499–507. (Cited on p. 121)
DOI: 10.1007/11830924_45

[Str09] Gilbert **Strang**. *Introduction to Linear Algebra*. Fourth edition. Wellesley: Wellesley-Cambridge Press, 2009. ISBN: 978-0980232714. (Cited on p. 57)

[Str79] John W. **Strohbehn**, Carter H. **Yates**, Bruce H. **Curran** and Edward S. **Sternick**. 'Image Enhancement of Conventional Transverse-Axial Tomograms'. In: *IEEE Transactions on Biomedical Engineering* 26.5 (May 1979), pp. 253–262. (Cited on p. 30)
DOI: 10.1109/TBME.1979.326400

[Str81] John William **Strutt** (Lord Rayleigh). 'On Copying Diffraction-gratings, and on some Phenomena connected therewith'. In: *Philosophical Magazine*. 5th ser. 11.67 (Mar. 1881), pp. 196–205. (Cited on p. 140)
DOI: 10.1080/14786448108626995

[Swi96] Alan Archibald Campbell **Swinton**. 'Professor Röntgen's Discovery'. In: *Nature* 53.1369 (Jan. 1896), pp. 276–277. (Cited on pp. 9, 10)
DOI: 10.1038/053276a0

[Sza47] Jacek **Szarski** and Tadeusz **Ważewski**. 'Sur un Problème Roentgenographique de M. S. Majerek [On a Roentgenographic problem by S. Majerek]'. In: *Annales de la Société Polonaise de Mathématique* 20 (1947), pp. 389–390. (Cited on p. 82)
URL: https://books.google.de/books?id=2_i6AAAAIAAJ (Visited on 30th June 2015)

[Tal36] Henry Fox **Talbot**. 'Facts relating to Optical Science'. In: *Philosophical Magazine*. 3rd ser. 9.56 (Dec. 1836), pp. 401–407. (Cited on p. 140)
DOI: 10.1080/14786443608649032

[Tay91] Russell H. **Taylor**, Howard A. **Paul**, Peter **Kazanzides**, Brent D. **Mittelstadt**, William **Hanson**, Joel **Zuhars**, Bill **Williamson**, Bela **Musits**, Edward **Glassman** and William L. **Bargar**. 'Taming the Bull. Safety in a Precise Surgical Robot'. In: *International Conference on Advanced Robotics (ICAR)*. Vol. 1. June 1991, pp. 865–870. (Cited on pp. 111, 132)
DOI: 10.1109/ICAR.1991.240565

[Ten02] C. R. **Tench**, P. S. **Morgan**, M. **Wilson** and L. D. **Blumhardt**. 'White Matter Mapping Using Diffusion Tensor MRI'. In: *Magnetic Resonance in Medicine* 47.5 (May 2002), pp. 967–972. (Cited on p. 159)
DOI: 10.1002/mrm.10144

[Ter75] Michel M. **Ter-Pogossian**, Michael E. **Phelps**, Edward J. **Hoffman** and Nizar A. **Mullani**. 'A Positron-Emission Transaxial Tomograph for Nuclear Imaging (PETT)'. In: *Radiology* 114.1 (Jan. 1975), pp. 89–98. (Cited on p. 42)
DOI: 10.1148/114.1.89

[Ter79] Michel M. **Ter-Pogossian**. 'Imaging Device for Computerized Emission Tomography'. Patent US 4,150,292. Apr. 1979. (Cited on p. 42)
URL: http://worldwide.espacenet.com/publicationDetails/biblio?CC=US&NR=4150292 (Visited on 5th July 2015)

[Tes96] Nikola **Tesla**. 'On Roentgen Rays'. In: *Electrical Review* 28.11 (Mar. 1896), pp. 131, 134–135. (Cited on p. 10)
URL: http://www.teslauniverse.com/nikola-tesla/articles/roentgen-rays (Visited on 4th Sept. 2015)

[Thi08] Pierre **Thibault**, Martin **Dierolf**, Andreas **Menzel**, Oliver **Bunk**, Christian **David** and Franz **Pfeiffer**. 'High-Resolution Scanning X-ray Diffraction Microscopy'. In: *Science* 321.5887 (July 2008), pp. 379–382. (Cited on p. 140)
DOI: 10.1126/science.1158573

[Tik63] Andrey N. **Tikhonov**. 'Solution of Incorrectly Formulated Problems and the Regularization Method'. In: *Soviet Mathematics* 4 (1963), pp. 1035–1038. (Cited on p. 72)

[Trü97] Joachim E. **Trümper**. 'X-rays from the Universe'. In: *Röntgen Centennial. X-rays in Natural and Life Sciences*. Ed. by Axel **Haase**, Gottfried **Landwehr** and Eberhard **Umbach**. Singapore: World Scientific, 1997, pp. 27–44. ISBN: 978-9810230852. (Cited on p. 10)

[Tur02] I. **Turai**, ed. *The Radiological Accident in Gilan*. Vienna: International Atomic Energy Agency, 2002. ISBN: 978-9201105028. (Cited on p. 28)
URL: http://www-pub.iaea.org/books/IAEABooks/6284/The-Radiological-Accident-in-Gilan (Visited on 5th July 2015)

[Uhl25] George E. **Uhlenbeck**. 'Over een Stelling van Lorentz en haar Uitbreiding voor Meerdimensionale Ruimten [On a Theorem of Lorentz and Its Extension for Multidimensional Spaces]'. In: *Physica. Nederlandsch Tijdschrift voor Natuurkunde*. Vol. 5. 1925, pp. 423–428. (Cited on p. 81)
URL: http://hdl.handle.net/2027/uc1.$b561889 (Visited on 30th June 2015)

[Vai72] B. K. **Vainshtein** and S. S. **Orlov**. 'Theory of the Recovery of Functions from Their Projections'. In: *Soviet Physics, Crystallography* 17.2 (Sept. 1972), pp. 213–216. (Cited on p. 82)

[Val30] Alessandro **Vallebona**. 'Una modalità di tecnica per la dissociazione radiografica delle ombre applicata allo studio del cranio [A Technical Method for the Radiographic Dissociation of the Shadows, Applied to a Study of the Skull]'. In: *La Radiologia Medica* 17.9 (1930), pp. 1090–1097. (Cited on p. 30)

[Val31] Alessandro **Vallebona**. 'Radiography with Great Enlargement (Microradiography) and a Technical Method for the Radiographic Dissociation of the Shadow'. In: *Radiology* 17.2 (Aug. 1931), pp. 340–341. (Cited on p. 30)
DOI: 10.1148/17.2.340

[Ves74] C. M. **Vest**. 'Formation of Images from Projections. Radon and Abel transforms'. In: *Journal of the Optical Society of America* 64.9 (Sept. 1974), pp. 1215–1218. (Cited on p. 82)
DOI: 10.1364/JOSA.64.001215

[Vog06] Hermann **Vogel**. 'Das Ehrenmal der Radiologie in Hamburg [The Radiology Monument in Hamburg]'. In: *Fortschritte auf dem Gebiet der Röntgenstrahlen und der bildgebenden Verfahren* 178.8 (2006), pp. 753–756. (Cited on p. 26)
DOI: 10.1055/s-2006-948089

[Vog08] Jakob **Vogel**. 'Quality Estimation for Non-Linear Optimization'. Project report. München: Technische Universität München, Department of Mathematics, Oct. 2008. (Cited on p. 177)

[Vog09a] Jakob **Vogel**. 'Automatic Multi-Organ Segmentation in the Abdomen'. Project report. München: Technische Universität München, Department of Computer Science, Jan. 2009. (Cited on p. 177)

[Vog09b] Jakob **Vogel**. 'Symbolic 3D+t Reconstruction from Cone-Beam Projections'. Diploma thesis. München: Technische Universität München, Department of Computer Science, Sept. 2009. (Cited on pp. 87, 96)

[VwReformG] 'Zweites Verwaltungsreformgesetz'. In: *Bayerisches Gesetz- und Verordnungsblatt*. 8. See Art. 17. Mar. 2000, p. 139. (Cited on p. 27)
URL: https://www.verkuendung-bayern.de/files/gvbl/2000/08/gvbl-2000-08.pdf (Visited on 16th Sept. 2015)

[Wak11] Ryotaro **Wake**, Minoru **Yoshiyama**, Hidetaka **Iida**, Hiroaki **Takeshita**, Takanori **Kusuyama**, Hitoshi **Kanamitsu**, Hideya **Mitsui**, Yukio **Yamada**, Shinichi **Shimodozono** and Kazuo **Haze**. 'History of Coronary Angiography'. In: *Advances in the Diagnosis of Coronary Atherosclerosis*. Ed. by Suna **Kirac**. Nov. 2011. Chap. 4, pp. 69–80. ISBN: 978-9533072869. (Cited on pp. 22, 87)
DOI: 10.5772/22578

[Wan14] Zhentian **Wang**, Nik **Hauser**, Gad **Singer**, Mafalda **Trippel**, Rahel A. **Kubik-Huch**, Christof W. **Schneider** and Marco **Stampanoni**. 'Non-invasive classification of microcalcifications with phase-contrast X-ray mammography'. In: *Nature Communications* 5 (May 2014), p. 3797. (Cited on p. 146)
DOI: 10.1038/ncomms4797

[Wat40] William **Watson**. 'X-ray Apparatus'. Patent US 2,196,618. Apr. 1940. (Cited on p. 32)
URL: http://worldwide.espacenet.com/publicationDetails/biblio?CC=US&NR=2196618 (Visited on 5th July 2015)

[Web15] Christian **Weber**. 'Sternen-Porno [Star Porn]'. In: *Süddeutsche Zeitung* (Apr. 2015). (Cited on p. 7)
URL: http://sz.de/1.2439548 (Visited on 18th Apr. 2015)

[Web90] Steve **Webb**. *From the Watching of Shadows. The Origins of Radiological Tomography*. Bristol: Adam Hilger, 1990. ISBN: 978-0852743058. (Cited on pp. 35, 39, 42)

[Wei00a] Irving N. **Weinberg**, Valera **Zawarzin**, Roberto **Pani** and Giuseppe **DeVincentes**. 'Implementing Reconstruction with Hand-Held Gamma Cameras'. In: *IEEE Nuclear Science Symposium and Medical Imaging Conference* 3 (Oct. 2000), pp. 21/101–21/104. (Cited on p. 106)
DOI: 10.1109/NSSMIC.2000.949360

[Wei00b] D. **Weiß**, G. **Schneider**, B. **Niemann**, P. **Guttmann**, D. **Rudolph** and G. **Schmahl**. 'Computed tomography of cryogenic biological specimens based on X-ray microscopic images'. In: *Ultramicroscopy* 84.3–4 (Aug. 2000), pp. 185–197. (Cited on p. 140)
DOI: 10.1016/S0304-3991(00)00034-6

[Wei01] Irving N. **Weinberg**, Valera **Zawarzin**, Pavel **Stepanov**, David **Beiline**, Roberto **Pani**, Giuseppe **DeVincentes**, Jian-Chao **Zeng** and Lee P. **Adler**. 'Flexible Geometries for Hand-held PET and SPECT Cameras'. In: *IEEE Nuclear Science Symposium and Medical Imaging Conference* 2 (Nov. 2001), pp. 1133–1136. (Cited on p. 106)
DOI: 10.1109/NSSMIC.2001.1009750

[Wei05] Timm **Weitkamp**, Ana **Diaz**, Christian **David**, Franz **Pfeiffer**, Marco **Stampanoni**, Peter **Cloetens** and Eric **Ziegler**. 'X-ray phase imaging with a grating interferometer'. In: *Optics Express* 13.16 (Aug. 2005), pp. 6296–6304. (Cited on p. 140)
DOI: 10.1364/OPEX.13.006296

[Wen07b] Thomas **Wendler**, Alexander **Hartl**, Tobias **Lasser**, Joerg **Traub**, Farhad **Daghighian**, Sibylle I. **Ziegler** and Nassir **Navab**. 'Towards Intra-operative 3D Nuclear Imaging. Reconstruction of 3D Radioactive Distributions Using Tracked Gamma Probes'. In: *Medical Image Computing and Computer-Assisted Intervention (MICCAI)*. Lecture Notes in Computer Science 4792 (Oct. 2007), pp. 252–260. (Cited on p. 101)
DOI: 10.1007/978-3-540-75759-7_110

[Wen10a] Thomas **Wendler**. '3D Intraoperative Functional Imaging with Navigated Probes'. PhD thesis. München: Technische Universität München, Department of Computer Science, Oct. 2010. (Cited on p. 106)
URL: http://nbn-resolving.de/urn/resolver.pl?urn:nbn:de:bvb:91-diss-20101005-997268-1-8 (Visited on 3rd July 2015)

[Wen10b] Thomas **Wendler**, Ken **Herrmann**, Andreas **Schnelzer**, Tobias **Lasser**, Joerg **Traub**, Olivier **Kutter**, Alexandra **Ehlerding**, Klemens **Scheidhauer**, Tibor **Schuster**, Marion **Kiechle**, Markus **Schwaiger**, Nassir **Navab**, Sibylle I. **Ziegler** and Andreas K. **Buck**. 'First demonstration of 3-D lymphatic mapping in breast cancer using freehand SPECT'. In: *European Journal of Nuclear Medicine and Molecular Imaging* 37.8 (Aug. 2010), pp. 1452–1461. (Cited on pp. 102, 117, 131)
DOI: 10.1007/s00259-010-1430-4

[Whe00] J. **Wheatley** and I. **Turai**, eds. *The Radiological Accident in Yanango*. Vienna: International Atomic Energy Agency, 2000. ISBN: 978-9201015006. (Cited on p. 28)
URL: http://www-pub.iaea.org/books/IAEABooks/6090/The-Radiological-Accident-in-Yanango (Visited on 5th July 2015)

[Wik15] **Wikipedia**. *Röntgenreihenuntersuchung*. 2015. (Cited on p. 27)
URL: https://de.wikipedia.org/w/index.php?title=R%C3%B6ntgenreihenuntersuchung&oldid=144704184 (Visited on 16th Sept. 2015)

[Wil14] Marian **Willner**, Julia **Herzen**, S. **Grandl**, S. **Auweter**, D. **Mayr**, A. **Hipp**, Michael **Chabior**, Adrian **Sarapata**, Klaus **Achterhold**, Irene **Zanette**, Timm **Weitkamp**, A. **Sztrókay**, K. **Hellerhoff**, M. **Reiser** and Franz **Pfeiffer**. 'Quantitative breast tissue characterization using grating-based x-ray phase-contrast imaging'. In: *Physics in Medicine and Biology* 59.7 (Apr. 2014), pp. 1557–1571. (Cited on p. 146)
DOI: 10.1088/0031-9155/59/7/1557

[Wil73] J. R. **Willis**. 'Self-Similar Problems in Elastodynamics'. In: *Philosophical Transactions of the Royal Society of London. A* 274.1240 (May 1973), pp. 435–491. (Cited on p. 82)
DOI: 10.1098/rsta.1973.0073

[Win97] Herman **Winick**. 'Synchrotron Radiation Sources: Past, Present and Future'. In: *Röntgen Centennial. X-rays in Natural and Life Sciences*. Ed. by Axel **Haase**, Gottfried **Landwehr** and Eberhard **Umbach**. Singapore: World Scientific, 1997, pp. 45–64. ISBN: 978-9810230852. (Cited on p. 15)

[Wre51] Frank R. **Wrenn** Jr., Myron L. **Good** and Philip **Handler**. 'The Use of Positron-emitting Radioisotopes for the Localization of Brain Tumors'. In: *Science* 113.2940 (May 1951), pp. 525–527. (Cited on p. 41)
DOI: 10.1126/science.113.2940.525

[Wu83] C. F. Jeff **Wu**. 'On the Convergence Properties of the EM Algorithm'. In: *Annals of Statistics* 11.1 (Mar. 1983), pp. 95–103. (Cited on p. 66)
URL: http://www.jstor.org/stable/2240463 (Visited on 27th June 2015)

[Yar13] Andre **Yaroshenko**, Felix G. **Meinel**, Martin **Bech**, Arne **Tapfer**, Astrid **Velroyen**, Simone **Schleede**, Sigrid **Auweter**, Alexander **Bohla**, Ali Ö. **Yildirim**, Konstantin **Nikolaou**, Fabian **Bamberg**, Oliver **Eickelberg**, Maximilian F. **Reiser** and Franz **Pfeiffer**. 'Pulmonary Emphysema Diagnosis with a Preclinical Small-Animal X-ray Dark-Field Scatter-Contrast Scanner'. In: *Radiology* 269.2 (Nov. 2013), pp. 427–433. (Cited on p. 146)
DOI: 10.1148/radiol.13122413

[Yoo06] Sungwon **Yoon**, Angel R. **Pineda** and Rebecca **Fahrig**. 'Level Set Reconstruction for Sparse Angularly Sampled Data'. In: *IEEE Nuclear Science Symposium and Medical Imaging Conference* 6 (Oct. 2006), pp. 3420–3423. (Cited on p. 91)
DOI: 10.1109/NSSMIC.2006.353736

[Zen11] Gengsheng L. **Zeng** and Grant T. **Gullberg**. 'Null-Space Function Estimation for the Three-Dimensional Interior Problem'. In: *Proceedings of International Meeting on Fully Three-Dimensional Image Reconstruction in Radiology and Nuclear Medicine (Fully3D)*. July 2011, pp. 241–245. (Cited on p. 117)

[Zer35] Frits **Zernike**. 'Das Phasenkontrastverfahren bei der mikroskopischen Beobachtung [The Phase Contrast Method for Microscopical Observation]'. In: *Zeitschrift für technische Physik* 16.11 (1935), pp. 454–457. (Cited on p. 139)
URL: http://hdl.handle.net/2027/mdp.39015011410357 (Visited on 5th July 2015)

[Zer36] Frits **Zernike**. 'Einrichtung zur Verdeutlichung optischer Abbildungen [Apparatus for the Clarification of Optical Images]'. Patent DE 636,168. Oct. 1936. (Cited on p. 139)
URL: http://worldwide.espacenet.com/publicationDetails/biblio?CC=DE&NR=636168 (Visited on 5th July 2015)

[Zer42a] Frits **Zernike**. 'Phase Contrast, a New Method for the Microscopic Observation of Transparent Objects. Part II'. In: *Physica* 9.10 (Dec. 1942), pp. 974–986. (Cited on p. 137)
DOI: 10.1016/S0031-8914(42)80079-8

[Zer42b] Frits **Zernike**. 'Phase Contrast, New Method for the Microscopic Observation of Transparent Objects. Part I'. In: *Physica* 9.7 (July 1942), pp. 686–698. (Cited on p. 137)
DOI: 10.1016/S0031-8914(42)80035-X

[Zer53] Frits **Zernike**. *How I discovered phase contrast*. Nobel Lecture. Dec. 1953. (Cited on p. 139)
URL: http://www.nobelprize.org/nobel_prizes/physics/laureates/1953/zernike-lecture.pdf (Visited on 5th July 2015)

[Zie00] Sibylle I. **Ziegler** and Bernd J. **Pichler**. 'Neue technische Entwicklungen in der Nuklearmedizin [Recent Technical Development in Nuclear Medicine]'. In: *Zeitschrift für Medizinische Physik* 10.4 (2000), pp. 237–245. (Cited on p. 43)
DOI: 10.1016/S0939-3889(15)70286-2

[Zie31] Bernard Georg **Ziedses des Plantes**. 'A Special Method of Making Roentgenograms of the Skull and Spinal Column'. In: *Nederlands Tijdschrift voor Geneeskunde* 75 (1931), pp. 5218–5222. (Cited on p. 30)

[Zie32] Bernard Georg **Ziedses des Plantes**. 'Eine neue Methode zur Differenzierung der Röntgenographie (Planigraphie) [A new Method for Differentiating Röntgenography (Planigraphy)]'. In: *Acta Radiologica* 13.2 (Mar. 1932), pp. 182–192. (Cited on p. 30)
DOI: 10.1177/028418513201300211

[Zik11] Darko **Zikic**. 'Contributions to Medical Image Registration'. PhD thesis. München: Technische Universität München, Department of Computer Science, Dec. 2011. (Cited on p. 101)
URL: http://nbn-resolving.de/urn/resolver.pl?urn:nbn:de:bvb:91-diss-20111220-1071971-1-4 (Visited on 3rd July 2015)

[Zin15] Kathrin **Zinkant**. 'Tücken der Bilanz [Pitfalls of the Balance]'. In: *Süddeutsche Zeitung* (June 2015). (Cited on p. 27)
URL: http://sz.de/1.2504049 (Visited on 10th June 2015)

List of Figures

List of Algorithms

Index